Department of Aeronautics

Imperial College London

Active Control of the Wake from a Rectangular-Sectioned Body

Sara Cabitza

This thesis is submitted in part fulfilment of the requirements for the degree of Doctor of Philosophy in Aeronautics of Imperial College London and the Diploma of Imperial College London

2014

Declaration

I certify that this is my original work and that all material in this dissertation which is not my own work has been properly acknowledged.

Sara Cabitza

Abstract

This work of thesis is part of a wider research project with the aim of developing an aerodynamic active device for drag reduction of ground vehicles. The system, previously studied on a bullet-shaped body by Qubain (2009) and Oxlade (2013), is applied to a bluff body that idealises a long vehicle, such as an articulated lorry or a coach. The model, tested in the Honda wind tunnel of the Department of Aeronautics at Imperial College, is equipped with a synthetic jet, or zero net-mass-flux actuator, composed of a cavity, a plate with a slot, and an oscillating diaphragm, placed at the rear end of the body. The effects produced by the actuator are studied by monitoring the base pressure on the model, and by measuring the aerodynamic forces and the moments acting on the body. During the experiments, performed at a constant $Re_H = U_\infty H/\nu = 4.1 \times 10^5$, a parametric study of the response of the mean base pressure, forces and moments to changes in the forcing parameters (frequency and amplitude), and slot width is performed.

The unforced wake is characterised by two main structures: the bubble-pumping mode, with Strouhal number $St_H \approx 0.08$, and the vortex shedding, with $St_H \approx 0.17$ and $St_H \approx 0.20$ on the vertical and horizontal plane, respectively. These structures, still visible in the forced wake at low forcing amplitudes, are almost completely suppressed when the forcing amplitude is increased. The suppression of the structures in the wake corresponds to a decrease in the integrated energy of the wake itself, associated to base pressure recovery and drag reduction. The optimal values achieved corresponds to 27.3% gain in base pressure and -13.1% reduction of drag. The higher sensitivity to changes in forcing amplitude rather than in frequency displayed by the system confirms the existence of a plateau of optimal base pressure

recovery/drag reduction at frequencies around 5 times the characteristic shear layer frequency.

Acknowledgements

I want to start with mentioning my supervisor, Professor Jonathan Morrison. Without your faith in me, I would never have been able to come to London, study at Imperial College, and survive to my PhD, which has been exceptional and very challenging both from the scientific and the human point of view. A big thank you for supporting me in so many different ways.

Another very special thank you goes to Dr. Nigel MacCarthy, who has been the best mentor I could ask for. Thank you for finding time for me in between your very busy schedule, for listening to me and giving me some of the best advice I got during the past five years, for being on my side when the majority of the Department pleaded to stop the noise, for teaching me so many invaluable skills, which are going to be extremely useful during my current job. Last but not least, thank you for accepting to be my internal examiner, and making my VIVA a pleasurable and insightful experience.

Also, my VIVA exam would not have been the same without Professor Kevin Garry. Thank you for accepting to be my external examiner, and for your very acute and sensible comments on my work.

Thank you to my colleagues and office mates. Anthony, Ivan, George and Marcos for giving me so much advice, Jumana and Rita for letting me feel less lonely as a girl in the department, Errikos and Omar, for making me smile and cheering me up so many times. In particular, thank you to Kevin, who has been one of my best friends.

My model, my set-up and the success of my experiments would not have been possible without the Aero workshop. Thank you to Roland Hutchins, Gary Senior,

Andrew Wallace, Mark Grant, Ian Pardew, Jon Cole and in particular to Joseph Meggyesi, Ian James and Alan Smith. You all have been great advisors and very good friends.

A unique thank you goes to Valentine, who has been my North Pole during my London years.

A big thank you to all my friends, the ones I met in London and the ones I left back home in Sardinia or somewhere else in the world. Siva, Maura, Gabriella, Cecilia, Simone, Roberta, Aggi, Cristina, Simona, Esther, Sofia, Roberto and Roberta and many more. You all have been my best fans.

Finally, I would like to thank my family. Dad for transmitting me the passion for engineering, Mum for trying her best in staying close to me, and Alice, for being the best sister in the world. Also thank you to my additional family, Antonio e Rosanna: unbeatable additional parents ever!

Last but not least, thank you to London, for making me feel at home.

Nomenclature

Acronyms

A/D	Analog–to–digital
B	Baseline (when subscript)
CC	Circulation Control
COP	Centre of pressure
CTA	Constant–temperature anemometry
D/A	Digital–to–analog
DOE	United States Department of Energy
E	*Endevco* transducer
F	Forced (when subscript)
GHG	Greenhouse Gas
GPD	Gross Domestic Product
LBM	Lattice Boltzmann Method
LES	Large Eddy Simulation
LPG	Liquefied Petroleum Gas
MEMS	Micro Electro–Mechanical Systems
OECD	Organisation for Economic Co–operation and Development

PID	Proportional–integral–derivative	
PIV	Particle–Image Velocimetry	
RANS	Reynolds–Averaged Navier-Stokes	
RNG	Re–Normalisation Group k–ϵ turbulence model	
SAE	Society of Automotive Engineers	
SaOB	Suction and Oscillatory Blowing	
SA	Steady Asymmetric Regime	
SS	Steady Symmetric Regime	
VG	Vortex Generator	
ZNMF	Zero–Net Mass–Flux	

Greek symbols

δ^*	Displacement thickness of boundary layer	m
δ	Boundary layer thickness	m
ν	Kinematic viscosity	$\mathrm{m^2\,s^{-1}}$
$\omega_{n,0}$	Shear layer natural frequency in radians	
φ	Base angle	$^\circ$
ρ	Fluid density	$\mathrm{kg\,m^{-3}}$
θ	Momentum thickness of boundary layer	m
μ	Mean	
σ^2	Variance	
γ	Skewness	
κ	Kurtosis	

Roman symbols

A_B	Area of the base of the aerodynamic model	m^2
A_j	Area of the jet slit	m^2
AR	Aspect ratio of the aerodynamic model, $AR = H/W$	
C_D	Drag force coefficient, $C_D = \frac{D}{\frac{1}{2}\rho U_\infty^2 A_B}$	
C_L	Downforce coefficient, $C_L = \frac{L}{\frac{1}{2}\rho U_\infty^2 A_B}$	
C_M	Pitch moment coefficient, $C_M = \frac{M}{\frac{1}{2}\rho U_\infty^2 A_B}$	
C_μ	Jet blowing coefficient, $C_\mu = \frac{U_j^2 A_j}{U_\infty^2 A_B}$	
C_N	Yaw moment coefficient, $C_N = \frac{N}{\frac{1}{2}\rho U_\infty^2 A_B}$	
C_p	Base pressure coefficient, $C_p = \frac{\hat{p}-p_\infty}{\frac{1}{2}\rho U_\infty^2}$	
C_R	Roll moment coefficient, $C_R = \frac{R}{\frac{1}{2}\rho U_\infty^2 A_B}$	
C_Y	Side force coefficient, $C_Y = \frac{Y}{\frac{1}{2}\rho U_\infty^2 A_B}$	
d	Slot thickness	m
$\Delta C_F/C_{FB}$	Change in force coefficient, $\Delta C_F/C_{FB} = \frac{C_F - C_{FB}}{C_{FB}}$	
$\Delta C_M/C_{MB}$	Change in moment coefficient, $\Delta C_M/C_{MB} = \frac{C_M - C_{MB}}{C_{MB}}$	
$\Delta C_p/C_{pB}$	Change in base pressure coefficient, $\Delta C_p/C_{pB} = \frac{C_{pB} - C_p}{C_{pB}}$	
$\mathscr{E}$	Average energy of a disturbance	
f	Frequency	s^{-1}
f_c	-3dB cut-off frequency	s^{-1}
$f_{n,0}$	Shear layer natural frequency, $f_{n,0} = \omega_{n,0}/2\pi$	s^{-1}
H	Height of the aerodynamic model	m

h	Distance of the aerodynamic model from ground	m
k	Wave number	
L	Total length of the aerodynamic model	m
$\hat{p}$	Area–weighted base pressure	$\mathrm{kg\,m^{-1}\,s^{-2}}$
$\tilde{p}$	Integrated mean square pressure	
R_a	Hot wire resistance at ambient temperature	Ω
Re	Reynolds number	
Re_H	Reynolds number based on H, $Re_H = U_0 H/\nu$	
R_H	Radius of the vertical front edge of the aerodynamic model	m
R_W	Radius of the horizontal front edge of the aerodynamic model	m
R_w	Hot wire resistance at high temperature	Ω
St	Strouhal number	
St_D	Strouhal number based on D, $St_D = fD/U_\infty$	
St_H	Strouhal number based on model height, $St_H = fH/U_\infty$	
St_θ	Strouhal number based on θ, $St_\theta = f\theta/U_\infty$	
t	Time	s
T_w	Hot wire temperature	°C
U_∞	Freestream velocity	$\mathrm{m\,s^{-1}}$
$\mathbf{U}_0$	Initial condition of the mean velocity vector	$\mathrm{m\,s^{-1}}$
U_j	Peak jet velocity	$\mathrm{m\,s^{-1}}$
u_τ	Wall friction velocity	$\mathrm{m\,s^{-1}}$
W	Width of the aerodynamic model	m

x, y, z	Cartesian co-ordinate system	m

Contents

List of Figures

List of Tables

Chapter 1

Introduction

1.1 Background

As stated by Stern (2006), climate change already affects the basic elements of life for thousands of people around the world. If no effective action is taken soon, the number of people suffering hunger, water shortages and coastal flooding as consequences of global warming will increase to hundreds of millions. According to the same document, not taking action is equivalent to losing at least 5% of global Gross Domestic Product (GPD) each year on a low risk scenario; if a wider range of risks and impacts are taken into account, the estimate of damage rises to 20% of GPD or more. In contrast, the cost of action can be limited to 1% of global GPD per year.

Unfortunately, climate scientists have observed that carbon dioxide (CO_2) concentration in the atmosphere has been increasing significantly during the past century, with an average growth of 2 ppmv/year in the last ten years (International Energy Agency, 2013). As shown in Figure 1.1, two sectors alone produced nearly two-thirds of the global CO_2 emissions in 2011: electricity and heat generation (42%), and transport (22%). The fast growth of the CO_2 concentration observed during the last century (394 ppmv in 2012, 40% higher than the mid-1800s), comes from the road sector, which increased its emissions by 52% since 1990 and reached almost three quarters of the total transport emissions in 2011. It is likely that trans-

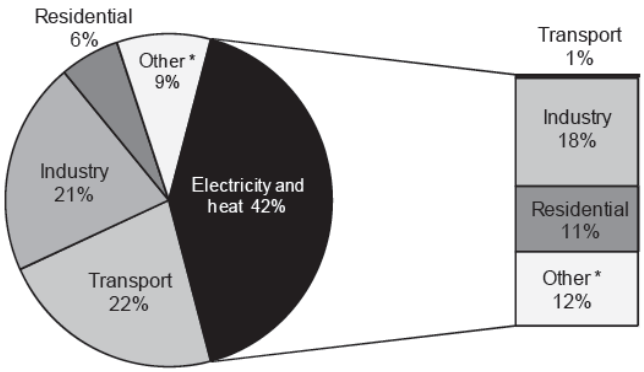

Figure 1.1: World CO_2 emissions by sector in 2011. Other includes commercial/public services, agriculture/forestry, fishing, energy industries other than electricity and heat generation, and other emissions not specified elsewhere. Also shows allocation of electricity and heat to end-use sectors (International Energy Agency, 2013).

port fuel demand will grow by up to 40% by 2035 (International Energy Agency, 2013).

According to the Department for Transport (2009), in 2009 cars and taxis accounted for 58% of UK domestic transport greenhouse gas emissions, followed by heavy goods vehicles with more than 17%. In 2011, the CO_2 UK emissions from heavy vehicles amounted to 23.2 millions tonnes, half of the amount from cars and taxis. However, while emissions from cars and taxis decreased from 75.2 millions tonnes in 1999 to 64.5 millions tonnes in 2011, the emissions from heavy goods vehicles have been constant during the same period (Department for Transport, 2013). This is confirmation of how the heavy goods transport sector deserves more attention and further research in order to decrease its impact on the environment.

Fortunately, according to Argonne National Laboratory (2008), a potential up to 20% of petroleum savings exists from now to 2050 for heavy truck class vehicles, if the technologies under development in the past few years are successful and applied in the near future (Figure 1.3). Most of the savings are accounted for class 7 and 8 of articulated lorries. Engine efficiency represents more than 80% of the potential savings, while aerodynamic reduction by electrification is the next most significant contributing technology, with 10% of the expected savings.

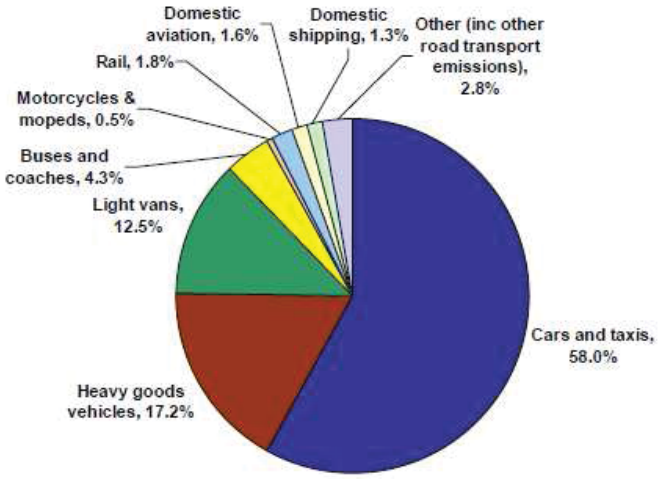

Figure 1.2: UK domestic transport greenhouse gas emissions, 2009. Total UK domestic transport GHG emissions in 2009 (122.2 $MtCO_2e$). 'Other' is mostly 'military aircraft and shipping', and also includes emissions from 'aircraft support vehicles' and from road vehicles running on liquefied petroleum gas (LPG) (Department for Transport, 2009). GHG include: water vapour (H_2O), carbon dioxide (CO_2), methane (CH_4), nitrous oxide (N_2O), ozone (O_3), CFCs (Department for Transport, 2009).

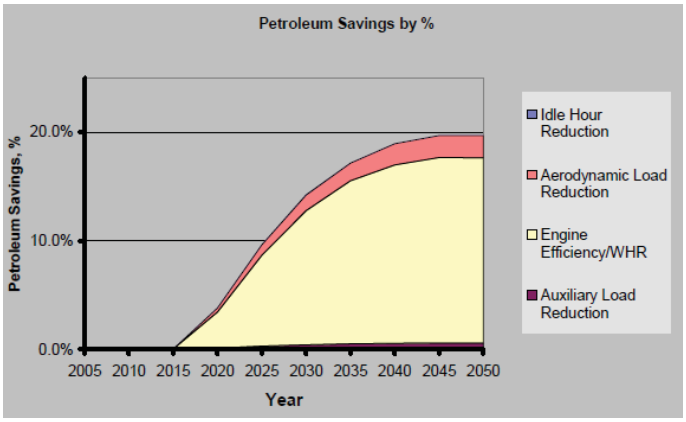

Figure 1.3: Petroleum reduction due to vehicle technologies as percentage of base consumption (Argonne National Laboratory, 2008).

1.2 Motivation

Shape optimisation or classic solutions for drag reduction have been developed and used extensively, especially in cars. However, many of the add-on devices studied for trucks in the eighties are still not widely in use. These devices include side skirts, boat-tails, tractor-trailer side extenders and mid-plan seals. Many reasons can be associated with them not being conventional yet. Fleet operators often own several trailers for every tractor, so trailer add-on devices are expected to be cheaper and more effective than tractor add-ons. Maintenance cost is another concern, since some of these devices, such as base-mounted boat-tails, have to be constantly manipulated to allow loading and unloading, while side skirts can restrict access to the underside of the trailer and tractor. Considering the reasons above, active flow control is probably one of the most promising solutions, since it allows minimal shape modification.

The drag experienced by a heavy vehicle at motorway speed is primarily due to pressure drag, which accounts to about 85% of the total aerodynamic drag, while the friction drag accounts for the remaining 15% (Wood, 2004). This arises mainly from the difference between the forces on the front and rear of the vehicle. The pressure drag has been successfully reduced by streamlining the tractor, installing air shields, and optimising the relative tractor-trailer height. On the other hand, the pressure drag generated at the rear (often referred as base drag) yet remains to be reduced effectively. Due to their function, the cargo-carrying portion of heavy vehicles cannot be easily streamlined, unless a "virtual streamlining" is achieved through flow alterations only. This is exactly the aim of this work: to control the wake from a rectangular section body, with minimal shape modification, in order to achieve vehicle drag reduction.

1.3 Objectives and Outline of the Thesis

The focus is on reducing aerodynamic drag by using a zero-net mass-flux active control device. The objectives are:

- Consider previous literature and existing gaps in the research on flow control applied to road vehicles. This has been accomplished in chapter 2, which focusses on the literature review.

- Develop an effective and reliable system which can be used for repeatable experiments and to measure both the dynamics of the flow and the forces acting on the body by using two independent measurement systems. The experimental set-up and the procedures followed during the experiments are described in chapter 3.

- Evaluate the static and dynamic characteristics of the system in the unforced configuration. The study of the 'baseline' configuration is described in chapter 4.

- Assess the effects produced by the control action on the wake and on the forces, establish the influence of the control parameters on the drag force in order to find the optimal system configuration and identify the relevant dimensional parameters in order to allow the scaling of the system. These topic are covered in chapters 5 and 6.

- Consider the applicability of the system to full-sized vehicles, and suggest additional work for future research. This is discussed in chapter 7.

Chapter 2

Literature Review

2.1 Flow Control Principles and Objectives

Gad-el-Hak (1996) cites two main classification schemes for flow control. The first one differentiates between techniques applied at the wall or away from it. Wall techniques include changes in surface roughness, shape, curvature, rigid-wall motion, compliance and porosity. Control methods applied away from the wall involve large-eddy breakup devices, external acoustic waves, additive injection in the middle of a shear layer, free stream turbulence, and magneto- and electro-hydrodynamic body forces.

The second classification scheme takes into account the energy consumption. A controlling method is called passive when the process utilises only energy extracted directly from the flow to be controlled. As also remarked by Fiedler & Fernholz (1990), the terminology 'flow management' may be more appropriate in this case, while the term 'control' should be reserved for systems where external energy is required. The latter are called active control methods, which are further divided into predetermined or reactive (also called interactive). In the case of predetermined control, steady or unsteady energy is applied regardless of the state of the flow. The control loop is open and no sensors are required. Conversely, in reactive control, the energy input is constantly modified according to a specific variable. The control loop can be open (feedforward) when the measured and the controlled variables are

distinct, or closed (feedback) if the controlled variable is measured, fed back and compared with a reference value. As reported by Moin & Bewley (1994), feedback control can be further categorised on the basis of the equations governing the flow phenomena to be controlled. Adaptive schemes develop models and controllers via some learning algorithm without considering the flow physics. Schemes based on physical arguments are successfully applied when the dominant physics is well understood. Dynamical systems are characterised by control schemes based on the dynamics of the modes in which turbulence is decomposed. Finally, optimal control schemes using a cost function are directly implemented with the Navier-Stokes equations, resulting in the most efficient scheme of all. However, these schemes are numerically intensive.

Another classification scheme distinguishes between control techniques aimed at modifying the shape of the instantaneous/mean velocity profile and those influencing exclusively the small dissipative eddies. A similar distinction is made by Fiedler & Fernholz (1990), who differentiate between "overall" control, aimed at managing turbulence, and "tailored" control, which affects only specific characteristics and flow structures. In the same paper, control techniques are also classified as "external" (open loop) and "adaptive" (closed loop). Choi *et al.* (2008) categorise bluff-body flow control techniques in 2D versus 3D, whether the control action stays constant or varies along the spanwise (or azimuthal) direction. Another classification distinguishes between boundary layer versus direct-wake control, whether drag is reduced by a delay in boundary layer separation, or through a direct action on wake characteristics.

In any of these cases, experiments can give a better understanding of flow structures and behaviour, or at an improvement of some process, with obvious consequences on the method applied. The goal can be lift increase, drag decrease, separation delay/prevention or promotion, turbulent mixing increase or reduction, control of pressure fluctuations and transition delay. Moreover, great influence on the control scheme is given by the flow characteristics, such as presence or lack of boundaries, Reynolds and Mach numbers, and type of instabilities arising. Unbounded flows, such as jets, wakes and mixing layers, for whom the main role in stability is played

by inertial and pressure forces (Lin, 1944), are easily exploited due to their intrinsically unstable nature. Common objectives in controlling these flows are transition delay or advancement, mixing improvement and noise suppression. Wall-bounded flows are instead intrinsically stable, and more difficult to control. Furthermore, because of their proneness to instability, free shear flows experience transition at low Reynolds numbers, hence encouraging transition is much easier than delaying it. Gad-el-Hak (1996) identifies three distinct Reynolds number regimes for wall-bounded flows which determine the most convenient control strategy to apply for skin friction reduction. For $Re < 10^6$ (based on distance from leading edge), methods to reduce laminar shear stress are investigated. For $10^6 \leq Re \leq 4\times10^7$ transition is delayed as much as possible with stability modifiers and wake cancellation methods. Finally, for $Re > 4 \times 10^7$ transition cannot be delayed without incurring a negative energy balance. Similarly, different Mach number regimes lead to different optimal control methods. Extremely important for successful application of any control strategy is also the distinction between absolute or convective instabilities, as defined by Huerre & Monkewitz (1990) on the basis of the response of the system to an initial localised impulse.

In conclusion, it is worth mentioning an interesting question posed by Choi *et al.* (2008) regarding the lowest possible drag achievable for bluff bodies. Considerable contribution to mean drag and lift fluctuations is given by vortex shedding. Thus the effort of the control community is directed to achieving its suppression. However, a bluff body with vortex shedding removed still has some drag due to the viscous forces (form drag). The ideal situation of minimum drag would be then a body with pressure distribution similar to that of potential flow and zero drag. This scenario indicates how the optimal control system for bluff body drag reduction should be formed by a combination of distinct devices, aimed at controlling different aspects of the flow.

2.2 Stability Theory

The subject of hydrodynamic stability has been part of the central interest of the scientific community since the end of the nineteenth century, with the studies performed by Stokes (1842), Helmholtz (1868) and Thomson (1871). After these initial contributions, Lord Rayleigh's criterion and Reynolds' experimental investigation on parallel stability followed in 1880 and in 1883 respectively (Darrigol, 2002). This list of names continues with Taylor (1915) and Prandtl (1921), linked to viscous stability theory, and Tollmien (1929) and Schlichting (1935) for boundary layer stability, and many others. There is an abundant literature on this topic; however attention here will be given to those aspects more inherently linked to flow control.

According to the classic definition, a flow which satisfies the Navier-Stokes equations is said to be stable if the disturbances added to its basic state decay as they evolve in space and time. Since the equations of motion describe the actual behaviour of the flow, any statement about the stability of their solutions applies to the stability of the flow itself. The problem is studied for different values of the initial condition of the velocity field $\mathbf{U}_0$ and of the kinematic viscosity ν. The perturbation of the zero initial value gives origin to the stability problem for the null solution $\mathrm{u}(\mathbf{x}, t) = \mathbf{u}_0 \equiv 0$. As stated by Joseph (1976) and recalled by Schmid & Henningson (2001), the concept of stability is better understood when associated to the average energy of a disturbance

$$\mathscr{E}(t) = \frac{1}{2} < |\mathbf{u}|^2 >, \tag{2.1}$$

where the angle brackets indicate the volume-averaged integral. On this basis, four different definitions of stability can be introduced for a flow with varying initial conditions and constant viscosity:

1. **Stability:** the null solution is *stable* if

$$\lim_{t\to\infty} \frac{\mathscr{E}(t)}{\mathscr{E}(0)} \to 0. \tag{2.2}$$

   It can be seen how the definition of stability implies an *asymptotic stability in the mean.*

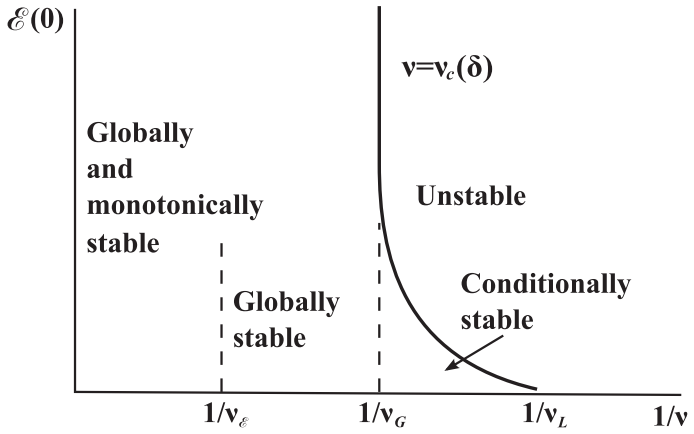

Figure 2.1: Sketch illustrating the stability limits for the basic flow. Reproduced from Joseph (1976).

2. **Conditional stability:** the null solution is said to be *conditionally stable* if a positive initial value threshold energy δ exists such that $\mathscr{E}(0) < \delta$; δ is called an *attracting radius* for the conditionally stable disturbances. It is clear how this definition considers the initial energy of the perturbation as the crucial parameter for stability.

3. **Global stability:** if $\delta \to \infty$, the solution is *globally stable*. This is a special case of the previous one.

4. **Monotonic stability:** the solution is said to be *monotonically stable* if for all $t > 0$

$$\frac{d\mathscr{E}(t)}{dt} < 0. \tag{2.3}$$

This definition introduces the additional restriction for the perturbations of decreasing energy not only in the asymptotic limit but at all times.

See Joseph (1976) and Schmid & Henningson (2001) for full details.

Following these definitions of stability, the *instabilities* can be of two kinds: not conditionally stable, or conditionally stable but not monotonically stable. In the last case, some growing disturbances may exist in a finite time period, called *transient growth*.

On the other hand, when the initial conditions are kept constant but the kinematic viscosity is changed, an additional *stability criterion* can be defined in terms of inequalities between the flow viscosity and its critical values:

$\nu_{\mathscr{E}}$: If $\nu > \nu_{\mathscr{E}}(\nu)$ the null solution is monotonically and globally stable. The Reynolds number $Re_{\mathscr{E}}$ associated with this value of viscosity is obtained by applying the energy theorem and derived by using the Reynolds-Orr equation.

ν_G : If $\nu > \nu_G$ the null solution is globally stable; when $\nu \leqslant \nu_G$ the null solution is unstable even though it can be conditionally stable. ν_G is called the *global stability limit*, and the corresponding Reynolds number Re_G can be determined by bifurcation analysis. For some flows, Re_G corresponds to the lowest Reynolds number for which turbulence can be sustained.

ν_L : If $\nu > \nu_L(\nu)$ the null solution is linearly unstable or not conditionally stable. An attracting radius $\delta(\nu)$ exists, which defines a set of values attracted to the conditionally stable solution; at the corresponding Reynolds number regime Re_L there is at least one infinitesimal unstable disturbance.

Two additional viscosity values, linked to the energy and to the linear theory respectively, are identified:

$\bar{\nu}_{\mathscr{E}}$: *energy stability limit*, the smallest critical viscosity of energy theory.

$\bar{\nu}_L$: *linear stability limit*, the smallest critical viscosity of linear theory.

The relationship between energy and viscosity, with the corresponding kinds of stability, are shown in Figure 2.1.

These concepts form the basis of the *energy methods*, and establish the sufficient criteria for stability, and in particular the smallest value of viscosity ν_G for which global stability can be guaranteed. If the flow viscosity is smaller than ν_G, the basic flow is unstable to some disturbances, but it might be conditionally stable to small ones, with more than one solution. To know the number of such solutions and their properties, bifurcation theory can be applied. The starting point for bifurcation theory is the linear theory of stability, which gives sufficient conditions for instability.

Different approaches are applied within the linear theory. The most widely used technique is the *normal-mode analysis*, which can be carried on either in *temporal*

mode or *spatial mode*. Since the spatial-mode analysis is mathematically more difficult (but more useful, especially for experimental work), most of the theoretical works are based on the temporal-mode one (Wu *et al.*, 2006). The perturbed equations are linearised and expressed as sum of *normal modes*, which can be studied separately as individual eigenvalue problems. Additionally, among the cornerstones of the linear theory, two theorems have to be mentioned. The first, valid for inviscid flows, is *Rayleigh's inflection point criterion*, which relates the existence of an unstable mode to the presence of an inflection point in the mean velocity profile. The second one is *Squire's theorem*, which states that two-dimensional wavelike perturbations grow in parallel shear flows at a Reynolds number smaller than any value for which an unstable three-dimensional perturbation may exist (Schmid & Henningson, 2001). The most important consequence of this postulate is that a great number of three-dimensional instability problems can be simplified and properly studied in a 2D domain.

Despite simplicity and a wide number of successful applications, the critical Reynolds numbers predicted by the normal-mode linear theory in many cases are larger (or even infinite) than values at which some flows become unstable. Examples are plane Couette flow, plane Poiseuille flow, boundary layers, free shear layers, and concentrated vortices (Wu *et al.*, 2006). The main explanation of these discrepancies is that real disturbances are never infinitesimal, but finite-amplitude perturbations are beyond the abilities of linear analysis. However, even if nonlinearity is inevitable and necessary in the transition to turbulence, other studies reassessed linear theory by investigating the equations from the point of view of an initial value problem. When the disturbance equations are used to generate a complete set of discrete eigenvalues and eigenvectors, the study in the Hilbert space of the orthogonality of the set allows one to determine if some disturbance mode or a linear combination of some of them may generate *transient algebraic growth*. A more general approach involves the definition of the function of maximum possible amplification of the initial energy density, which allows the identification of the condition of optimal energy growth for the system at every time. It has to be noted that, in the transient phase, the behaviour of the growth function does not depend on the stability of the

flow, which is only revealed for $t \to \infty$. The transient growth for stable flow is a short-time phenomenon compared to the infinite growth for unstable flow. However, it has been shown that, under specific conditions, this growth can reach very large amplitudes on a very short time scale (Schmid & Henningson, 2001). This kind of transient growth is responsible for triggering transition at Reynolds numbers much lower than ones predicted by normal-mode theory. For this reason, transient growth study implies the inclusion of both normal and non-normal operators in the linear stability theory (Wu *et al.*, 2006).

Other theories have been developed to deal with nonlinear stability of systems perturbed by disturbances of finite amplitude, but due to the high complexity of the problem only a few general theories exist. Instead, many approximate techniques, often applicable only to special cases, have been developed. None of them are relevant to this specific work, therefore this aspect of stability theory will not be discussed here.

The theories discussed until now consider flow stability from the temporal point of view. However, the spatio-temporal development of the response to an impulsive disturbance is much more interesting and more useful from the flow control point of view. The hydrodynamic stability theory of *spatially developing flows*, here described from the point of view of open parallel shear flows, as in Huerre & Monkewitz (1990), discriminates between absolute/convective and local/global instabilities. A flow is said to be *convectively unstable* if its response to an impulsive disturbance propagates away from the source, in the downstream direction. It is *absolutely unstable* if the response spreads around the source and contaminates the whole medium, both downstream and upstream. For flows which are invariant under Galilean transformation, it can be easily argued that the distinction between absolute and convective does not hold, since the flow reference can be changed without affecting the physics of the flow itself. However, in spatially developing flows, flows with a definite origin, or forced at a specific streamwise station, the Galilean invariance is broken and the above mentioned definition becomes very useful. The distinction between *local* and *global* refers to instabilities of the local velocity profile or of the whole flow field, respectively. At this point it has to be mentioned that, for these concepts to be

appropriate, the flow must be slowly evolving over a typical instability wavelength (Huerre & Monkewitz, 1990). These concepts allow classification of open shear flows according to the qualitative nature of their dynamical behaviour. Shear flows which are globally convectively unstable display *extinsic dynamics* and can be classified as *noise amplifiers*. Examples of this kind of flow are mixing layers and plane wakes. The spatial evolution of the flow is determined by the character of the excitation, which can be tailored to meet specific control goals. On the other hand, flows with a pocket of absolute instability of sufficiently large size display *intrinsic dynamics* and behave as *oscillators*. Examples of this are bluff-body wakes and low-density jets. The flow evolution relies on the growth of the initial disturbances in time. The presence of a region of local absolute instability in the wake of bluff bodies which makes the Kármán vortex street a self-sustained disturbance has been shown by the work of Hannemann & Oertel (1989), Monkewitz (1988), Sevilla & Martínez-Bazán (2004), Chomaz *et al.* (1988) and many others.

From the mathematical point of view, fluctuations are decomposed as elementary instability waves $\phi(y;k)exp\{i(kx-\omega t)\}$ with complex wave number k and complex frequency ω. The cross-stream distribution $\phi(y;k)$ is shown in most cases to satisfy an Orr-Sommerfeld equation, which admits non-trivial solutions only if the complex wavenumber k and frequency ω satisfy a dispersion relation of the form:

$$D(k,\omega;Re)=0. \tag{2.4}$$

The *temporal modes* $\omega(k;Re)$ refer to cases where ω is determined as a function of k. *Spatial branches* $k(\omega;Re)$ are obtained by complex wave numbers when ω is real. By studying the impulse response of the flow $G(x,t)$ (Green's function), the flow is said to be (Huerre, 2002):

- *linearly stable* if along all rays $x/t=const$

$$\lim_{t\to\infty} G(x,t)=0. \tag{2.5}$$

- *linearly unstable* if along all rays $x/t=const$

$$\lim_{t\to\infty} G(x,t)=\infty. \tag{2.6}$$

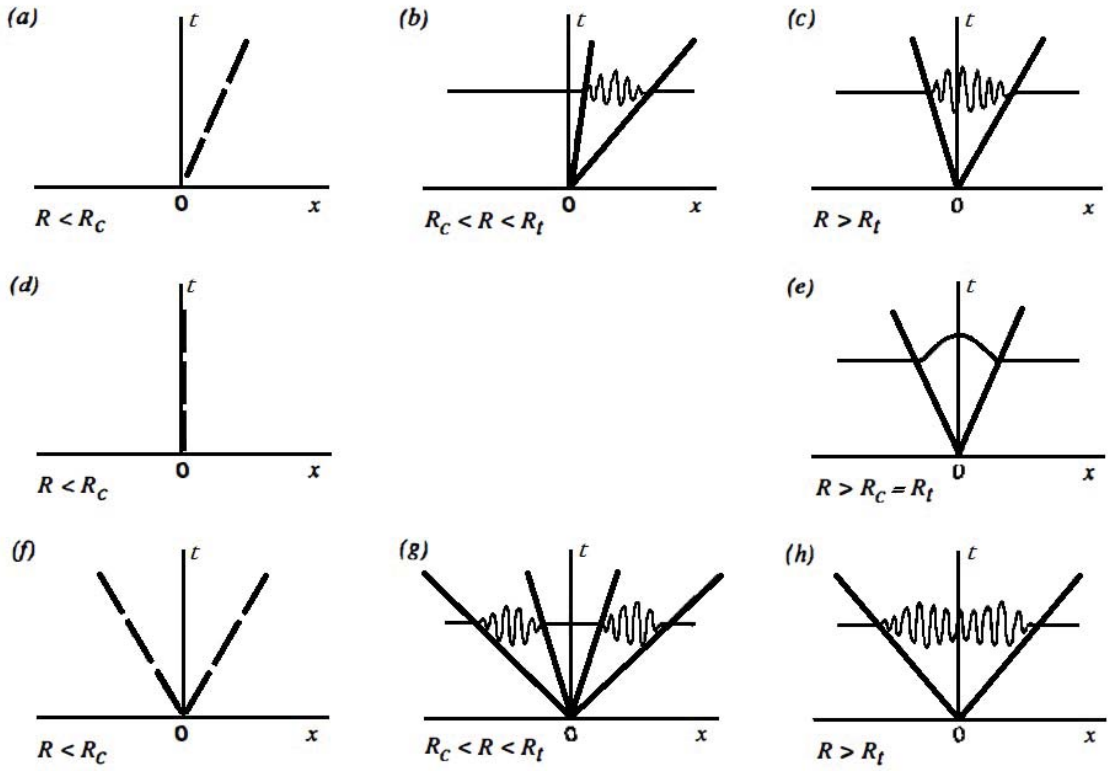

Figure 2.2: Sketches of typical impulse responses. Single travelling wave: (a) stable, (b) convectively unstable, (c) absolutely unstable. Stationary mode: (d) stable, (e) absolutely unstable. Counter-propagating travelling waves: (f) stable, (g) convectively unstable, (h) absolutely unstable. R represents a control parameter (Reynolds number). Reproduced from Huerre & Monkewitz (1990).

- *convectively unstable* if along all rays $x/t = 0$

$$\lim_{t\to\infty} G(x,t) = 0. \tag{2.7}$$

- *absolutely unstable* if along all rays $x/t = 0$

$$\lim_{t\to\infty} G(x,t) = \infty. \tag{2.8}$$

A graphic interpretation of the impulse response is given in Figure 2.2.

2.2.1 Receptivity

An objection made by Balsa (1988) to normal mode theories is that the mode evolution and in particular its relationship with the strength of the input distur-

bance, called *receptivity of the flow*, is neglected. A measure of this relationship is given by the ratio between the amplitude of the instability wave to that of the external disturbance, called *receptivity* or *coupling coefficient* (Asai & Kaneko, 2000). Linear stability theory is able to describe the growth (or decay) of a mode only until the onset of nonlinear interactions. Since the flow receptivity will in some way influence the initial amplitude spectrum, it will also have a substantial role on the flow characteristics. Thus, an understanding of the receptivity mechanisms is an important tool for flow control (Johnson, 1998, pp.25-39).

The study of receptivity is linked to the initial-value problem and to the excitation of the instability modes by the initial disturbance. Balsa (1988) found a measure of receptivity in terms of wave packets and spatial instability modes, expressed through two independent relationships proportional to each other in functional form. In the first case, the receptivity is evaluated as a function of the observer velocity, while in the second one it is a function of the excitation frequency. According to Crighton (1985), the key to the receptivity problem in shear flows around bodies is the imposition of a *Kutta condition* to the unsteady perturbations of trailing-edge flows, attached leading-edge flows, and separated flows past bluff bodies. Experimental studies conducted for small amplitudes, small Mach numbers, and small Strouhal numbers – when the Kutta condition is applicable – confirmed this model (Ho & Huerre, 1984). However, as reported also by Crighton (1981), at higher Strouhal numbers and in particular close to the shear layer's natural frequency, the Kutta condition breaks down due to the local separation. It is in this range of frequencies that more recent investigations have put most of their effort. As suggested by Ho & Huerre (1984) and then confirmed by Vukasinovic *et al.* (2010), the natural receptivity band of the shear layer is about $2f_{n,0}$, being $f_{n,0} = \omega_{n,0}/2\pi$ the natural frequency of the shear layer itself. The most receptive region is limited to the near-field domain, and is dominated by coherent motions at the most amplified frequency. Analytical and experimental results show that, when the shear layer is forced at a frequency higher than about twice the natural one, the usual near-field behaviour is suppressed. However, high frequency forcing (above the receptivity band) also requires high actuation levels in order to be effective in altering the characteristics

of the base flow.

For mixing layers that develop downstream of a thin splitter plate, the point of highest receptivity occurs near the edge of the plate itself, while for a jet flow it is near the lip of the nozzle from which the flow emanates (Johnson, 1998, pp.25-39). In the case of bluff body wakes, Grandemange *et al.* (2012*b*) recalled that zones of high sensitivity have been found in the recirculating bubble, around the separatrix.

2.3 Bluff-Body Aerodynamics

As accurately described by Roshko (1993) and Bearman (1997), the main aerodynamic characteristics which identify bluff bodies are a large region of separated flow, high values of pressure drag, and the occurrence of vortex shedding. The main cause of these phenomena is the interaction between viscous and inviscid regions of the flow field, which impose an adverse pressure gradient often too great for the flow to stay attached. The main consequence of this is a high value of drag over a long-time average, experienced mainly as (i) difference in pressure between the windward and leeward faces of the body, and (ii) establishment of vortex shedding in the region of separated flow immediately behind the body. Even though vortex shedding is mainly associated with two-dimensional bodies, it can be found in the wake of three-dimensional ones in a weaker form. Above some critical Reynolds number, vortex shedding from nominally two-dimensional bodies displays a three-dimensional nature through oblique shedding, splitting or dislocation of vortices, and looping of vortices across the other side of the wake. At higher Reynolds numbers, the wake is dominated by various three-dimensional motions. Some of them are linked to the spanwise instabilities of the Kármán vortices, some of smaller-scale to the shear layer instability, and others to the turbulence in the flow past the body (Bearman, 1997).

The variation of the wake dynamics of a smooth cylinder with Re in terms of base pressure coefficient is displayed in Figure 2.3. The shedding starts to develop at low Reynolds numbers ($Re = 49$ to $140 - 194$, regime A–B, referred as *laminar vortex shedding regime*). The base suction values associated with this regime are higher

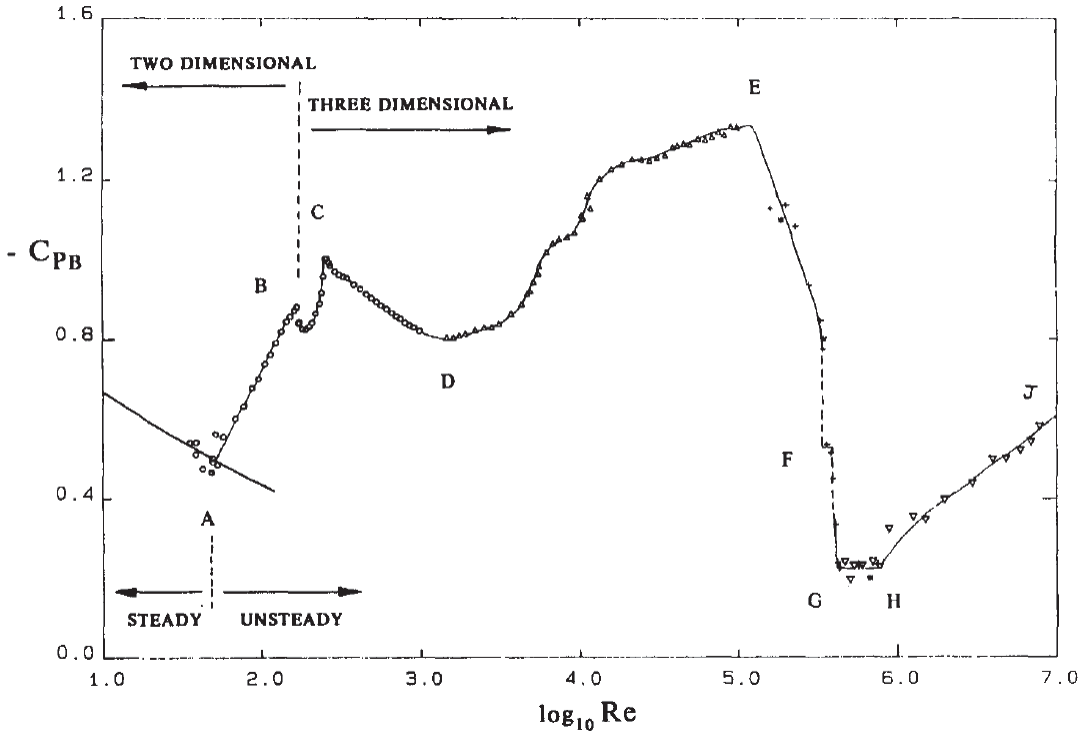

Figure 2.3: Plot of base suction coefficients ($-C_{PB}$) over a large range of Reynolds numbers in the case of a smooth 2D cylinder – experimental and computational data from various authors. Regimes: Up to A: Laminar Steady Regime; A–B: Laminar Vortex Shedding; B–C: 3-D Wake-Transition Regime; C–D: Increasing Disorder in the Fine–Scale Three Dimensionalities; D–E: Shear-Layer Transition; E–G: Asymmetric Reattachment; G–H: Symmetric Reattachment; H–J: Boundary-Layer Transition (Williamson, 1996).

than what would be found in a steady flow at the same value of Re. The base suction, hence the drag, keep increasing until a fully three-dimensional flow is developed: from $Re = 260$ to $Re \approx 10^3$ (regime C–D) the two-dimensional Reynolds stresses are reduced, as well as the base suction, while the vortex formation length is increased. In the following regime, up to $Re \approx 2 \times 10^5$ (D–E), the opposite is observed: the level of Reynolds stresses and the base suction increase again, while the Strouhal number and vortex formation length decrease. A drastic drag and base suction decrease is observed between $Re \approx 10^5$ and $Re \approx 10^6$, due to the presence of one (E–G) or two (G–H) separation-reattachment bubbles. At very high Reynolds numbers ($Re > 10^6$, regime H–J, called the *boundary-layer transition regime* or *post-critical regime*) the turbulent transition point moves further upstream, so that the boundary layer on the surface of the cylinder itself becomes turbulent. As shown by Roshko (1961), periodic vortex shedding is still detected at the very high Re flow regime. These results show a clear connection between vortex shedding and base pressure suction/drag on bluff bodies, as can be observed from the evident correlation between drag and changes in wake dynamics. However, a body with vortex shedding removed, as in the experiments conducted by many authors (see Roshko, 1961; Bearman, 1965; Apelt *et al.*, 1973), still exhibits the main characteristics of a bluff-body flow, with high levels of base suction and drag (Roshko, 1993). The reason for this is that vortex shedding is only one of the various coherent structures found in the wakes of bluff bodies. In addition, energy dissipation in the mean flow does not arise only by the action of coherent motions, but also by means of incoherent turbulence and from the time-independent component of the flow itself, as illustrated in Figure 2.4.

Turbulence has a significant influence on the drag of bluff bodies. Nakamura (1993) describes the flow around a bluff body as characterised by two basic flow modules: boundary layer separation and reattachment, and formation of the Kármán vortex street. Two basic length scale correspond to these phenomena: the thickness of the separated shear layer, and the distance between the separated shear layers (equal to the body size). Therefore, turbulence can influence the mean flow only if its scale is comparable to the shear-layer thickness (small-scale turbulence), or to the body size (body-scale turbulence). The main effect of small-scale turbulence

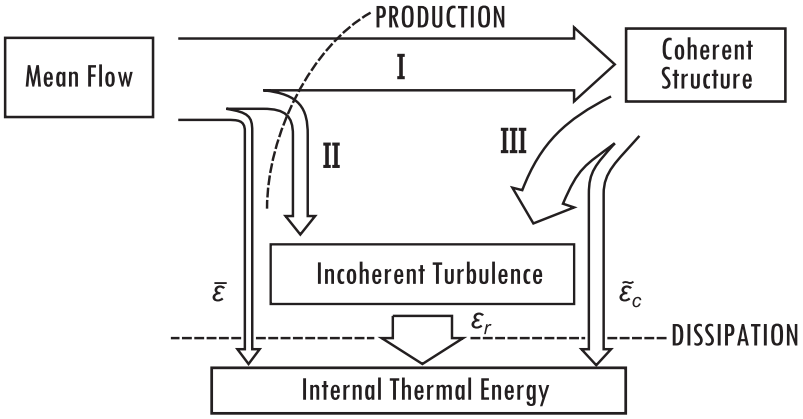

Figure 2.4: Schematic of the energy fluxes between the mean, coherent and incoherent fields, reproduced from Hussain (1983); I: production of coherent kinetic energy by the action of the average coherent Reynolds stresses; II: production of incoherent turbulence by the action of the incoherent Reynolds stresses; III: production of incoherent turbulence by the phase-average incoherent Reynolds stresses against the coherent strain rate; $\bar{\varepsilon}$: dissipation of time-independent component; $\tilde{\varepsilon}_c$: dissipation of coherent component; ε_r: dissipation of incoherent component.

is the increase of the shear layer entrainment from the near wake and the external flows, and the encouragement of the shear-layer/edge interaction. On the other hand, body-scale turbulence is able to strongly influence vortex shedding, hence the mean flow, from short bodies. It can considerably decrease or increase base pressure through resonant interaction in 3-D bodies, or by decrease of spanwise correlation in 2-D ones. Elongated bodies, both 2-D and 3-D, show little sensitivity to changes in turbulence scale.

2.3.1 Simplified Ground Vehicles

Ground vehicles can be described as bluff bodies moving in vicinity to the road surface. The shape of vehicles is dictated mainly by style, market demand, and intended purpose. The last is particularly true for commercial vehicles. However, the growing concern about global warming and future availability of fuel encouraged manufacturers and scientific community to study vehicle aerodynamics with the aim of minimising fuel consumption. With this goal in mind, Ahmed *et al.* (1984) developed the first model of a simplified ground vehicle, later adopted as a standard

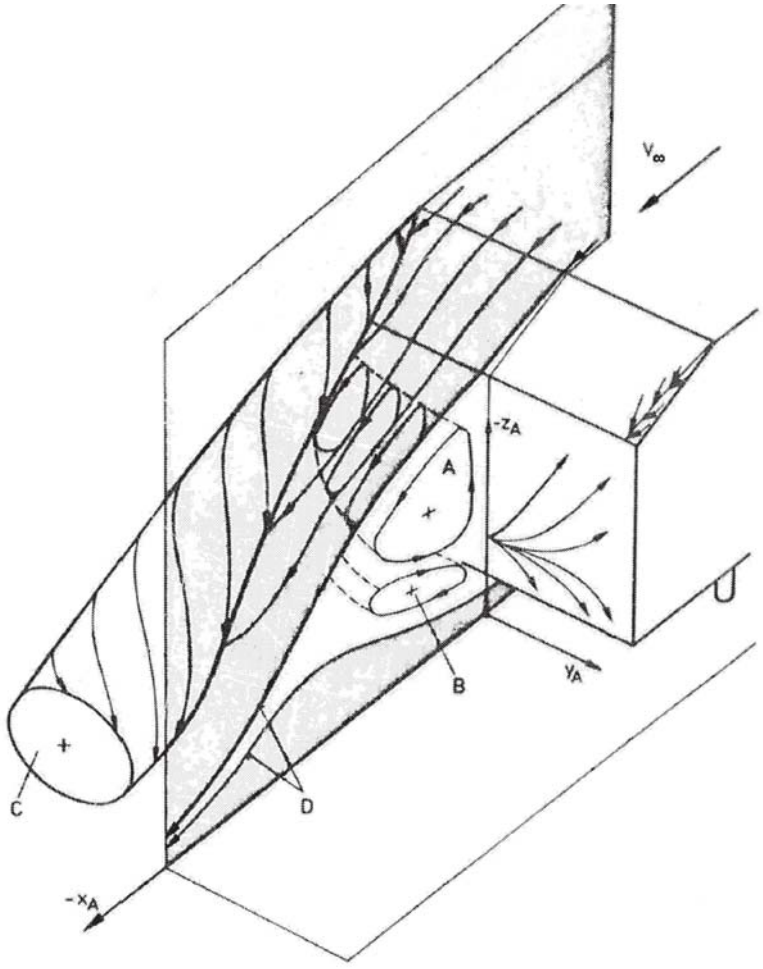

Figure 2.5: Schematics of the time averaged flow structures in the wake of an Ahmed body with base slant angle φ below the critical value; recirculatory bubbles A and B, separation bubble D, longitudinal vortex C (Ahmed *et al.*, 1984).

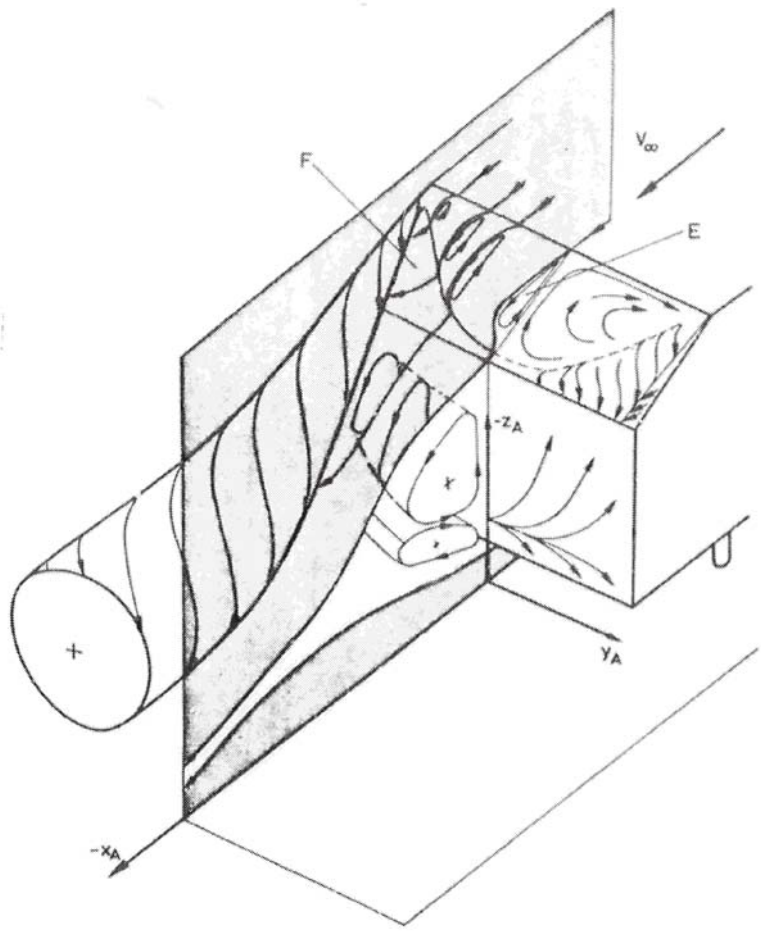

Figure 2.6: Schematics of the time averaged flow structures in the wake of an Ahmed body with high drag configuration $\varphi = 30°$; half elliptic region of circulatory flow E, attached flow region F (Ahmed *et al.*, 1984).

with the name 'Ahmed body'. The essential requirements were a strong three-dimensional displacement flow at the front, a relatively uniform flow at the centre, and a large structured wake at the rear. The effects of rotating wheels, engine and passenger compartment flows, and rough underside were neglected. The first experimental results on this model (Ahmed *et al.*, 1984) revealed a weak interaction between rear and fore body, and a notable sensitivity to the base slant angle, φ. Of the total drag measured, pressure drag varied between 76% to 85% in the different configurations, with friction drag accounting for the remaining 24% to 15%. When the base angle φ was set to zero, the main pressure drag contribution was due to the rear flat base. By increasing φ, the contribution of the flat base to the total drag was reduced, while the pressure acting on the slanted surface added positively to the drag. The optimal drag was reached for $\varphi = 12.5°$, whereas $\varphi = 30°$ appeared to be a critical value. In the low-drag configuration, the time averaged wake displayed two re-circulatory regions, A and B in Figure 2.5, placed one on top of the other inside the separation bubble D. The strength of vortex A is influenced by the vortex C coming from the slant side edge, with which A mixed downstream of the separation bubble. At the same time, the strength of vortex C is dependent on φ, as well as the whole wake behaviour. The influence of φ on vortex C is clearly shown in Figure 2.6 (high-drag configuration), where the time-averaged structures observed for $\varphi = 30°$ are shown. As a consequence of the increased angle, the flow in the middle of the slant surface separated at the upstream edge, giving rise to a region of recirculatory flow E, delimited by two regions of attached flow, F. A low-drag configuration for the same critical value of φ was obtained by fixing a splitter plate vertically on the ground board in the plane of symmetry behind the model. The total pressure drag coefficient (evaluated by integration of the axial component of the measured pressure over the surface) changed from 0.321 for the configuration with $\varphi = 30°$ and no splitter plate to 0.209, against a value of 0.175 for the optimal drag configuration ($\varphi = 12.5°$).

Similar results have been obtained by other researchers, who focussed their investigations on the various aspects of the three-dimensional flow generated by this kind of model. Bayraktar *et al.* (2001) repeated the Ahmed experiment for a rear angle

of 0°, 12.5°, and 25° with a model at true automotive scale, in order to examine Reynolds number effects. To complement the experimental results, some simulations based on the Re-Normalisation Group (RNG) $k-\epsilon$ turbulence model were also run. Among the main characteristics of the wake, the asymmetry of the shedding from top and bottom of the base, due to the effect of the ground, appeared the most notable one. The analysis in the frequency domain of the forces acting on the model revealed a Strouhal number based on the body height equal to 0.106 and 0.086 for lift and side force, respectively, which agreed well with other data previously reported in the literature. Other important computational work was conducted by Krajnovic & Davidson (2005), who studied the instantaneous and time-averaged flow at the front and rear of a body with a rear slant angle of 25° through a Large Eddy Simulation (LES). The most recognisable instantaneous structures appeared to be the large steady-like cone vortices along the rear slant edges, and the small quickly varying hairpin vortices in the regions of separated flow on the front and at the rear of the model. The simulations also enriched the knowledge of the time-averaged flow by pointing out the presence of three pairs of cone-like vortices on the rear slanted surface, compared to the two pairs found from the previous experimental studies. Roumeas *et al.* (2008) simulated with the lattice Boltzmann method (LBM) the near wake close to the rear surface of the body. The results showed a flow separation at the end of the roof and its reattachment at the bottom of the rear window, with a strong interaction between the separated region and the longitudinal vortices. An additional study of the time-averaged wake topography at a 25° rear angle was conducted by Wang *et al.* (2013), who investigated the effect of the ground clearance on the coherent structures. The absence of the gap between floor and bottom of the model (i) altered the recirculatory bubble A and suppressed B, (ii) eliminated the recirculation region observed at the very bottom of the base, close to the ground, and (iii) changed the strength of the C-pillar vortex C and of the side vortex generated by the shear layer detachment at the vertical sides of the base.

Other authors preferred to conduct their studies at a zero rear angle, on models more closely resembling buses and lorries rather than passenger cars. Duell & George

(1993) investigated the effect of ground clearance and moving floor on the wake. No sensible difference between stationary and moving floor results was found in the case of the higher ground clearance tested ($C/H = 0.48$). However, the base pressure along the vertical axis exhibited a completely different distribution for a clearance ratio $C/H = 0.04$. This happened as the gap size became of the same order as the sum of the displacement thickness of the boundary layers on the bottom of the model and the floor. Similarly, the streamwise mean velocity downstream of the model showed a change in the distribution at small x only for $C/H = 0.04$. The same model was used to collect further information on the dynamic behaviour of the wake at a later time (Duell & George, 1999). During these subsequent experiments, the velocity signal at some strategic locations in the wake and the fluctuating pressures on the base were recorded. The power spectral density of the velocity data acquired near the separation point at the base revealed a characteristic frequency around 254 Hz. The following wake dynamics could be observed: the shear layer vortices were shed firstly from the top of the model; then, half a period later, from the bottom. A pseudo-helical vortex structure was formed, and vortices formed from vortex pairing were convected downstream in the shear layer. Pairing continued until the free stagnation point, where the vortices left at a frequency of 15 Hz. The same frequency value was found also when looking at the pressure fluctuations on the base. These numbers were recognised as the shedding ($St_{H(shed)} = 1.157$) and the pumping ($St_{H(pumping)} = 0.069$) characteristic frequencies of the wake. A similar value for the pumping frequency was measured by Khalighi *et al.* (2001), who found a Strouhal number of 0.07 for the pressure signal measured on the base of their model for different free stream velocities. A deeper analysis of the wake dynamics was carried out by Grandemange *et al.* (2012*a*) in a low speed hydrodynamic tunnel for a Reynolds number range between 260 and 1300. The different regimes observed were classified according the following bifurcation scenario: steady symmetric regime (SS) for $Re < 340$, steady asymmetric (SA) for $340 < Re < 410$, and unsteady asymmetric (UA) for $Re > 410$. The same geometry was then placed in a wind tunnel at a Reynolds number equal to 9.5×10^4. The analysis showed the existence of two preferred positions; the wake seemed to switch randomly between them, so that

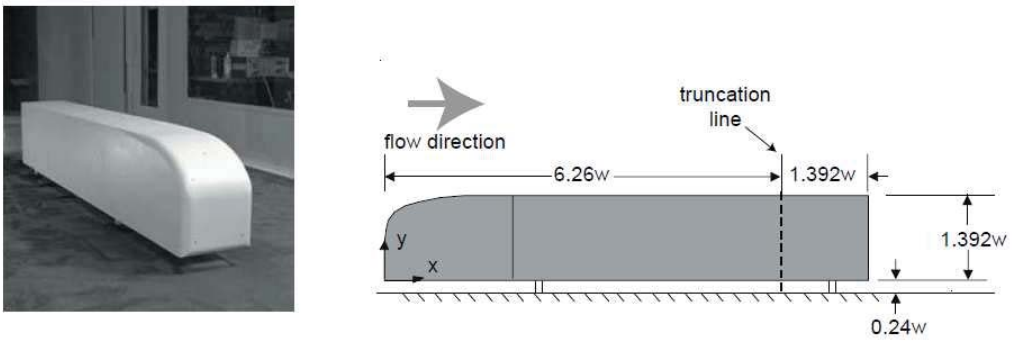

Figure 2.7: Photo and schematic of the Ground Transportation System geometry in the NASA Ames 7 ft × 10 ft wind tunnel; w=0.3238 m is the width of the model (Ortega *et al.*, 2004).

the symmetry was still statistically recovered in the mean flow. The bi-stability was confirmed by a new series of measurements performed in a wind tunnel at Reynolds numbers from 4.6×10^4 to 1.2×10^5 (Grandemange *et al.*, 2013). The rate of shift between the two asymmetric positions (order of magnitude of 1 Hz) appeared to increase with velocity, and was suppressed for ground clearances smaller than a critical value of 0.1 times the height of the body. In addition to this oscillation in the horizontal direction, the wake exhibited lateral and top/bottom shear layer interaction. On the other hand, the low-frequency pumping mode was not observed during this investigation.

Additional models have been developed over the years as alternatives to the geometry proposed by Ahmed. Among many, the Ground Transportation System (GTS), shown in Figure 2.7, is worth mentioning. The GTS resulted from the collaboration of seven American organisations under the supervision of the United States Department of Energy (DOE) with the aim of designing effective drag reduction devices employable on heavy vehicles, as stated in McCallen *et al.* (2004). The model has a simplified geometry, with cab-over-engine design, no tractor-trailer gap and no wheels. A computational and experimental investigation conducted by Ortega *et al.* (2004) showed that the wake was characterised by coherent flow structures originating from the corners of the model, described as fairly robust and recognisable far downstream in the wake. Moreover, two counter-rotating flow structures, one on top of the other, were observed in the region of separated flow.

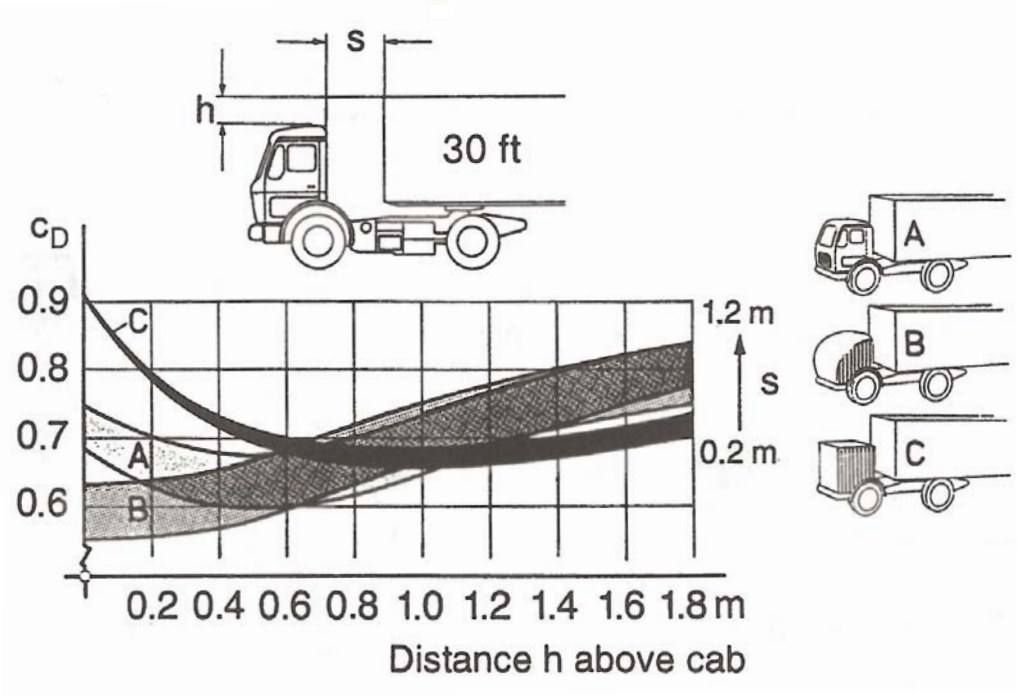

Figure 2.8: Influence of cab shape taking into account different body heights h and gap widths s (Hucho, 1998).

2.3.2 Trucks

From an aerodynamic point of view, trucks are entities composed of several single bodies that interact with each other. The total drag of a lorry can be subdivided in the partial drag of body, cab and chassis. It is also influenced by many different factors, such as the gap between tractor and trailer, the body height, and the cab shape. As shown in Figure 2.8, the drag coefficient increases with the distance between the tractor and the trailer, while it shows distinct behaviours for different projecting body heights, depending on the shape of the cab, as clearly illustrated in Figure 2.9. Trucks composed of identical trailers but towed by different tractors, can have very similar drag coefficient, but with different contributions from front and rear of the vehicle. Sharp-edge cabs generate almost the complete drag of the vehicle, while drag coefficients of ideally streamlined cabs are much lower. On the other hand, the trailer carried by a sharp-edge tractor experiences a null or even negative drag, while the body of the streamlined cab lorry has a drag coefficient of the same order of magnitude of the complete vehicle. A more detailed representation of the dominant drag regions for a typical tractor-trailer is shown in Figure 2.10.

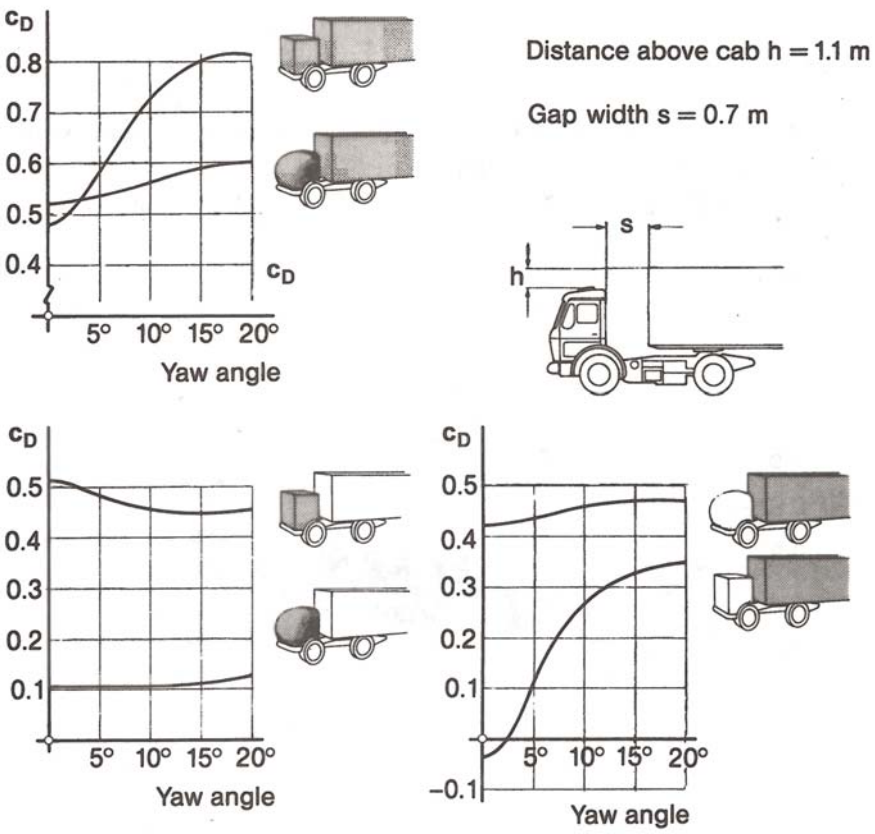

Figure 2.9: Influence of cab shape on partial drags of cab and body for semitrailer (Hucho, 1998).

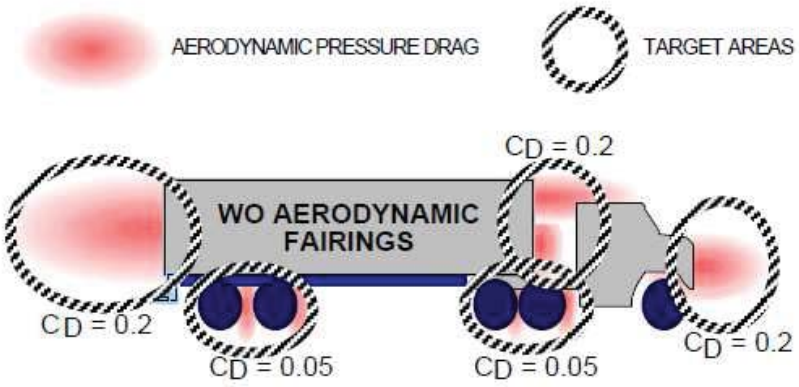

Figure 2.10: Graphic representation of the drag distribution for a heavy vehicle tractor trailer truck, without aerodynamic fairings (Wood & Bauer, 2003).

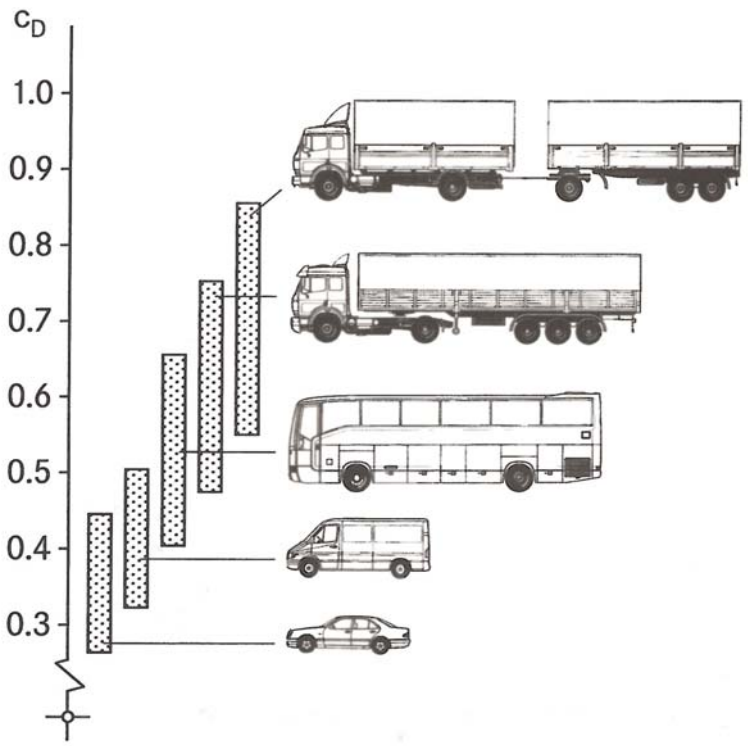

Figure 2.11: Drag coefficients for different commercial vehicles (Hucho, 1998).

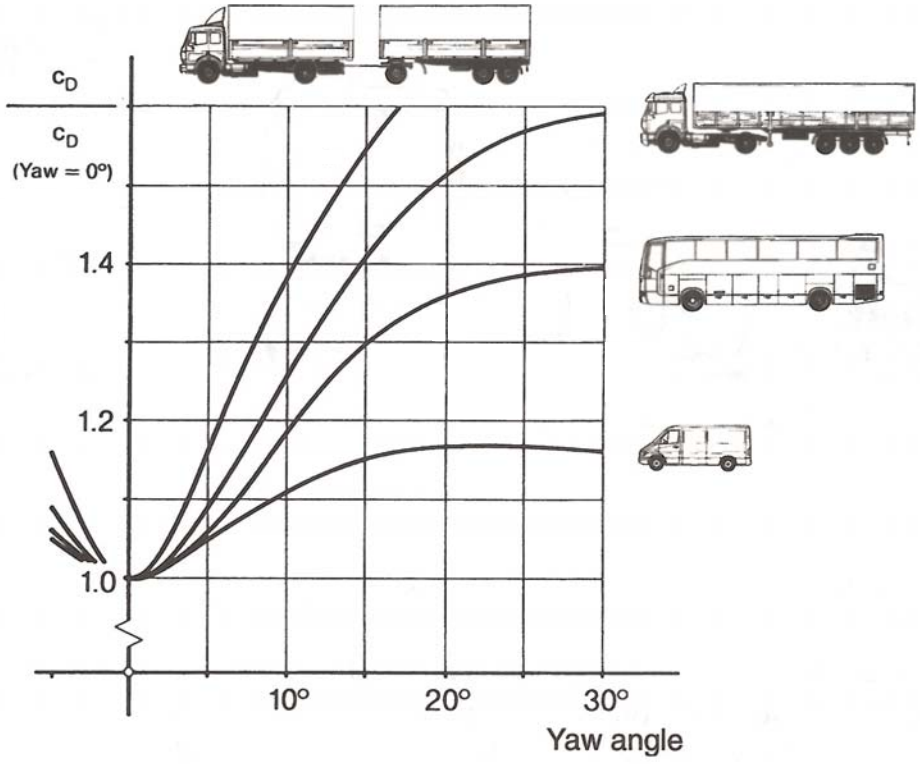

Figure 2.12: Drag versus yaw angle for different vehicle types (Hucho, 1998).

When looking at the drag of a full lorry, still air and actual operating conditions have to be distinguished. Drag coefficients for still-air conditions for a variety of commercial vehicles are shown and compared to the coefficients for cars in Figure 2.11. The change shown by these coefficients in actual operating conditions are illustrated in Figure 2.12, where the drag coefficients corresponding to crosswind conditions are compared to drag coefficients at zero yaw angle, equivalent to driving in still air. Alternatively, road-wind influence can be taken into account by calculating a wind-averaged drag coefficient with various formulae (see Hucho, 1998; Cooper, 2003). Since these kind of formulae make use of reliable wind statistics over a year, they provide a much better estimated of the averaged drag experienced by a vehicle than the values measured in a wind tunnel at different yawing angles (Hucho, 1998).

2.4 Examples of Flow Control for Road Vehicles Drag Reduction

2.4.1 Passive Control Applications

Following success in suppressing the vortex shedding and raising the base pressure of generic bluff bodies, Duell & George (1993) tested the effects of splitter plates and cavities applied to a zero back-angle Ahmed body. Splitter plates of different lengths (0.8, 0.6, 0.4 and 0.2 times the height of the model) placed at three different inner locations (at the centre of the base, one quarter of the height above and one quarter below the centre) were tested. A vortex able to produce a strong suction was formed in the corner between the base and the plate; nonetheless, the mean pressure on the opposite side of the plate was raised. The best results were obtained with the longest plate, positioned above the centre of the base, for a total pressure raise of 7% compared to the baseline case. The position of the free stagnation point was not altered by the plate, but the mean velocity in the near-wake was reduced, and the recirculation bubble suppressed. However, this configuration was very sensitive to yaw angles as small as 3°. To overcome this difficulty, a configuration with a

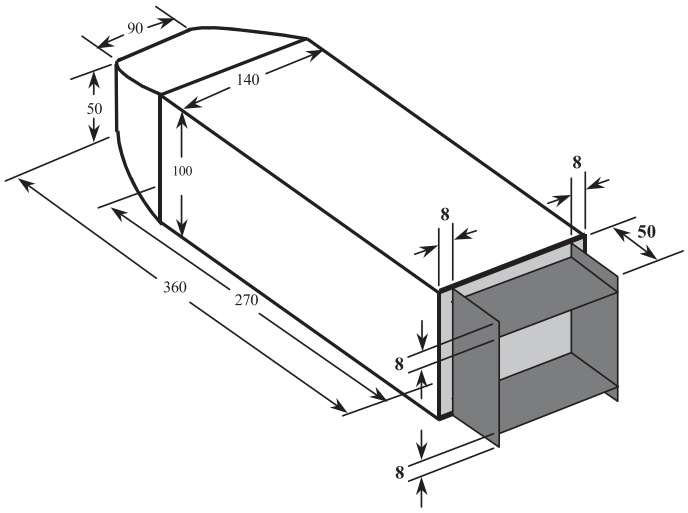

Figure 2.13: Schematic of the model – all sizes are in mm (Khalighi *et al.*, 2001).

complete cavity, formed by four equal length plates placed around the perimeter, was tested. No vortices were formed inside the cavity, and the pressure distribution uniformity increased with the cavity depth. The overall mean pressure was raised by 4% for a cavity depth of 0.2 times the height of the body, while a cavity deep 0.8 times the height increased the base pressure by 11%. The recirculation bubble was not observed, and the turbulent intensity was reduced both outside and inside the cavity. A further set of experiments (Duell & George, 1999) showed that a shorter cavity increased the recirculation length by 10%, while the longer one was able to increase it up to 60–80%. In addition, the effects on the unsteady pressure were investigated by correlating two signals. While the baseline case showed high coherence at 15 Hz between signals from opposite locations on the vertical symmetry plane of the base, no coherence peaks were measured with the cavity in place. This confirmed that the low-frequency bubble pumping mode was totally suppressed. Moreover, the coherence phase angle was close to 0° for the signal pairs considered in the range between 0 and 50 Hz, suggesting that the pressure field was in-phase across the model. The near-wake outside the cavity was still found to be unsteady, but with no evidence of periodic flow structures.

Similar results were obtained by Khalighi *et al.* (2001), who tested both experimentally and through simulations the unsteady wake of an Ahmed body with four

base plates, as in Figure 2.13. The modified model showed an increased pressure coefficient and a more uniform base pressure distribution. The shape and magnitude of the power spectra were also significantly modified: the spectral peak was reduced by 40% compared to the baseline case at the highest free stream velocity tested. Again, the authors inferred that the near wake outside the cavity was unsteady, but with no evidence of periodic flow structures. The pumping action of the shear flow close to the base was suppressed by the cavity, and the unsteady velocity fluctuations were shifted downstream. The turbulent intensity were found to be approximately 10% lower than the reference case. The PIV data showed a narrower recirculation region and an aerodynamic boat-tail effect induced by the cavity. Due to the unsteadiness of the wake, the behaviour of the flow could be represented correctly only by means of an unsteady RANS simulation, which predicted a 18% reduction of the drag coefficient, very close to the 20% measured experimentally.

An unsteady simulation and some PIV measurements were carried out by the same authors (Khalighi *et al.*, 2012) to compare the cavity configuration with a boat-tail device. The results showed two main recirculation regions, different length of the separation bubble, and a narrow wake region in comparison to the simple square back model. Furthermore, both the devices induced an upward deflection of the underbody flow and a strong reduction of the intensity of the recirculation velocity in the base region. As a consequence, the vortex shedding and the unsteadiness in the wake were reduced and the pressure at the base increased. A total drag reduction of 18% and 30% was measured for the cavity and the boat-tail configuration respectively.

Owing to the impracticality of adding a splitter plate or a cavity to a vehicle, some alternative solutions have also been studied. Beaudoin & Aider (2008) tested the efficiency in reducing lift and drag of flaps located at five strategic locations at the rear of a slightly modified Ahmed body with back angle of 30°, Figure 2.14. A single flap located at the junction between the roof and the rear slant of the body (number 1 in the figure), corresponding to the classic roof spoiler, reached the minimum drag at an angle $\alpha \approx 25°$ (measured from the slant surface), while the minimum lift was reached for $\alpha = 52°$. A flap at the junction between the rear slant and the base (number 2 in the figure), again a classic spoiler position, displayed the minimum

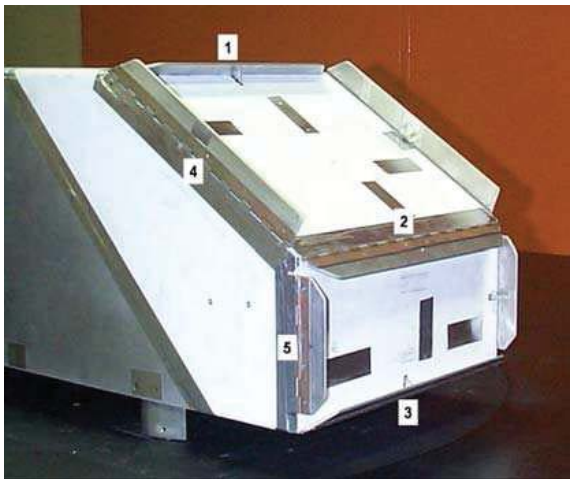

Figure 2.14: Rear view of the model equipped with the seven flaps on all the rear edges as in Beaudoin & Aider (2008).

lift and drag for the same $\alpha = 95°$. The third single flap tested was located at the junction between the base and the underbody (number 3), and showed the optimal drag and lift for $\alpha \approx 80°$. The last two configurations were tested with pairs of flaps. The flaps located on the side edges of the rear slant (number 4) had their minimum drag orientation at $\alpha \approx 75°$. Finally, the flaps located at the side edges of the rear base exhibited the optimal drag at $\alpha \approx 75°$, while the lift was barely influenced. This last configuration provided the best drag reduction, for a $\Delta C_D = -17.7\%$. Various combinations of the different flaps were also studied. The best results were obtained with the combination of all the best individual configurations, for a drag reduction of $\Delta C_D = -25.2\%$. PIV measurements showed that, for the optimal drag configurations, the flow was fully separated over the rear slant and the longitudinal vortices previously found in the reference case were completely suppressed.

Another possible alternative to the rear cavity is the application of vortex generators (VGs), as experimentally investigated by Aider *et al.* (2010). The VGs were applied to the modified Ahmed body shown in Figure 2.15. A parametric study identified the influence of longitudinal position, angle, spacing and distribution of the VGs on their efficiency in reducing drag and lift on the model. The Reynolds number dependence was also analysed. Both the angles tested, $\alpha = 60°$ and $\alpha = 120°$, reduced the body drag by 12%, while the maximum lift reduction of 54% was obtained for $\alpha = 60°$. In terms of longitudinal position, the VGs were shown to be efficient in

Figure 2.15: Picture of the rear of the model equipped with a set of VGs attached on a motorized rotating axis (Aider *et al.*, 2010).

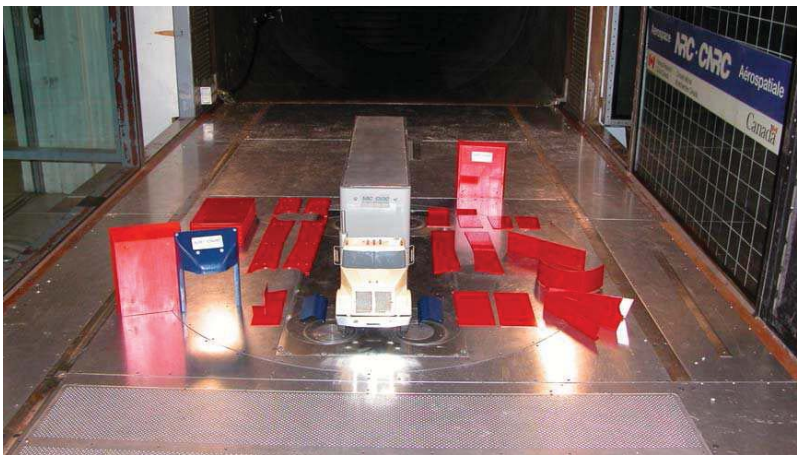

Figure 2.16: Realistic 1:10-scale model with optional parts to be tested (Cooper & Leuschen, 2005).

a quite large region. Their efficiency was also improved by a larger spacing between them. Moreover, the best results were obtained by removing the VGs close to the sides of the model. Finally, the increase in the Reynolds number produced a drop of the VGs efficiency, which was found to be recoverable by changing their angle. From the data collected, it was evident that the drag reduction was obtained by triggering the flow separation, rather than delaying it. It was shown that the action of the VGs located at the centre of the body was exerted on the recirculation bubble, while the ones located at the sides were able to strengthen the trailing vortices, leading to drag increase.

Results obtained from simplified models are crucial to the development of drag

Figure 2.17: Volvo VN 660 and 28-ft trailer in the NRC 9 m × 9 m wind tunnel (Leuschen & Cooper, 2006).

(a) (b) (c)

Figure 2.18: Gap seal devices: (a) Laydon Composites nose fairing; (b) Labyrinthine gap seal, (c) Manac prototype leading edge fairing – all from (Leuschen & Cooper, 2006).

(a) (b) (c)

Figure 2.19: Boat-tail devices: (a) TrailerTail^{TM} sold by ATDynamics; fuel savings up to 6.58%, (b) Transtex Composites folding rear trailer deflector (Leuschen & Cooper, 2006), (c) Aerovolution inflatable boat-tail (Leuschen & Cooper, 2006).

reducing devices. However, additional data collected from realistic models (Figure 2.16) and real vehicles (Figure 2.17), both inside wind tunnels and on the road, are needed before any device could be made commercially available. Some examples of appliances developed over the last 40 years are given in Cooper (2003), where they are classified as *first-generation* and *second-generation* technologies. Cab shaping, cab-mounted deflectors, trailer front-end fairings, cab-side extenders and body front-edge rounding are part of the first group, and they were widely available and already utilised in the late Nineties. The wind-averaged drag coefficient reductions reported by Cooper (2003) for roof fairings and side extenders (relative to a speed of 55 mph) were of order $0.15 \leq \Delta C_D \leq 0.25$. In the same document, a reduction of $0.15 \leq \Delta C_D \leq 0.20$ is also reported for cab edge rounding and roof fairings. The existence of a range of efficiencies is due to yaw effects, especially important for cab extenders and splitter plates, as reported also by Hyams *et al.* (2011) and McCallen *et al.* (2004). Other technologies came in use later and are still not widely applied due to their lower efficiency and practicality. Examples of these are gap seals, side skirts and boat-tail devices. Gap seals aim at reducing the drag produced by the flow trapped between the tractor and the trailer. This can be accomplished by a single (Cooper, 2003) or multiple (Wood & Bauer, 2003) vertical panels, dome-, cylindrical- or cone-shaped add ons, or inflatable devices (Figure 2.18). Side skirts are flat panels attached to both sides of the tractor, and those of the trailer, which limit the effects of wind on the undercarriage. For this reason skirts, as well as gap seals, have their maximum efficiency at high yaw angles. Finally, boat-tails have been tested and developed in different shapes: cavities with flap or inclined sides, panels covering only three sides, inflatable round add ons, telescopic devices and similar (Figure 2.19).

Other drag reducing devices that are now commercially available are vortex generators and undercarriage devices. The device shown in Figure 2.20, studied by Wood & Bauer (2003), is formed by two aerodynamically contoured surfaces aimed at changing the low-momentum flow into a coherent high-momentum flow. The counter-rotating vortex structure produced had the effect of energising the wake.

The studies mentioned above made possible the development of complete aero-

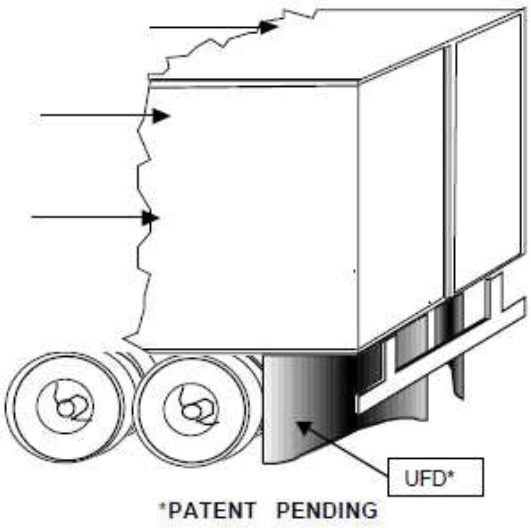

Figure 2.20: Sketch of the undercarriage flow treatment device (UFD) installed on the aft trailer undercarriage (Wood & Bauer, 2003).

dynamic packages now sold by various companies all over the world. Some examples are TrailerTail sold by Advanced Transit Dynamics, Inc. (2013), BMI by BMI Corporation (2009), Mudguard by Mudguard Technologies (2009–2010) in the United States and the packages sold by Aerodyne (2009), Scania (2013) and Iveco (2013) in Europe. Vortex generators, aerodynamically-shaped roof lines, wheel covers, and rear air diffusers at the top and the bottom of the trailer are also sold by companies such Montracon (2013), Airtabs (2010), Don-Bur (2010) and Jost (2013).

2.4.2 Active Control Applications

The examples of active control applications found in literature are less numerous than the passive ones, even though their popularity has steadily increased during the last 15 years. The reasons for the general preference given to passive control are not only the difficulty of simulating and building active devices, but also the challenge of keeping a positive balance between the gain and the energy spent in obtaining a drag reduction. However, the constant rise of fuel prices and the need to reduce emissions from vehicles and industry in general, are well worth the extra effort required. The examples described in this section compare open-loop systems for control of wakes from bluff bodies through constant or alternate blowing and/or

(a) (b) (c)

Figure 2.21: Aerodynamic devices applied to commercial vehicles: (a) vortex generators, (b) rear air diffuser and (c) roof line on both straight frame and double-deck that cants at the front (Montracon, 2013).

suction.

An example of steady blowing at the base of a square back Ahmed model is the work by Wassen *et al.* (2010). The effects of constant blowing from a continuous slot placed along the rear edges of the model were investigated by means of an LES simulation. The drag reduction ranged from a minimum of 3% for a 0° blowing angle, to a maximum of 11.1% for an angle of 45°. A further increase of the angle up to 60° lowered the drag reduction to 10.4%. A thorough observation of the flow structures revealed that the long-time-average symmetry was lost due to the stabilising of the wake. Larger areas of high pressure compared to the reference flow were also observed in the pressure distribution of the controlled cases. Unfortunately, the drag reduction went down to 6.1% when the optimal blowing angle was tested in the "low energy expenditure" mode (blowing omitted at the corners in order to save energy). The results proved the method to be rather effective, but the calculated efficiency appeared to be negative for all cases, apart from a 0.1% net gain obtained when forcing with a 60° angle.

The study carried out by Rouméas *et al.* (2009) with a LBM simulation for continuous blowing from a slot along the rear edges a square back geometry (Figure 2.22) produced very similar results. The optimal drag reduction of 28.9% was obtained with a blowing angle of 45°, while different orientations appeared less effective (-17.9% at 30°, -20.8% at 60°, and -17.1% at 75°). The control method

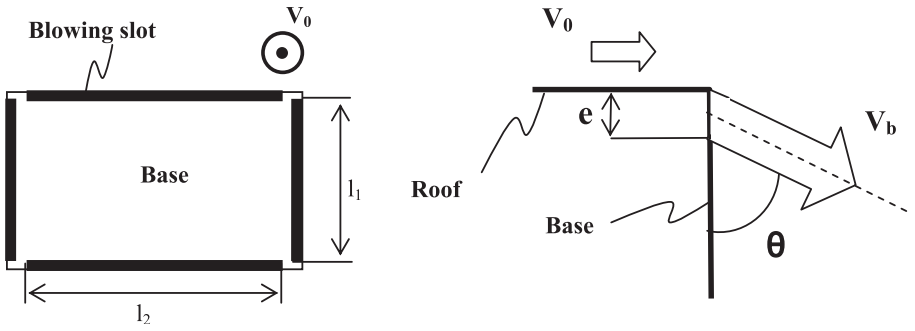

Figure 2.22: Schematic of the blowing device (Rouméas *et al.*, 2009).

produced a reduction of the wake section and of the total pressure loss, with an increase of the static pressure on the base. A formula for the efficiency calculation was also developed, which showed that power saving of 7 times the supply power was possible.

Continuous blowing was also applied in between the tractor and the trailer by Ortega *et al.* (2004). When compared to drag reduction from traditional side extenders, this control method was found more effective both by the tests on a 1:20 realistic wind tunnel model and by a full scale CFD simulation. By increasing the bleeding coefficient, the rate of entrainment from the free stream into the gap was decreased, as well as the difference between the averaged pressure coefficients on tractor base and trailer frontal face.

Continuous blowing was also tested with side extenders, the combination of active and passive control was investigated by Khalighi *et al.* (2012) with a simulation of a Coanda jet blowing device at the rear of a square back geometry. The recirculation region in the wake was completely suppressed, and a drag reduction of approximately 50% was measured. The efficiency of Coanda jets in reducing drag was also proved by the experiments of Geropp & Odenthal (2000) and discussed by Englar (2000).

An alternative approach was chosen by Roumeas *et al.* (2008), who applied continuous suction to the upper part of the rear window of a simplified fastback geometry. The three-dimensional simulation showed reattachment of the flow on the wall and the reduction of the total pressure loss in the wake. A maximum drag reduction of 17% was achieved for a suction velocity equal to 0.6 times the free-stream velocity. Considering the power consumed, the suction velocity which

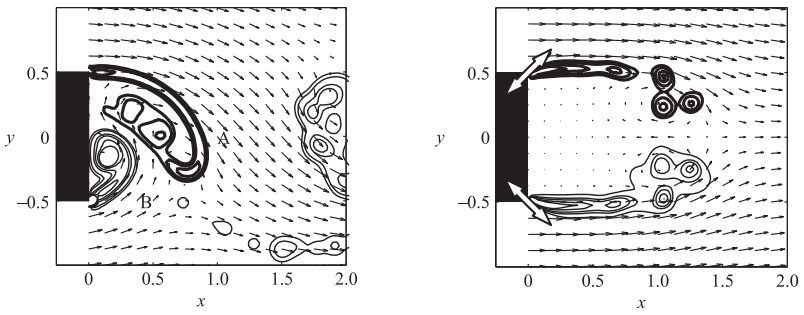

Figure 2.23: Unforced flow (right) and symmetric forcing (left) on a D-shaped 2D bluff body (Pastoor *et al.*, 2008).

maximised the efficiency was found equal to 0.375 times the free stream velocity.

Since one of the main issues encountered by active control methods with constant blowing has been the net balance of the energy involved, Joseph *et al.* (2013) investigated experimentally the efficiency of micro-electro mechanical system (MEMS) based jets to control the wake of an Ahmed body, with the aim to save energy by pulsed blowing. The drag reduction ranged from a maximum of 10% for $Re = 1.1 \times 10^6$, to 8.8% for $Re = 1.4 \times 10^6$, and to 4.9% for $Re = 2.1 \times 10^6$. Similar results were obtained by means of macro-actuation (using conventional magnetic valves), but with a higher injected momentum. Moreover, a very strong difference was observed in the flow structures produced by micro- and macro-actuation. While the shear layer profile was left almost unchanged by the MEMS action, the magnetic valves caused an increase in the energy of the high frequency structures, and a decrease of the low frequency ones. In addition, the MEMS actuators saved almost 16 times the power spent, while the valves used nearly 2 times the energy saved on the drag.

Pulsed blowing was combined with steady suction in the experimental work by Seifert *et al.* (2009). The Suction and Oscillatory Blowing (SaOB) actuator produced a 35% of drag reduction on a cylinder. When the same cylinder was added at the top aft edge of a 2D truck model, it produced a passive effect of about 5% drag reduction, and up to 20% and 5%, at low and higher speeds, respectively, with active control. An additional control cylinder, with suction only, located at the lower edge of the base, provided 20% drag reduction at highway speeds, equivalent to about 10% net fuel savings for heavy vehicles.

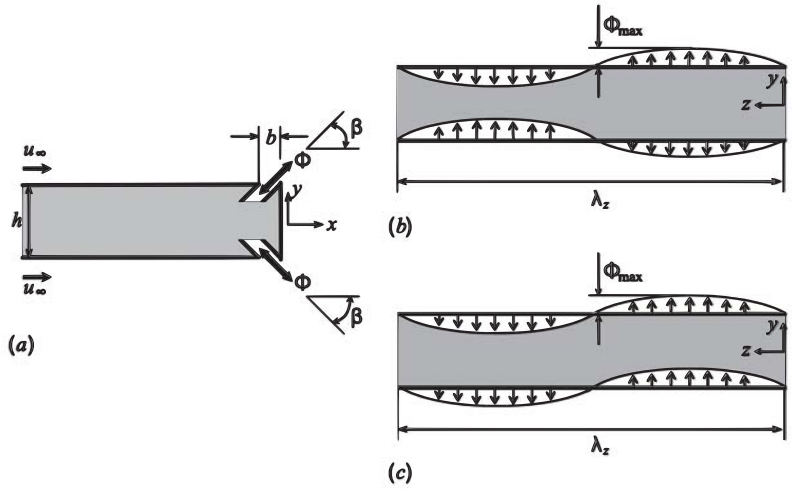

Figure 2.24: Schematic diagram of the distributed forcing over a model vehicle as in Choi (2003) and Kim *et al.* (2004) (blowing and suction sinusoidally varying in the spanwise direction but steady in time): (a) side view, (b) front view of the in-phase forcing, (c) front view of the out-of-phase forcing (Kim *et al.*, 2004).

A two-dimensional geometry, an elongated D-shaped body, was also used by Pastoor *et al.* (2008) to test the effect of open and closed-loop wake control by means of synthetic jets. The actuation was performed by loudspeakers through two slots located at the upper and lower trailing edge of the model and extended to half the span of the body. Both in-phase and out-of-phase forcing were tested. The base pressure was monitored by means of 3×3 difference pressure gauges, and the structure of the wake was investigated through a series of PIV measurements carried out at various conditions. The out-of-phase forcing showed no difference on the wake, while a base pressure recovery of 40% with a drag reduction of 15% was obtained both with the open and the closed-loop actuation. However, the most important part of the study was the physical understanding of the flow and of the effects of control, obtained with the aid of a reduced-order vortex model. The controller action synchronised the roll-up of the top and bottom shear layers, delaying the onset of asymmetries. As a consequence, the region of stagnating flow at the back was enlarged and the model base pressure increased, as shown in Figure 2.23.

A similar kind of control was applied to a three-dimensional body by Choi (2003), who tested using numerical simulations the effectiveness of time-varying low- and

high-frequency forcing, and distributed forcing (steady in time but spatially varying), for drag and lift reduction. The first two methods were not successful in reducing the drag of a cylinder and a sphere at Reynolds numbers of order $< 10^4$: the low-frequency forcing enhanced vortex shedding, while the high-frequency forcing increased the shear layer instability. At high Reynolds numbers ($Re = 10^5$), the high-frequency forcing decreased the drag of a sphere by up to 50% in the absence of a trip, and by 30% in the presence of it. The distributed forcing, applied as shown in Figure 2.24, effectively reduced the drag of a cylinder even at low Reynolds numbers with in-phase forcing, whilst it had almost no effect when applied out-of-phase. At higher Reynolds numbers, for a three-dimensional and fully turbulent base flow, both in-phase and out-of-phase action reduced drag significantly. In the case of a two-dimensional model of a vehicle, the time-averaged base pressure was increased by about 30% with in-phase forcing, while it was left unchanged with out-of-phase forcing both at low and high Reynolds numbers. In contrast to the previous two cases, the distributed forcing increased the drag of a sphere, probably because of the very specific vortical structures contained in its wake.

The same control was applied to a vehicle model with square-back geometry by Kim *et al.* (2004), who tested the effectiveness of distributed forcing both through an LES simulation and wind tunnel experiments. The simulations with in-phase-forcing produced drag reductions of 30%, 36% and 18% at $Re = 4,200$, $Re = 20,000$ and $Re = 40,000$, respectively, while the out-of-phase forcing did not show any appreciable effect. The simulation showed a complete suppression of the Kármán vortex shedding by means of in-phase forcing, which lead to a substantial base pressure recovery. The experiments, conducted with in-phase forcing at $Re = 20,000$ and $Re = 40,000$, confirmed the wake modifications predicted. It is worth remarking that the experimental implementation of the distributed forcing on the model guaranteed a zero-net mass flow rate.

Even though these kinds of devices are not yet available on the market, active control has also been applied to real vehicles in order to assess their efficiency in terms of fuel savings. An example of this is the work by El-Alti *et al.* (2010), who combined passive and active devices on a Volvo test vehicle. The work that led to this

(a) (b)

Figure 2.25: Full scale test vehicle: (a) mounted flaps, (b) actuators (El-Alti *et al.*, 2010).

first prototype is thoroughly described in El-Alti (2012). The size of the wake was decreased by incorporating synthetic jet actuators to three inclined flaps mounted at the rear end of the trailer (sides and roof), as shown in Figure 2.25. The flaps as well as the actuator configuration were previously studied, both computationally and experimentally, on laboratory models. The full scale tests were conducted according to the *Joint ATA/SAE Fuel Consumption Test Procedure, Type II*, in order to ensure consistency. The actuators mounted on the truck were optimised for low frequency forcing, and powered from two small power stations situated in the trailer. Six of them were located at the sides, and five at the roof. The results showed a reduction in fuel consumption of 5.4% (actuation cost not included) for the case with flap angle of 30° and a slot angle of 45°. Among the two forcing frequencies used during the tests, 16.7 Hz and 23.3 Hz, the highest gave a slight improvement in the drag reduction. However, the two cases of passive control (flaps only with no jet forcing) showed a higher fuel consumption than the baseline case.

A similar work in terms of the combination of passive and active control is the one carried out by Englar (2005). A device called 'Circulation Control' (CC), previously developed to reduce drag on aerofoils, was adapted to road vehicles and applied to a truck model (Englar, 2001). In the CC application to airfoils, the trailing-edge

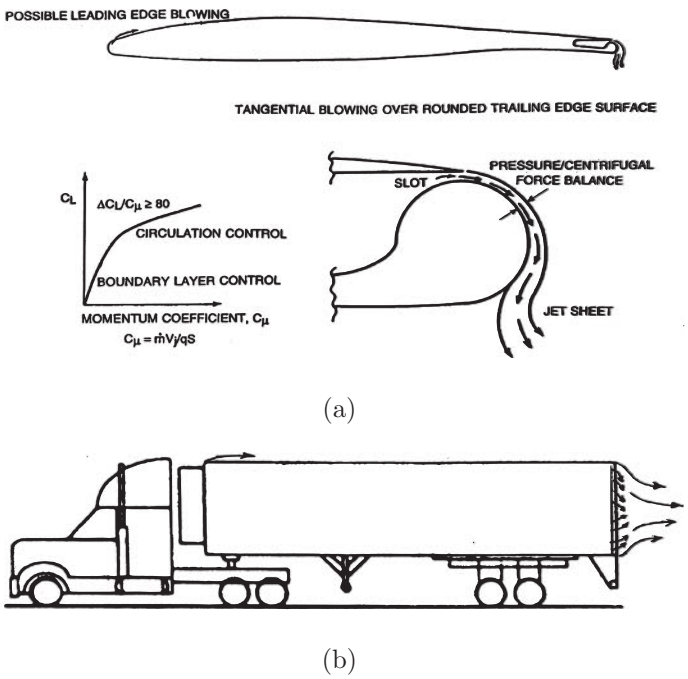

(a)

(b)

Figure 2.26: Circulation Control aerodynamics: (a) on a two-dimensional airfoil, (b) application of GTRI Pneumatic Aerodynamic Technology to heavy vehicles (Englar, 2000).

flap was replaced with a fixed curved surface with a tangential slot ejecting a jet over the surface (Figure 2.26 (a)). Owing to the Coanda effect, the jet remained attached to the curved surface, with a great increase in the circulation. For heavy vehicles, four aft blowing slots, one on each corner edge of the afterbody, and a fifth slot at the leading edge of the trailer were employed (Figure 2.26 (b)). The system was operated on a test vehicle supplied by Volvo, and further developed in between two testing periods. The final tests were conducted according to the *SAE Type II* regulations. The aerodynamic efficiency of the vehicle was also improved by means of cab extenders with a 60% closure of the gap between tractor and trailer, and by wheel fairings covering the trailer suspensions, axles and wheels.

The results obtained during the on-road tests for the complete set-up and for the blowing system only are shown in Figure 2.27. Successfully, a Fuel Economy Increase ratio (*FEI*) of 8–9% was reached even when considering the fuel burnt to power the blowing engine.

A final example of an active-control full-scale test is that by Seifert *et al.* (2010) using the SaOB actuator described previously. The device was scaled up by a factor

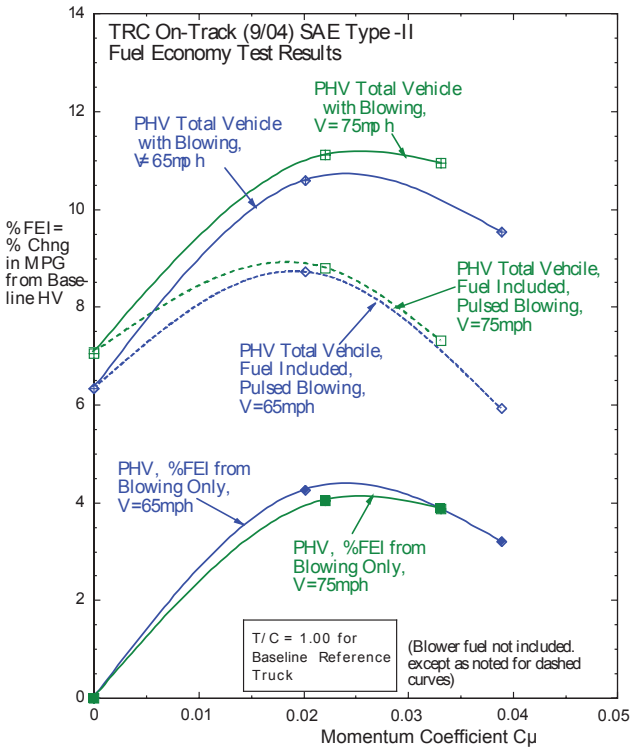

Figure 2.27: *SAE Type-II* fuel economy results for the pneumatic system components (Englar, 2005).

(a) (b)

Figure 2.28: SaOB actuators in place on the test vehicle: (a) isometric rear-view of the device installed on the trailer, (b) external image of the device (top) and interior of the device with actuator block and covers removed (bottom) (Seifert *et al.*, 2010).

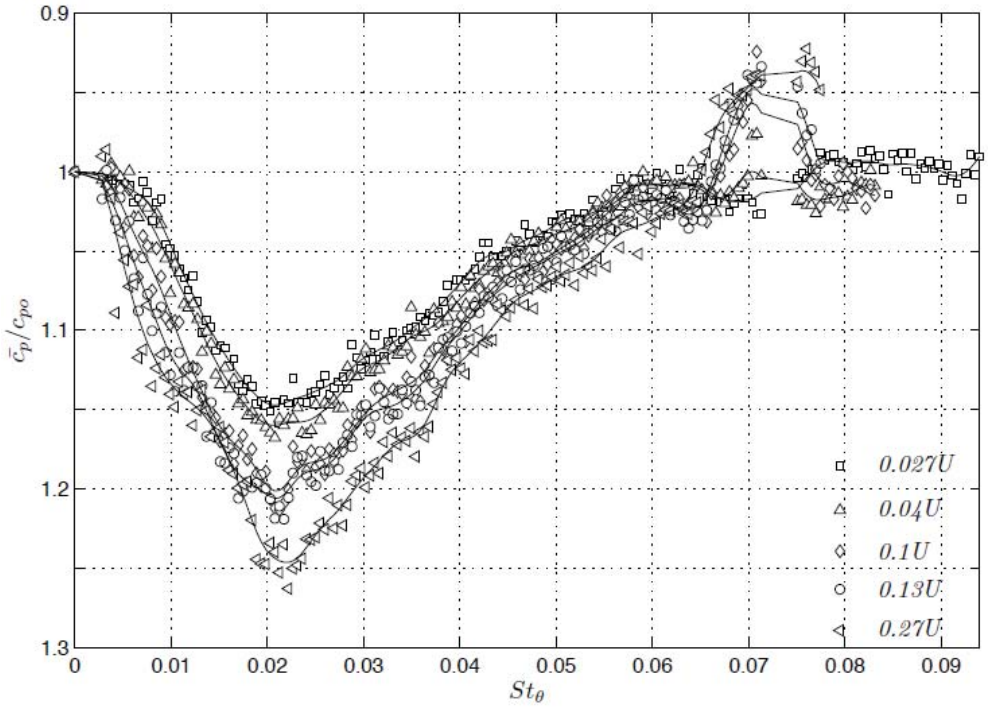

Figure 2.29: Coefficient of base pressure as a function of frequency for several different forcing amplitudes - □ $0.027U$, △ $0.04U$, ◇ $0.1U$, ○ $0.13U$, ◁ $0.27U$ (Qubain, 2009).

of about 50% from the size of the original prototype (Seifert *et al.*, 2009), and assembled in cells located at the aft sides and roof of the vehicle (Figure 2.28). The maximum flow rate of 150 ls^{-1} at 0.5 bar, which was required to feed the almost 100 actuators located on the truck, was provided by a suitable pump, driven by a 16 hp gasoline engine. The low efficiency of this pressure supply imposed a penalty on the whole system, which had an overall efficiency of less than 15%. No drag reduction was obtained.

2.5 Precursory work

From the examples given above, it appears that the application of active flow control to three-dimensional wakes from bluff bodies is still a developing field, where much more can be done. The present project started at Imperial College with the work by Qubain (2009), who used periodic jet blowing to modify the turbulent wake of an axisymmetric cylinder with a blunt trailing edge. The open-loop forcing was

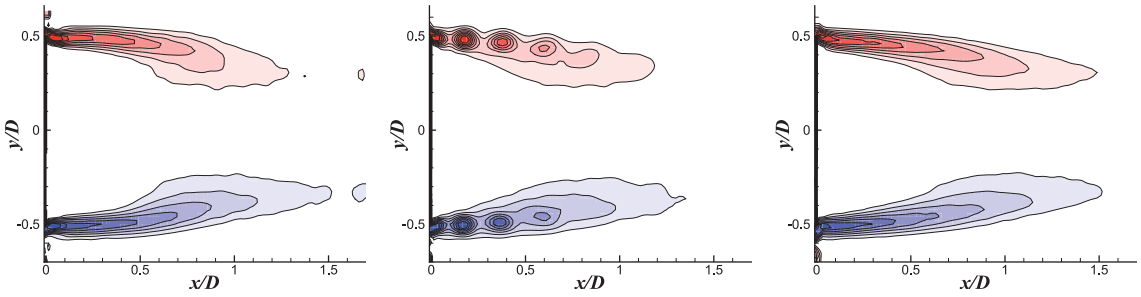

(a) (b) (c)

Figure 2.30: Phase-averaged vorticity data for (a) $v_f/U_\infty = 0.27$ for $St_\theta \approx 0.003$, (b) $St_\theta \approx 0.024$ and (c) $St_\theta \approx 0.07$ (Qubain, 2009).

obtained by means of a high-fidelity speaker located inside the body, used to generate an annular pulsating jet with zero-net-mass exchanged with the flow. By varying the forcing frequency of the jet, the base pressure could be lowered or increased, as show in Figure 2.29. The results showed that the wake exhibited specific responses at three distinct frequency ranges:

- At very low frequencies ($St_\theta \approx 0.003$) there was a slight increase of the base pressure due to a weak effect on the instability mechanism, identified as "pumping mode" by Berger *et al.* (1990), normally observed in the unforced wake at this frequency;

- At $St_\theta \approx 0.022$ the base pressure decreased with increasing the forcing amplitude. This minimum was not influenced by Reynolds number variations, suggesting that this mode is uncoupled from the wake instabilities;

- At high frequencies ($St_\theta \approx 0.07$) a rise in the base pressure over a restricted range of frequencies was found. From the velocity spectra, a reduction of energy in the large scales but an enhancement of energy in the small scales (and therefore dissipation) was found.

The effect of forcing observed on the wake structure using PIV is shown in Figure 2.30, where the phase-averaged vorticity data referred to the three characteristic frequencies mentioned above are presented. The phase averaging was computed using eight phases, which covered the whole of the actuation cycle. The time step

between each frame was $\pi/4$, based on the frequency of actuation, and the first frame started at the beginning of the blowing phase.

The work was continued by Oxlade (2013), who answered some questions about the wake structure of this particular model and of axisymmetric bluff bodies in general. The wake structure was studied by means of azimuthal decompositions of the base pressure spectra, and by spatially and temporally resolved measurements of the centre of pressure. The results of the analysis showed that:

- The wake was dominated by a mode with wave number $m = \pm 1$, referred to as the very low frequency mode, with Strouhal number $St_D \approx 0.0015$. This mode was found to be responsible for the wake asymmetry observed with short-time average statistics. The axisymmetry is eventually recovered in the long time average statistics. Similarly, the instantaneous position of the centre of pressure was found to be offset from the central axis of the body.

- A subharmonic of the vortex shedding was observed at $St_D \approx 0.1$. Its energy, higher than the vortex shedding mode itself, was distributed between the wavenumbers $m = \pm 1$ and $m = \pm 2$. Due to its frequency content, it was supposed to be the result of a pairing vortex mechanism.

A parametric study of the pressure recovery (Figure 2.31) showed an increase in base pressure for forcing frequencies above $St_\theta \approx 0.07$ and blowing coefficients above $C_\mu \approx 0.005$. A maximum increase of 33% was achieved for $St_\theta = 0.107$ and $C_\mu = 0.04$. The pressure recovery scaled linearly with forcing frequency up to a value equal to about five times the natural frequency of the shear layer. It also scaled linearly with the blowing coefficient up to $C_\mu \approx 0.04$.

The investigation of the origin of the pressure rise showed that it was not due to a suppression of the natural wake instabilities. Measurements of the vortex shedding and shear layer amplitudes confirmed that the control method achieved drag reduction by suppressing the entrainment of fluid at the turbulent/non-turbulent interface and hence the energy of all modes without any mode selection. See Oxlade (2013) for further details.

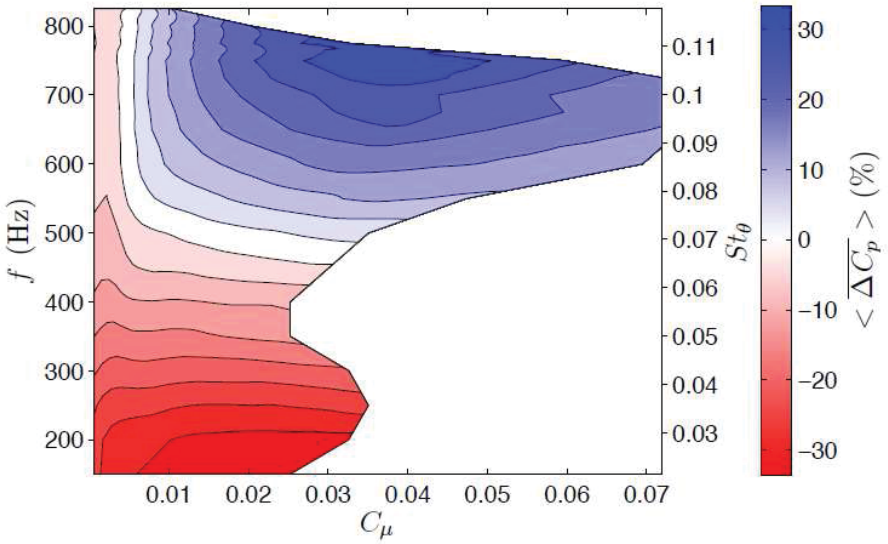

Figure 2.31: Colour map of change in base pressure as a function of forcing coefficient and frequency; the contour levels are spaced at intervals of 4.2% (Oxlade, 2013).

2.6 Summary

The literature review discussed some of the many devices tested in order to reduce the drag of road vehicle. The most significant results can be summarised as follows:

- The efficiency of splitter plates and base cavities in suppressing vortex shedding, increasing base pressure and reducing drag of an Ahmed body was demonstrated by multiple authors. Splitter plates increased the base pressure up to 7%, while base cavities achieved up to 11% of base pressure increase and 20% of drag reduction.

- Boat-tail devices were tested on a vehicle model with drag reductions up to 30%.

- Investigations using flaps located in different positions at the rear end of a vehicle model produced drag reductions up to 25%, while vortex generators reduced drag and lift by 12% and 54% respectively.

- Passive control devices and shape modifications such as roof fairing, side extenders, cab rounding and roof fairings applied to real vehicles achieved drag

reductions between 15% and 25%.

- Tests with continuous blowing, which were performed on different kinds of models and for numerous testing conditions, showed drag reductions between 3% and 29%, which increased to 50% when used in combination with the Coanda effect. The continuous blowing system used in combination with the Coanda effect tested on a real vehicle by Englar (2005), produced a Fuel Economy Increase ratio of 8-9%.

- Various kinds of pulsating blowing devices were also tested. MEMS achieved up to 10% of drag reduction (Joseph *et al.*, 2013). The Suction and Oscillatory Blowing (SaOB) system provided up to 20% of drag reduction when tested on a model (Seifert *et al.*, 2009), while it was found unsuccessful on a real vehicle (Seifert *et al.*, 2010).

- Systems with zero-net mass-flux exchange, similar to the one used in this study, were also tested. Up to 40% base pressure recovery with 15% drag reduction was obtained through a 2D simulation by Pastoor *et al.* (2008), whilst Choi (2003) reduced the drag of a sphere by 50% and of a 2D vehicle model by 30% through a 3D simulation.

- A combination of zero-net mass-flux active devices and flaps (passive device) was applied to a real vehicle by El-Alti (2012) with no success.

2.7 Aim of the Investigation

The aim of the present study is to investigate the effects of a zero-net mass-flux active device applied at the rear end of simplified heavy vehicle model. Some questions still need to be answered, and this investigation is an attempt to partially fill the gap in the literature. In particular, special attention was been given to:

- Changes induced by pulsed-jet forcing in the near wake of the model in terms of base pressure distribution and dynamics of the wake.

- Importance of control parameters such as forcing frequency, forcing amplitude and slot size, on the effectiveness of the system.
- Effects produced by the high frequency forcing on forces and moments acting on the body, directly measured with a 6-axis balance.
- Relationship between modifications induced in the base pressure distribution and changes found in forces and moments.

The efficiency of the actuation system was not taken into consideration in this analysis. Therefore the design requirements of the actuator resulted in a non-optimised device from the energy point of view.

Chapter 3

Experimental Set-up and Procedures

As suggested by Ahmed *et al.* (1984), the model designed for this investigation was shaped to reproduce the main characteristics of a ground vehicle flow field, apart from the effects introduced by wheels, engine cooling, passenger compartment aeration and rough underside. The coordinate system is defined as x in the stream-wise direction, z normal to the ground and y perpendicular to both. The origin is located at the centre of the base plate of the model (Figure 3.1).

3.1 The Honda Wind Tunnel

The experiments were conducted in the Honda wind tunnel, a closed-return closed-section type low-speed facility, designed primarily for road vehicle testing but also suitable for a variety of experiments. It is equipped with a rolling road, boundary layer removal control, a servo-motor controlled vehicle support and positioning system, contoured walls and a multi-directional traverse system. It is provided with two direct drive Leroy-Somer 106 kW DC variable speed motors, driven by a Mentor 2 drive system.

The test section is 3.048 m wide x 1.524 m high x 9 m long. The maximum air speed of the empty tunnel is 45 ms^{-1}. The rolling road is 1.8 m wide x 2.5 m

long, and it can reach a maximum velocity of 40 ms^{-1}. It is positioned below the main support sting, and it has a rubber/neoprene belt running on an aluminium water-cooled platen. The belt is prevented from lifting when testing high down-force cars by a variable profile suction system and the rolling road can be yawed up to an angle of 20°. The boundary layer is removed by a suction system that draws air through two perforated plates mounted in the floor. The suction plates are positioned upstream of the rolling road, one as wide as the belt and placed directly in front of it, and the other one 1.37 m upstream and spanning 3/4 of the width of the test section. The system can be calibrated in order to optimise the boundary layer removal for the conditions chosen. The calibration was not performed in this case since the belt and the suction system were not used.

With the aim of facilitating race car testing, the walls of the test section are shaped to follow the streamlines around a generic 50% scale model of an open-wheel racing car. Contouring removes the viscous blockage without the need of any additional correction if the model frontal area is kept below about 6% of the test cross-sectional area.

The flow downstream of a model can be fully inspected using the tunnel traverse system, which offers a rigid support for probes and a three-dimensional positioning anywhere in the test section. This is achieved using a nacelle, mounted at the vertical mid-point of the test section, which can be traversed in the x and y directions. The nacelle is also equipped with a movable arm inclined at 60°. The combination of rotations of the arm about the nacelle axis and the arm linear movements makes it possible to reach positions in the vertical direction, z.

During the experiments, the tunnel operating speed was calculated from measurements of dynamic head measured by the reference Pitot tube, atmospheric pressure, and temperature, sampled at 2.5 Hz by a *Furness* FCO510 digital manometer. A PID algorithm embedded in the *LabView* experimental code was used in conjunction with the tunnel fan motor controller to maintain a free-stream velocity, U_∞, equal to 15.0 ms^{-1} ($Re_H = U_\infty H/\nu = 4.1 \times 10^5$). The convergence criterion was based on the filtered velocity error (1^{st} order digital filter, $f_c = 0.07$ Hz) and on the 'raw' error calculated from a 20 s velocity moving average, which were both kept

below 0.1% throughout the duration of measurements.

3.2 The Model

The model designed for this investigation is a bluff body that idealizes a long vehicle, such as an articulated lorry or a coach. The model is shown in Figure 3.1, where also the configuration used for the wind tunnel tests is outlined. During the experiments, the model was placed on top of the rolling road, not used in this investigation, by means of a strut. The strut, which is part of the equipment of the Honda Wind tunnel, was made of two parts: a frontal aerofoil shaped, and a smaller auxiliary one, used to change the pitch angle of the model. The front and the rear strut positions could be independently adjusted by acting on two dedicated servo-motors, which were encased in a streamlined box partially protruding inside the test section from the ceiling of the tunnel. The strut system allowed a maximum distance h of the bottom of the model from the ground equal to 250 mm. As shown in Figure 3.2, the model was placed at 1.5 m from the beginning of the test section, in order to limit the boundary layer growth on the floor and allow maximum space (5.1 m) for the wake to develop.

The main body of the model was designed as a parallelepiped with rectangular faces, while the front was obtained by merging two half-spheres with diameter respectively equal to height and width of the body. The overall dimensions were chosen on the basis of different factors. Firstly, a survey about proportions and load capacities of some of the most common lorries available on the market, and the study of the maximum permissible dimension for trucks and coaches in Europe (OECD, 2011, 2012) showed that it was possible to maintain $\sim$15% model scale (14.7%) without suffering any appreciable error from the wind tunnel blockage, equal to 4.39%. Secondly, the width and the height of the body were chosen in order to optimise the design of the zero-net mass-flow actuator, described in Section 3.4.

The maximum dimensions admissible in Europe for articulated lorries are at least 4 m height, 2.5 m width, and 16.5 m length. Considering that the standard containers carried by articulated vehicles have a maximum length of 13.7 m, with

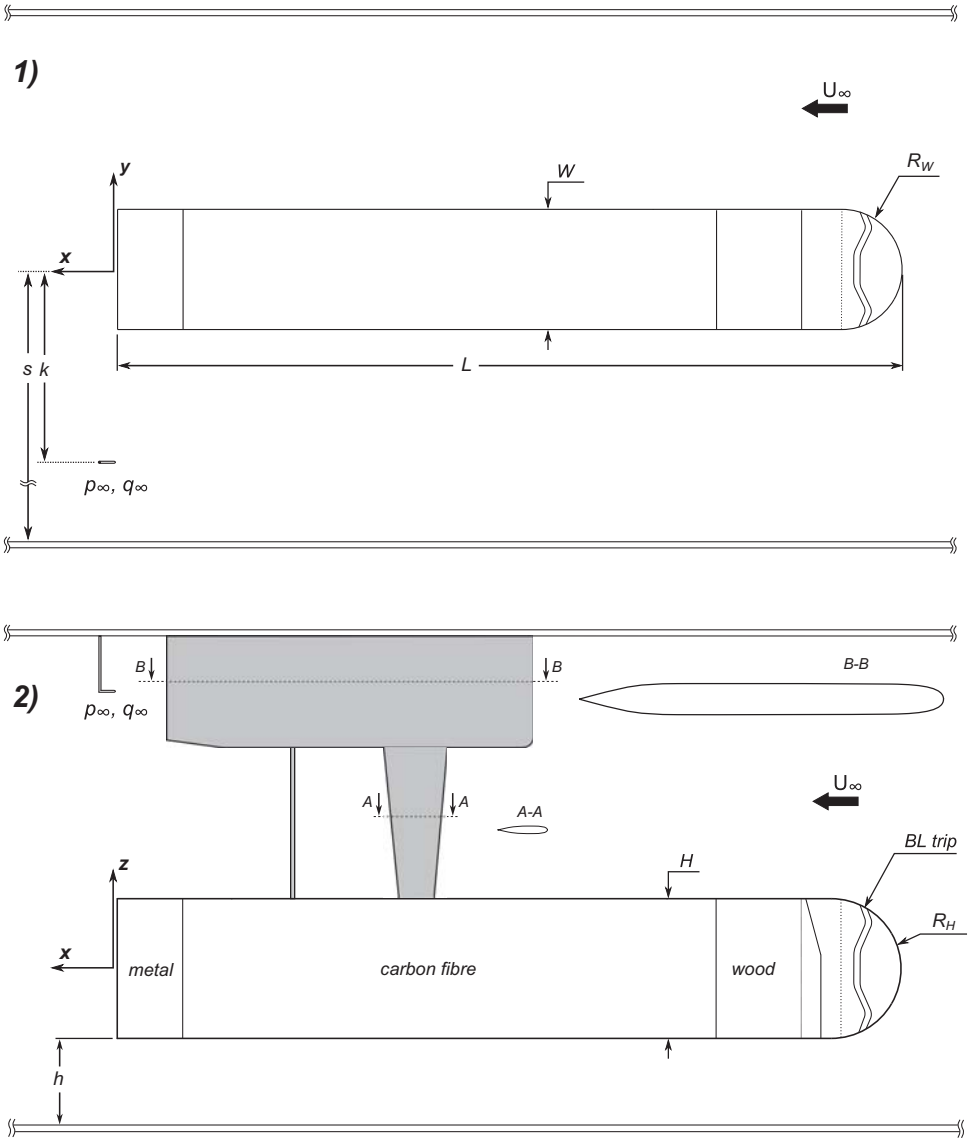

Figure 3.1: Model scheme and wind tunnel set up: 1) bottom view, 2) side view. $L = 2395$, $W = 367$, $R_W = 183.5$, $s = 1708$, $k = 720$, $H = 427$, $h = 240$, $R_H = 213.5$; dimensions in mm, strut represented in grey colour.

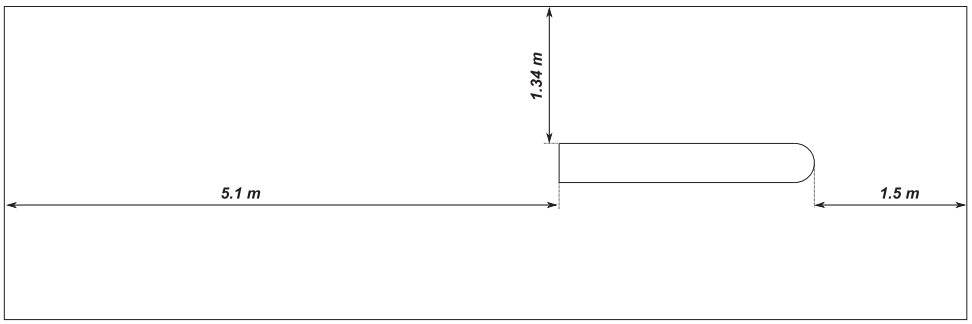

Figure 3.2: Model position respect to the test section; dimensions in m.

Parameter	Full Size Lorry (m)	14.7% Scaled Model (m)
Width (W)	2.50	0.367
Height (H)	2.91	0.427
Aspect Ratio ($AR = H/W$)	1.16	1.163
Total Length (L)	16.31	2.395
Body Length	12.47	1.830
Cab Length	2.30	0.345

Table 3.1: Model dimensions.

an aspect ratio defined as height to width equal to 1.2, and that, according to the survey mentioned before, cab lengths vary from 1.6 m to 3.1 m, the model dimensions were: length $L/H = 5.61$, width $W/H = 0.86$, front radius $R_H/H = 0.50$ and $R_W/H = 0.38$. The distance from the floor was $h/H = 0.56$. Detailed dimensions are shown in Table 3.1, where they are also compared with a full size vehicle.

The frontal area lead to a blockage of only 3.37%. By contrast, the considerable length of the body meant that the constructing materials had to ensure light weight, stiffness, ease of manufacturing and high precision. The forebody, initially shaped as a lorry cab, was built with ply wood. Unfortunately, some preliminary tests revealed that this configuration was able to trigger a flow instability of the kind described by Cooper (1985). For this reason, a rounded block of foam was added in front of the wood in order to promote a stable behaviour of the flow. On the rounded nose, the boundary layer was tripped by a 25 mm-wide strip of 120 grit emery paper located at an angle of 80°. To reduce the weight while still ensuring stiffness and precision, the mid section was built in two parts, connected through aluminium rails reinforced to improve strength and minimise distortion. The rear end, where the actuator was placed, was built with an aluminium alloy, while the remaining parts were covered by carbon fibre panels. The bottom of the body was reinforced with an aluminium plate in order to securely fasten the load cell used to measure the forces acting on the model, while the top was designed to be easily removed in order to facilitate access to the instrumentation stored inside the model itself. Finally, the interior of the body was filled with sound-absorbing material in order to prevent vibration and

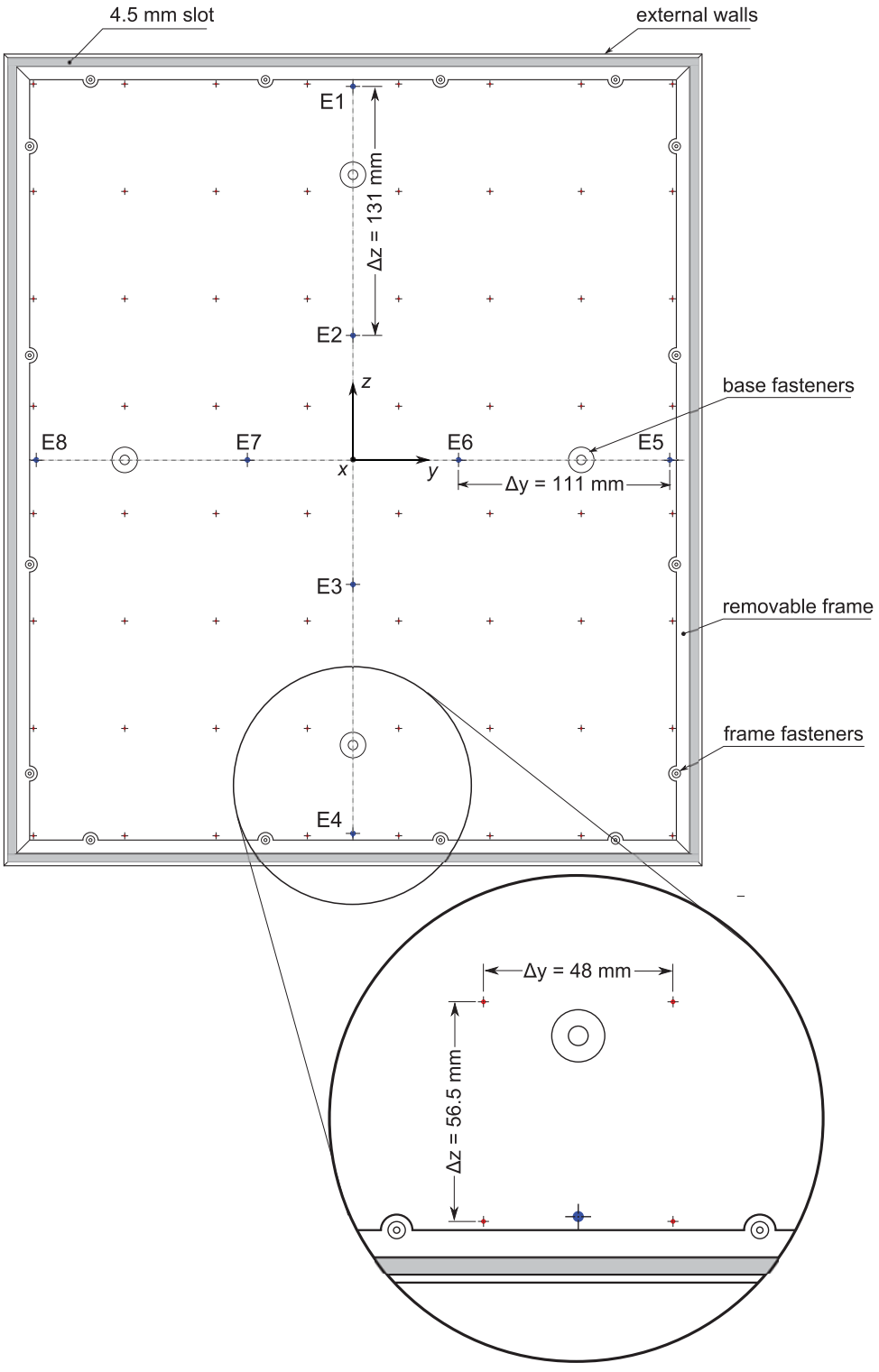

Figure 3.3: Frontal view of the base of the model. Static pressure taps in red, dynamic transducers in blue, synthetic jet slot in grey. Dynamic transducers names: vertical column, plane xz, from top to bottom: E1, E2, E3, E4; horizontal row, plane xy, from right to left: E5, E6, E7, E8.

soundwave reflections during the actuator operation.

To monitor the wake behaviour, 64 static taps connected to a miniature electronic pressure scanner (8 rows by 8 columns), and 8 dynamic transducers (4 in the xz-plane, and 4 in the xy-plane), as shown in Figure 3.3, were located on the base.

The natural frequencies of the system (model plus strut, which can be simplified by a mass supported by a cantilever beam), were studied by subjecting the model to an impulse force and recording the resulting displacement via a laser sensor (*optoNCDT* 2200). A spectral analysis of the data showed a pitch resonance frequency of 5.34 Hz, a yaw resonance frequency of 3.36 Hz and a roll resonance frequency of 5.07 Hz.

Additional information about the model set-up can be found in Appendix D, where the schemes of measuring system and electrical connections are reported.

3.3 Data Analyses

3.3.1 Pressure Data Interpretation

- **Area-weighted base pressure**: base pressure calculated as weighted average from the 64 static pressure taps located on the base of the model

$$\hat{p} = \frac{1}{A_B} \int_y \int_z p_i(y,z)\, \mathrm{d}y\mathrm{d}z. \tag{3.1}$$

- **Centre of Pressure on the Base**: point on the base where all of the pressure field may be represented by a single force vector, with no moment is

$$COP_y = \frac{\int_y \int_z p_i(y,z)\, y\, \mathrm{d}y\mathrm{d}z}{\int_y \int_z p_i(y,z)\, \mathrm{d}y\mathrm{d}z}, \tag{3.2}$$

$$COP_z = \frac{\int_y \int_z p_i(y,z)\, z\, \mathrm{d}y\mathrm{d}z}{\int_y \int_z p_i(y,z)\, \mathrm{d}y\mathrm{d}z}. \tag{3.3}$$

- **Probability Densitiy Function of the Centre of Pressure:** function that describes the relative likelihood for the COP to take on a given value in y and z, respectively.

$$p_y(COP_y) : COP_y \mapsto \lim_{dy \to 0} \frac{P(y < COP_y < y + dy)}{dy}. \tag{3.4}$$

$$p_z(COP_z) : COP_z \mapsto \lim_{dz \to 0} \frac{P(z < COP_z < z + dz)}{dz}. \tag{3.5}$$

P is the Cumulative Distribution Function.

3.3.2 Dimensionless Quantities

- **Base pressure coefficient**: differential static pressure divided by the dynamic head; the pressure $\hat{p}$ is defined in Equation 3.1:

$$C_p = \frac{\hat{p} - p_\infty}{\frac{1}{2}\rho U_\infty^2}. \tag{3.6}$$

- **Change in base pressure coefficient**: difference between base pressure coefficients relative to baseline and forced flow, referenced to the baseline flow pressure coefficient is

$$\Delta C_p / C_{pB} = \frac{C_{pB} - C_p}{C_{pB}}. \tag{3.7}$$

This definition allowed to get a positive $\Delta C_p / C_{pB}$ for a base pressure increase and a negative one in case of decrease.

- **Force and moment coefficients**: force (moment) measured by the force balance, divided by the dynamic head multiplied by the area of the base is

$$C_{F(M)} = \frac{F(M)}{\frac{1}{2}\rho U_\infty^2 A_B}. \tag{3.8}$$

- **Change in force (F) and moment (M) coefficients**: difference between force (moment) coefficients relative to forced and baseline flow, referenced to the baseline flow force (moment) coefficient is

$$\Delta C_{F(M)}/C_{F(M)B} = \frac{C_{F(M)} - C_{F(M)B}}{C_{F(M)B}}. \tag{3.9}$$

This definition allowed to get a positive $\Delta C_{F(M)/C_{F(M)B}}$ for a force/moment increase and a negative one in case of decrease.

- **Strouhal number**: non-dimensional frequency based on the height of the model is

$$St_H = \frac{fH}{U_\infty}. \tag{3.10}$$

- **Blowing coefficient**: since all the experiments were conducted at constant free-stream velocity, the same simplified definition of momentum coefficient used by Oxlade (2013) was adopted:

$$C_\mu = \frac{U_j^2 A_j}{U_\infty^2 A_B}. \tag{3.11}$$

It should be noted that this definition does not take into account the appropriate description of momentum flux, or thrust, of the jet according to the self-similarity theory $J = \rho U_j A(U_j - U_\infty)$. With this definition, the momentum coefficient becomes:

$$C_\mu = \frac{U_j A_j (U_j - U_\infty)}{U_\infty^2 A_B}. \tag{3.12}$$

However, Equation 3.11 is used both here and by Oxlade (2013), who used the same tunnel speed $U_\infty = 15$ ms^{-1}.

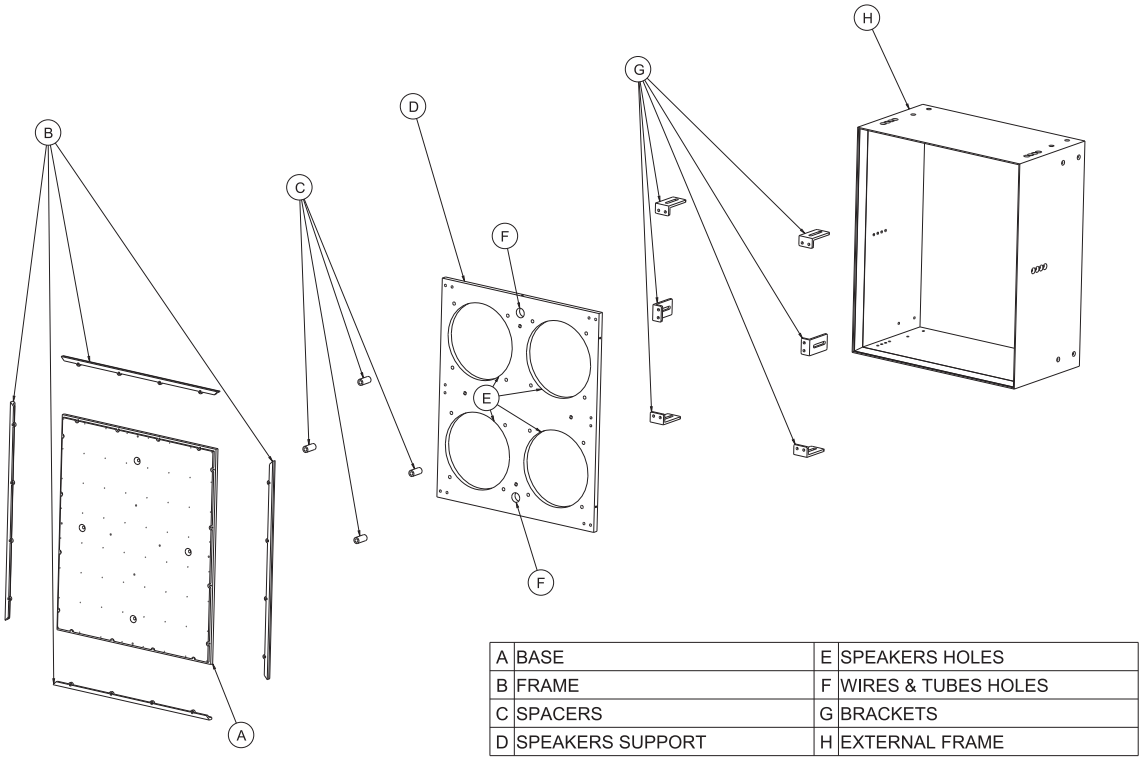

Figure 3.4: Exploded view of the ZNMF actuator.

3.4 The Zero-Net Mass-Flux Actuator

The main elements constituting a typical synthetic jet, or zero-net mass-flux (ZNMF) actuator, are a cavity delimited by rigid side walls, a plate with an orifice or a slot, and an oscillating diaphragm. The cavity-orifice system forms a Helmholtz resonator. As the diaphragm oscillates, fluid is periodically forced into and out of the cavity. When the conditions described by Holman *et al.* (2005) are met, a train of vortex rings propagates away from the orifice, the induced velocity forming a time-averaged jet. During one cycle of oscillation, the average flow out from the cavity equals the average inflow, such that the total averaged mass flow rate is zero. However, the momentum transfer with the surrounding flow is non-zero, because the jet momentum induces entrainment.

On the basis of the results previously obtained by Qubain (2009), the actuator was placed at the base of the model. A continuous slot, adjustable in size, was placed all around the perimeter of the base, as close as possible to the external sides. The slot sizes used in this study were $d_1/H = 0.008$, $d_2/H = 0.011$ and $d_3/H = 0.013$

($d_1 = 3.5$ mm, $d_2 = 4.5$ mm and $d_3 = 5.5$ mm), chosen on the basis of the detaching boundary layer thickness at the base. A detailed scheme of the actuator is shown in Figure 3.4.

The operating frequency range of the actuator was defined following the guidelines dictated by previous research. Vukasinovic *et al.* (2010) showed that, when forcing the shear layer at its natural frequency $f_{n,0} = \omega_{n,0}/2\pi$, the global modes of the base flow are amplified, whereas the 'natural' near-field behaviour is suppressed when the flow is forced at about twice the natural frequency (i.e. $\omega > 2\omega_{n,0}$). The most amplified Strouhal number for turbulent flows equals to 0.022–0.024, as reported by Ho & Huerre (1984), and confirmed by Qubain (2009).

The wind tunnel velocity, U_∞, was fixed at 15 ms^{-1}, and a preliminary Strouhal number $St_\theta = f\theta/U_\infty$ was calculated using the momentum thickness θ given by one of the simplified methods[1] developed by Schlichting *et al.* (1968). According to these calculations, the actuator had to provide a frequency of at least 80 Hz approximately.

Due to the shape and size of the model, a single vibrating membrane was considered unsuitable to meet the forcing requirements. Moreover, the diaphragm had to be driven so that it could produce an adequate volume displacement across a relatively wide frequency range, and be able to maintain a velocity output. These criteria are met only by two types of actuator: piezoelectric diaphragms and moving coil speakers. The first ones offer a more compact and lightweight solution, but the higher reliability, availability and ease of use of coil speakers made them the preferred choice. The loudspeakers chosen for this application were the *Beyma* 6P200Nd (Beyma, n.d.), characterised by a wide frequency range 60–9,000 Hz (resonance frequency 56 Hz), a high sensitivity of 92 dB and a power capacity of 200 W. The actuator driving signal was generated by a code specifically developed for this experiment and converted to an analogue signal by a D/A converter sampling at 200 kHz. It was sent to the speakers through a *Yamaha* P2500S high fidelity power amplifier.

[1]Assuming that the model can be approximated with a flat plate of length equal to that of the model, placed in the flow at zero angle of incidence, and that the flow is two-dimensional, fully

3.4.1 Actuator Characterisation

3.4.1.1 Dynamic Response

The dynamics of the system were identified via the study of its frequency response, derived by applying a variant of the Blackman-Tukey spectral analysis method with frequency-dependent resolution, available in the *Matlab* environment as SPectral Analysis with Frequency Dependent Resolution (SPAFDR). More details about this method can be found on-line in the *MatWorks* Documentation Centre.

Traditional techniques to determine experimentally the frequency response of a system imply the use of pulse or sinusoidal input variations, followed by a simple analysis of the output response. A pulse applied at low amplitudes, though, would have introduced large errors, because of the noise naturally existing in the system. On the other hand, large amplitudes could easily damage the speakers. Harmonic forcing removes these issues, even if the need to repeat the test for a large number of frequencies would have lead to very long experimentation periods. For these reasons, the use of a band-limited white noise signal, among the many kinds suggested by Ljung (1999), was chosen as the most preferable input to use.

The result for this analysis for a 4.5 mm slot is showed in the Bode diagram in Figure 3.5. The input of the system is the voltage sent to the speakers, while the output is the signal acquired by the pressure transducer located inside the cavity. The first noticeable rise in the magnitude plot is around 80 Hz, and it corresponds to the mechanical resonance of the system, dictated by the properties of the oscillating membrane, while the main peak is the Helmholtz resonance, placed in this case at 473 Hz. The other small peaks are due to standing waves inside the cavity, which could not be eliminated in a selective way. For both resonances, the change in phase equals 180°. Above the range of frequencies affected by the Helmholtz resonance, there is a loss of coherence: the pressure inside the cavity and the velocity in the

turbulent at the leading edge and with a zero-pressure gradient, the momentum thickness θ can be calculated as

$$\theta(x) = 0.036x \left(\frac{U_\infty x}{\nu} \right)^{-\frac{1}{5}}. \tag{3.13}$$

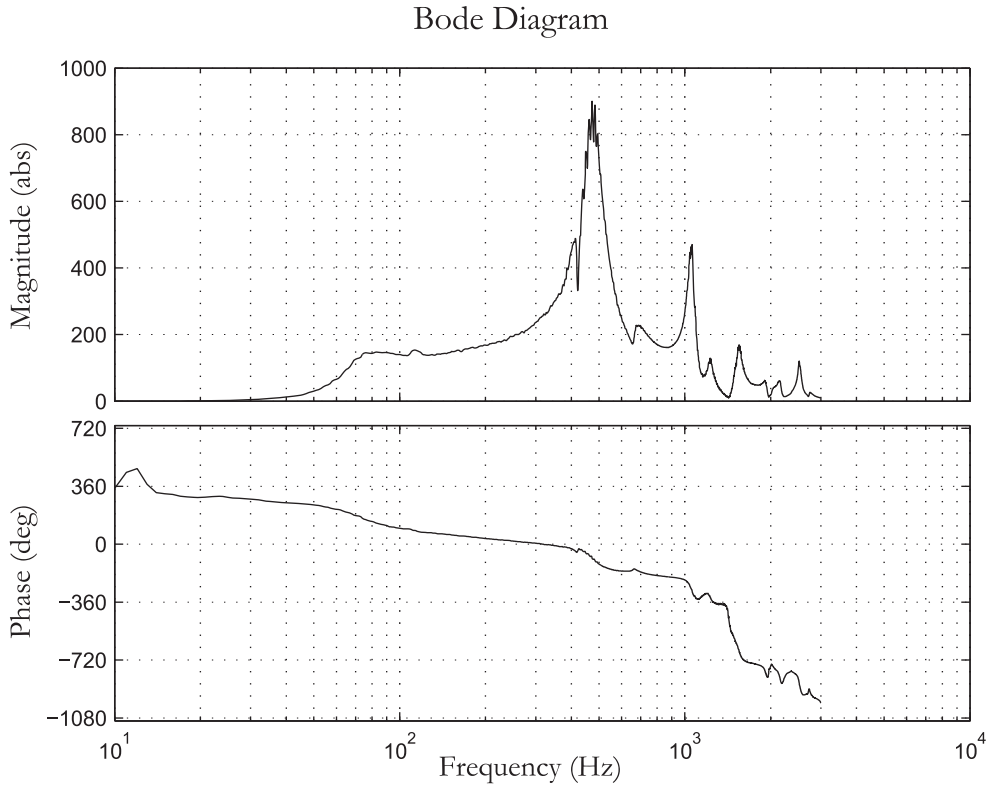

Figure 3.5: Bode Diagram of the System for a 4.5 mm slot.

neck of the resonator are in anti-phase, and the actuator is not able to produce a velocity output. As a consequence, the position of the Helmholtz resonance and the damping determine the maximum frequency of the system.

The values of the Helmholtz resonances for the different slots sizes used during the investigations are shown in Table 3.2; the corresponding Bode diagrams can be found in Appendix A. It is worth mentioning that the gain measured at resonance is subjected to a substantial error due to the considerable variation in amplitude

Slot Size	Helmholtz Resonance		Gain at Helmholtz
(mm)	(Hz)	St_{fH}	(abs)
3.5	460	13.09	∼900
4.5	473	13.46	∼900
5.5	485	13.81	∼900

Table 3.2: Resonances for different slot sizes.

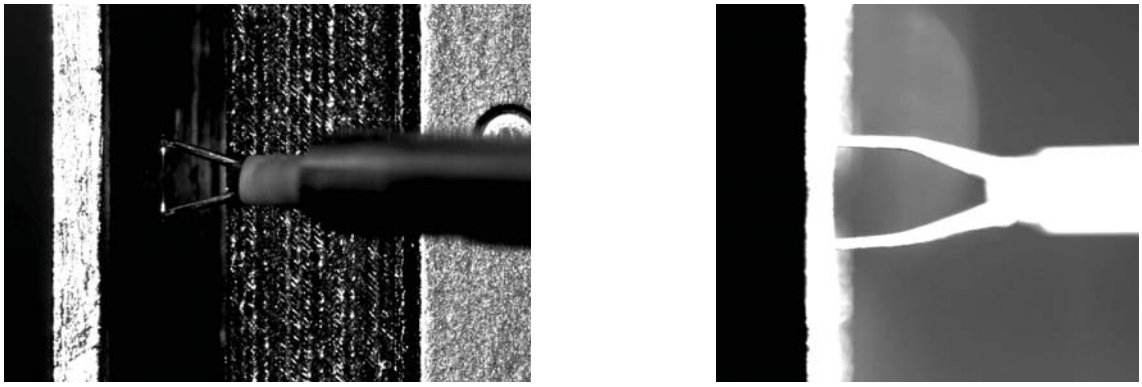

(a) (b)

Figure 3.6: Optical positioning of the hot-wire sensor: (a) centreline, (b) orifice plane.

corresponding to small changes in frequency.

3.4.1.2 Calibration

The static characterisation of the actuator was obtained via a calibration of the pulsed jet velocity with constant-temperature single-wire anemometry. The probe consisted of an in-house modified 55P15 *Dantec* boundary layer probe with 10% platinum-rhodium Wollaston wire soldered to the prongs. The wire had a diameter of 5 μm and was etched to a length of 1 mm, for a cold resistance of 8.9 Ω. The sensor was operated in constant temperature mode by a 54T42 miniCTA from *Dantec*. The heating ratio R_w/R_a, as defined by Bruun (1995), was equal to 1.5, for an operating resistance of 13.31 Ω and a sensor temperature T_w of 330 $°C$. The sampling frequency was fixed at 40 kHz to minimise aliasing. More details about the use of thermal anemometry in this study are given in section 3.5.3 .

During the calibration, the model was placed in a large and isolated room of quiescent air in order to avoid any disturbance. The wire was positioned optically in the exit plane of the jet, at the centre of the orifice, in the middle of the long side of the base, as shown in Figure 3.6. Due to the rectangular shape of the base, the mean velocity distribution along the slot was not uniform. For this reason, the speed measured at the chosen point has to be considered only as a representative value. A sinusoidal waveform with amplitude determined by the rms cavity pressure

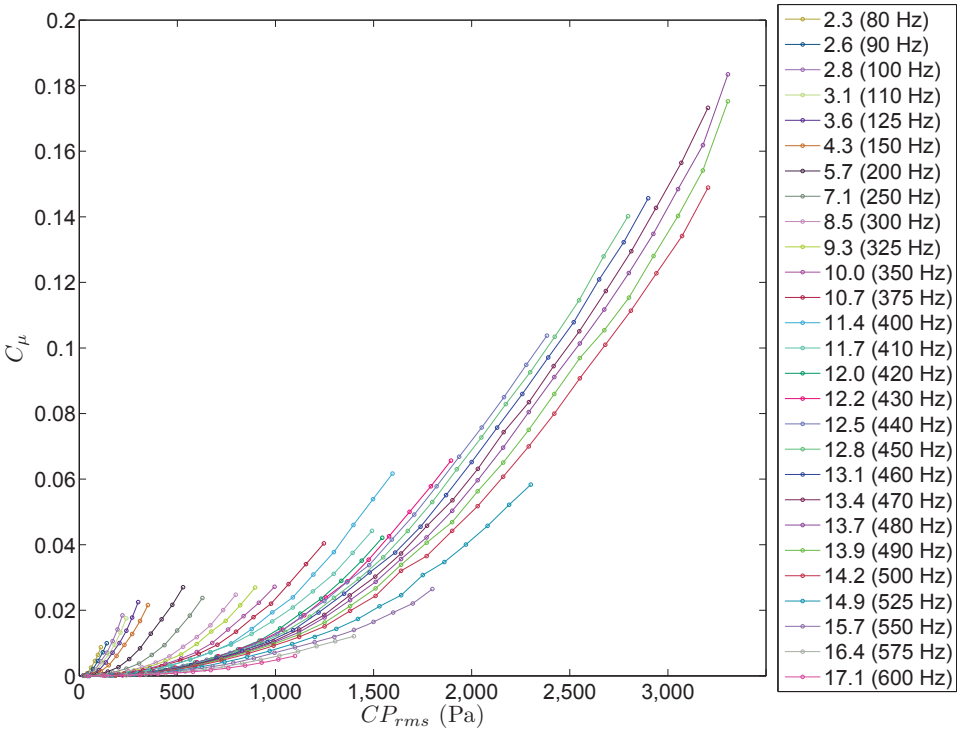

Figure 3.7: Actuator Calibration for a 4.5 mm slot.

p_{rms} was used as the actuation signal. This parameter was preferred to the speakers driving voltage as the input for the system, in order to remove the effects of non-linearities and resistive heating. Both during the calibration and the experiments, the cavity pressure was kept constant by a PID feedback controller developed as part of the experimental code. The PID input and output variables were respectively the cavity pressure rms and the voltage amplitude. PID convergence was reached when the rms set-point error was less than 0.5%, based on a 7 s moving average and a low pass Butterworth filter with $f_c = 0.5$ Hz. A gain-scheduling system was also used during the experiments to adapt the controller to the actuator behaviour at different frequencies. The system was then run through the range of available forcing frequencies (from 80 to 600 Hz) starting from a minimum cavity pressure between 20 and 40 $\sqrt{\text{Pa}^2}$ up to the maximum value determined by the coil heating. This was different for each frequency. The instantaneous current and voltage across the speakers were constantly measured both during the calibration and the experiments, in order to prevent the system exceeding a power of 40 VA.

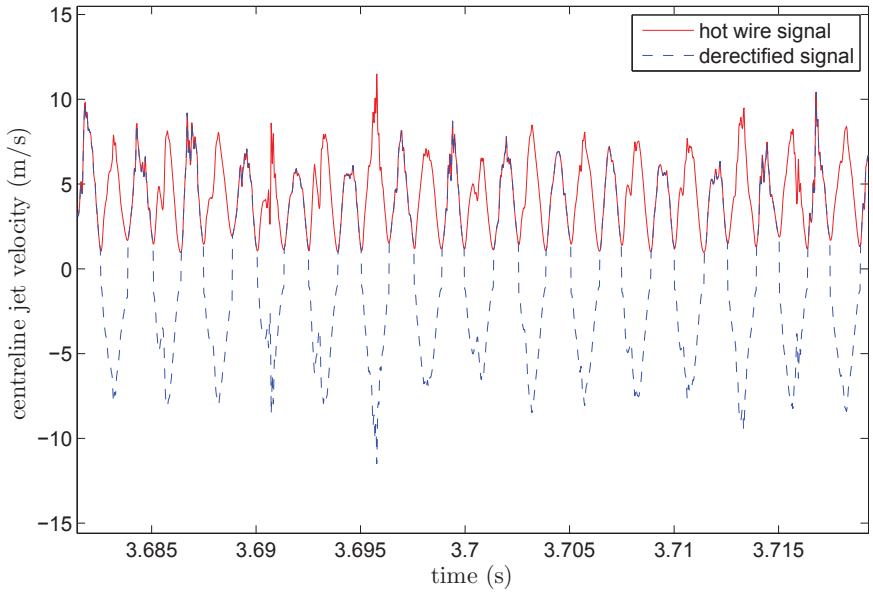

Figure 3.8: Hot wire signal and de-rectified signal of the centreline jet velocity.

The results for the calibration of the 4.5 mm wide slot are shown in Figure 3.7 in terms of the blowing coefficient C_μ. Further results for the actuator calibration for this slot size and for the other slot sizes used during this study can be found in Appendix A.

As a consequence of the directional insensitivity of hot wires, the calibration output was the velocity magnitude of the jet (rectified signal), rather than its true value, as shown in Figure 3.8. In order to recover a sinusoidal velocity profile, a procedure similar to what described by Chaudhari *et al.* (2009) was used. The signal was first de-rectified using a peak/trough detection algorithm. Then, since the high level of turbulence made it difficult to define the value of the peaks unambiguously, the velocity amplitude U_j was detected via a spectral analysis conducted with the periodogram method: the signal was divided into 100 independent windows and the subsequent Fourier amplitudes were averaged. Leakage errors were prevented by applying a window length which was an integer multiple of the forcing period (known *a priori*). It should be noted that the hot-wire probe was not calibrated for negative velocities, and that, due to the aerodynamic disturbance introduced by stem and prongs, the sensitivity of the wire is not necessarily the same for blowing

and suction. Since sometimes the two parts of the cycle could not be distinguished in the rectified signal, it is possible that the amplitude values are affected by an unknown bias. Despite these difficulties, this procedure was followed since it was the only one able to differentiate the velocity component at a forcing frequency from the turbulence effects and from errors close to zero.

Some thought is now given to the quality of the calibration itself. As stated by Doebelin (1990), a static calibration is a process in which all inputs, except the one under study, are kept constant. The relationship between the input variations and the consequent output changes form the static calibration of the system, which is "valid only under the stated constant conditions of all the other inputs". (Doebelin, 1990, p.38). This is not strictly the case in the present study, since during the wind tunnel acquisitions the pressure acting on the reference transducer depends on the velocity around the model. Nevertheless, the calibration from the test described above was utilised since the jet velocity could not be measured in full operating conditions.

3.5 Instrumentation and Measurement Techniques

In order to ensure the reliability and repeatability of the results, the experimental technique was fully automated, and maximum care was taken in designing the experimental set up.

For the schemes of measuring system and electrical connections see Appendix D.

3.5.1 Pressure Measurements

All differential pressure measurements were referenced to the Pitot-static tube positioned laterally from the model, in the same streamwise section of the base. This was considered the most accurate position for the Pitot-static probe in order to limit any effects from the model blockage on the reference pressure.

3.5.1.1 Static Pressure

The static pressure on the base was measured by means of 64 surface taps connected to a miniature differential Electronically Scanned Pressure transducer (ESP-64HD DTC) and a *Chell* CANdaq 14 bit digital to analogue converter. The pressure signal was brought to the scanner via 2 m long 1 mm internal diameter silicone tubing. Both the ESP scanner and the CANdaq were placed inside the model, and they communicated with the experimental code via a TCP network. The scanner was factory set at a channel rate of 20 kHz; the maximum data delivery available was therefore 312 Hz.

3.5.1.2 Fluctuating Pressure

Time-dependent pressure was monitored through 8 dynamic *Endevco* 8507C-1 piezo-resistive differential transducers, with full scale output of 1 psi (6895 kPa). The average sensitivity was 26.53 mV/kPa (factory calibrated). The output signal, sampled at 20 kHz, was low-pass filtered at 10 kHz and amplified by 3 *Endevco* Model 136 DC amplifiers (3 channels each). The high gain made available by these units allowed to overcome the difficulties introduced by the small pressure variations in the wake, and to take advantage of the high spatial resolution and of the low noise level (typically 5 μV rms) offered by these transducers to accurately resolve the flow.

3.5.1.3 RMS Cavity Pressure

The cavity pressure was measured by means of an *Endevco* 8507C-2 piezo-resistive differential transducer, with full scale output of 2 psi. This particular transducer was calibrated in house against an FCO *Furness* manometer over 15 points in the range -770 to 1460 Pa = -18 to 35 mV. The resulting sensitivity was 23.96 mV/kPa with a 95% confidence bounds of $\pm$0.01 mV/kPa. More details about this calibration can be found in Appendix B. The same model 136 DC amplifier was used also in this case, with the same cut-off frequency but a lower gain than in the other cases. Except for the actuator calibration, when the cavity pressure was sampled at 40 kHz, the sampling frequency was always set to 20 kHz and low-pass

Figure 3.9: 6-axis internal balance used during the investigation.

filtered at 10 kHz.

3.5.2 Force Measurements

The aerodynamic forces acting on the model were measured by means of a 6-axis internal balance, consisting of two small platforms (top and bottom) encasing 7 load cells (Figure 3.9), defined as a "floating frame balance" by Ewald (2000). The top plate was secured to the strut through a pitch beam, used to change the pitch angle of the model via the auxiliary smaller strut. The bottom plate was secured onto a 10 mm thick aluminium plate fastened to the metallic structure of the body. In this way, forces acting on the model could be measured. The front and rear strut positions could be independently adjusted using two dedicated servo-motors for pitch. The yaw angle could be adjusted manually using the rotation available in the connection between the front strut and the pitch beam. In view of the large weight of the actuator, the balance was positioned towards the rear of the body with ballast added at the front and keeping the total weight below 40 kg, as recommended by previous users.

A calibration was performed by loading the balance with known weights. The

procedure was carried out with the balance placed outside the model, on a dedicated calibration rack equipped with pulleys for force loading. A first order calibration was deemed satisfactory for the present investigation, therefore great care was taken in not to apply any combination of loads (forces or moments) to the balance, since combined loads would have required a second order calibration. The system response to every configuration was recorded twice, when loading and when unloading the instrument, in order to take into account the hysteresis effects typical of this kind of transducer. A linear relationship (first order calibration) between the output voltage and the force/moment used was then calculated for each load cell. The gradients obtained with this process were then used, after inverse matrix transformation, to derive a 6×6 calibration matrix employed to interpret the readings. The calibration range and the sign convention are shown in Table 3.3. More information about this calibration can be found in Appendix B.

During the experiments, the data from the balance were acquired through a dedicated acquisition board at a sampling frequency of 100 Hz. No filtering was deemed necessary due to the damping introduced by the balance itself, which behaves as a 2^{nd} order system with cut-off frequency at $\sim$4 Hz. The calibration was also performed at the same sampling frequency.

3.5.3 Velocity Measurements

Hot-wire anemometry was used for velocity measurements not only during the actuator calibration, but also for the analysis of the boundary layer profiles on the body. Both studies were conducted using the same measurement system set-up.

The probe was calibrated in the free-stream of the same facility where the measurement were taken, or in an open-circuit tunnel close to the model in the case of the actuator calibration. These choices were driven by the need of not modifying the measurement system configuration and ground reference of the anemometer in between the calibration and the experiment, in order to avoid any additional uncertainties. The Pitot tube taken as a reference was located as close as possible to the hot-wire probe, taking care of avoiding any aerodynamic disturbances. The

Load	Convention	Calibration Range
Downforce	positive downwards	0 to 46.0 N
Drag	positive backwards	0 to 40.0 N
Side	positive to the right	-15.0 to 15.0 N
Pitch	positive nose down (clockwise as viewed from the right looking towards left)	-4.0 to 4.0 Nm
Roll	positive right wing down (clockwise as viewed from behind looking forward)	-4.0 to 4.0 Nm
Yaw	positive nose to the right (clockwise as viewed from above looking down)	-5.6 to 5.6 Nm

Table 3.3: Calibration range and sign convention for balance loads.

calibration data were fitted by a least-square algorithm to King's law:

$$E^2 = A + BU^n, \tag{3.14}$$

where E is the mean voltage across the bridge, U is the mean flow velocity, and A, B and n are the calibration constants. No temperature correction was used in the case of the actuator calibration, while in the case of the boundary layer study, the probe was calibrated before and after the measurements, and the curves interpolated linearly in time. The drift between the calibrations was regularly checked, and the measurements were repeated if it was found bigger than 1.5%. The goodness of the fit for the calibration data was also checked, and always kept below 1%. The total uncertainty was calculated as a combination of the uncertainties due to calibration equipment, linearisation, A/D board resolution and air density variation with temperature. The influence of probe position and air humidity were considered negligible, while that of changes to the ambient pressure were minimised by measuring it and introducing its value in the reference velocity calculation. The resulting uncertainty came to a maximum of 4.3% of the measured velocity.

The results were also checked for any blockage effects of the hot-wire probe on

the jet. These were excluded by comparing hot-wire traces recorded at different distance from the exit of the orifice, which did not show any sensible difference.

3.6 Procedures

In both baseline and forced cases, the balance zero was obtained from the average of the pre-run and the post-run zero acquisitions. Each sample, baseline or forced, required 7 minutes to complete. The wind tunnel was always run for at least one hour and a half before recording any data in order to contain the effects of the temperature change on the flow. The temperature was used to rise by 8-10 degrees during the first hour, and by 2-5 degrees during the following 30 minutes. Tests were usually carried on at a wind tunnel air temperature between 24°C and 26°C.

3.6.1 Model Alignment

The model had to be aligned both on the horizontal and on the vertical plane. To start with, the model was placed at 0° of incidence to the horizontal plane, verified by means of a digital protractor (resolution $\pm 0.1°$, accuracy $\leq 0.1°$) both at the front and at the rear of the body. Then, the pitch moment measured by the balance was zeroed by adding a ballast at the front of the model. The counterweight was made of calibrated weights for a total of 3.113 kg and a final pitch balance reading of -0.565 Nm.

The transverse alignment was done in two steps. Firstly, the sides were geometrically aligned with the tunnel. Then, the alignment was refined with an iterative procedure similar to the described for the baseline flow in Section 3.6.2, but with a sample length of 600 s. The final baseline flow average, based on 85 independent samples each 100 s long (equivalent to 2 hours and 22 minutes), showed a maximum difference between symmetric pressure taps of 0.63 Pa.

3.6.2 Baseline Flow

The baseline flow was sampled every day at the beginning and at the end of the experiments, and roughly every hour in order to take into account the evolution of the flow in the tunnel with temperature. The procedure for this part of the experiments is summarised below:

1. User activates the control code and A/D acquisition commences. The A/D and the CanDAQ buffers are reset.

2. The FCO manometer and CanDAQ are zeroed, and the signals from the balance are saved as first zero.

3. The tunnel is turned ON and the tunnel PID controller, previously enabled, brings the free-stream velocity up to 15 ms^{-1} within an rms error <0.1%.

4. When the tunnel PID is in range, the data from the two A/D acquisition boards, the FCO manometer and the CanDAQ are saved for 100 s.

5. Once the saving process is complete, the tunnel is turned OFF.

6. When the average free-stream velocity is <0.3 ms^{-1}, the CanDAQ is zeroed again and the post-run zero values from the balance are saved.

After the procedure described above, the system was ready to start a new sample acquisition. Some longer samples (600 s) were also taken in order to check the drift of the system and to resolve flow structures at very low frequencies.

3.6.3 Forced Flow

The forced flow samples were taken with a procedure very similar to the one described for the baseline flow. Steps 1, 2 and 3 are the same listed for the baseline sample.

4. The ZNMF actuator is turned ON at the frequency specified for the requested sample, and the actuator PID controller brings the rms cavity pressure to the indicated value with an rms error <0.5%.

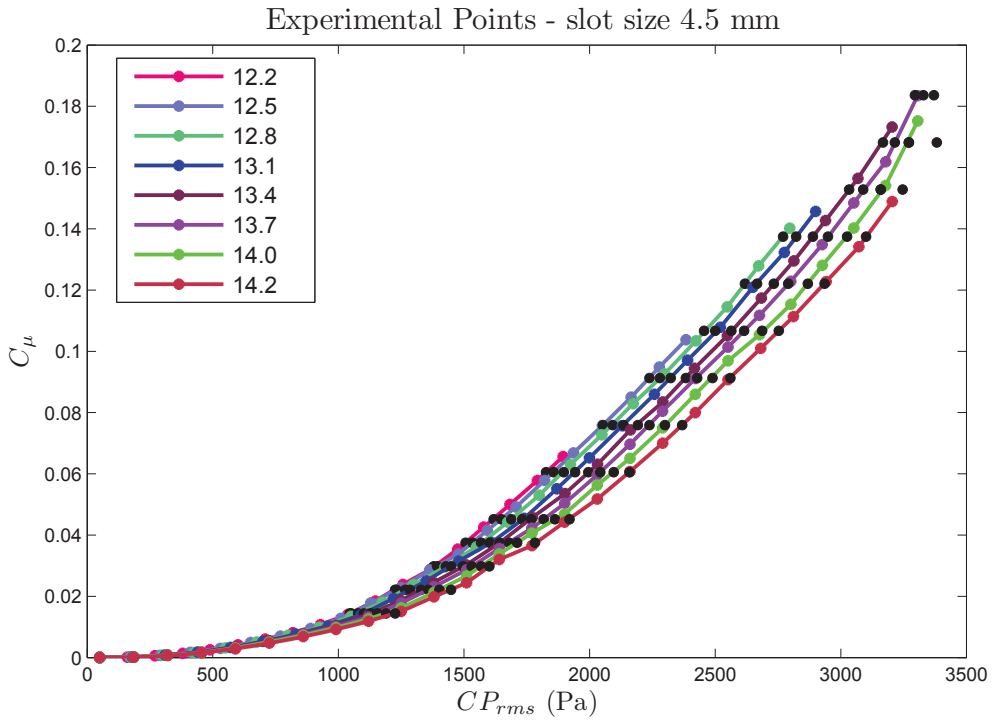

Figure 3.10: Forcing grid for the 4.5 mm wide slot; (•) experimental points.

5. When the tunnel and the actuator PID controllers are stable, the data from the A/D boards, the FCO manometer and the CanDAQ are saved for 100 s.

6. Once the saving process is complete, first of all the actuator, then the tunnel are turned OFF.

7. Same as step 6 for the baseline flow.

The forcing frequency and amplitude were dictated by the grid shown in Figure 3.10 for the 4.5 mm wide slot, and by the grids in Figure 3.11 (a) and (b) for the 3.5 mm and 5.5 mm slots respectively. For each grid the forcing amplitudes were interpolated, and sometimes extrapolated, on the calibration curves while keeping constant the values of the blowing coefficient C_μ among the frequencies, and when changing slot size, in order to make possible a direct comparison of the results. The 4.5 mm slot was tested in the frequency range comprised between 430 Hz and 500 Hz ($St_{Hf} = 12.2$ to $St_{Hf} = 14.2$), which some preliminary tests showed as the most profitable in terms of base pressure increase and drag reduction. Each point was sampled at least 8 times for 100 s, for a total of 891 samples. The comparison with

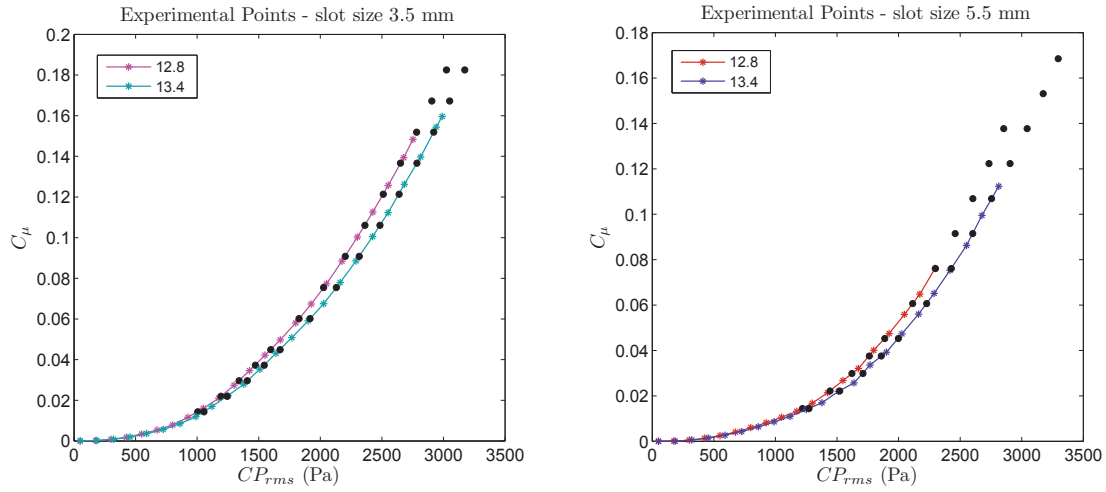

(a) (b)

Figure 3.11: Forcing grid for (a) the 3.5 mm wide slot and (b) 5.5 mm; (•) experimental points.

the other two slot was performed on two frequencies, 450 and 470 Hz ($St_{Hf} = 12.8$ and $St_{Hf} = 13.4$). Each point was sampled for 4 times, for a total of 204 samples.

Finally, the change in base pressure was calculated taking as reference the averaged daily baseline, obtained as average of all the baseline samples taking during the day. This allowed to remove the effects of changes in atmospheric and wind tunnel conditions.

3.6.4 Uncertainty

The pressure, force and moment uncertainties were calculated with a 95% confidence interval according to the procedure described by Moffat (1988) and Castrup (2004). Each 100 s acquisition was treated as an independent sample, and it was repeated, for each configuration, a sufficient number of times to lower the uncertainty to the same order of magnitude (third decimal) for every measurement.

The uncertainty in the hot-wire calibration was calculated as the combination of the uncertainties coming from calibration equipment, curve fitting errors (linearisation), A/D board resolution, and air density variations due to temperature alone. The ambient pressure was monitored during the whole process and its contribution to the total uncertainty reduced to approximately zero.

The changes in hot-wire resolution with speed are not included in the calculation of the uncertainties since they were compensated through a logarithmic distribution of the calibration points.

3.6.5 Temperature Correction and Data Rejection

Throughout the testing period, the data showed a trend in time that seemed attributable to temperature variation. The heat built by the instrumentation located inside the model introduced a bias on the measurements. However, the temperature inside the model was not recorded during the experiments, and no clear correlation was found between the tunnel temperature and the changes in C_p and C_D. Therefore, no bias correction was applied to the data.

Random errors were removed by means of the Chauvenet's criterion, applied as described by Taylor (1997). This method allowed to reject some measurements suspiciously different from the others. It defines as outliers the data that fall outside a probability band centred around the mean of a Normal Distribution, which should ideally contain all the n samples of the data set. The points are rejected if the probability of obtaining their variation from the mean is more than $\frac{1}{2n}$. No more than one sample per data set was rejected.

Chapter 4

The Baseline Configuration

The comparison between the present results and those from some of the previous literature confirms the main characteristics of wakes from square bodies, described below. Some observations strictly linked to this particular model, such as the characteristic frequencies of the forces acting on the body, are also presented here. All uncertainties are expressed with a 95% confidence interval.

4.1 Expected Mean Flow Structures

The extensive literature on square-body aerodynamics, in conjunction with the results from the base-pressure distribution and the analysis of the forces acting on the body, make it possible to assume some plausible scenarios about the flow structures surrounding the model.

Despite the symmetry of the whole set up about the vertical plane, the flow is expected to produce some asymmetry, as stated by Bayraktar *et al.* (2001). The preliminary tests conducted with a cab-shaped nose, and the results from Cooper (1985), Grandemange *et al.* (2013), Krajnovic & Davidson (2005) and Spohn & Gilliéron (2002), show how the forebody can cause flow separation at the front, leading to characteristic flow structures and even to periodic recirculation induced by pulsating separation bubbles. Ahmed *et al.* (1984), Bayraktar *et al.* (2001) and Khalighi *et al.* (2012) affirmed that the interference between the front and the rear

	Top	Bottom	Side
Boundary layer thickness, δ (m)	0.0948	0.0888	0.0884
Displacement thickness, δ^* (m)	0.0066	0.0067	0.0051
Momentum thickness, θ (m)	0.0046	0.0047	0.0037
Friction velocity, u_τ (m/s)	0.63	0.64	0.68

Table 4.1: Boundary layer characteristics.

could be taken to be negligible, but the unsteady behaviour of the shear layer at the trailing edge, induced by the periodic boundary conditions at the front, were considered detrimental for control applications. Hence, in order to overcome these unwanted effects, the cab shape was changed to a hemispherical nose, resulting in a fully-attached leading-edge flow, as described by Cooper (1985). The separated flow at the back, highly three-dimensional and unsteady, is described by Khalighi *et al.* (2001) and Wassen *et al.* (2010), and is assumed to be the result of the almost uniform growth of the boundary layer on top and at the sides, creating the structure described by Grandemange *et al.* (2013) which is a torus-like recirculation bubble in the long-time-average view. The development of the shear layer at the bottom, as well as the shedding in the vertical plane, is influenced by the ground plane, and leads to a base-pressure asymmetry in the z direction. Further influences on the wake, especially in the y direction, can be attributable to a separation bubble on the tunnel floor downstream of the base, as described by Khalighi *et al.* (2012) and Wassen *et al.* (2010); Grandemange *et al.* (2013) related the wake asymmetry in the y-direction to the ground clearance.

4.2 Boundary Layer at Separation

The velocity profile at the trailing edge is studied at the top, bottom and side of the base. For each location, Figure 4.1 shows a well developed turbulent boundary layer, with a logarithmic region extending roughly from $y^+(z^+) = 50$ to $y^+(z^+) = 500$. The distance between the probe and the wall, and the friction velocity u_τ are calculated following the method described by Kendall & Koochesfahani (2008).

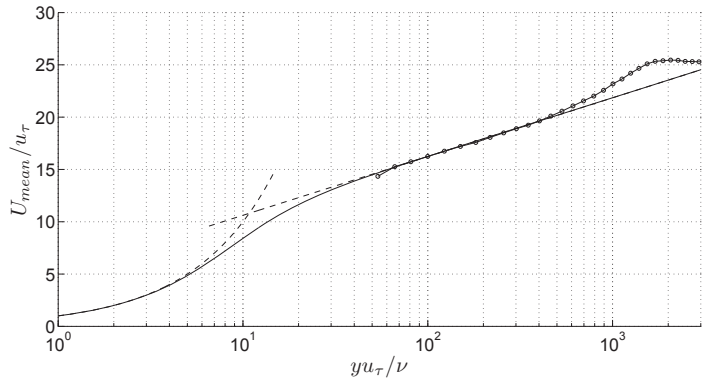

(a)

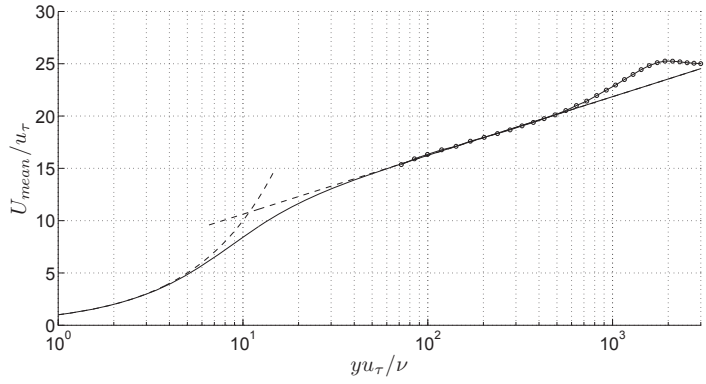

(b)

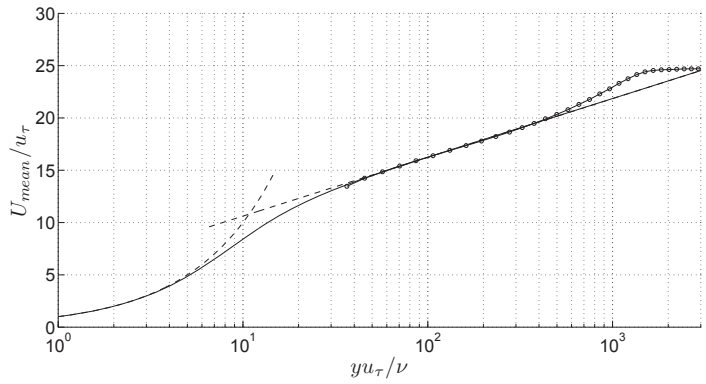

(c)

Figure 4.1: Distribution of U/u_τ against $yu_\tau/\nu(zu_\tau/\nu)$ for the boundary layer at (a) the top, (b) bottom and (c) side of the base. Measurements are superimposed on the composite Musker profile with $\kappa = 0.41$ and $B = 5.0$.

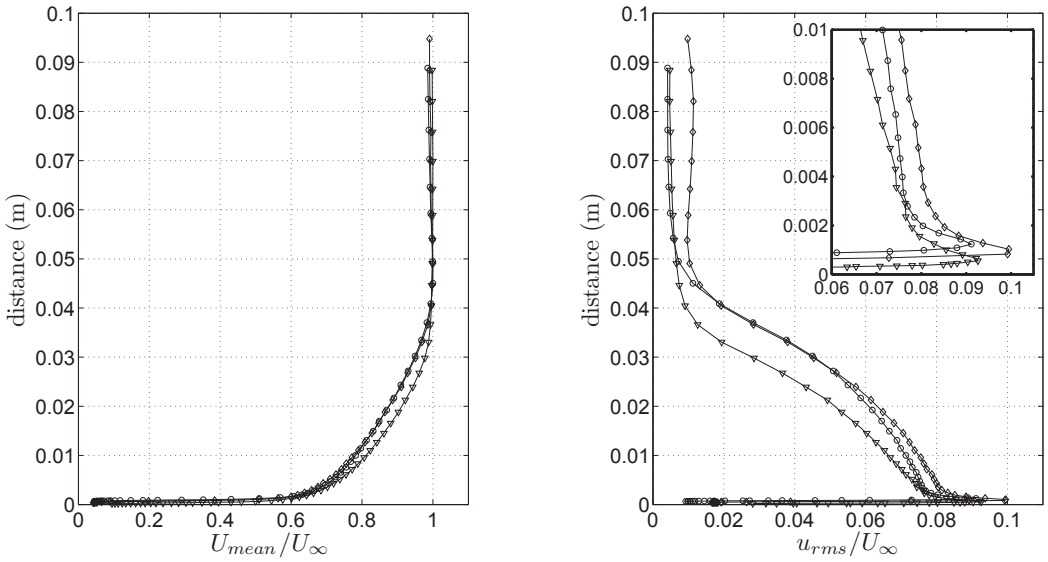

(a) (b)

Figure 4.2: (a) velocity profile and (b) turbulence intensity comparison among top ($\diamond$), bottom ($\circ$) and side ($\triangledown$).

As can be seen from the key results, listed in Table 4.1, and from the velocity profiles and the turbulence intensities reported in Figure 4.2, the boundary layer is found to be slightly thinner on the side, and with a larger turbulence intensity at the top and at the bottom of the base. The data from top and bottom indicate also a larger turbulence intensity of the free stream at the top (Figure 4.2 (b)).

4.3 Base Pressure

4.3.1 Averaged Distribution

The dimensionless averaged pressure distribution on the base of the model, and the position of the centre of pressure ($y = 0.0002$ m, $z = -0.0220$ m), are shown in the colour map in Figure 4.3. The pressure distribution is obtained as linear interpolation between the values read at each pressure tap by the ESP sensor. The plot is based on 85 samples, each 100 s long ($\sim$ 2 hours and 22 minutes). The overall value of the averaged base pressure coefficient is -0.133$\pm$0.002. A slight asymmetry in the y direction, and a stronger one along z, can be observed. The pressure

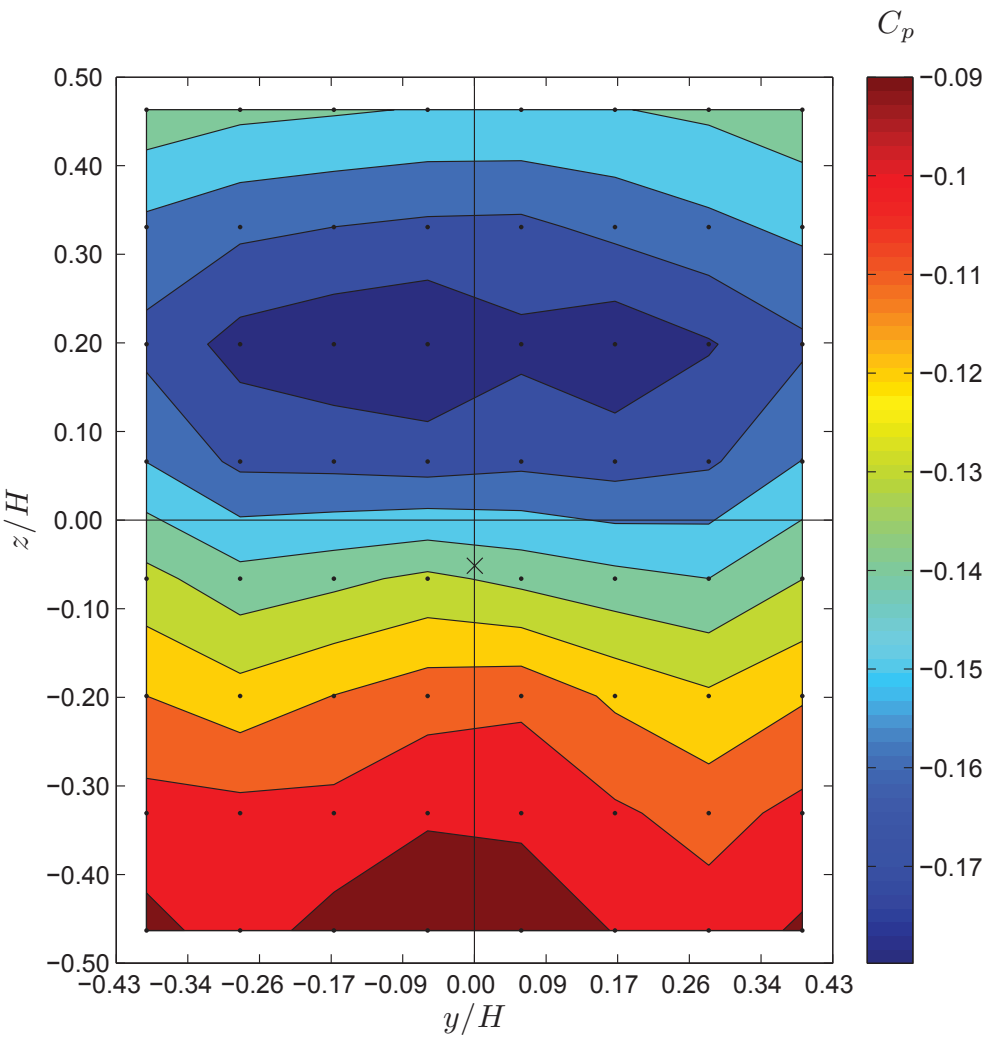

Figure 4.3: C_p contours on the base of the model for the baseline case. Also shown: centre of pressure (×), ESP static pressure taps (.), and area occupied by removable frame, jet slot and external walls of the model, equal to 15.2% of the total area (white frame).

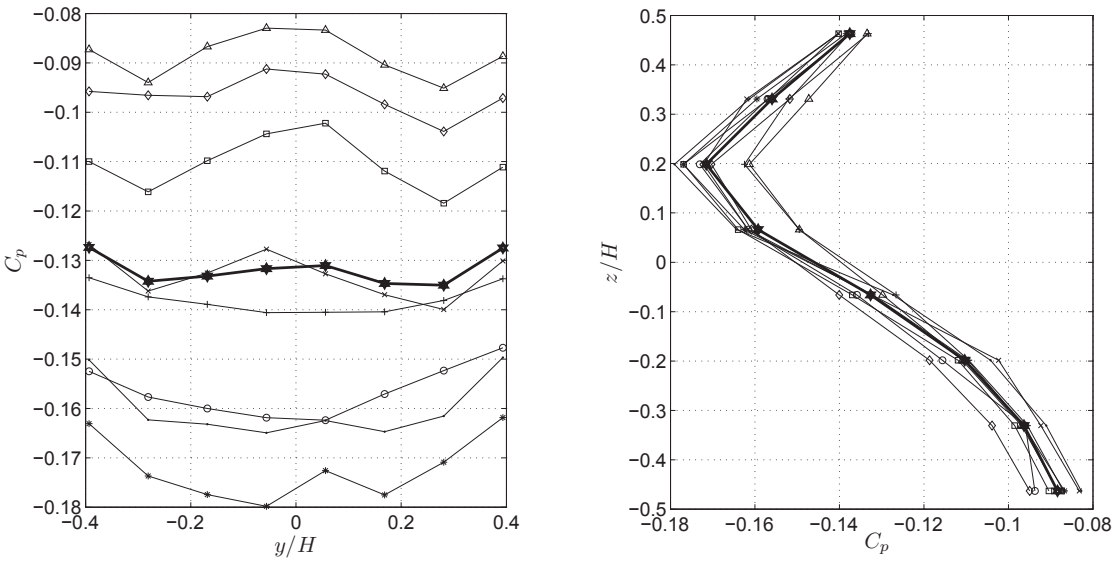

(a) + z/H=-0.46, ∘ z/H=-0.33, ∗ z/H=-0.20, · z/H=-0.07, × z/H=0.07, □ z/H=0.20, ◇ z/H=0.33, △ z/H=0.46, ⋆ average.

(b) + y/H=-0.39, ∘ y/H=-0.28, ∗ y/H=-0.17, · y/H=-0.06, × y/H=0.06, □ y/H=0.17, ◇ y/H=0.28, △ y/H=0.39, ⋆ average.

Figure 4.4: C_p spatial distribution as a function of (a) y/H by row and (b) z/H by column.

distribution in the y direction, and the central position of the centre of pressure in y within measurement error, confirm the model was well-aligned in yaw. In analogy to what found by previous investigations (Duell & George, 1993; Grandemange *et al.*, 2012a, 2013; Krajnovic & Davidson, 2001), the asymmetry in the z direction can be attributed to the proximity to the ground. The vertical asymmetry can also be observed in Figure 4.4, where the time-averaged C_p distribution is plotted as a function of y/H and z/H.

With regard to the position of the centre of pressure, the spectral analysis does not detect any characteristic frequency of its expected movement around $(y = 0, z = 0)$ as described by Grandemange *et al.* (2013), Grandemange *et al.* (2012a) and Oxlade (2013). This is discussed further in Section 4.3.2.

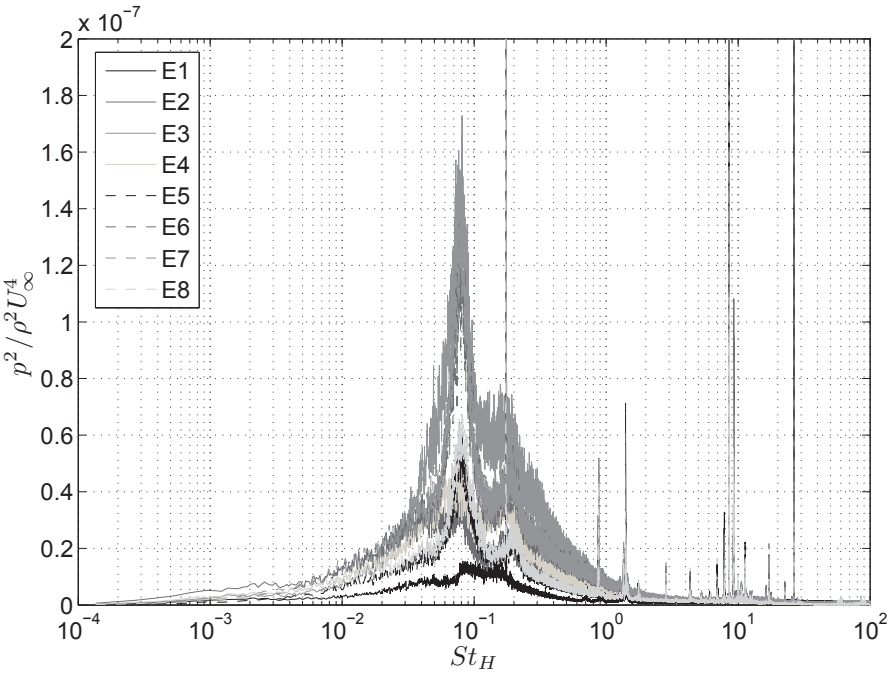

Figure 4.5: Pre-multiplied spectra from the dynamic transducers, shown here as a function of $St_H = fH/U_\infty$ and resolved for low frequencies.

	Vertical Plane	Horizontal Plane
Transducers	E1, E2, E3, E4	E5, E6, E7, E8
Bubble-pumping mode (St_{fH})	0.08	0.08
Vortex shedding mode (St_{fH})	0.17	0.20

Table 4.2: Characteristic frequencies of the wake.

4.3.2 Wake Dynamics

The spectral analysis was carried out entirely using the signals from the dynamic pressure transducers. An introductory study, resulting from the average of 20 samples each 600 s long (3 hours and 20 minutes), shown in Figure 4.5, gave the first important information about the characteristic frequencies of the wake. The Welch average is carried out with a transform window of 4,194,304 points in order to resolve any low-frequency mode. The lowest characteristic frequency is at about $St_H \approx 0.08$.

Hence, the final calculations are performed on the data from 85 samples organised

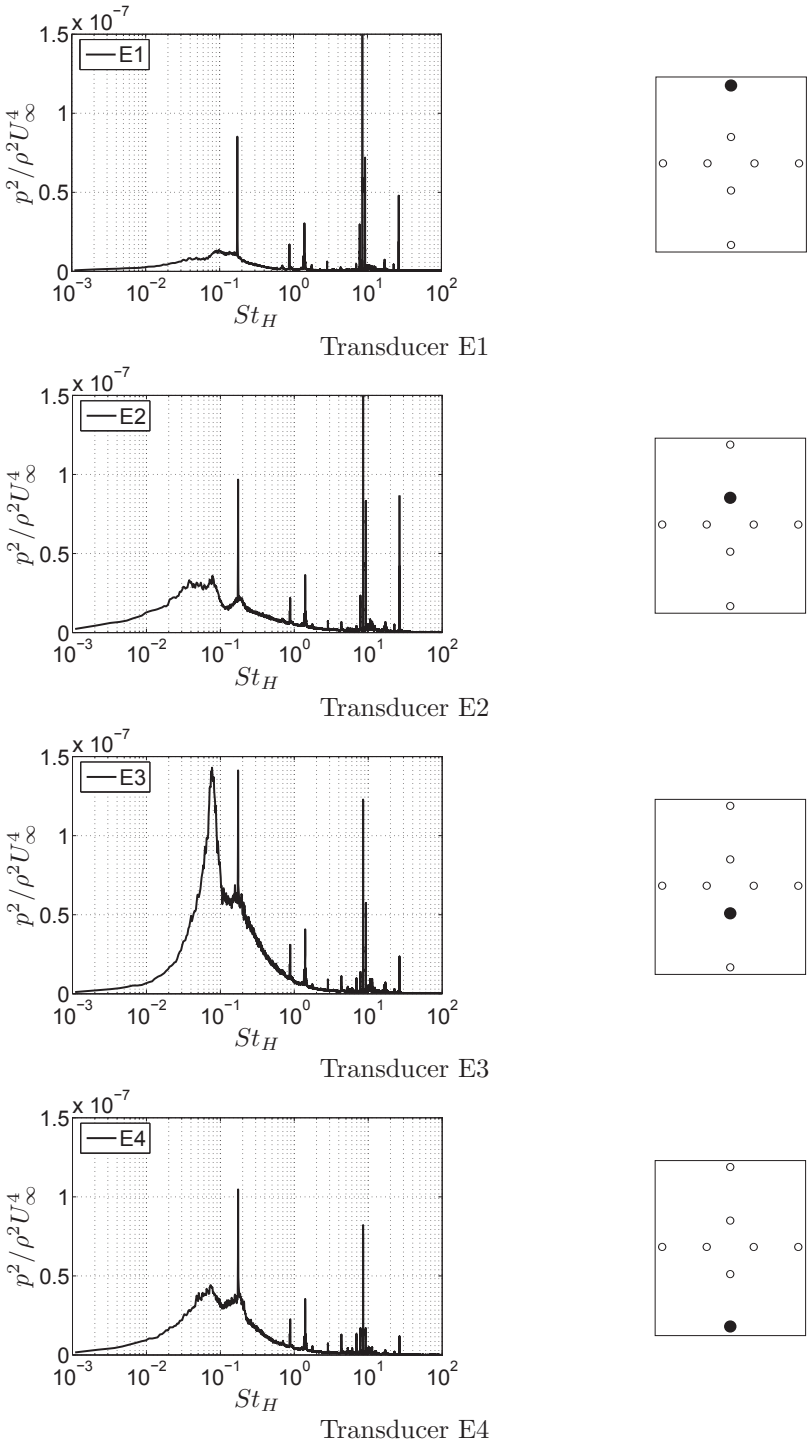

Figure 4.6: Dimensionless pre-multiplied spectra from dynamic transducers E1–E4 as a function of $St_H = fH/U_\infty$, where H is the height of the base.

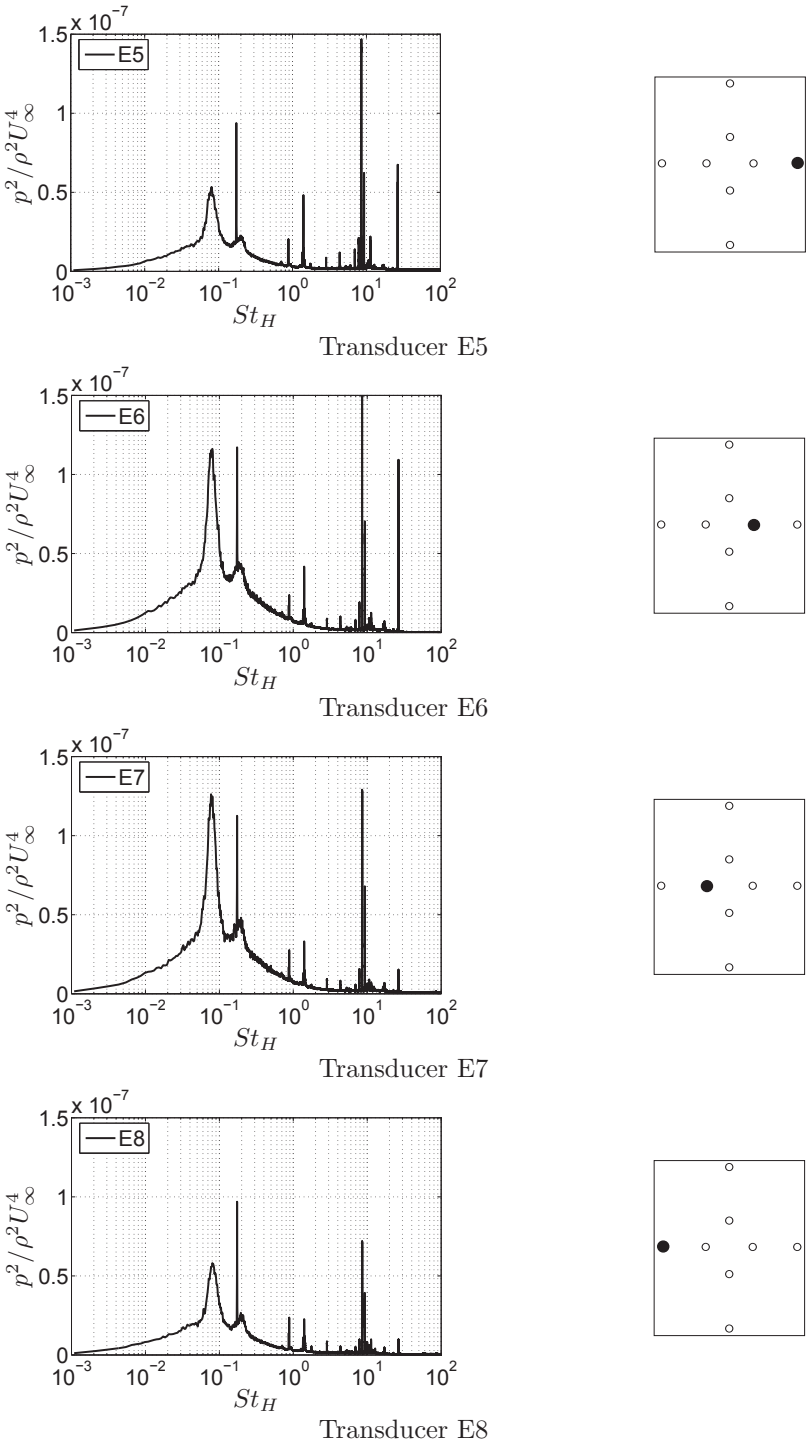

Figure 4.7: Dimensionless pre-multiplied spectra from dynamic transducers E5–E8 as a function of $St_H = fH/U_\infty$, where H is the height of the base.

in 100 s blocks. In this calculation, the window size for the Welch average is set to 524,288 points. The resulting spectra is shown in Figures 4.6 and 4.7.

Two characteristic frequencies (see Table 4.2) are easily distinguished: the first one, related to bubble-pumping mode, at $St_H \approx 0.08$, and the second one, linked to the shedding frequency, at $St_H \approx 0.17$ in the vertical plane and at $St_H \approx 0.20$ in the horizontal plane. Note that the frequency of the convective instability of the shear layer, expected for $2 \lesssim St_H \lesssim 3$, is not detected in the unforced case.

The recurrence of the peak at $St_H \approx 0.08$ in every graph, apart from the one relative to transducer E1, is a confirmation that this frequency is linked to the bubble oscillation. Similar values of Strouhal number are reported in the literature by Bayraktar *et al.* (2001), Duell & George (1999), Khalighi *et al.* (2001), Khalighi *et al.* (2012), Krajnovic & Davidson (2001) and Krajnovic & Davidson (2004). All these studies explain this mode as the characteristic frequency of the trapped vortex in the near wake. Grandemange *et al.* (2013) however, did not observe this structure during their experiments. In the current study, a bubble-pumping mode is evident.

As expected, the vortex shedding appears at different frequencies on the two symmetry planes. Similar values are reported in the literature by Grandemange *et al.* (2013) and by Khalighi *et al.* (2012). When normalising the frequency measured along the horizontal plane against the width of the model, the resulting Strouhal number becomes $St_W \approx 0.17$, as reported previously by Grandemange *et al.* (2013).

On top of the hydrodynamic frequencies just described, some spikes are clearly visible in all spectra in Figures 4.6 and 4.7: the one at $St_H = 0.17$ is a standing acoustic wave of frequency ~ 6 Hz corresponding to the wind tunnel length, the second one, at $St_H = 0.88$ (~ 31 Hz), is a sound wave that matches the blade passing frequency of the wind tunnel fans. The third spike, at $St_H = 1.41$, coincides with the 50 Hz frequency. Harmonics of these are then visible at higher frequencies.

To conclude, as anticipated in section 4.3.1, the very-low frequency mode characterised by a time scale $f \sim 10^{-3} U_\infty / H$ ($St \sim 10^{-3}$) described by Grandemange *et al.* (2013), Grandemange *et al.* (2012*a*) and Oxlade (2013) is not detected in this study. Evidence of this is not only the absence of a very-low frequency peak in the spectra from the dynamic transducers (Figures 4.5, 4.6 and 4.7), but also

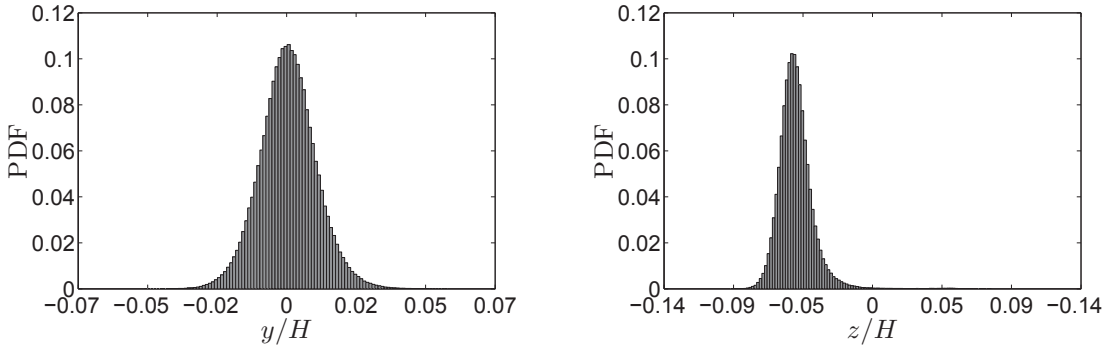

(a) (b)

Figure 4.8: PDF of the position of the centre of pressure (a) in the y direction as in Equation 3.4 (mean = 5.6×10^{-4}, variance = 9.1×10^{-5}, skewness = 0.12, kurtosis = 3.66) and (b) in the z direction as in Equation 3.5 (mean = -5.2×10^{-2}, variance = 1.5×10^{-4}, skewness = 2.48, kurtosis = 19.37).

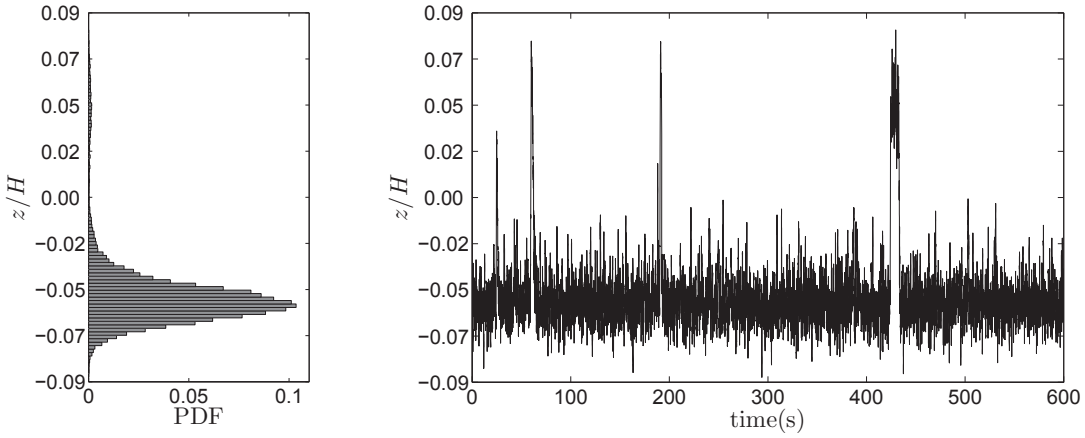

(a) (b)

Figure 4.9: PDF of the position of the centre of pressure (a) in the z direction as in Equation 3.5 and (b) corresponding time series for one 600 s sample (mean = -5.2×10^{-2}, variance = 3.3×10^{-4}, skewness = 3.60, kurtosis = 20.54).

the Probability Density Function (PDF) of the position of the centre of pressure in the y and the z directions shown in Figure 4.8 and defined in Equations 3.4 and 3.5. A movement of the centre of pressure is actually observed in the z direction, as can be seen from the 'tail' displayed by the distribution in Figure 4.8 (b) and more clearly in Figure 4.9 (one sample), but this is a random phenomenon with no assigned frequency. A further analysis, with major attention to the wind tunnel modes and disturbances, should be carried out. Nevertheless, some of the possible causes for the absence of the very-low frequency mode can already be excluded. The time scale for this mode is calculated equal to be ~ 30 s for the current set-up and conditions; the sample length was 600 s, therefore an average of approximately 10 wavelengths is attained. The ground clearance, $h/H = 0.56$, is above the critical value for bi-stability suppression equal to $h/H = 0.10$ measured by Grandemange *et al.* (2013). A misalignment of the model can also be excluded. However, when the same flow structure was measured by Wassen *et al.* (2010) ($h/H = 0.17$), it was clearly stated that it was induced by the influence on the wake of a small separation bubble on the floor downstream the model. The same kind of interaction between the wake and a separation bubble on the floor was also observed by Khalighi *et al.* (2012) ($h/H = 0.20$) and Ortega *et al.* (2004) ($h/H = 0.17$). The presence/absence of a similar bubble was not investigated in this case. In addition, the influence of the strut on the wake should be studied.

The data can be also analysed in terms of dimensionless integrated mean-square pressure $\tilde{p} = \overline{p^2}/(\rho U_\infty^2)^2$ for each transducer, shown in Figure 4.10. The wake asymmetry along the vertical plane, and the contrasting symmetry characterising the horizontal plane, are made even more evident by this representation. The highest levels of $\tilde{p}$ are detected by transducer E3, placed below the horizontal symmetry plane, while transducer E1 shows the minimum $\tilde{p}$ among all. However, the fact that the energy content (proportional to $\tilde{p}$) is almost the same in both planes suggests that the shedding in the vertical plane is not highly damped as reported by Grandemange *et al.* (2013) and Khalighi *et al.* (2012), where the model was placed much closer to the wind tunnel floor. In the present study, the ground effect is probably responsible for promoting the asymmetry along the vertical plane.

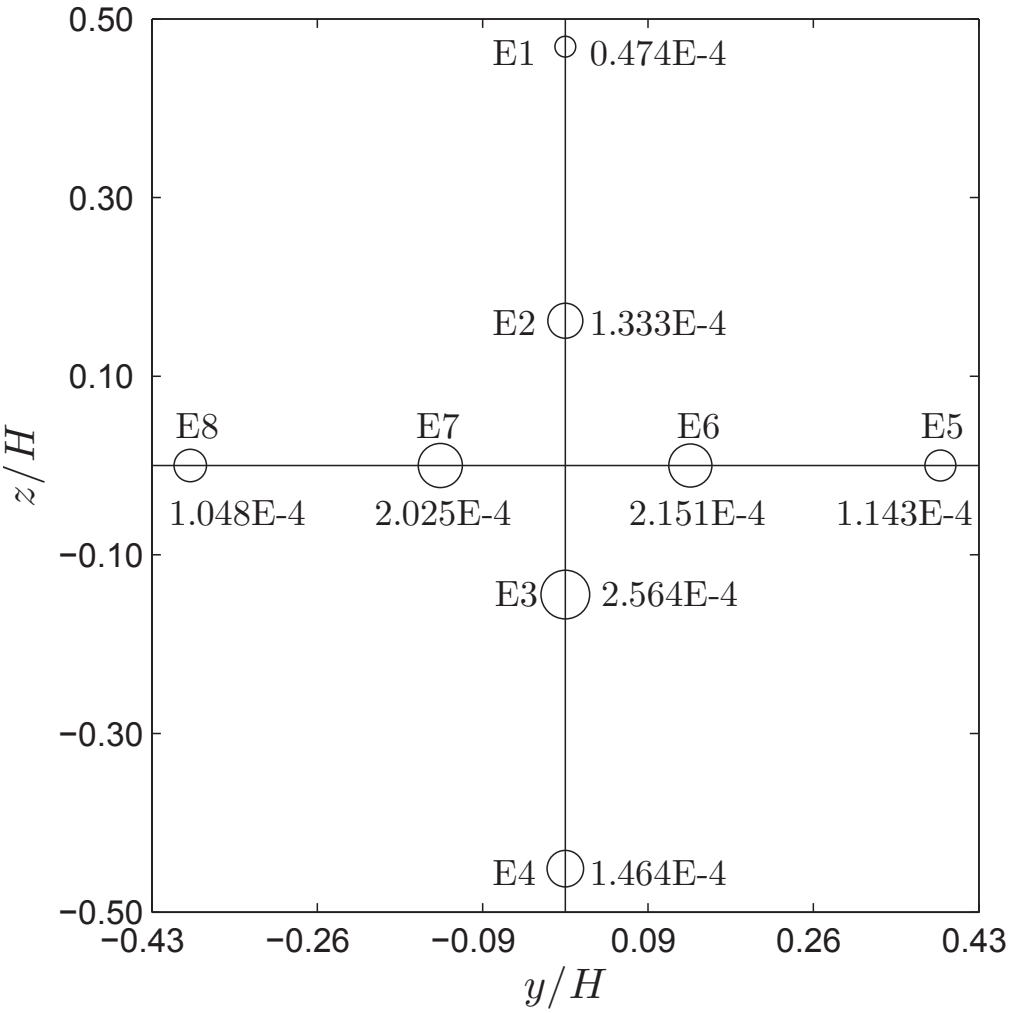

Figure 4.10: The area of the circles is proportional to the dimensionless integrated mean-square pressure $\tilde{p} = \overline{p^2}/(\rho U_\infty^2)^2$ for the baseline case.

	Value	Uncertainty %
Downforce coefficient (C_L)	0.031	±0.015
Drag coefficient (C_D)	0.259	±0.012
Side force coefficient (C_Y)	0.011	±0.029
Pitch coefficient (C_M)	-0.020	±0.008
Roll coefficient (C_R)	0.002	±0.006
Yaw coefficient (C_N)	-0.017	±0.005

Table 4.3: Averaged force and moment coefficients (baseline 4.5 mm slot).

4.4 Forces Acting on the Body

Table 4.3 summarises the dimensionless coefficients for forces and moments measured on the body. The main component is drag, which is an order of magnitude larger than the others. The pitch moment and downforce readings indicate that the centre of pressure of the body is located towards the rear of the model, while the values of yaw and side-force coefficients suggest a slight misalignment between the flow and the model itself. With the chosen conventions, the action of the flow changes the model configuration from neutral to nose up and toward the left.

An unsteady analysis of the forces was also performed, by computing the spectra of each force and moment measured by the balance. As can be seen from Figure 4.11, the flow excites the resonance frequencies of the model, mentioned in Section 3.2. The peak centred at $f = 3.46$ Hz ($St_H \approx 0.098$), observed in the yaw moment, is very close to the resonance measured in the same direction, while the peak at $f = 5.09$ Hz ($St_H \approx 0.145$), found for the side force, corresponds to the roll resonance. Finally, the peaks at $f = 5.71$ Hz ($St_H \approx 0.163$) for the lift force and the pitch moment, almost match the pitch resonance. Electronic disturbances were excluded by studying the noise floor of the force measuring system, showed in Figure 4.12. The spectra are presented such that $\int f\Phi(f)df = \overline{F^2} \equiv N^2$ for forces and $\int f\Phi(f)df = \overline{M^2} \equiv N^2m^2$ for moments.

Bayraktar *et al.* (2001) calculated the Strouhal numbers for the lift and the side forces to be 0.106 and 0.086, but no interpretation of these numbers was given, nor

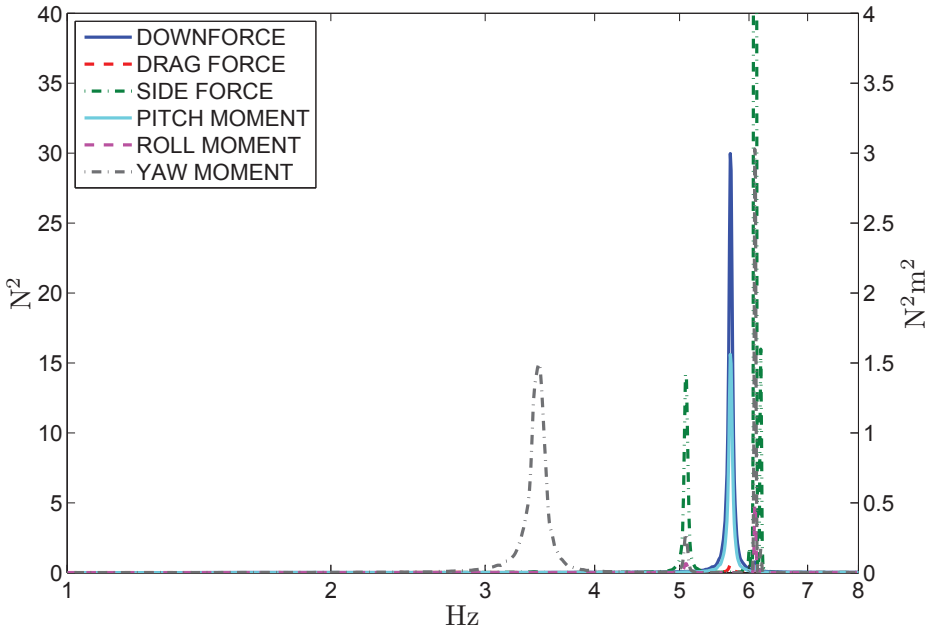

Figure 4.11: Pre-multiplied spectra of force balance readings as a function of frequency.

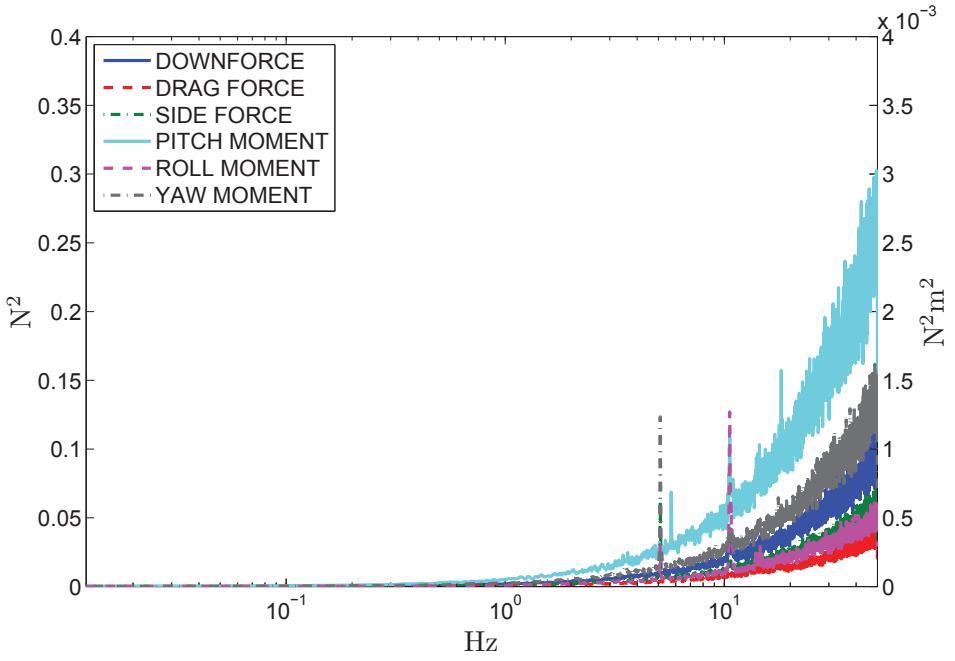

Figure 4.12: Pre-multiplied spectra of the noise floor of force balance readings.

the structural resonances of the system reported.

Chapter 5

The Forced Flow

This chapter focuses on the effects of the forcing introduced in the flow through the slot of width 4.5 mm. A preliminary analysis confirmed the trend documented by Qubain (2009) and Oxlade (2013), with a base pressure decrease at forcing frequencies around $St_\theta \approx 0.02$ ($St_D \approx 1.84$) at all amplitudes. However, since the main goal of this study was to verify the possibility of a base pressure increase and a drag reduction when applying high frequency forcing to a rectangular sectioned body, the measurements focus on the range of forcing frequencies and amplitudes which could lead to the largest base pressure increase.

5.1 Integrated Base Pressure and Drag

The overall results for the forced flow relative to the 4.5 mm wide slot for the range of forcing frequencies from $St_{Hf} = 12.2$ to $St_{Hf} = 14.2$ (430 Hz to 500 Hz) are shown in Figure 5.1 and 5.2. As can be seen from the figures, and read more clearly in Table C.1 and C.2 in Appendix C, the minimum base pressure increase and drag reduction are 5.7% and 1.3%, respectively. The maximum base pressure recovery $\Delta C_p/C_{pB}$, equal to $27.7\% \pm 0.6\%$, is reached for a frequency $St_{Hf} = 13.9$ (490 Hz) and an amplitude of $C_\mu = 0.168$; the corresponding change in drag $\Delta C_D/C_{DB}$ is $-12.1\% \pm 0.2\%$. The maximum drag reduction $\Delta C_D/C_{DB}$, equal to $-13.1\% \pm 0.1\%$, is found for the same frequency but at a forcing amplitude $C_\mu = 0.184$; the change

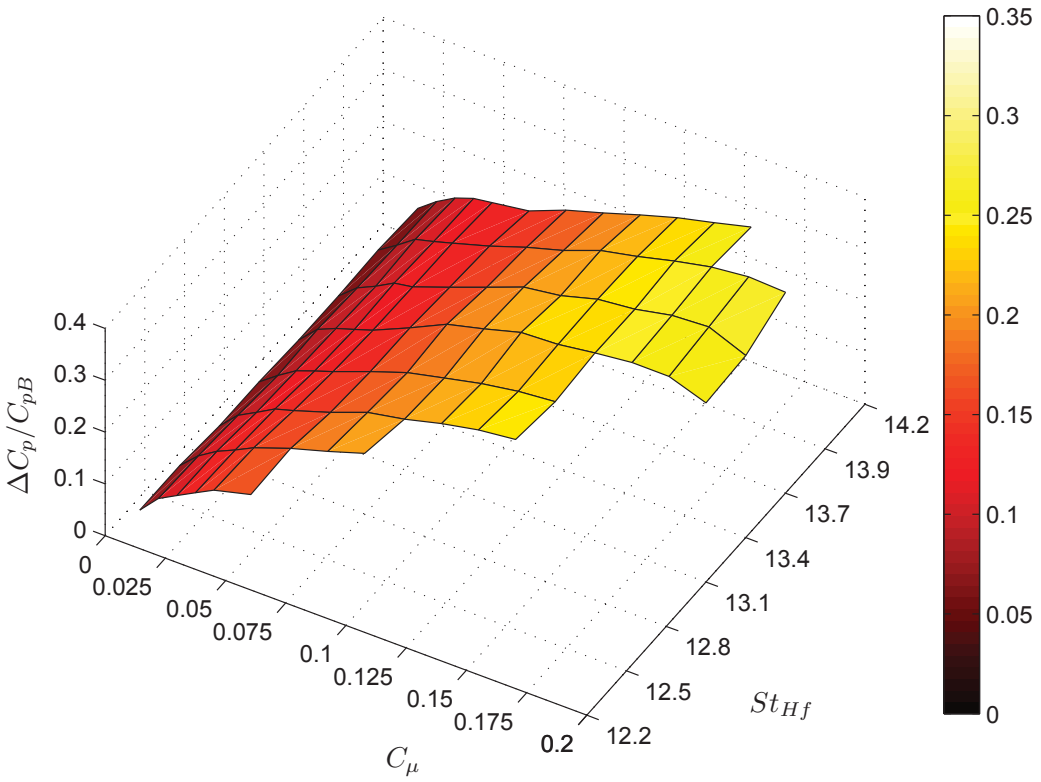

Figure 5.1: Change in pressure coefficient $\Delta C_p/C_{pB}$ with frequency St_{Hf} and forcing amplitude, C_μ.

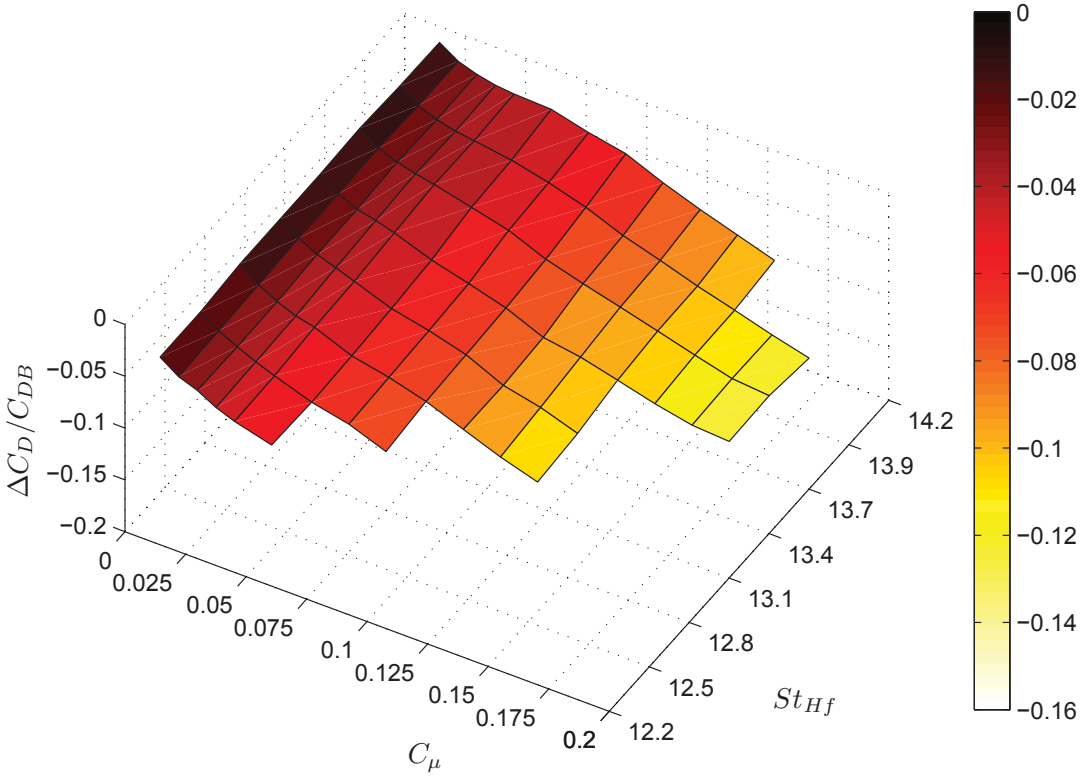

Figure 5.2: Change in drag coefficient $\Delta C_D/C_{DB}$ with frequency St_{Hf} and forcing amplitude, C_μ.

in pressure $\Delta C_p/C_{pB}$ is 27.3% $\pm$ 0.5 %. As shown by Oxlade (2013), a plateau of frequencies over which the optimum of base pressure rise occurs can be defined for a tolerance of $\pm$2%.

The changes in C_p and C_D are accompanied at all frequencies by considerable alterations of wake structure and dynamics, as well as forces and moments, which reflect a modification of the flow around the model.

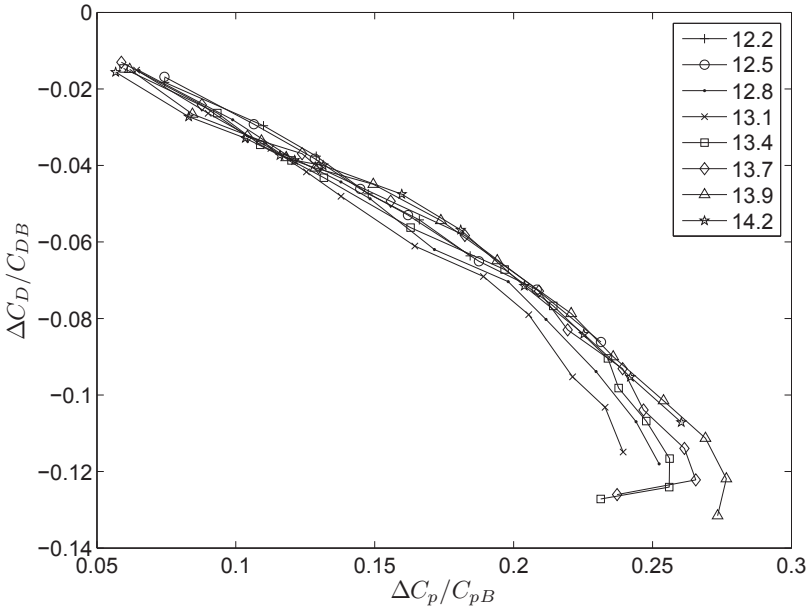

Figure 5.3: Change of the drag coefficient, $\Delta C_D/C_{DB}$, as a function of the change of the pressure coefficient, $\Delta C_p/C_{pB}$, for different forcing frequencies, St_{Hf}.

The correlation between pressure increase and changes in drag force, downforce, and pitch moment, is shown in Figures 5.3 – 5.5. The behaviour of the balance coefficients as functions of $\Delta C_p/C_{pB}$ is an indication of the effect of the base pressure rise on the flow around the body.

Figure 5.3 shows that the drag coefficient C_D decreases linearly with the pressure increase up to $\Delta C_p/C_{pB} \approx 0.27$; above this value the drag continues to decrease despite the almost constant value of base pressure. The departure from the linear behaviour is anticipated by the divergence of the curves above $\Delta C_p/C_{pB} \approx 0.22$, below which they collapse well. This characteristic could be considered as an indication that, up to a drag reduction of about 12%, the drag decrease registered by

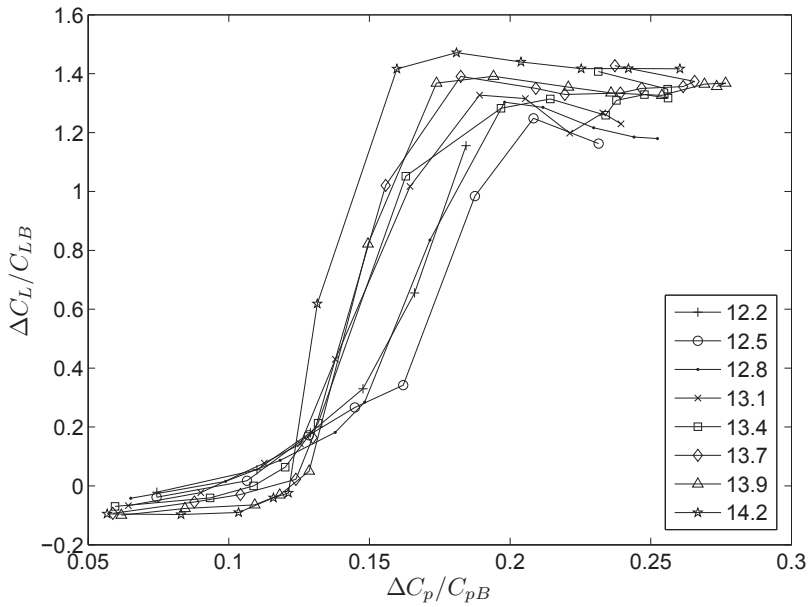

Figure 5.4: Change of the downforce coefficient, $\Delta C_L/C_{LB}$, as a function of the change of the pressure coefficient, $\Delta C_p/C_{pB}$, for different forcing frequencies, St_{Hf}.

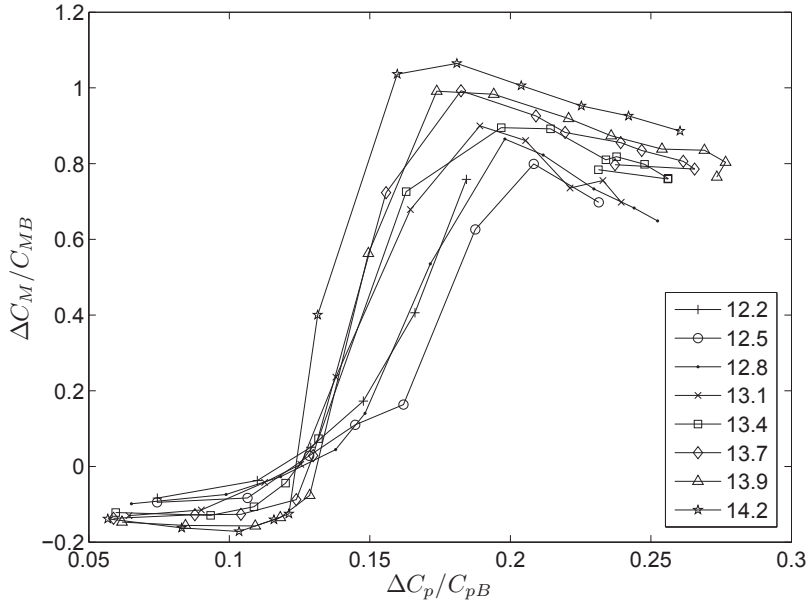

Figure 5.5: Change of the pitch moment coefficient, $\Delta C_M/C_{MB}$, as a function of the change of the pressure coefficient, $\Delta C_p/C_{pB}$, for different forcing frequencies, St_{Hf}.

the balance is entirely due to the increase in base pressure; what happens at higher values of the blowing coefficient, where the drag continues to decrease even though the base pressure does not rise, should be further investigated.

The changes in downforce coefficient $\Delta C_L/C_{LB}$ and pitch moment coefficient $\Delta C_M/C_{MB}$ are mapped with the change of the pressure coefficient $\Delta C_p/C_{pB}$ in Figures 5.4 and 5.5. They show some similarities with the drag coefficient, but also some interesting differences. The curves almost collapse up to $\Delta C_p/C_{pB} \approx 0.12$, above which they begin to diverge, starting with the highest value of forcing frequency, $St_{Hf} = 14.2$, down to the curve corresponding to $St_{Hf} = 12.5$. The curve for $St_{Hf} = 12.2$ shows an atypical trend, different from all the others. As in the case of the drag coefficient, the downforce and pitch moment coefficients do not show a change in their trends with the pressure plateau at high forcing amplitudes. Again, this phenomenon requires further analysis.

5.2 Conditions of Maximum Base Pressure Recovery and Drag Reduction for $St_{Hf} = 13.9$ and $C_\mu = 0.168$

	C_μ	St_{Hf}	θ/H (baseline case)
Top & Bottom	0.168	13.9 (490 Hz)	0.011
Sides	0.168	13.9 (490 Hz)	0.009

Table 5.1: Conditions for maximum base pressure increase $\Delta C_p/C_{pB} = 27.7\%$ (measured drag reduction $\Delta C_D/C_{DB} = -12.1\%$).

5.2.1 Averaged Base Pressure Distribution

Figure 5.6 shows the dimensionless pressure levels and the position of the centre of pressure ($y = 0.0206$ m, $z = 0.0129$ m) for the case of maximum base pressure recovery. A strong asymmetry in the pressure distribution is evident, with higher

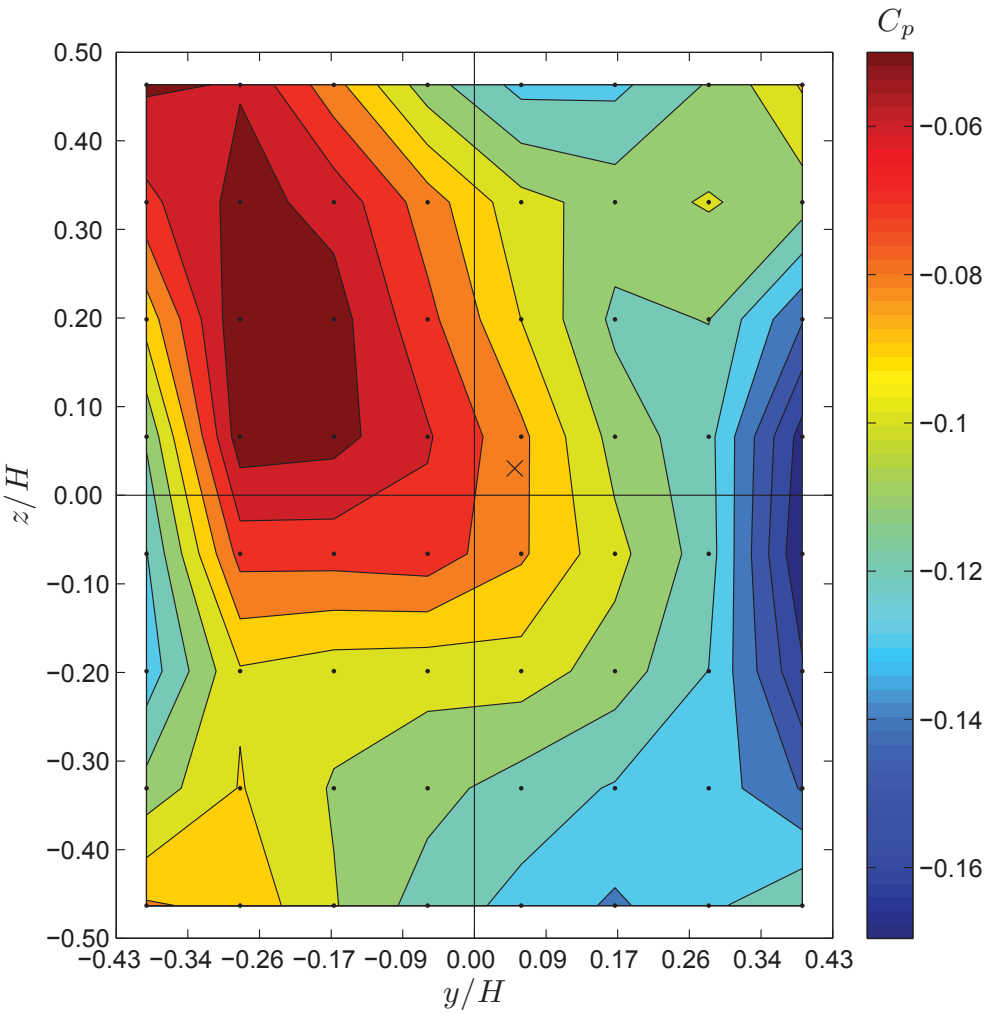

Figure 5.6: C_p contours on the base of the model for forcing parameters $St_{Hf} = 13.9$ and $C_\mu = 0.168$. Also shown: centre of pressure (×), ESP static pressure taps (▪), and area occupied by removable frame, jet slot and external walls of the model (white frame).

values on the top left corner of the base and lower ones at the right side and bottom. This is observed not only at this forcing frequency and amplitude, but at all frequencies for values of the blowing coefficient C_μ above 0.076, not only for this slot width, but also for the 5.5 mm slot. A similar result was observed also during a previous tunnel installation with a different base plate. As a consequence, it is unlikely that this flow structure is due to a misalignment of the model. More plausible causes could be one or more phenomena such as wind-tunnel upstream

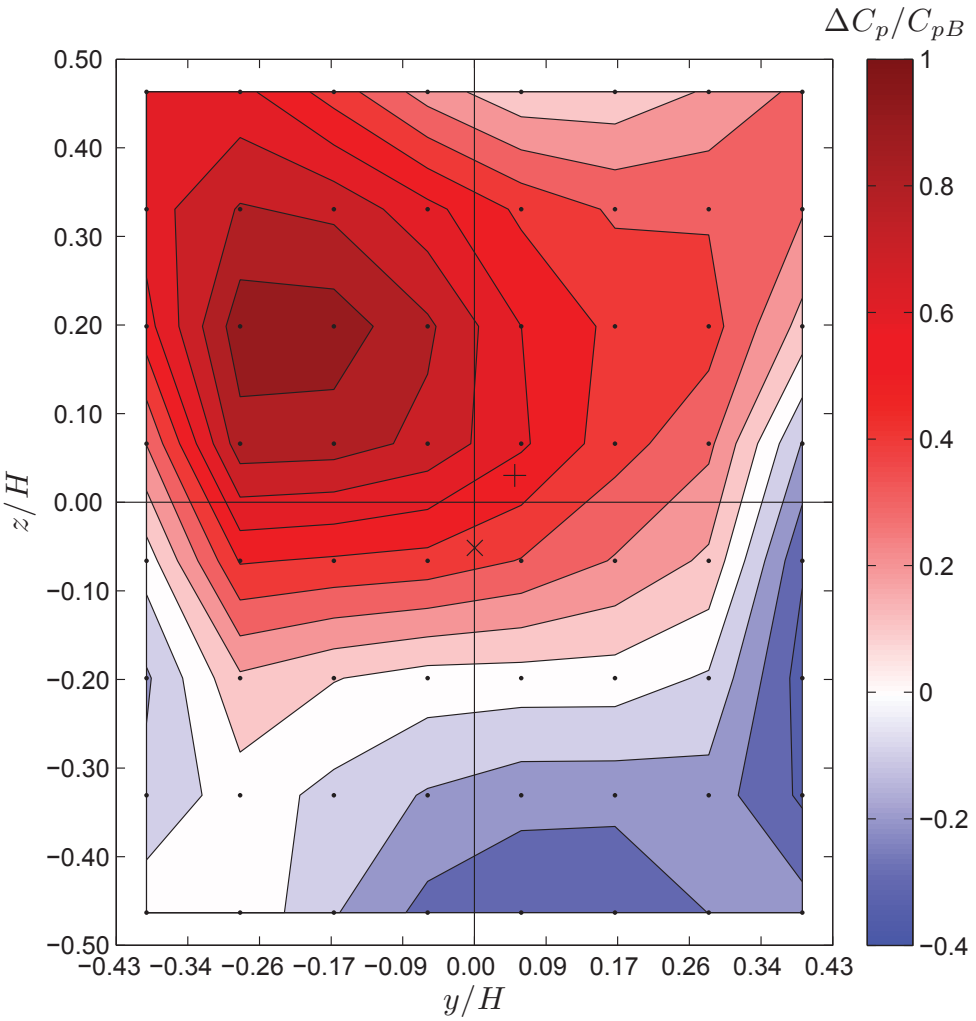

Figure 5.7: Dimensionless difference $(\overline{C_{pB}} - \overline{C_p})/\overline{C_{pB}}$ between C_p contours for baseline case and forced case with $St_{Hf} = 13.9$ and $C_\mu = 0.168$; $\times$ denotes the position of the centre of pressure in the baseline case, $+$ denotes the position of the centre of pressure in the forced case.

conditions, asymmetry in the forcing jet, flow boundary conditions or imperfections in the model geometry.

Together with the strong asymmetry in the pressure distribution, the main difference compared to the baseline case is the base pressure rise $(\overline{C_{pB}} - \overline{C_p})/\overline{C_{pB}}$, up to 96% at $(y/H = -0.28,\ z/H = 0.20)$ and $(y/H = -0.17,\ z/H = 0.20)$, as shown in Figure 5.7. The displacement of the centre of pressure due to forcing is also evident in the same figure.

Transducer	Baseline$\times 10^{-3}$	Forced$\times 10^{-3}$
E1	0.423	2.108
E2	1.287	0.464
E3	2.524	0.404
E4	1.440	1.822
E5	0.977	1.080
E6	1.980	0.466
E7	2.078	0.493
E8	1.106	1.535

Table 5.2: Dimensionless integrated mean-square pressure $\tilde{p} = \overline{p^2}/(\rho U_\infty^2)^2$ for baseline and forced conditions, as in Figure 5.10.

5.2.2 Wake Dynamics

This significant change produced by the forcing is even more evident when comparing the spectra to those for the baseline case, as shown in Figures 5.8 and 5.9. The characteristic frequencies discussed in Section 4.3.2 (Table 4.2) are almost completely suppressed, while a peak with significant level of energy can be found in the spectra from the transducers close to the sides (E1, E4, E5 and E8) in the range from $St_H \approx 1.2$ to $St_H \approx 3.7$. Taking the ratio θ/H, equal to 0.011 for the top and bottom boundary layers, and to 0.009 for the ones at the side (Table 5.1), the peaks from transducers E1, E5 and E8 correspond to the value suggested as most amplified frequency in a turbulent boundary layer by Ho & Huerre (1984) and Morris & Foss (2003) ($St_\theta = 0.22 - 0.24$). The peak for transducer E4 is located at a lower frequency than the one suggested above; this is likely to be caused by the influence of the ground. Once more the symmetry between the top and bottom transducers, E1 and E4, is lost, but unlike the baseline case, they show almost the same value of $\tilde{p}$, as shown also in Figure 5.10 and Table 5.2. The values in Figure 5.10 are calculated by integrating the normalised pressure spectra up to $St_{Hf} \approx 7.1$, to exclude the energy added through forcing. By contrast, the spectra from the transducers located at the sides, E5 and E8, are more similar in shape, but with a shift in frequency and a difference in the energy content. Finally, the forcing frequency is found as $St_H \approx 14$

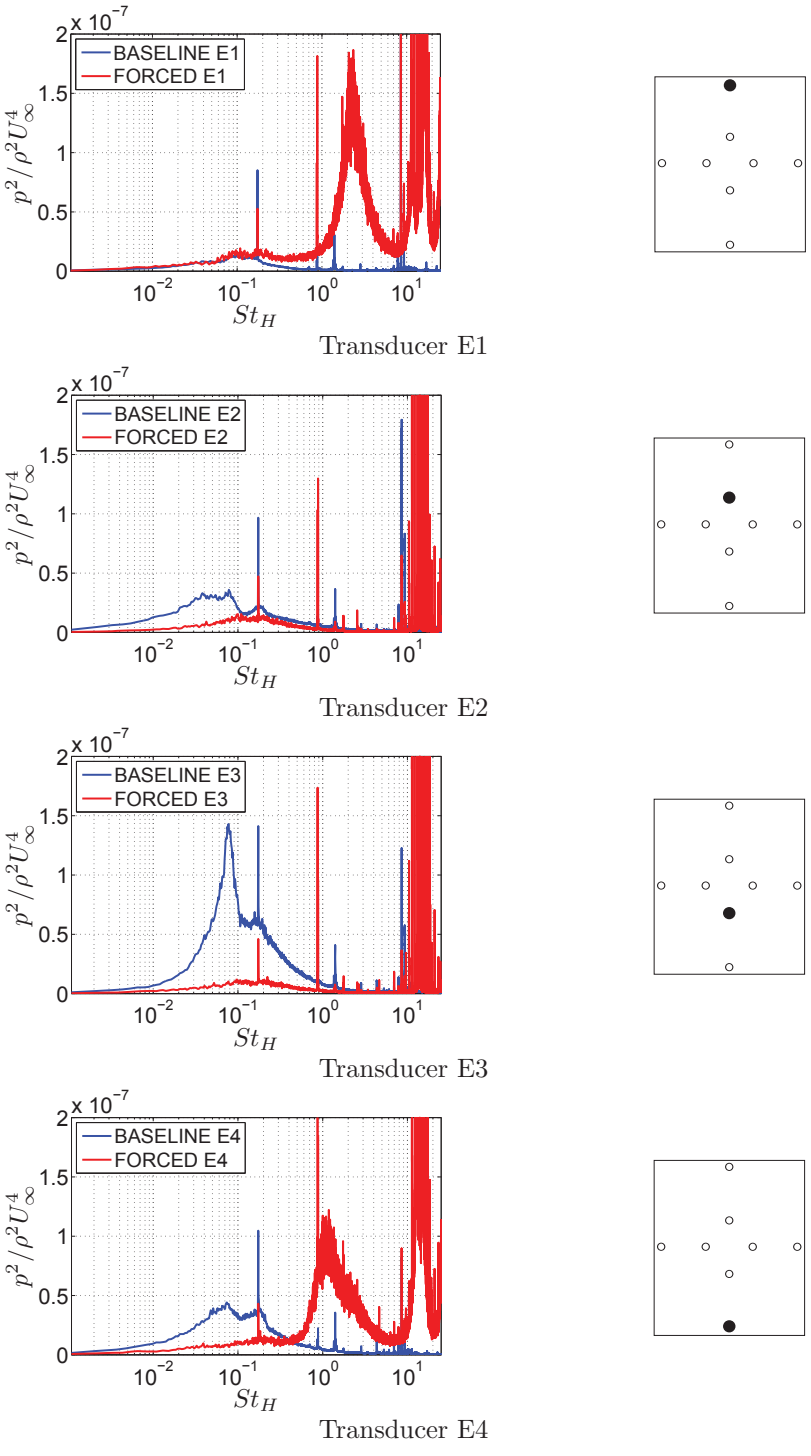

Figure 5.8: Dimensionless pre-multiplied spectra from dynamic transducers E1–E4 as a function of $St_H = fH/U_\infty$. Comparison between forced cases for $St_{Hf} = 13.9$ and $C_\mu = 0.168$ (red) and baseline (blue). Transducers from E1 to E4.

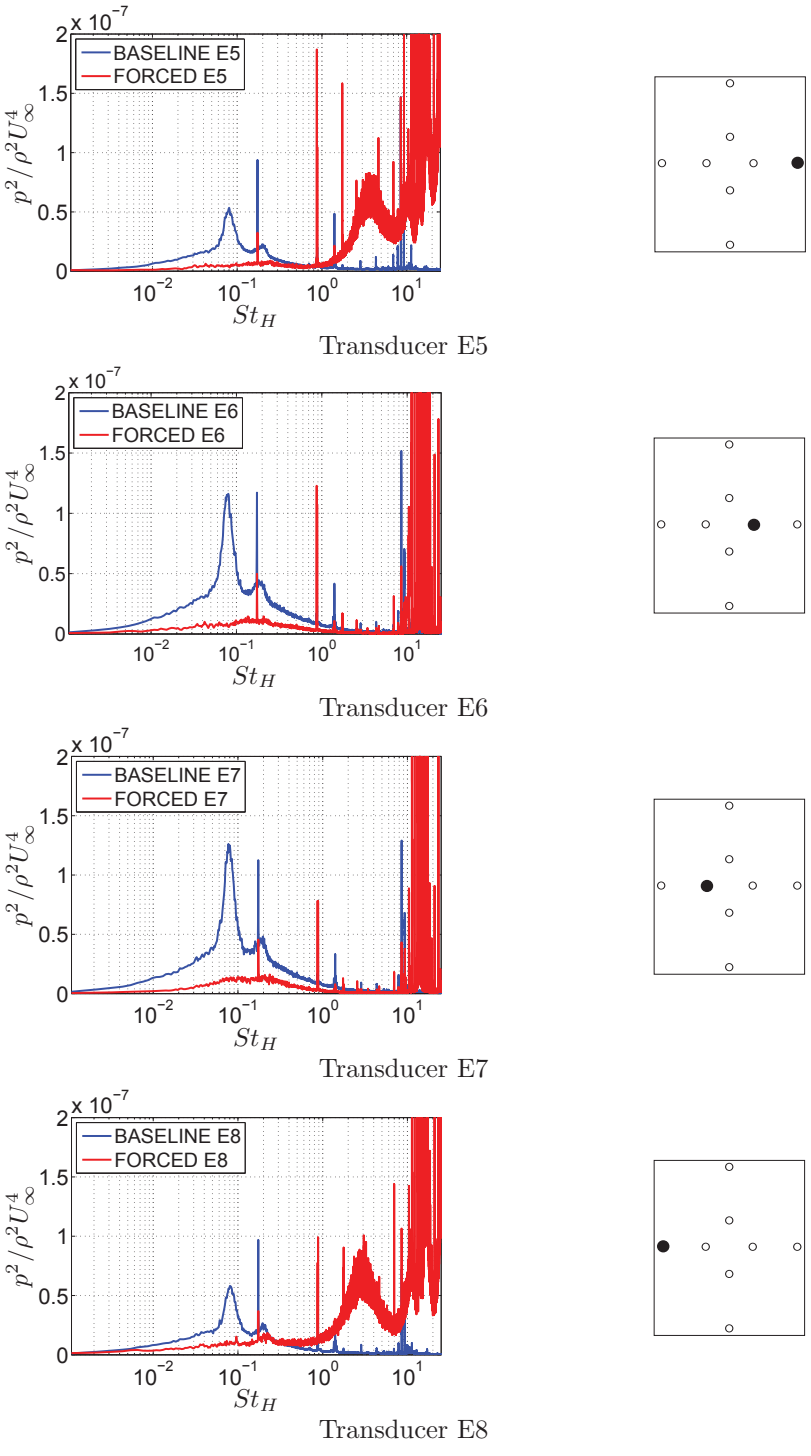

Figure 5.9: Dimensionless pre-multiplied spectra from dynamic transducers E5–E8 as a function of $St_H = fH/U_\infty$. Comparison between forced cases for $St_{Hf} = 13.9$ and $C_\mu = 0.168$ (red) and baseline (blue). Transducers from E5 to E8.

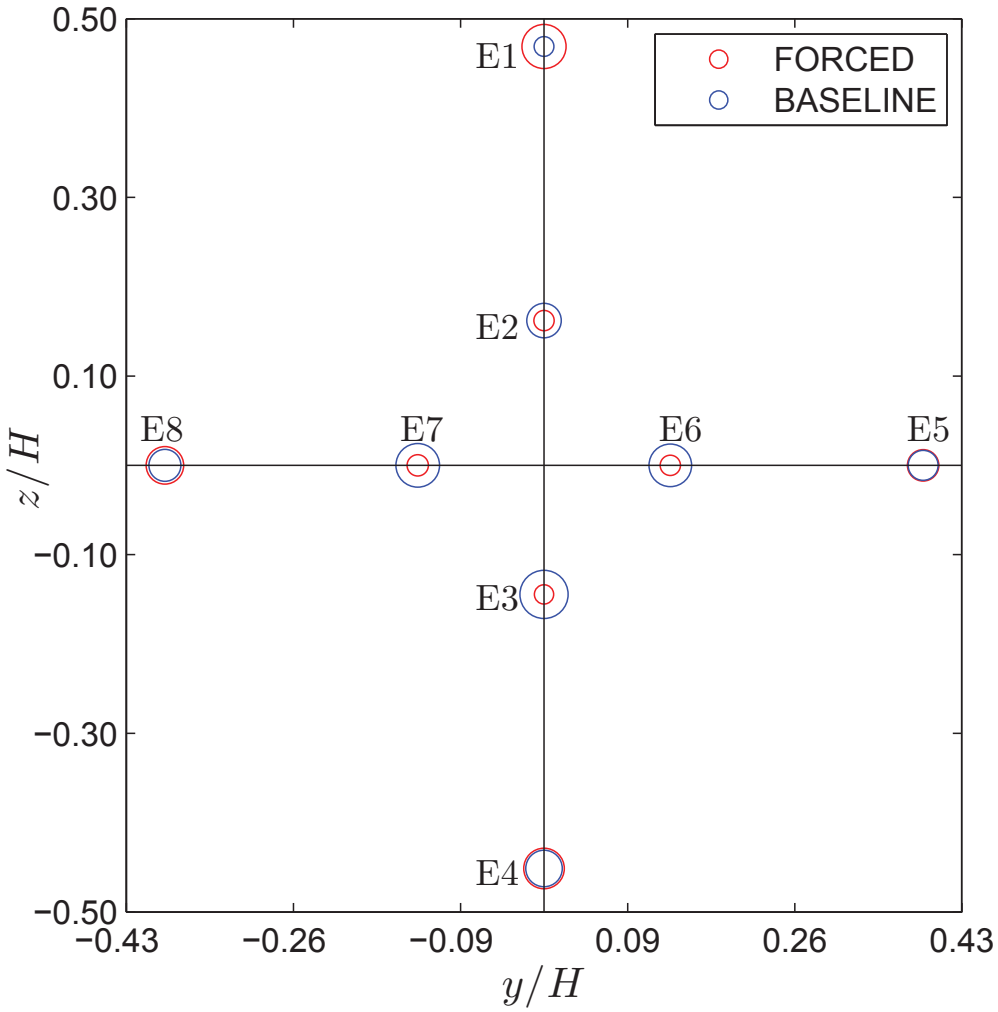

Figure 5.10: The area of the circles is proportional to the dimensionless integrated mean-square pressure $\tilde{p} = \overline{p^2}/(\rho U_\infty^2)^2$ for forced conditions $St_{Hf} = 13.9$ and $C_\mu = 0.168$ (maximum base pressure increase – red) and baseline case (blue) – see Table 5.2.

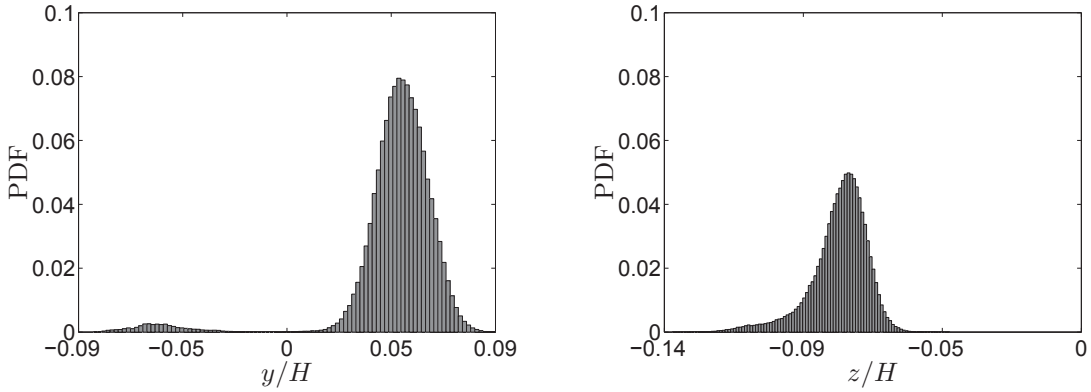

(a) (b)

Figure 5.11: PDF of the position of the centre of pressure (a) in the y direction as in Equation 3.4 (mean = 4.9×10^{-2}, variance = 4.9×10^{-4}, skewness = -3.43, kurtosis = 17.82) and (b) in the z direction as in Equation 3.5 (mean = 3.0×10^{-2}, variance = 5.9×10^{-4}, skewness = -1.15, kurtosis = 5.26) for forced conditions $St_{Hf} = 13.9$ and $C_\mu = 0.168$.

in all signals.

The PDF of the position of the centre of pressure in the y and z directions for $St_{Hf} = 13.9$ and $C_\mu = 0.168$ is shown in Figure 5.11. The bi-stability in the y direction is still not detected in this case. In the z direction, rather than an alternation between two distinct positions, the centre of pressure takes a wide range of positions around the zero, with a preference for the locations with $z > 0$.

5.2.3 Forces Acting on the Body

The coefficients for forces and moments measured in the condition of maximum base pressure recovery are listed in Table 5.3, which also shows the changes with respect to the baseline flow, calculated as in Equation 3.9. The downforce and pitch moments increase by 137% and 80% respectively, and drag decreases by 12%. The changes in side force and roll moment, even if large, are associated with a higher uncertainty. The unsteady forces show that the forcing action of the jet is able to partially damp the oscillations of the model at the frequencies identified in the baseline case, as shown by the pre-multiplied spectra in Figure 5.12. The spectra are

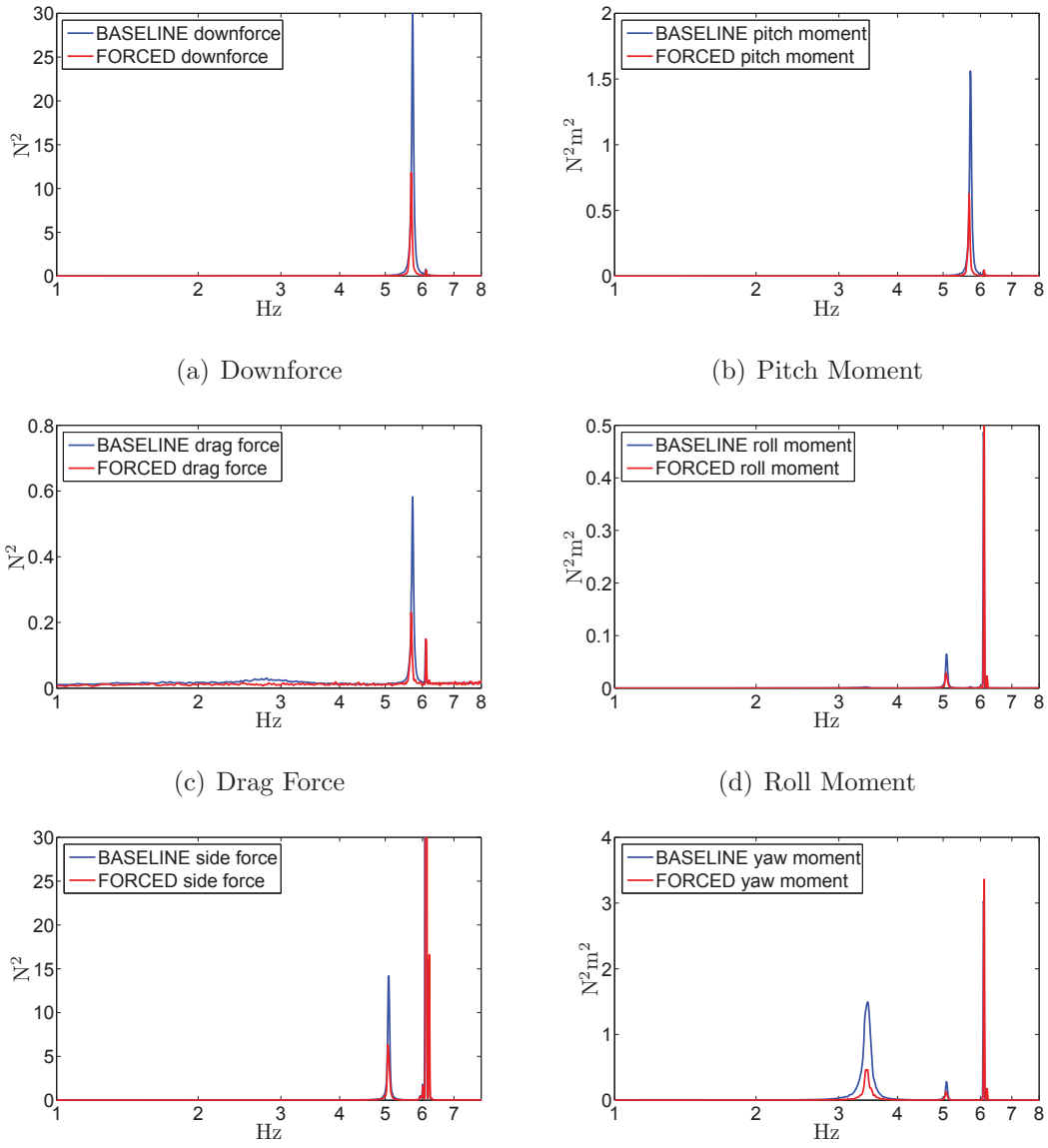

(a) Downforce

(b) Pitch Moment

(c) Drag Force

(d) Roll Moment

(e) Side Force

(f) Yaw Moment

Figure 5.12: Pre-multiplied spectra of force balance readings as a function of frequency. Comparison between baseline (grey) and forced cases (black).

	Value	Uncertainty %	$\frac{\Delta C}{C_B}$ %	$\frac{\Delta C}{C_B}$ Uncertainty %
Downforce coefficient (C_L)	0.075	±0.07	137.1	±2.4
Drag coefficient (C_D)	0.228	±0.05	-12.2	±0.2
Side force coefficient (C_Y)	0.018	±0.16	70.3	±15.4
Pitch coefficient (C_M)	-0.036	±0.04	80.1	±2.2
Roll coefficient (C_R)	0.004	±0.03	110.9	±17.4
Yaw coefficient (C_N)	-0.020	±0.05	17.9	±2.9

Table 5.3: Averaged force and moment coefficients for the case of maximum base pressure recovery. The changes from the baseline case are calculated as in Equation 3.9.

presented such that $\int f\Phi(f)df = \overline{F^2} \equiv N^2$ for forces and $\int f\Phi(f)df = \overline{M^2} \equiv N^2m^2$ for moments.

5.3 Response to Changes in Forcing Amplitude

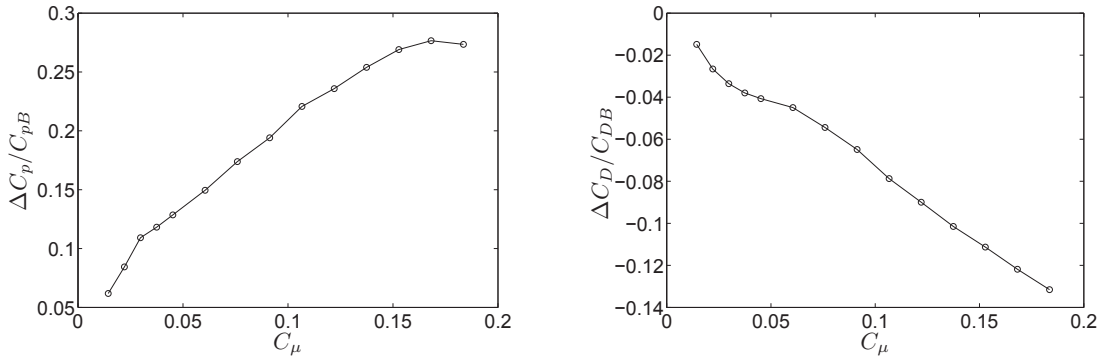

(a) (b)

Figure 5.13: Dimensionless change of (a) weighted base pressure $\Delta C_p/C_{pB}$ and (b) drag force $\Delta C_D/C_{DB}$ as a function of the blowing coefficient C_μ for $St_{Hf} = 13.9$.

The effects of increasing forcing amplitude are shown using the data for the frequency of highest pressure recovery ($St_{Hf} = 13.9$). The behaviour of the forces and moments, as well as those for the base pressure distribution, the PDF of the

centre of pressure, and the spectral analysis, suggest a clear alteration of the wake. Significant changes are observed for a forcing amplitude $C_\mu \approx 0.05$ and a different wake organisation for $C_\mu > 0.06$, as discussed below.

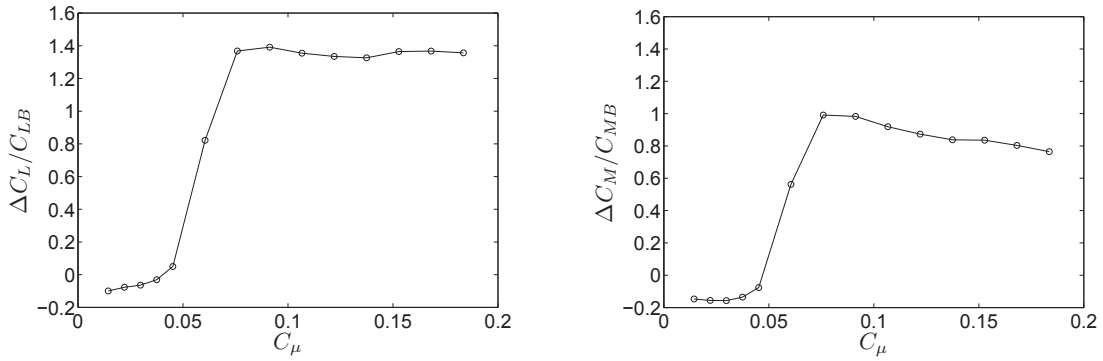

(a) (b)

Figure 5.14: Dimensionless change in (a) downforce $\Delta C_L/C_{LB}$ and (b) pitch moment $\Delta C_M/C_{MB}$ as a function of the blowing coefficient C_μ for $St_{Hf} = 13.9$.

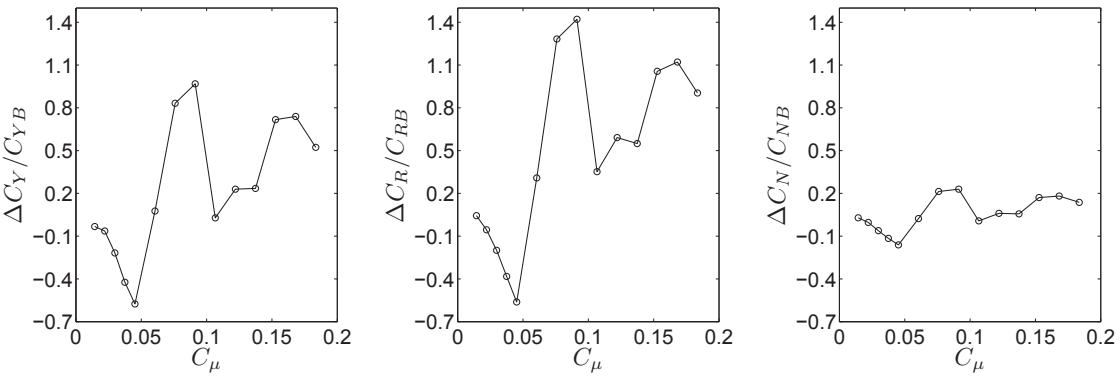

(a) (b) (c)

Figure 5.15: Dimensionless change of (a) side force $\Delta C_Y/C_{YB}$, (b) roll moment $\Delta C_R/C_{RB}$ and (c) yaw moment $\Delta C_N/C_{NB}$ as a function of the blowing coefficient C_μ for $St_{Hf} = 13.9$.

Figure 5.13 shows that the changes in pressure and drag have a fairly linear trend with increasing forcing amplitude, with an inflection point at $C_\mu \approx 0.04$. By contrast, the downforce and pitch moments show a sudden change at $C_\mu \approx 0.05$ (Figure 5.14); a similar change is found for side force, roll and yaw moments,

shown in Figure 5.15. A closer examination of the pressure and drag plots (Figure 5.13) confirms that the maximum base pressure recovery does not correspond to the minimum drag.

Concerning the impact of the forcing amplitude on the average organisation of the wake, values of the blowing coefficient between $C_\mu = 0.014$ and $C_\mu = 0.045$ do not show substantial variations in base pressure distribution and position of the centre of pressure compared to the baseline (Figure 5.16 (a) – (f)). However, the established structure of the wake appears to brake up for $C_\mu > 0.06$: the pressure on the base becomes almost uniform, with C_p between -0.14 and -0.09 (g), and the centre of pressure moves to a central position with an almost symmetric but bimodal behaviour in the y and in the z directions. For higher values of the blowing coefficient, the wake switches to its 'final' configuration, with an asymmetric base pressure distribution and the centre of pressure located towards the right upward corner of the base. A disruption in the wake behaviour occurs for $C_\mu = 0.107$, with a smaller range of C_p values measured on the base and the restoration of the bimodal behaviour in y (Figure 5.16 (j)). Bimodal PDFs persist also for $C_\mu = 0.122$ and $C_\mu = 0.137$ (Figure 5.16 (k) and (l)), while the base pressure distribution goes back to the asymmetry previously shown. Apart from some changes in the C_p values, and in the weighted average on the base, no significant wake modifications are found with further increases in the forcing amplitude (Figure 5.16 (m) – (o)). The moments for the PDFs of the position of the centre of pressure for Figure 5.16 are shown in Table 5.4 and plotted as functions of C_μ in Figure 5.17. The mean (Figure 5.17 (a)) follows, in the y direction, the behaviour of side force, roll and yaw moments (Figure 5.15), and, in the z direction, the behaviour of side force and pitch moment (Figure 5.14). The variance (Figure 5.17 (b)) increases significantly in both directions for $C_\mu > 0.045$, confirming that significant changes happen at $C_\mu \approx 0.05$. Similarly, the skewness in the y direction becomes negative for $C_\mu > 0.045$ (Figure 5.17 (c)), while in the z direction it increases its value at $C_\mu = 0.045$ to return to zero and to negative values for $C_\mu \geq 0.076$. The kurtosis (Figure 5.17 (d)), indicates a shape close to a mesokurtic distribution (*e.g.* normal distribution, $\kappa = 3$) in both y and z for most of the forcing amplitudes tested.

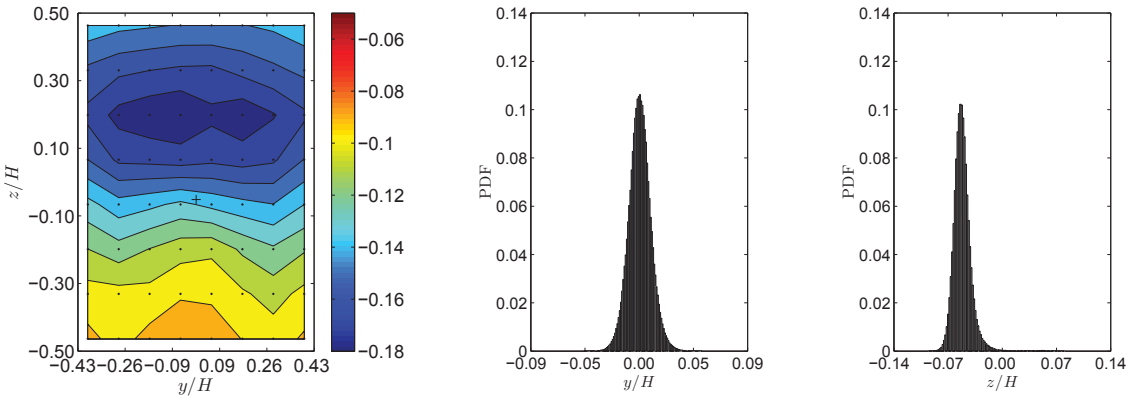

(a) Baseline

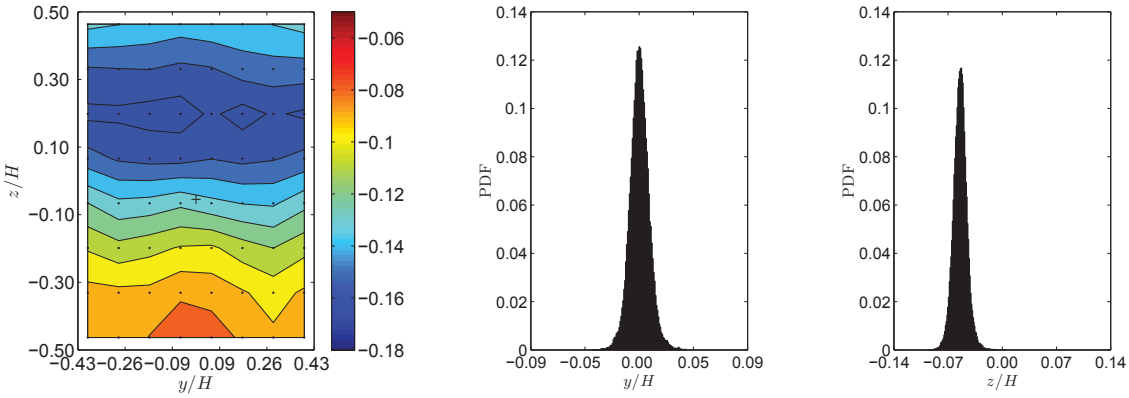

(b) $C_\mu = 0.014$

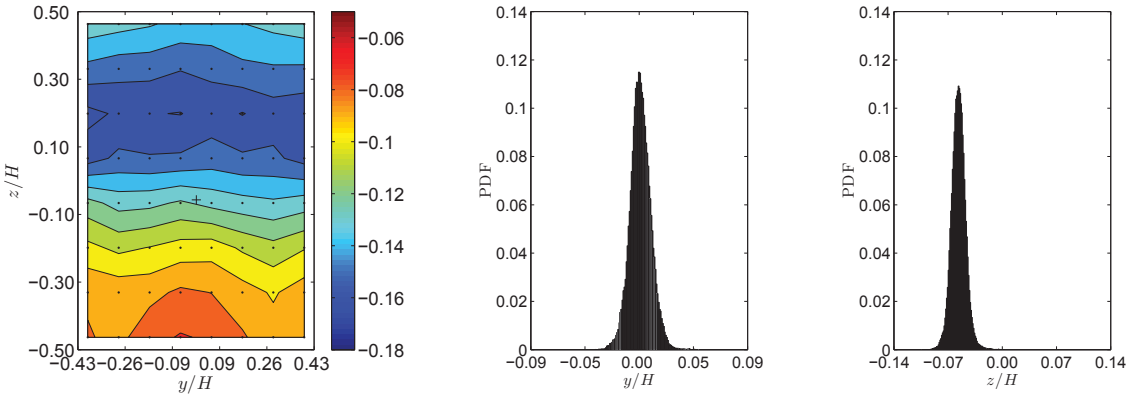

(c) $C_\mu = 0.022$

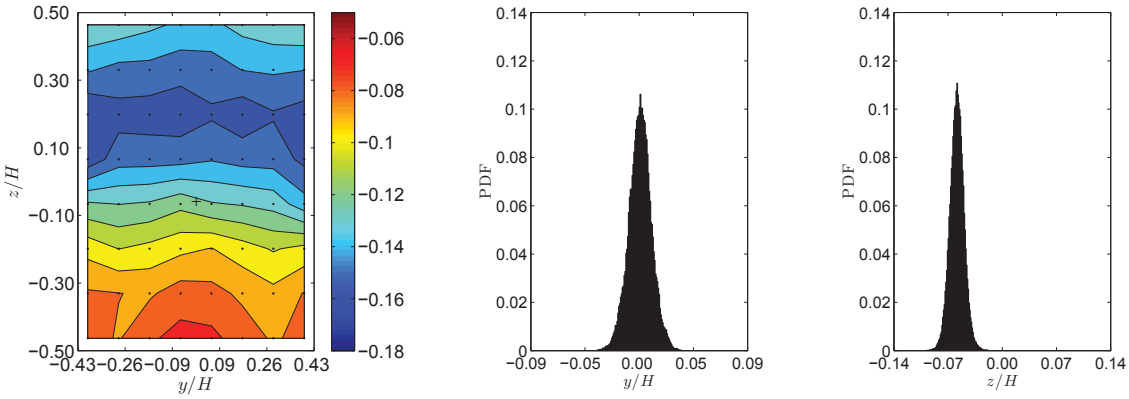

(d) $C_\mu = 0.030$

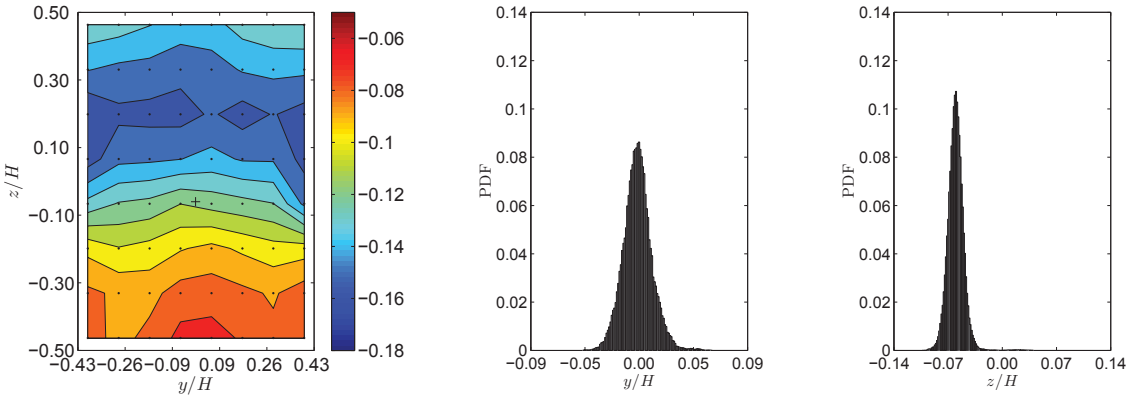

(e) $C_\mu = 0.037$

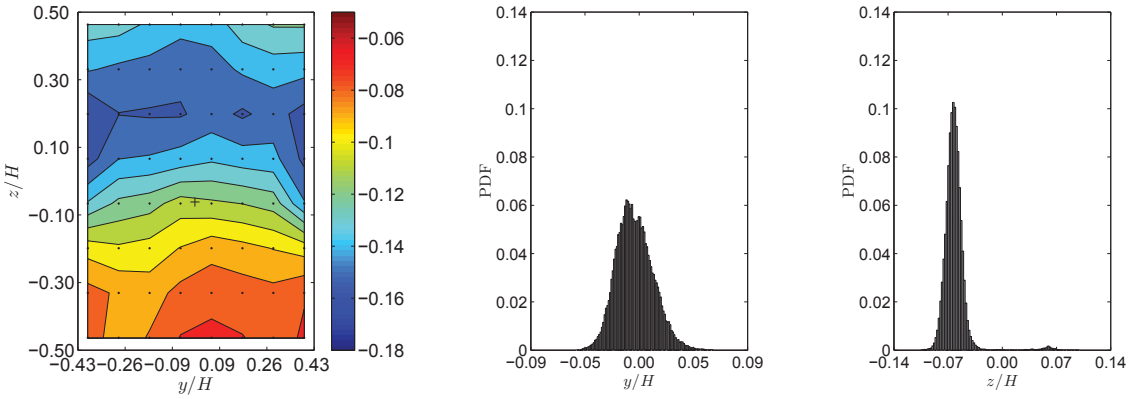

(f) $C_\mu = 0.045$

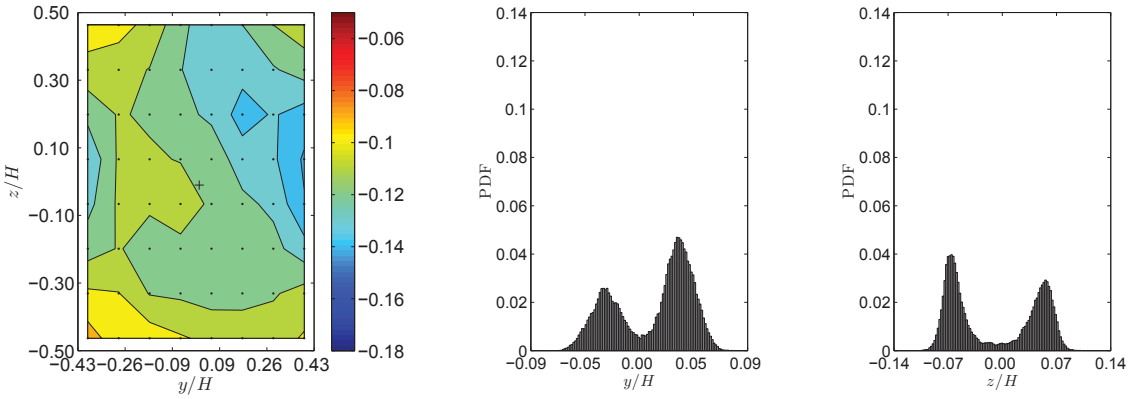

(g) $C_\mu = 0.061$

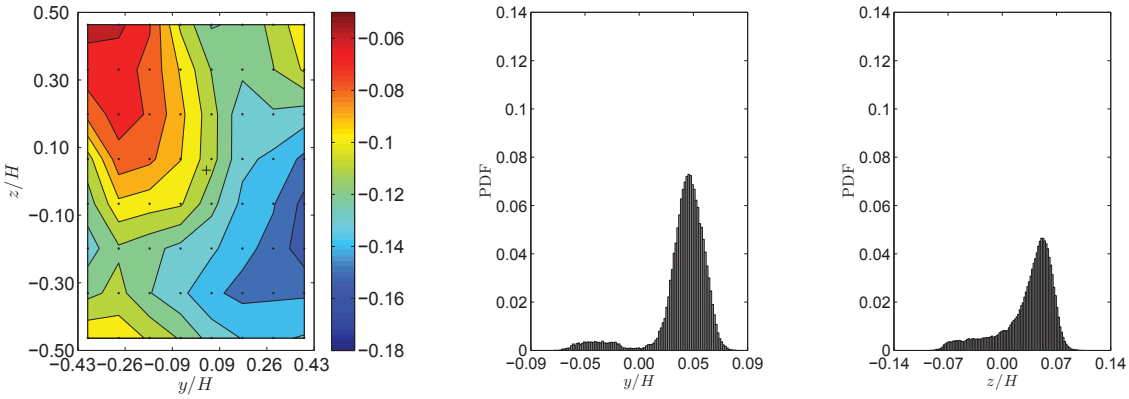

(h) $C_\mu = 0.076$

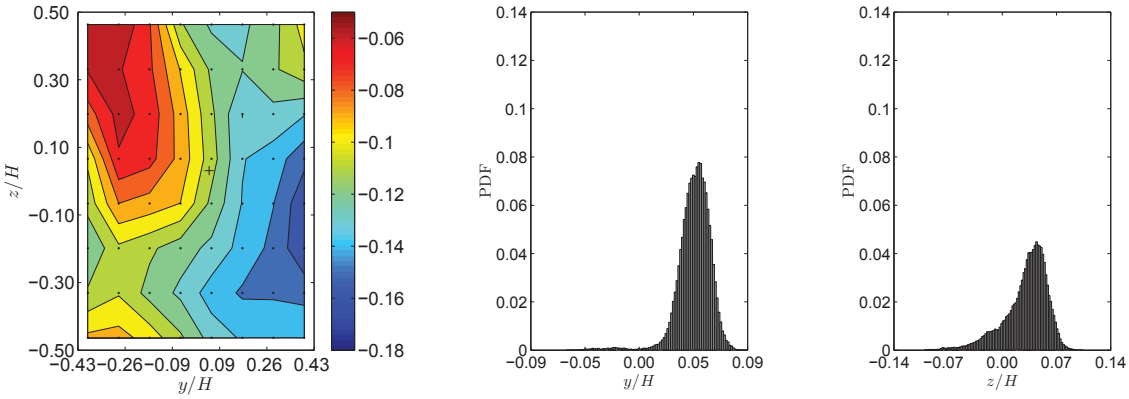

(i) $C_\mu = 0.091$

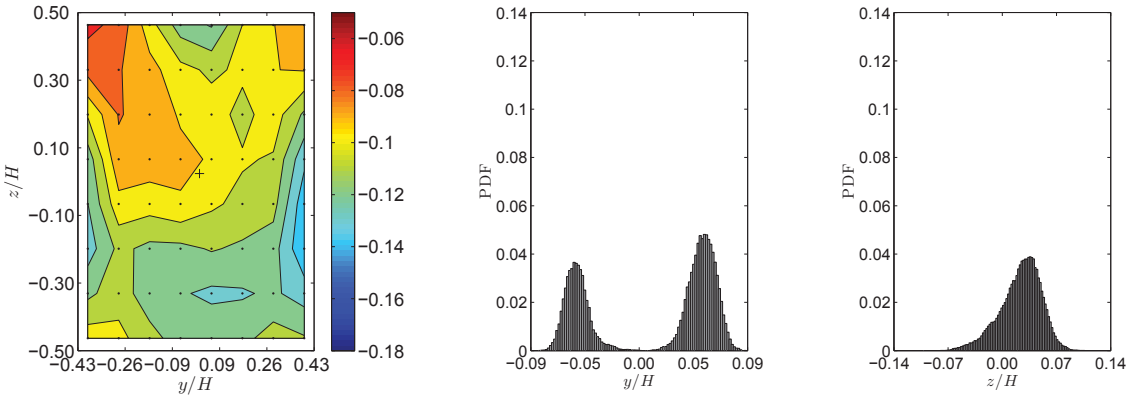

(j) $C_\mu = 0.107$

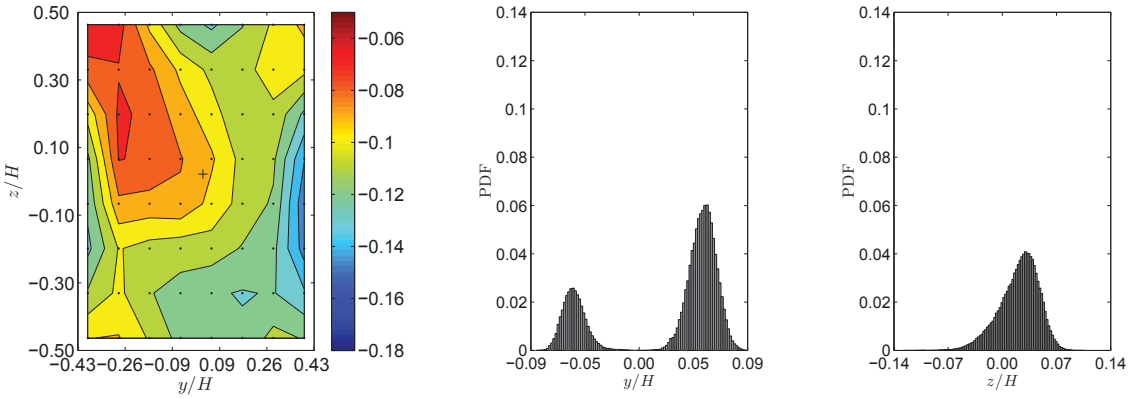

(k) $C_\mu = 0.122$

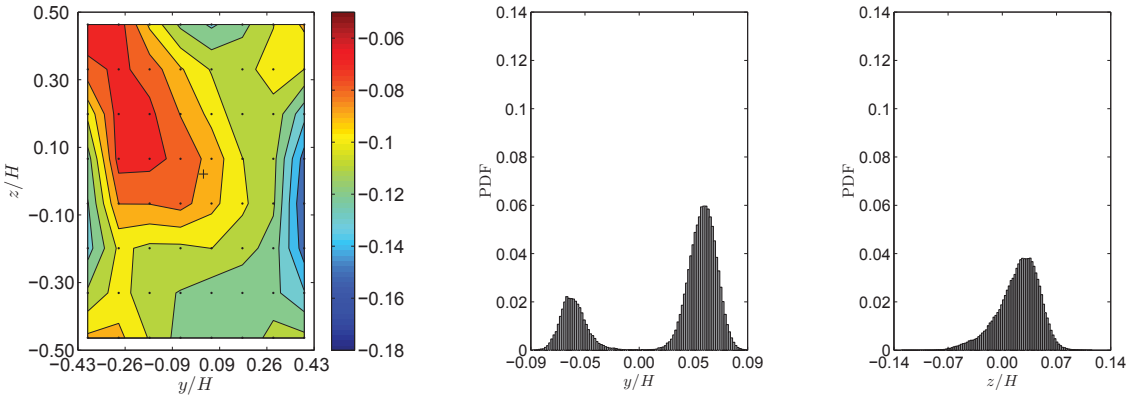

(l) $C_\mu = 0.137$

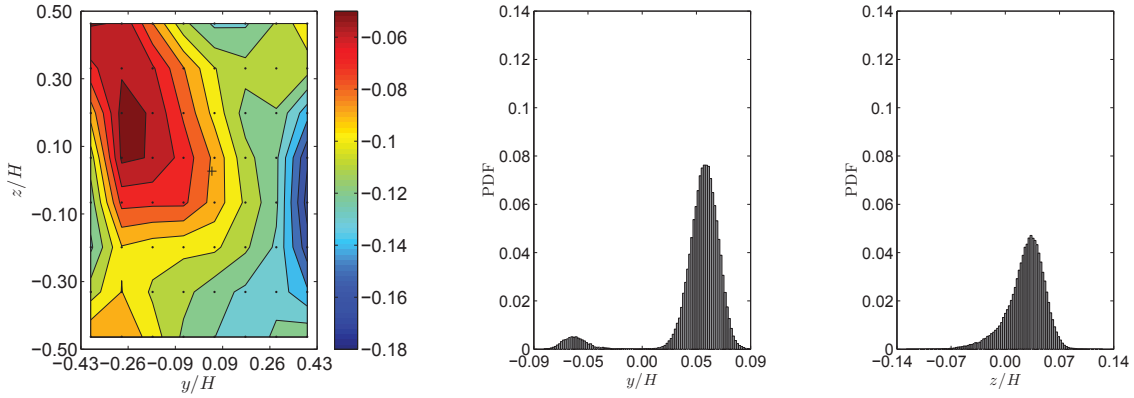

(m) $C_\mu = 0.153$

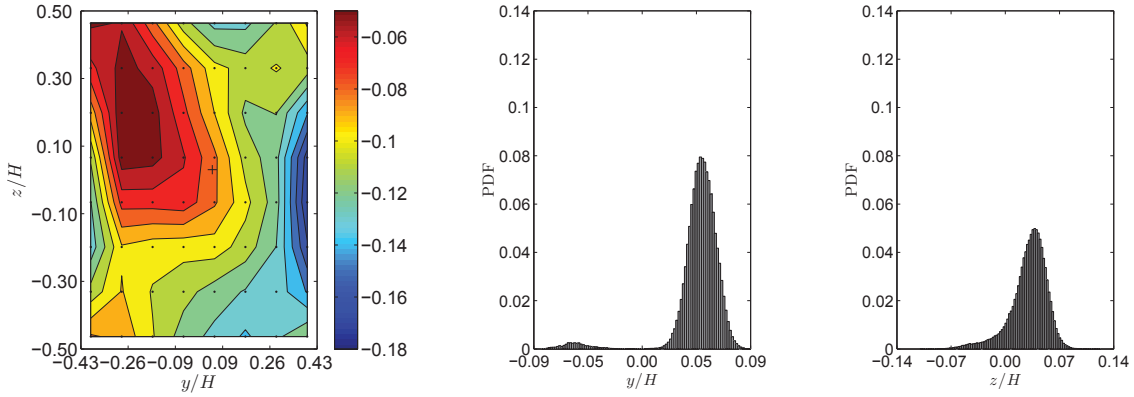

(n) $C_\mu = 0.168$

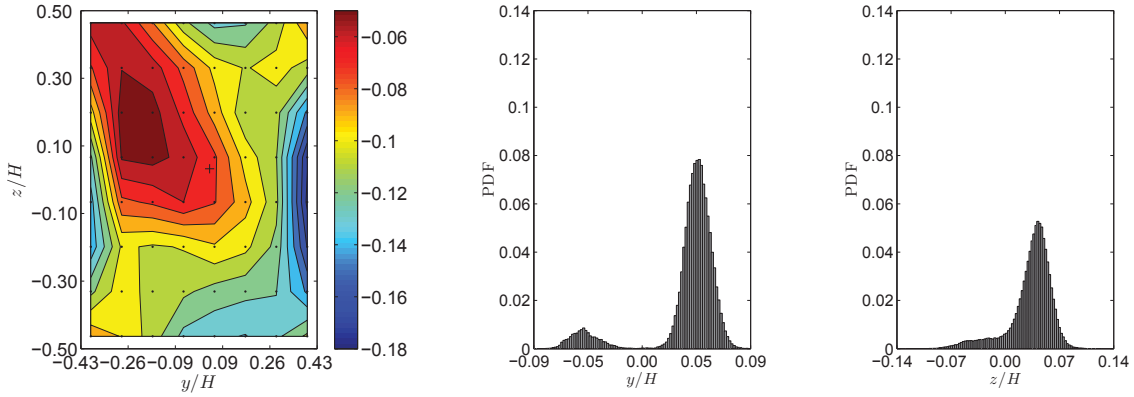

(o) $C_\mu = 0.184$

Figure 5.16: C_p contours showing position of centre of pressure (+) (left), PDF of centre of pressure along the y direction (centre) as in Equation 3.4 and z direction (right) as in Equation 3.5. Forcing frequency $St_{Hf} = 13.9$ (490 Hz).

Forcing Amplitude C_μ		Mean $\mu \times 10^{-3}$	Variance $\sigma^2 \times 10^{-3}$	Skewness γ	Kurtosis κ
Baseline	y	0.6	0.09	0.12	3.7
	z	-51.6	0.02	2.48	19.4
0.014	y	0.4	0.07	0.13	4.1
	z	-54.6	0.08	0.22	4.4
0.022	y	1.0	0.08	0.10	3.8
	z	-56.8	0.09	0.23	4.4
0.030	y	0.9	0.09	-0.03	3.3
	z	-58.6	0.08	0.05	3.7
0.037	y	-1.4	0.15	0.31	4.1
	z	-60.3	0.11	1.31	12.7
0.045	y	-4.5	0.25	0.36	3.1
	z	-61.9	0.24	4.67	37.0
0.061	y	12.0	1.10	-0.51	1.9
	z	-7.3	3.20	0.06	1.3
0.076	y	37.9	0.53	-2.24	8.8
	z	33.1	1.20	-1.32	4.2
0.091	y	47.6	0.21	-1.90	11.6
	z	30.5	0.81	-1.13	4.6
0.107	y	17.1	2.80	-0.60	1.5
	z	24.8	0.70	-0.64	3.5
0.122	y	27.7	2.40	-1.06	2.4
	z	21.0	0.66	-0.67	3.7
0.137	y	27.2	2.40	-1.07	2.4
	z	20.7	0.74	-0.69	3.7
0.153	y	47.4	0.79	-2.91	11.7
	z	26.5	0.60	-0.92	4.7
0.168	y	48.5	0.49	-3.43	17.8
	z	30.1	0.59	-1.15	5.3
0.184	y	38.6	0.98	-2.23	7.1
	z	32.4	0.84	-1.52	5.9

Table 5.4: Moments of the PDF distributions of the position of the centre of pressure for $St_{Hf} = 13.9$ – see Figures 5.16 – 5.17.

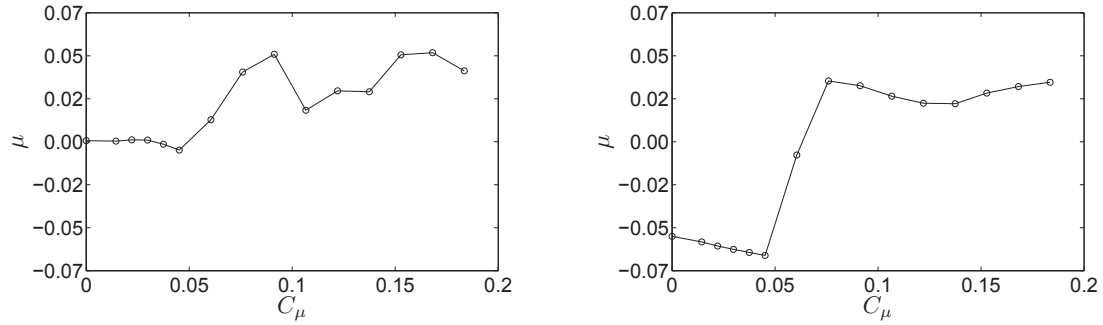

(a) mean in the y direction (left) and z direction (right)

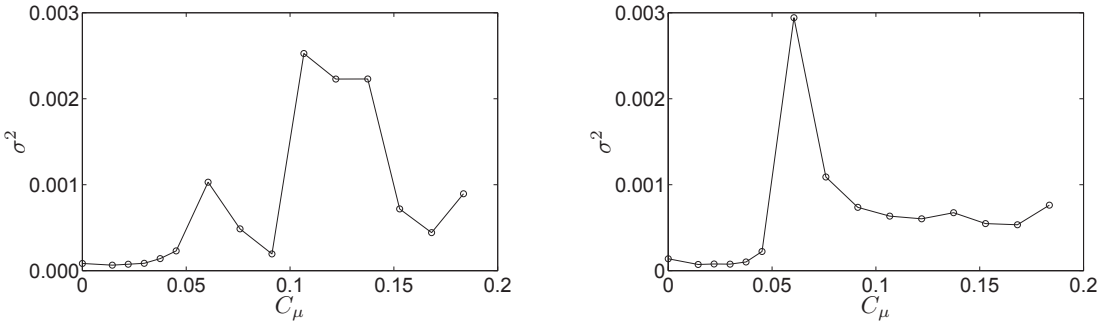

(b) variance in the y direction (left) and z direction (right)

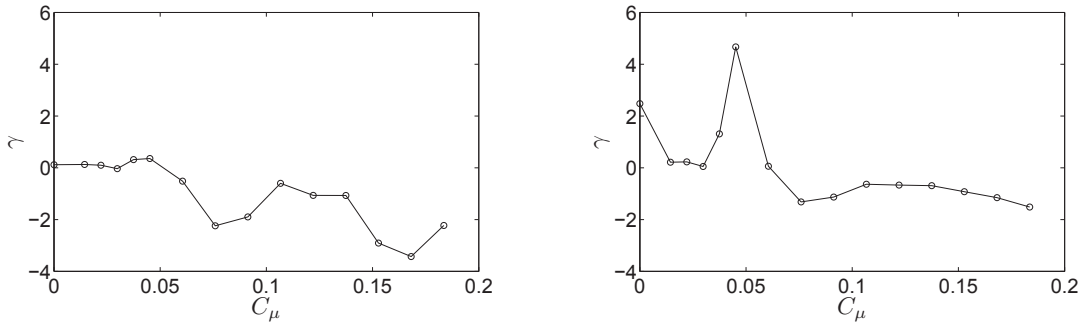

(c) skewness in the y direction (left) and z direction (right)

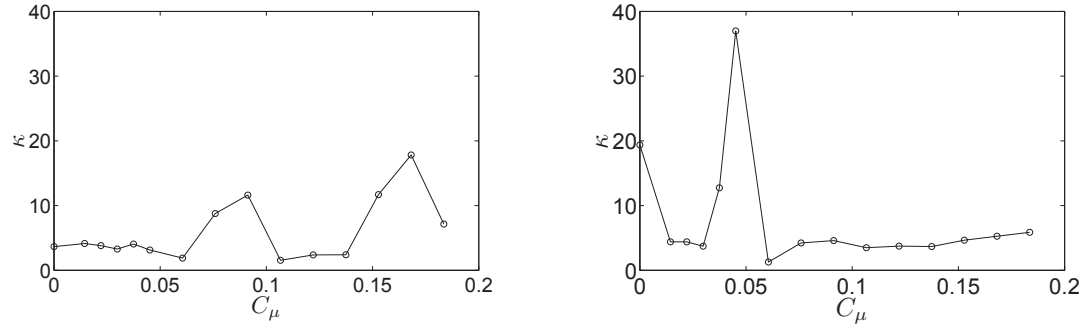

(d) kurtosis in the y direction (left) and z direction (right)

Figure 5.17: Statistical moments of the position of the centre of pressure in the y (left) and z (right) directions as a function of C_μ for $St_{Hf} = 13.9$.

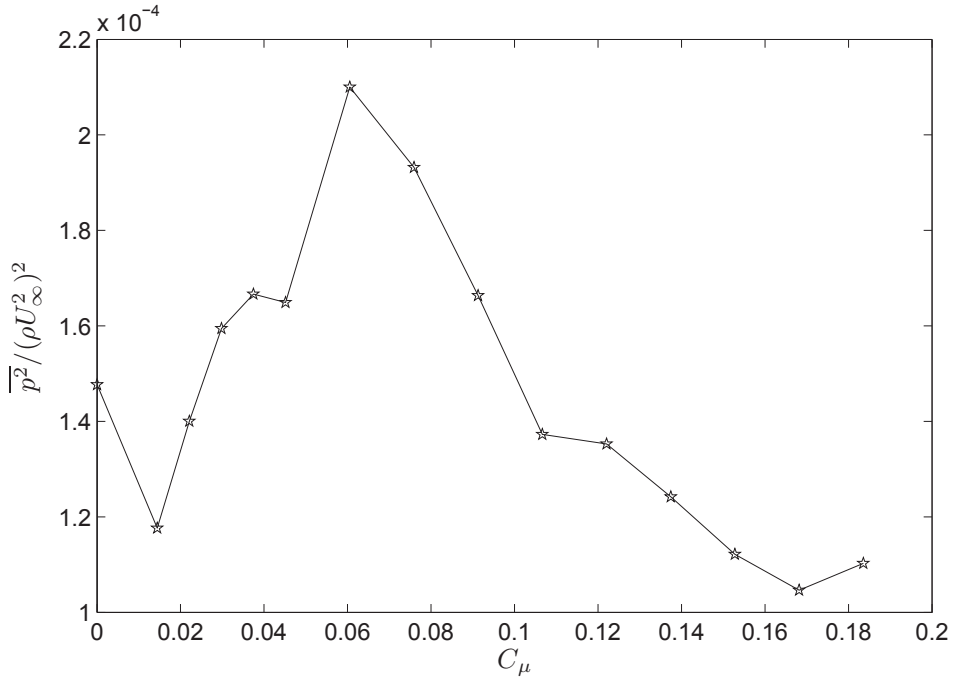

Figure 5.18: Non-weighted spatial-averaged normalised integrated mean-square pressure $\tilde{p} = \overline{p^2}/(\rho U_\infty^2)^2$ as a function of forcing amplitude C_μ (zero corresponds to the baseline case).

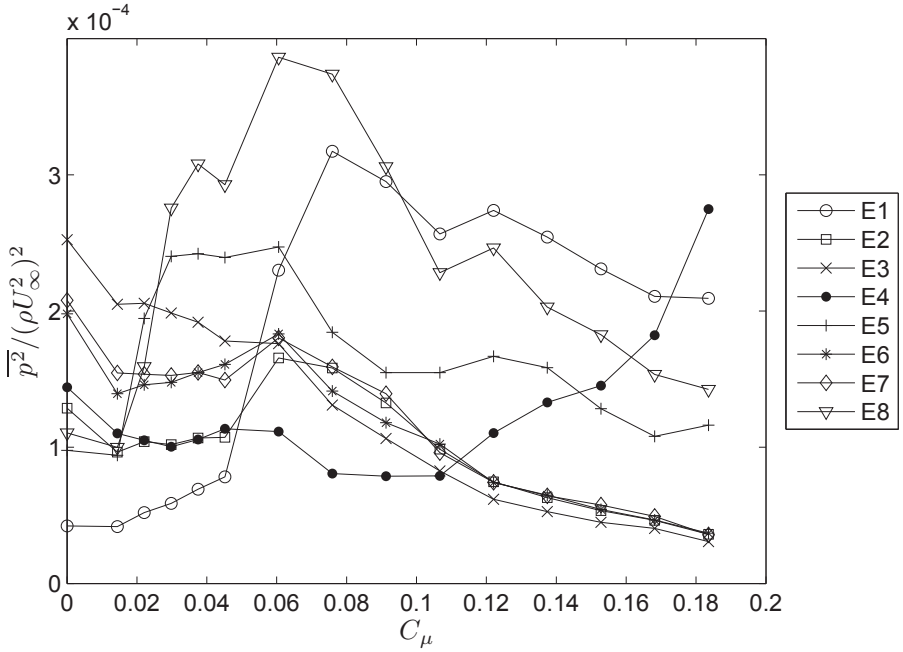

Figure 5.19: Normalised integrated mean-square pressure $\tilde{p} = \overline{p^2}/(\rho U_\infty^2)^2$ by transducer as a function of forcing amplitude C_μ (zero corresponds to the baseline case).

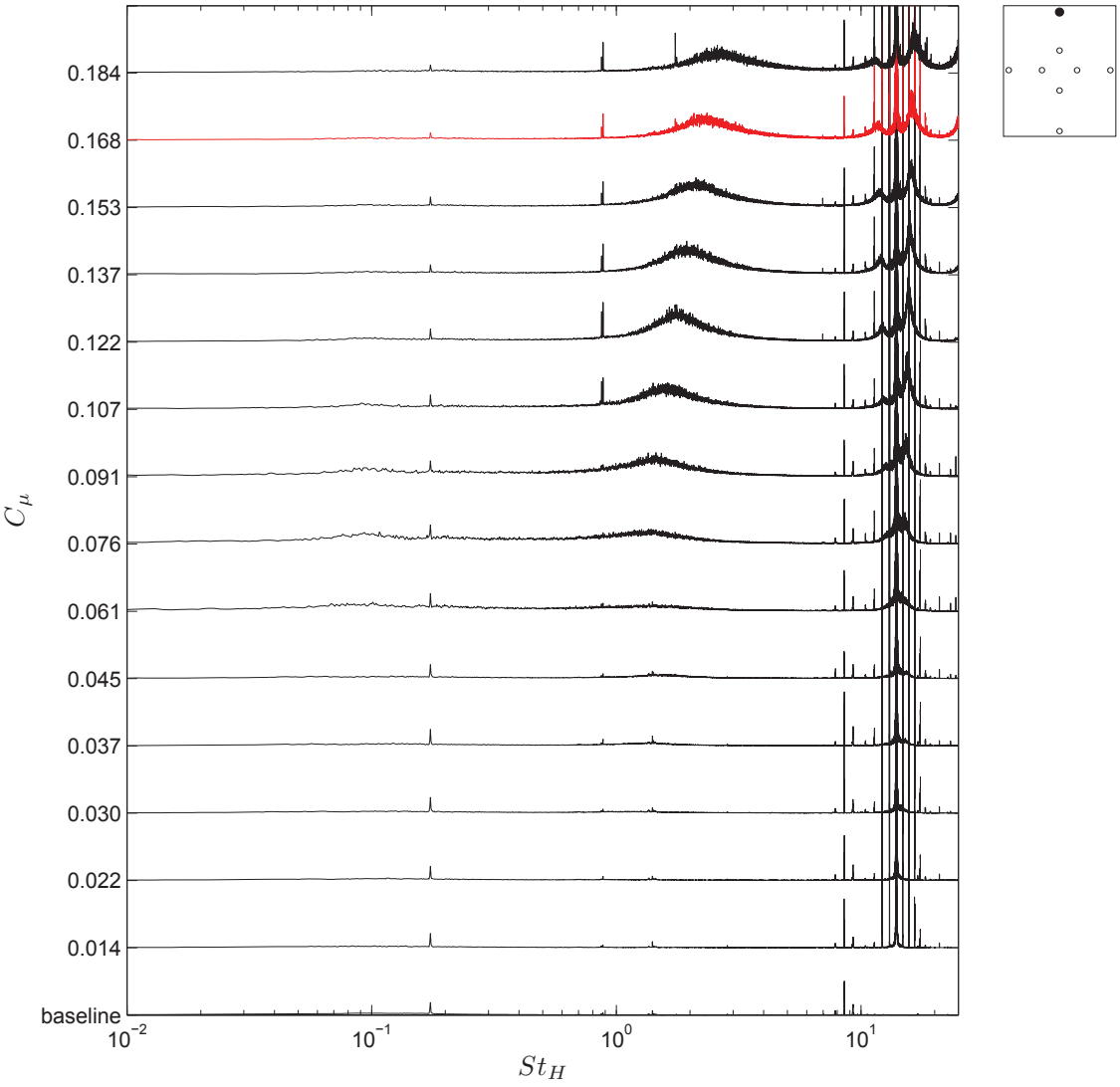

Figure 5.20: Pre-multiplied spectra for dynamic transducer E1 and $St_{Hf} = 13.9$ as a function of $St_H = fH/U_\infty$ and forcing amplitude C_μ. The case of maximum base pressure recovery is plotted in red.

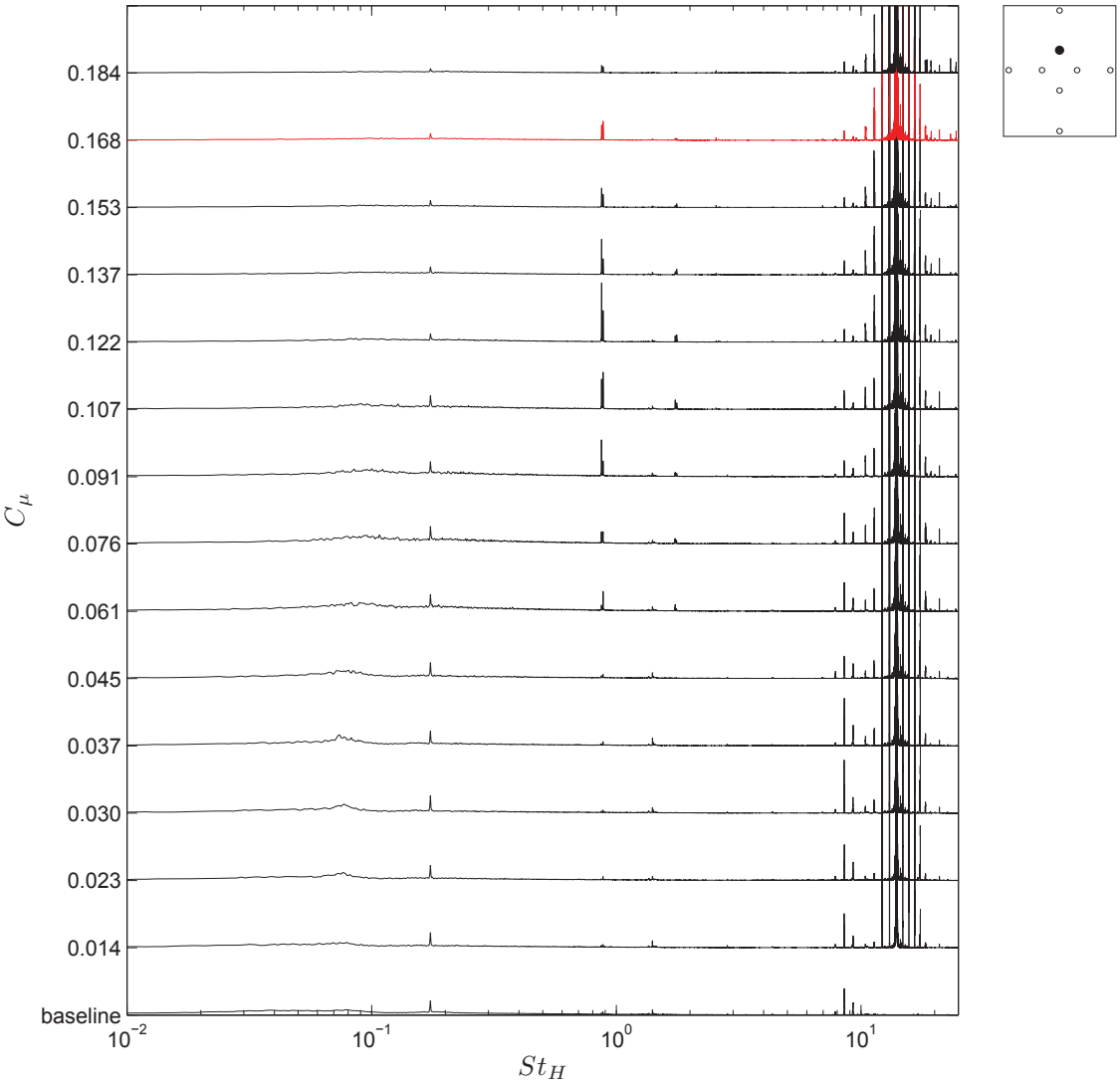

Figure 5.21: Pre-multiplied spectra for dynamic transducer E2 and $St_{Hf} = 13.9$ as a function of $St_H = fH/U_\infty$ and forcing amplitude C_μ. The case of maximum base pressure recovery is plotted in red.

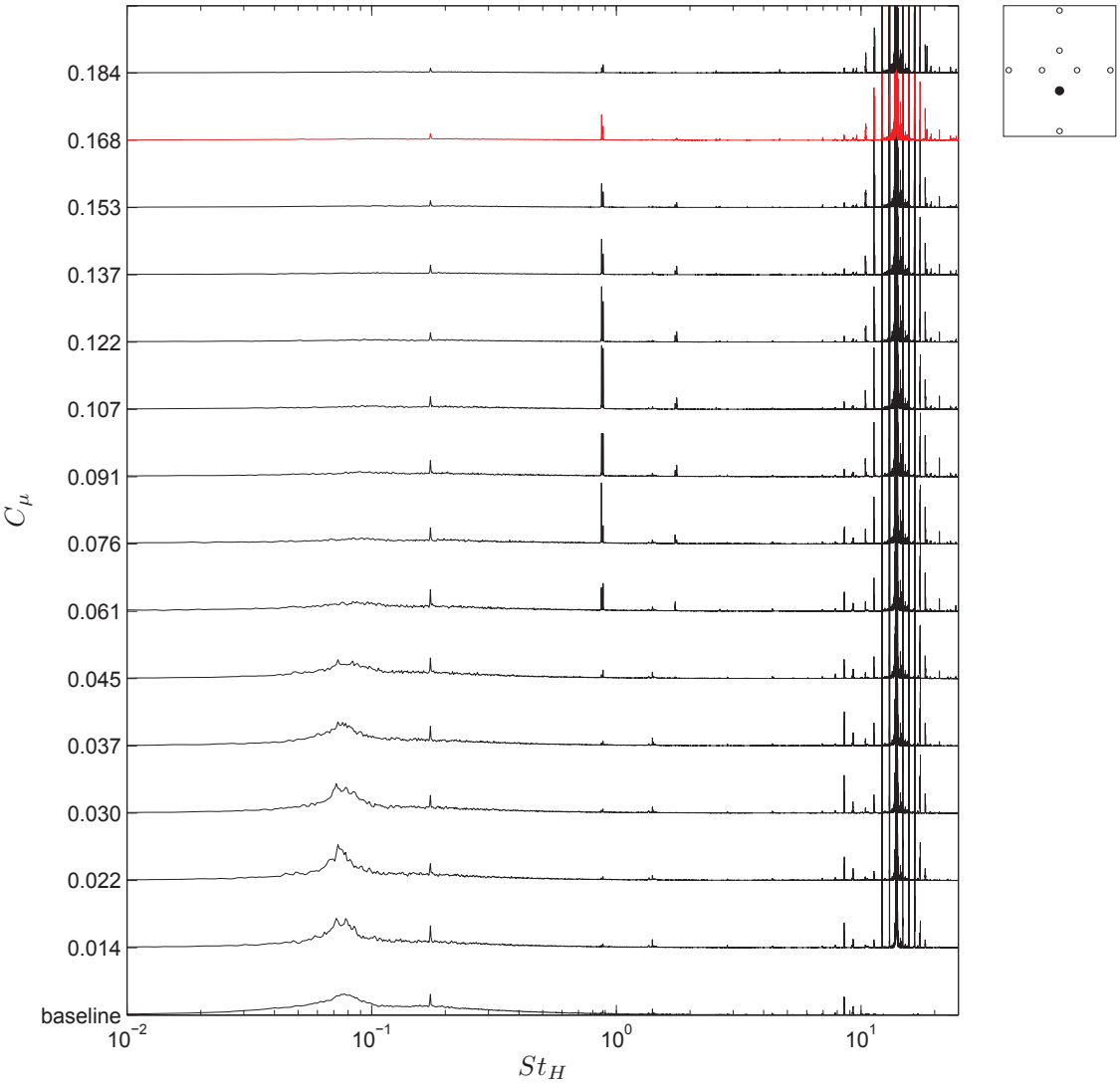

Figure 5.22: Pre-multiplied spectra for dynamic transducer E3 and $St_{Hf} = 13.9$ as a function of $St_H = fH/U_\infty$ and forcing amplitude C_μ. The case of maximum base pressure recovery is plotted in red.

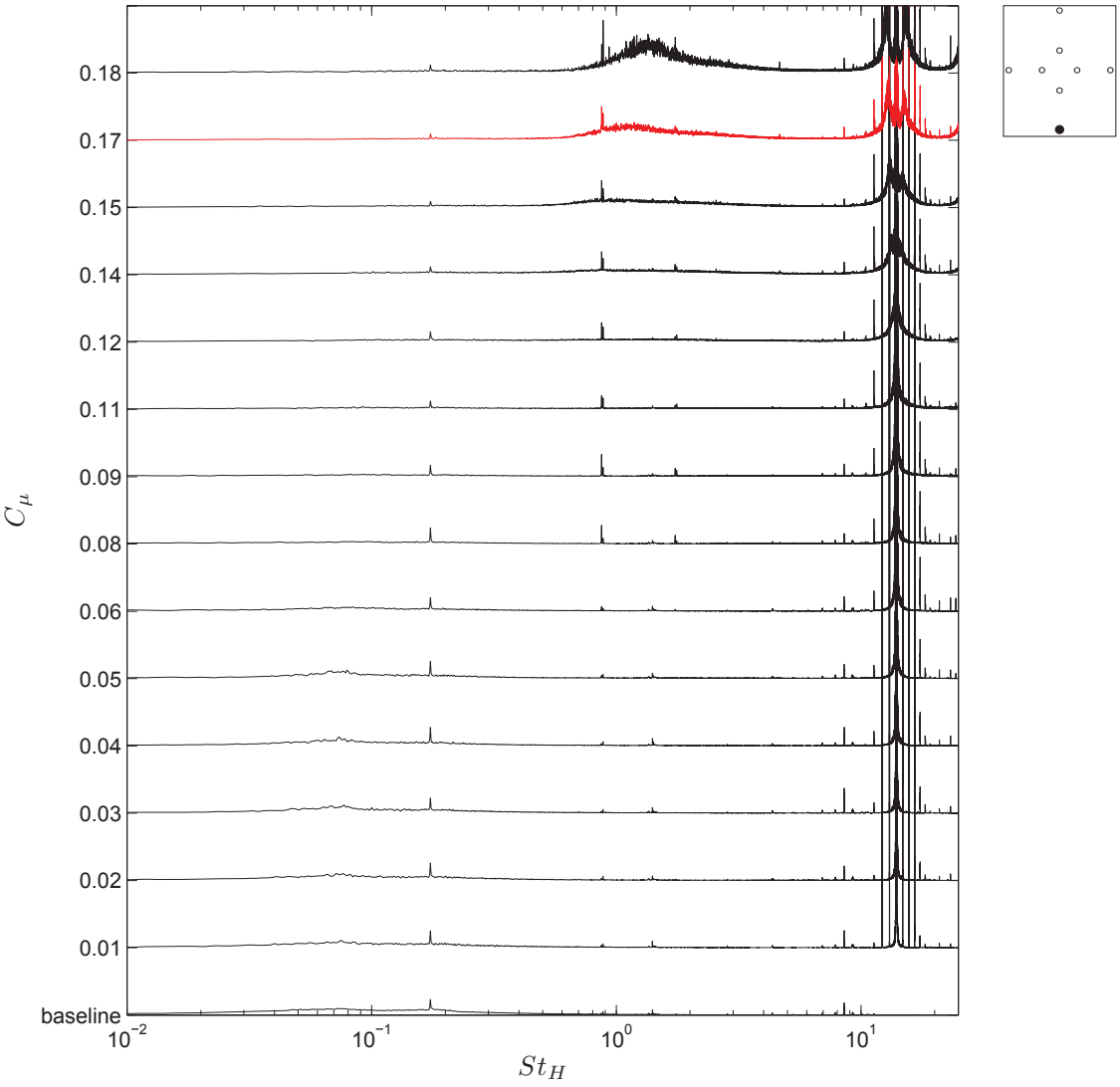

Figure 5.23: Pre-multiplied spectra for dynamic transducer E4 and $St_{Hf} = 13.9$ as a function of $St_H = fH/U_\infty$ and forcing amplitude C_μ. The case of maximum base pressure recovery is plotted in red.

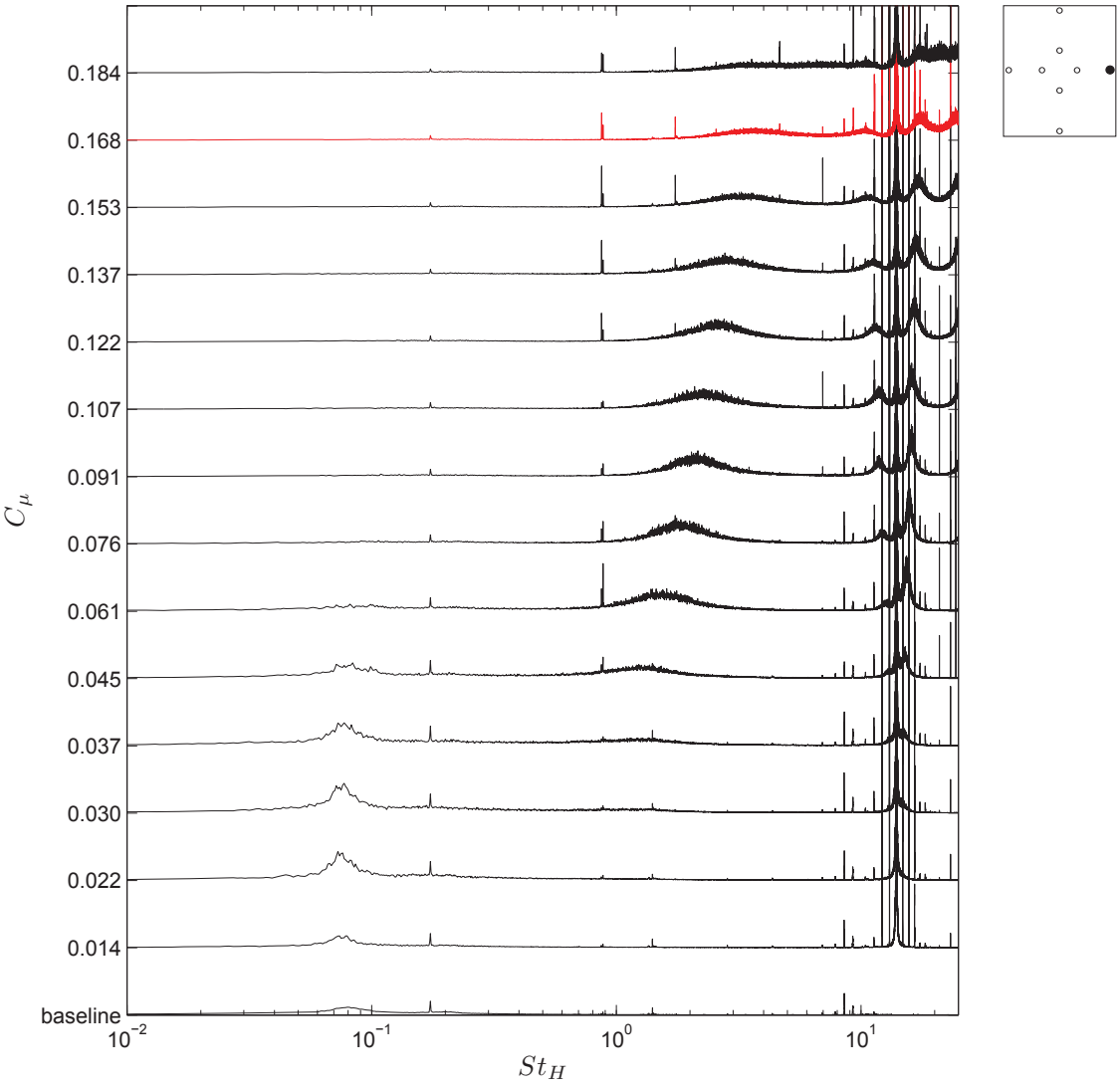

Figure 5.24: Pre-multiplied spectra for dynamic transducer E5 and $St_{Hf} = 13.9$ as a function of $St_H = fH/U_\infty$ and forcing amplitude C_μ. The case of maximum base pressure recovery is plotted in red.

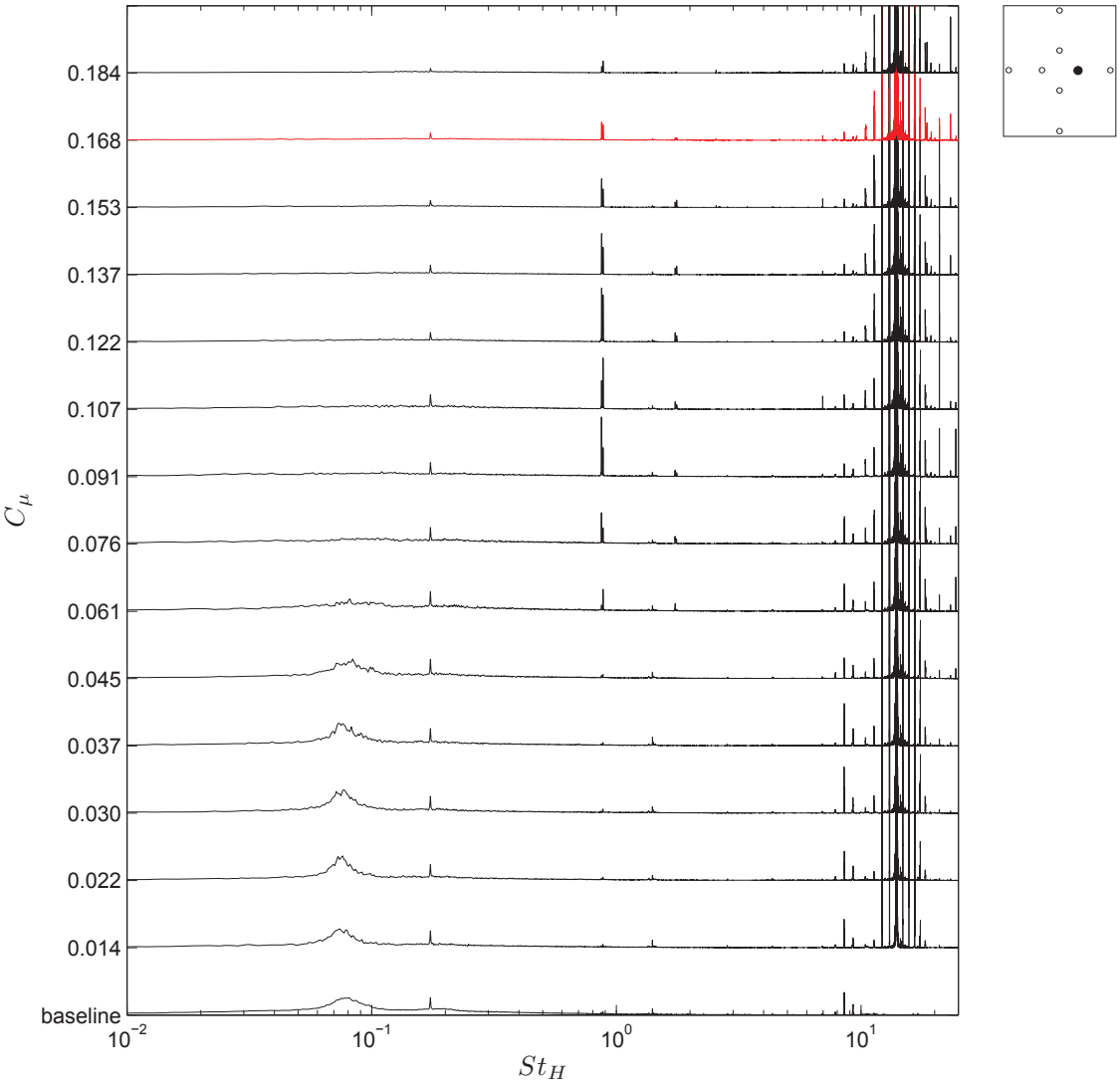

Figure 5.25: Pre-multiplied spectra for dynamic transducer E6 and $St_{Hf} = 13.9$ as a function of $St_H = fH/U_\infty$ and forcing amplitude C_μ. The case of maximum base pressure recovery is plotted in red.

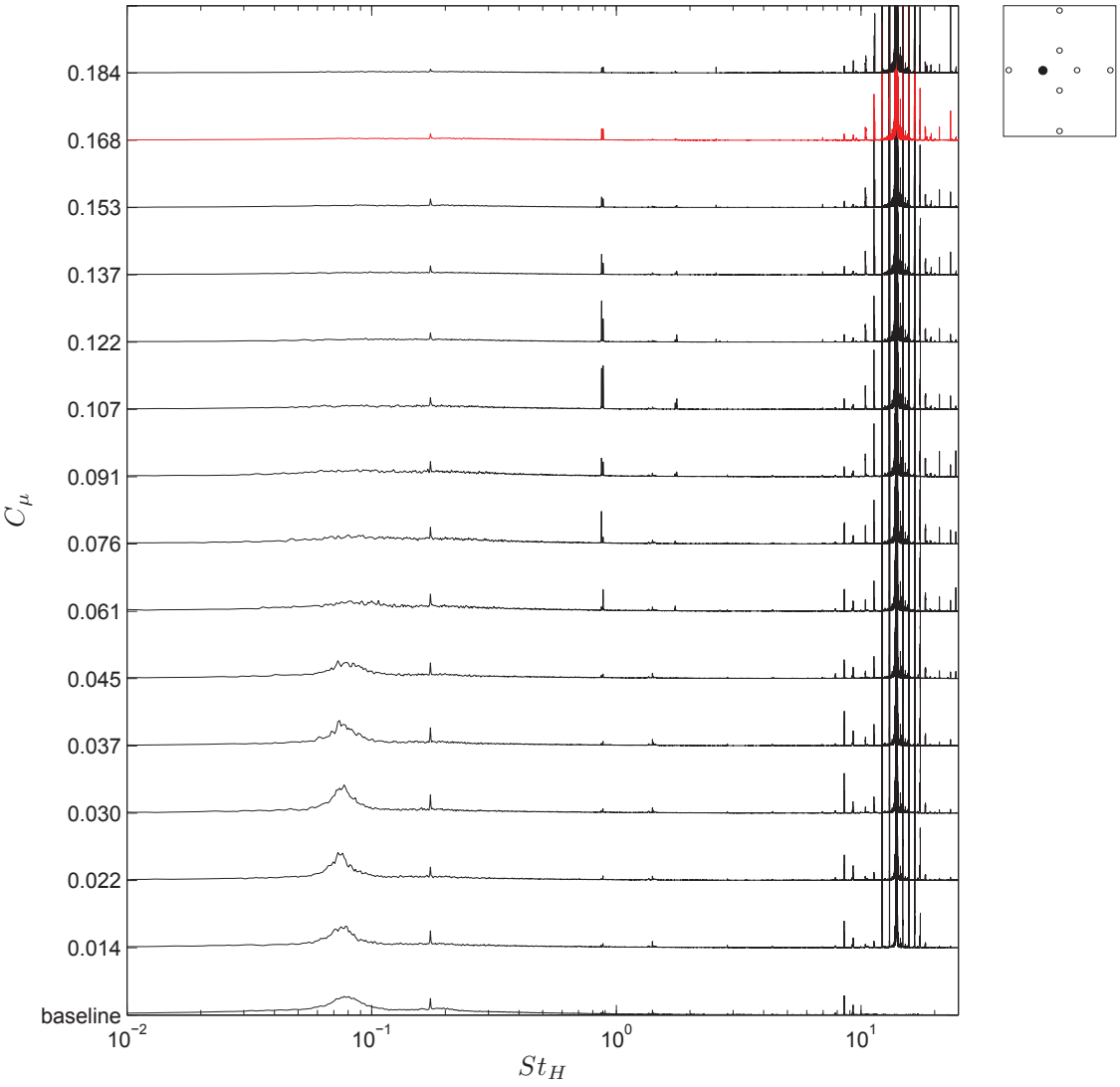

Figure 5.26: Pre-multiplied spectra for dynamic transducer E7 and $St_{Hf} = 13.9$ as a function of $St_H = fH/U_\infty$ and forcing amplitude C_μ. The case of maximum base pressure recovery is plotted in red.

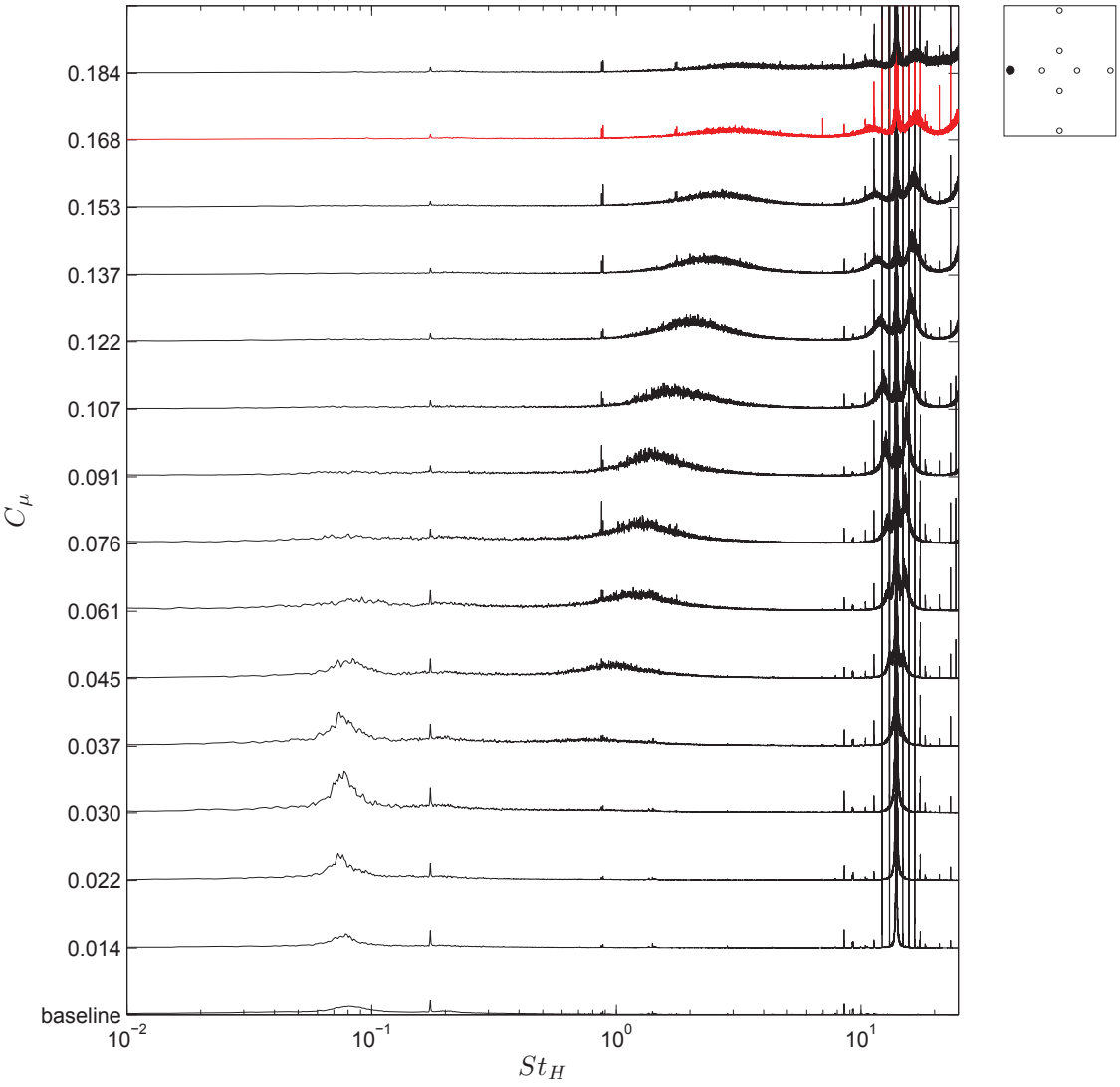

Figure 5.27: Pre-multiplied spectra for dynamic transducer E8 and $St_{Hf} = 13.9$ as a function of $St_H = fH/U_\infty$ and forcing amplitude C_μ. The case of maximum base pressure recovery is plotted in red.

Figures 5.18 and 5.19 show the changes with forcing amplitude of the normalised integrated mean-square pressure $\tilde{p}$ measured by the *Endevco* transducers with forcing amplitude C_μ. The maximum base pressure recovery, at $C_\mu = 0.168$ corresponds to the minimum for the non-weighted spatial-averaged value of $\tilde{p}$. However, base pressure recovery $\Delta C_p/C_{pB}$ (Figure 5.13 (a)) and $\tilde{p}$ show a different behaviour with forcing amplitude C_μ. The values of $\tilde{p}$ for the single transducers (Figure 5.19) show a trend to similar to the spatial-averaged mean-square pressure (Figure 5.18) apart from transducer E4, probably because of the ground effect. It is also interesting to note that the values for the transducers close to the centre of the base (E2, E3, E6 and E7) collapse. As in the previous paragraphs, the forcing energy is not included.

A clearer view of the effects of the forcing amplitude on the dynamics of the wake is given by the evolution of the pre-multiplied spectra from the *Endevco* transducers located on the base. Figure 5.20 displays the changes in the frequency content measured by the transducer located close to the top edge of the base E1. The pumping and the shedding modes ($St_H \approx 0.08$ and $St_H \approx 0.17$), as well as the shear layer mode ($St_H \approx 2$), are perturbed for $C_\mu \geq 0.037$. However, while the low-frequency modes are suppressed by a stronger jet-forcing, the shear layer peak grows in amplitude and moves to a slightly higher frequency with the increasing blowing coefficient. By contrast, transducer E4, located close to the bottom edge (Figure 5.23), shows an amplification of the shear layer ($St_H \approx 1$) for only $C_\mu \geq 0.137$, while the low-frequency modes are weakened for $C_\mu \geq 0.061$. The shear layer frequency is visible also in the spectra from transducers E5 and E8 ($St_H \approx 3$), respectively, those close to the right and left edge shown in Figures 5.24 and 5.27. The low-frequency modes are first amplified, reaching a maximum at $C_\mu = 0.030$; at the same forcing amplitude the shear layer frequency begins to be visible. As opposed to the pumping and shedding modes (see Table 4.2), which are attenuated by higher forcing amplitudes, the shear layer grows in amplitude and frequency with C_μ. Eventually, it decreases and merges with the forcing frequency peak at the highest amplitude. In contrast to all the others, the transducers located closer to the centre of the base (E2, E3, E6 and E7) do not capture any disturbance from the shear layer, and all display a similar behaviour, as can be seen in Figures 5.21, 5.22, 5.25 and

5.26 respectively. Only the low frequency structures of the wake, which are also damped by the forcing, are noticeable in the spectra. Finally, the peaks visible for all transducers for $10 \lesssim St_H \lesssim 10^2$ are caused by the forcing action, equal to $St_{Hf} = 13.9$. As expected, they grow in energy with C_μ.

In contrast to the results of Oxlade (2013), no correlation is found between the amplification of the shear layer frequency and a decrease in the base pressure recovery.

5.4 Response to Changes in Frequency

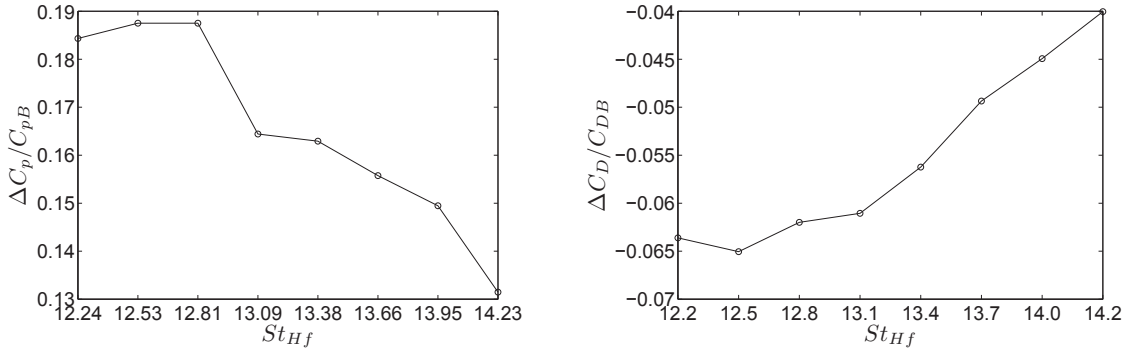

(a) (b)

Figure 5.28: Changes of (a) averaged base pressure $\Delta C_p/C_{pB}$ and (b) drag $\Delta C_D/C_{DB}$ for $C_\mu = 0.061$ as a function of forcing frequency St_{Hf}.

The analysis is conducted comparing forces and pressure results for the various forcing frequencies for a value of the blowing coefficient $C_\mu = 0.061$.

Neither the change in pressure nor the changes in forces and moments show a linear behaviour with frequency. As shown in Figure 5.28, the base pressure recovery shows a maximum at $St_{Hf} = 12.5$ and $St_{Hf} = 12.8$, while the drag reduction has an optimum only at $St_{Hf} = 12.5$. The changes in downforce and pitch moment (Figure 5.29), which are always positive, show their maximum at $St_{Hf} = 12.2$ and minimum at $St_{Hf} = 14.2$, with a local minimum and maximum at $St_{Hf} = 12.8$ and $St_{Hf} = 13.4$, respectively. Lastly, the changes in side force and in roll and

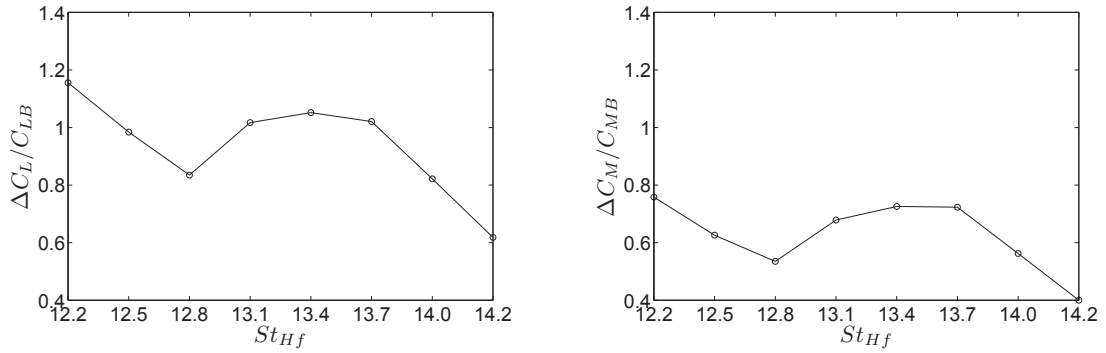

(a) (b)

Figure 5.29: Changes of (a) downforce $\Delta C_L/C_{LB}$ and (b) pitch moment $\Delta C_M/C_{MB}$ for $C_\mu = 0.061$ as a function of forcing frequency St_{Hf}.

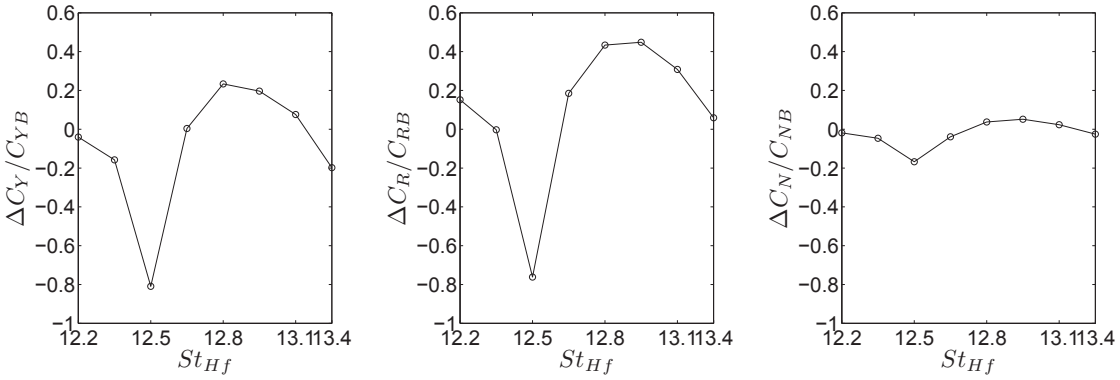

(a) (b) (c)

Figure 5.30: Changes of (a) side force $\Delta C_Y/C_{YB}$, (b) roll moment $\Delta C_R/C_{RB}$ and (c) yaw moment $\Delta C_N/C_{NB}$ for $C_\mu = 0.061$ as a function the forcing frequency St_{Hf}.

yaw moments (Figure 5.30) show a trend similar to downforce and pitch moment, but with the minimum, corresponding also to a decrease, at $St_{Hf} = 12.8$, while an increase is recorded in all of them between $St_{Hf} = 13.4$ and $St_{Hf} = 13.9$.

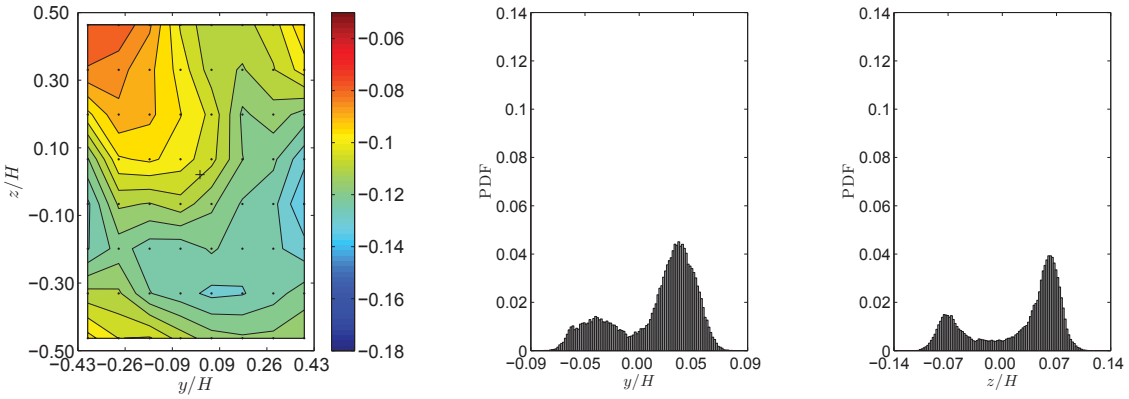

(a) $St_{Hf} = 12.2$

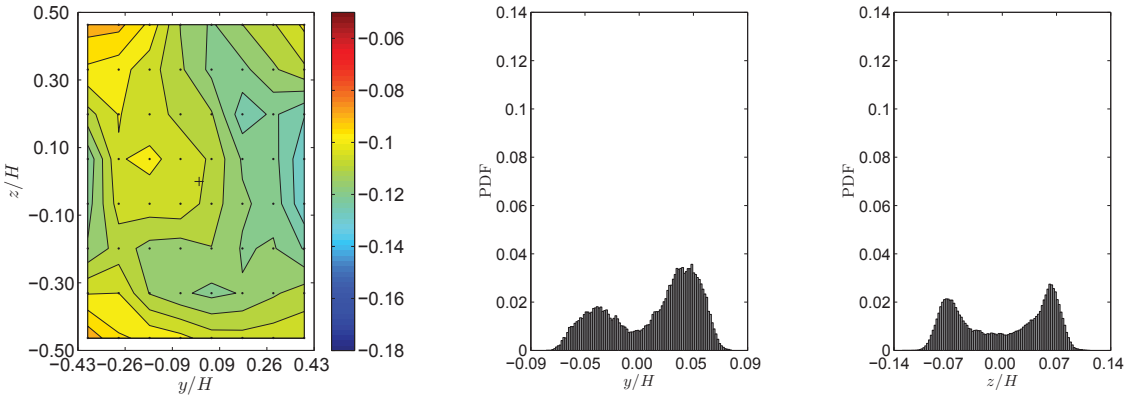

(b) $St_{Hf} = 12.5$

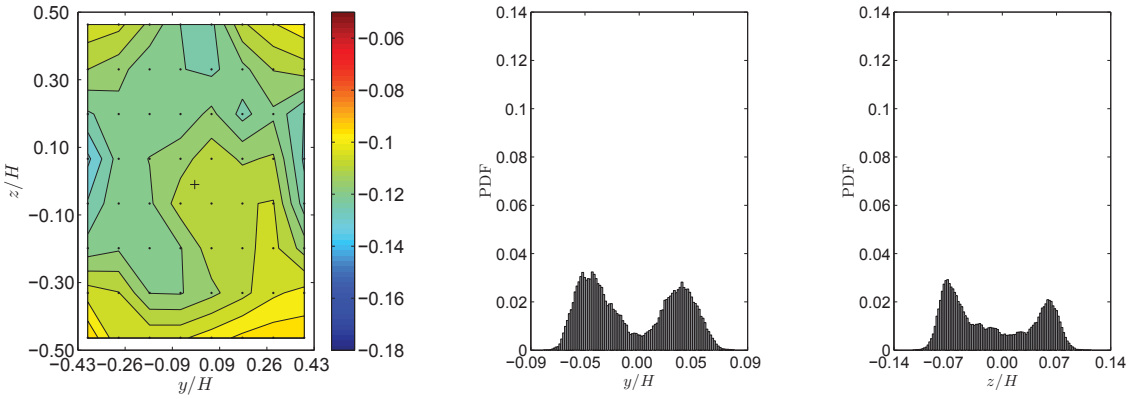

(c) $St_{Hf} = 12.8$

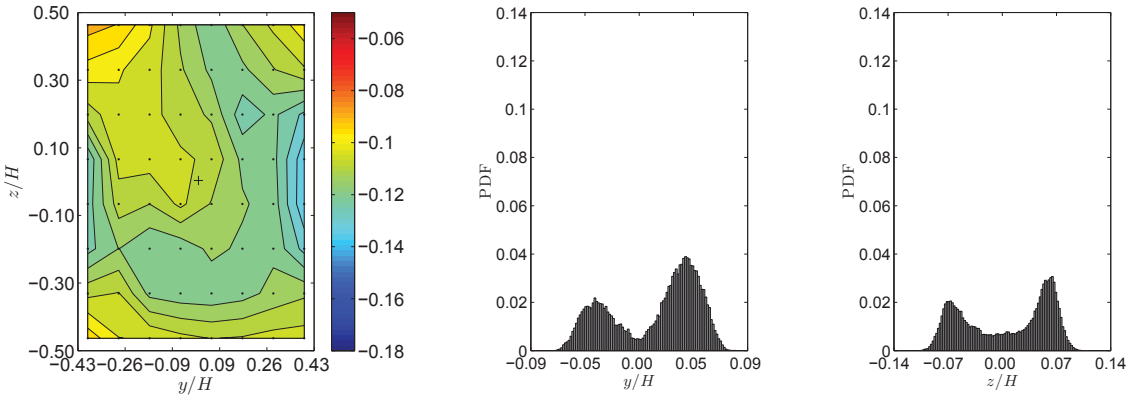

(d) $St_{Hf} = 13.1$

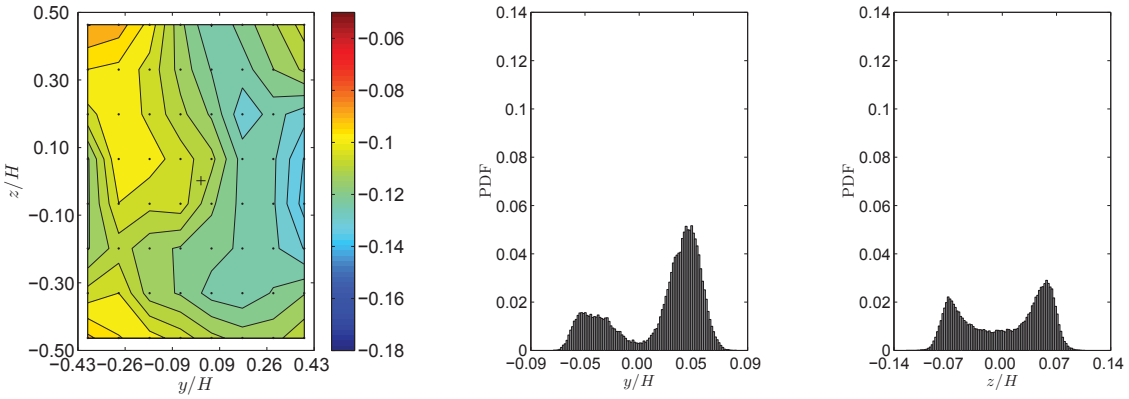

(e) $St_{Hf} = 13.4$

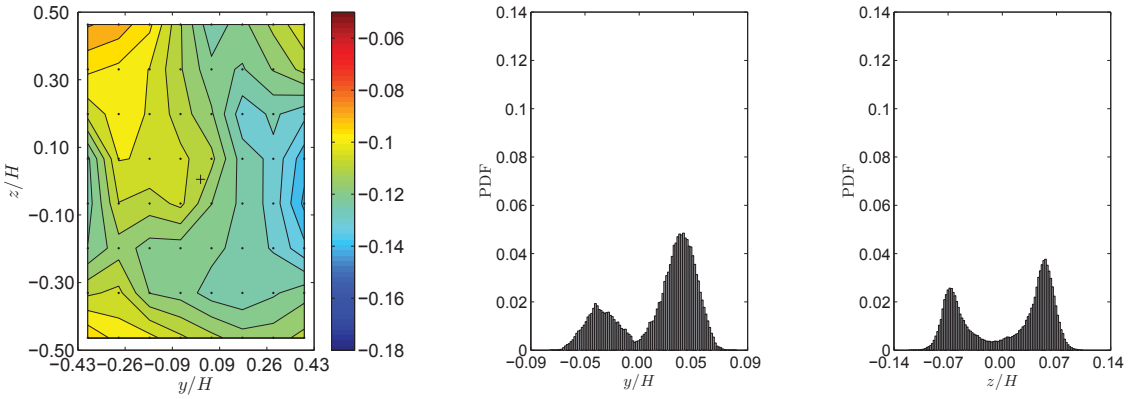

(f) $St_{Hf} = 13.7$

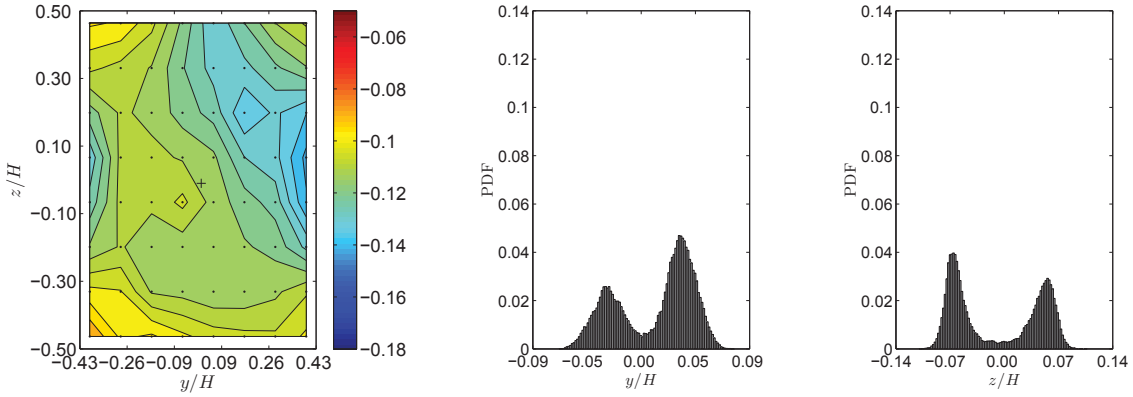

(g) $St_{Hf} = 13.9$

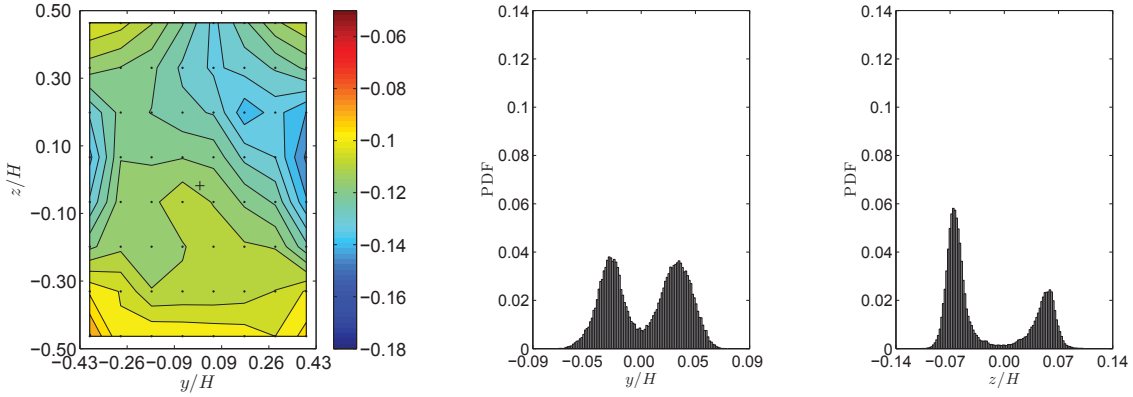

(h) $St_{Hf} = 14.2$

Figure 5.31: C_p contours showing position of centre of pressure (+) (left), PDF of centre of pressure along the y direction (centre) as in Equation 3.4 and z direction (right) as in Equation 3.5. Forcing amplitude $C_\mu = 0.061$.

The base pressure distributions shown in Figure 5.31 look all similar, except for higher values of pressure at the left top corner of the base for $St_{Hf} = 12.2$ and lower values of C_p at the right side af the base for $St_{Hf} = 14.3$. The centre of pressure is central in all cases, with a bimodal behaviour confirmed at all frequencies both in y and z directions (see Table 5.5 and Figure 5.32). Figure 5.32 (a) shows that, as seen before, the mean in the y direction follows the trend shown by side force, roll and yaw moments (Figure 5.30), while the mean in the z direction resembles to the plots of downforce and pitch moment (Figure 5.29). The variance (Figure 5.32 (b)) is high in both directions at all frequencies. The skewness (Figure 5.32

Forcing Frequency St_{Hf}		Mean $\mu \times 10^{-3}$	Variance $\sigma^2 \times 10^{-3}$	Skewness γ	Kurtosis κ
12.2	y	14.6	1.19	-0.80	2.47
	z	20.7	3.15	-0.76	2.07
12.5	y	11.7	1.43	-0.49	1.90
	z	-0.1	3.42	-0.11	1.46
12.8	y	-5.2	1.55	0.15	1.54
	z	-12.4	3.15	0.26	1.56
13.1	y	13.1	1.42	-0.49	1.83
	z	5.0	3.12	-0.23	1.49
13.4	y	18.2	1.37	-0.85	2.28
	z	2.6	2.81	-0.23	1.55
13.7	y	16.5	1.12	-0.76	2.28
	z	5.3	3.14	-0.33	1.46
13.9	y	12.0	1.13	-0.51	1.89
	z	-7.3	3.23	0.06	1.27
14.2	y	4.1	0.98	-0.08	1.63
	z	-23.5	3.04	0.64	1.65

Table 5.5: Statistical moments of the PDF distributions of the position of the centre of pressure for $C_\mu = 0.061$ – see Figure 5.31 – 5.32.

(c)) is around zero, showing the symmetry of the two peaks shown by the bi-modal distributions. Finally, the kurtosis (Figure 5.32 (d)) stays between 1.2 and 2.5.

Figures 5.33 and 5.34 show the limited influence of the forcing frequency on the wake from the point of view of the normalised integrated mean-square pressure $\tilde{p}$. The non-weighted spatial-averaged normalised integrated mean-square pressure (Figure 5.33) stays almost constant apart for $13.4 < St_{Hf} < 13.9$, where it decreases. The lack of correlation between spatial-averaged $\tilde{p}$ and maximum base pressure raise and drag decrease (Figure 5.28) might be due to the forcing amplitude $C_\mu = 0.061$, which has been shown in Paragraph 5.3 to establish a peculiar wake structure. The minimum at $St_{Hf} \approx 13.7$ could be due to the resonance of the actuator, found at $St_{Hf} = 13.5$. The values of $\tilde{p}$ for the single transducers (Figure 5.34) show again

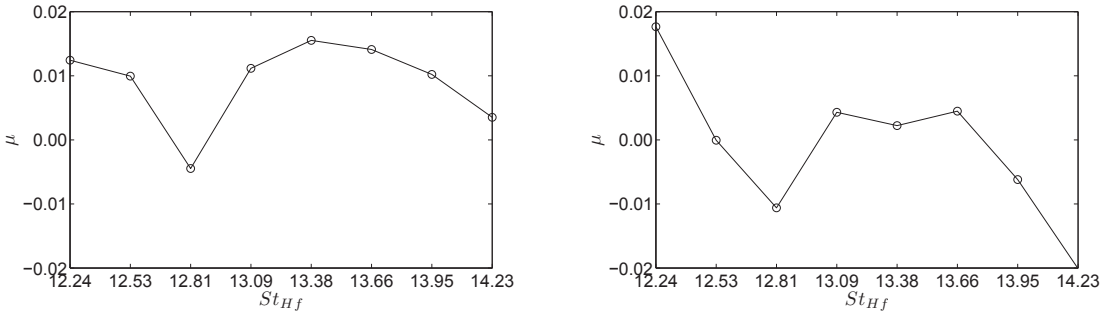

(a) mean in the y direction (left) and z direction (right)

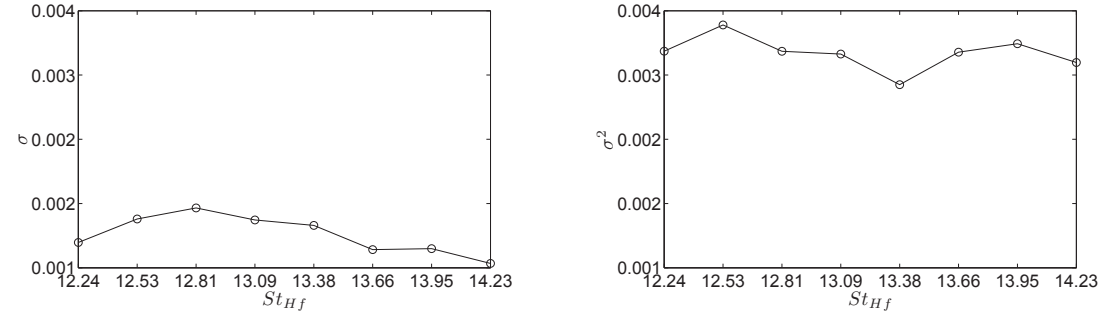

(b) variance in the y direction (left) and z direction (right)

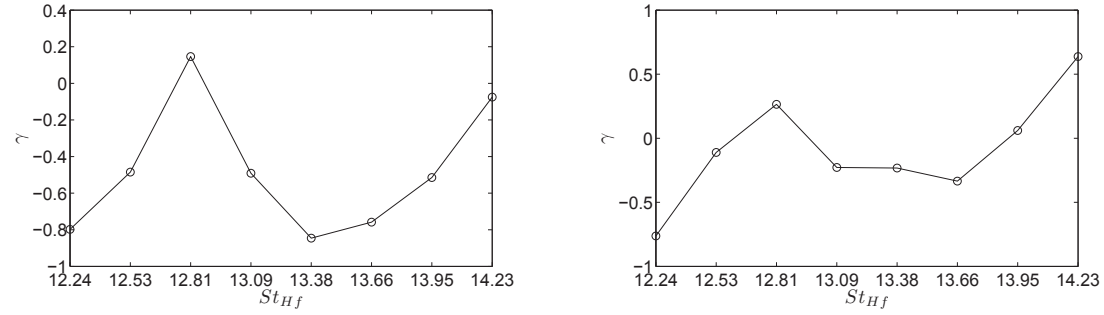

(c) skewness in the y direction (left) and z direction (right)

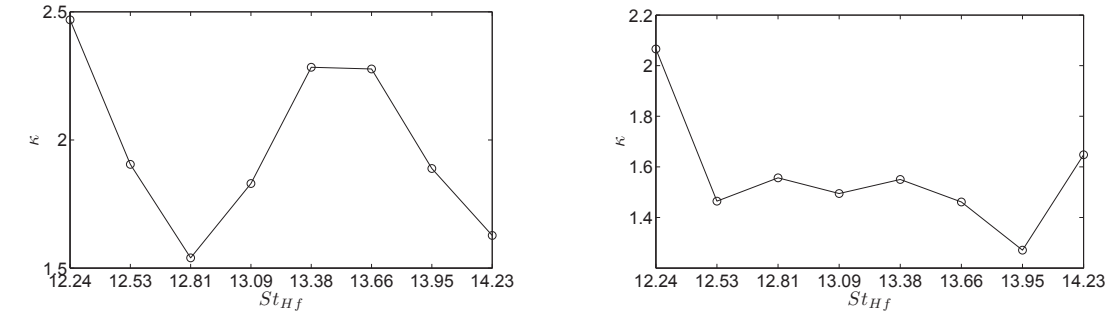

(d) kurtosis in the y direction (left) and z direction (right)

Figure 5.32: Statistical moments of the position of the centre of pressure in the y (left) and z (right) directions as a function of St_{Hf} for $C_\mu = 0.061$.

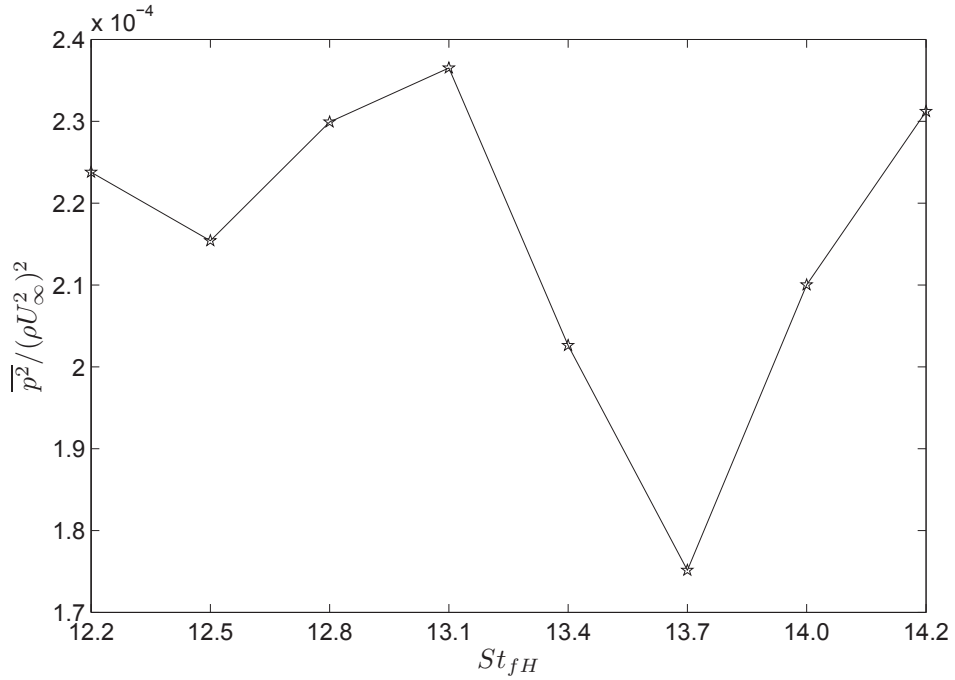

Figure 5.33: Non-weighted spatial-averaged normalised integrated mean-square pressure $\tilde{p} = \overline{p^2}/(\rho U_\infty^2)^2$ as a function of forcing frequency St_{Hf}.

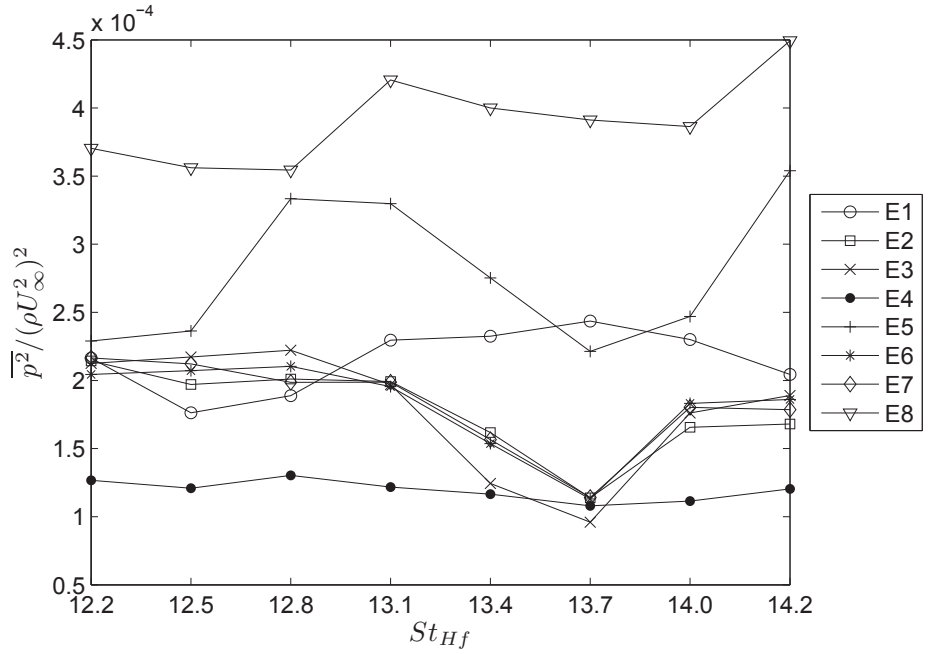

Figure 5.34: Normalised integrated mean-square pressure $\tilde{p} = \overline{p^2}/(\rho U_\infty^2)^2$ by transducer as a function of forcing frequency St_{Hf}.

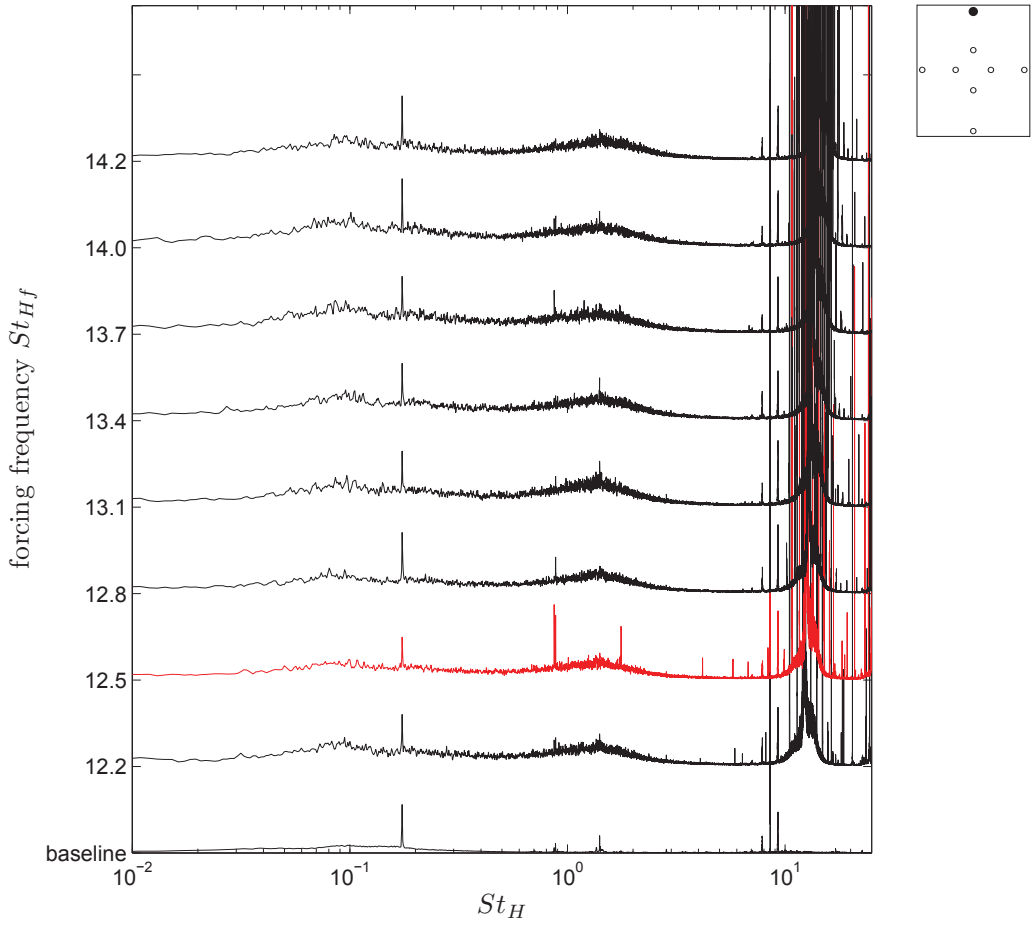

Figure 5.35: Pre-multiplied spectra from dynamic transducer E1 as a function of $St_H = fH/U_\infty$ and forcing frequency St_{Hf}. The case of maximum base pressure recovery ($\Delta C_p/C_{pB} = 0.188 \pm 0.005$) is plotted in red.

little variation with St_{Hf}; as seen before, the values for the transducers close to the centre of the base (E2, E3, E6 and E7) collapse.

The spectral analysis shows that for all forcing frequencies the amplitude of the low frequency modes is reduced (Figures 5.35 – 5.42). The figures largely reproduce the information deduced from the previous section:

- The bubble-pumping mode is found at $St_H \approx 0.08$ in all spectra.
- The vortex-shedding, is visible at $St_H \approx 0.17$ for the vertical plane (E1, E2, E3 and E4) and at $St_H \approx 0.20$ for the horizontal plane (E5, E6, E7 and E8).

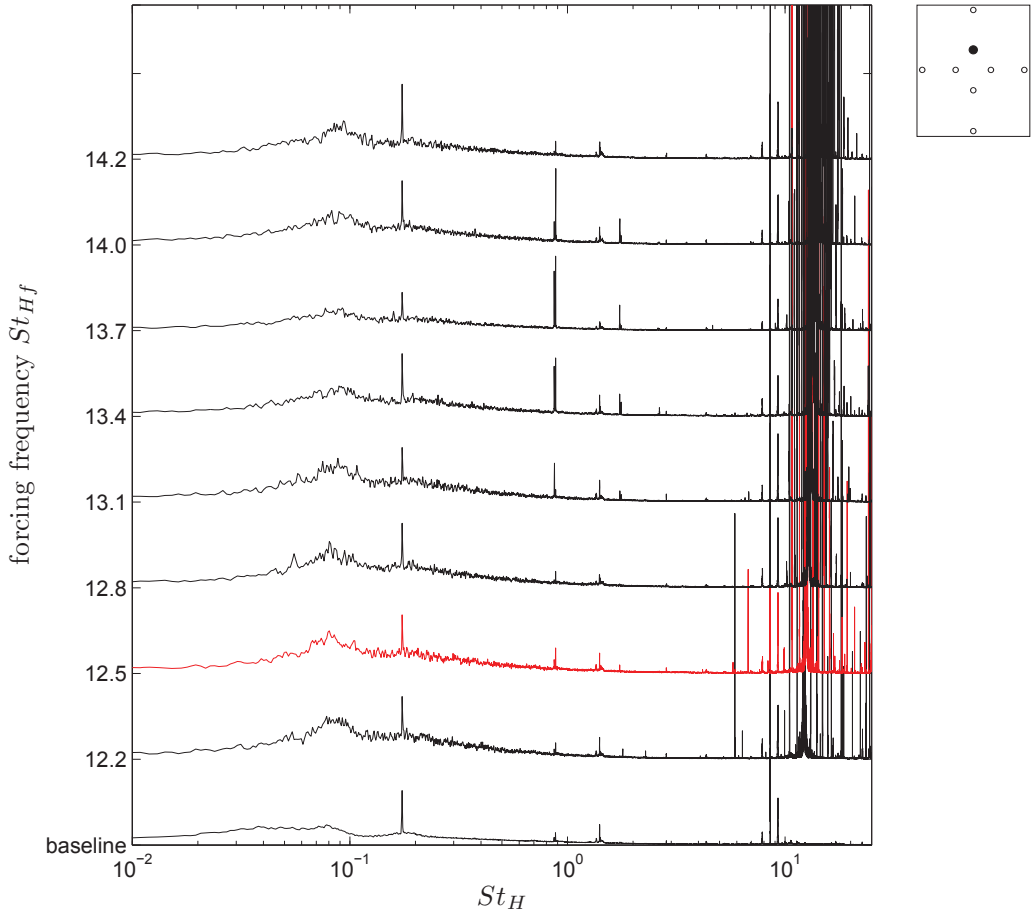

Figure 5.36: Pre-multiplied spectra from dynamic transducer E2 as a function of $St_H = fH/U_\infty$ and forcing frequency St_{Hf}. The case of maximum base pressure recovery ($\Delta C_p/C_{pB} = 0.188 \pm 0.005$) is plotted in red.

- The shear layer, found in the range from $St_H \approx 1.2$ – 3.7, is amplified by the forcing and is visible only for the transducers close to the sides.

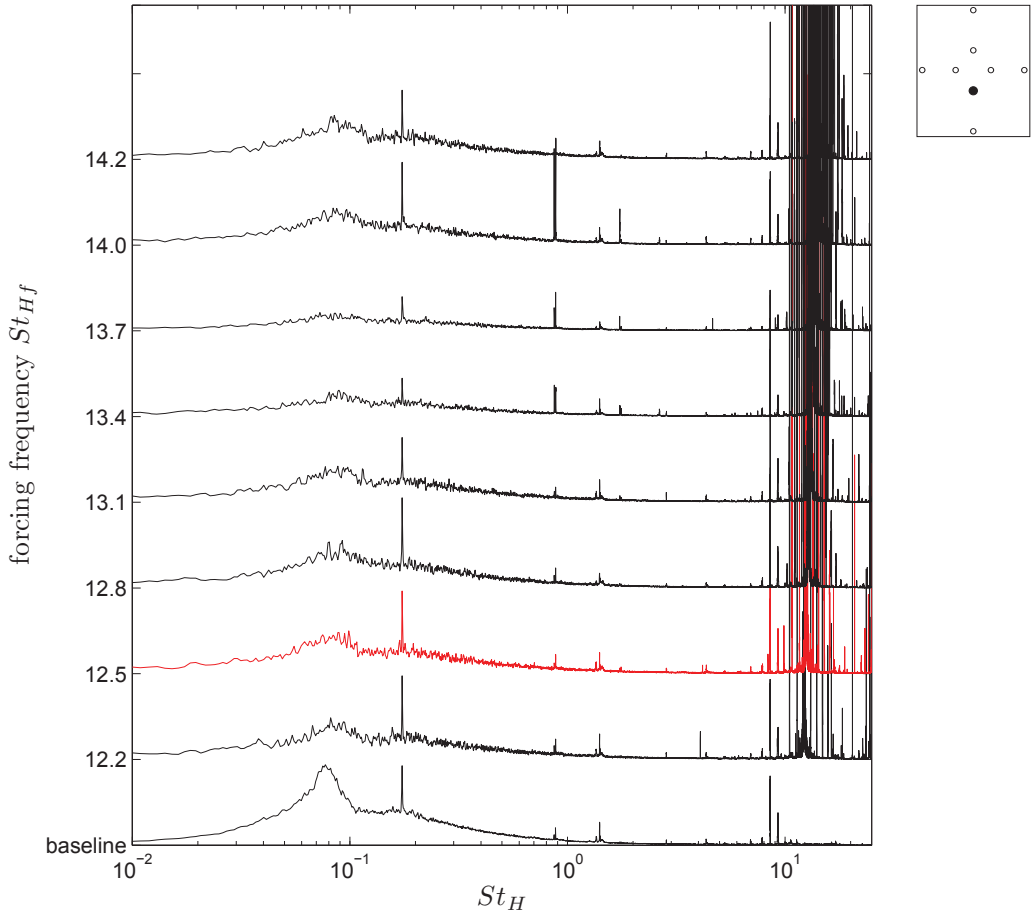

Figure 5.37: Pre-multiplied spectra from dynamic transducer E3 as a function of $St_H = fH/U_\infty$ and forcing frequency St_{Hf}. The case of maximum base pressure recovery ($\Delta C_p/C_{pB} = 0.188 \pm 0.005$) is plotted in red.

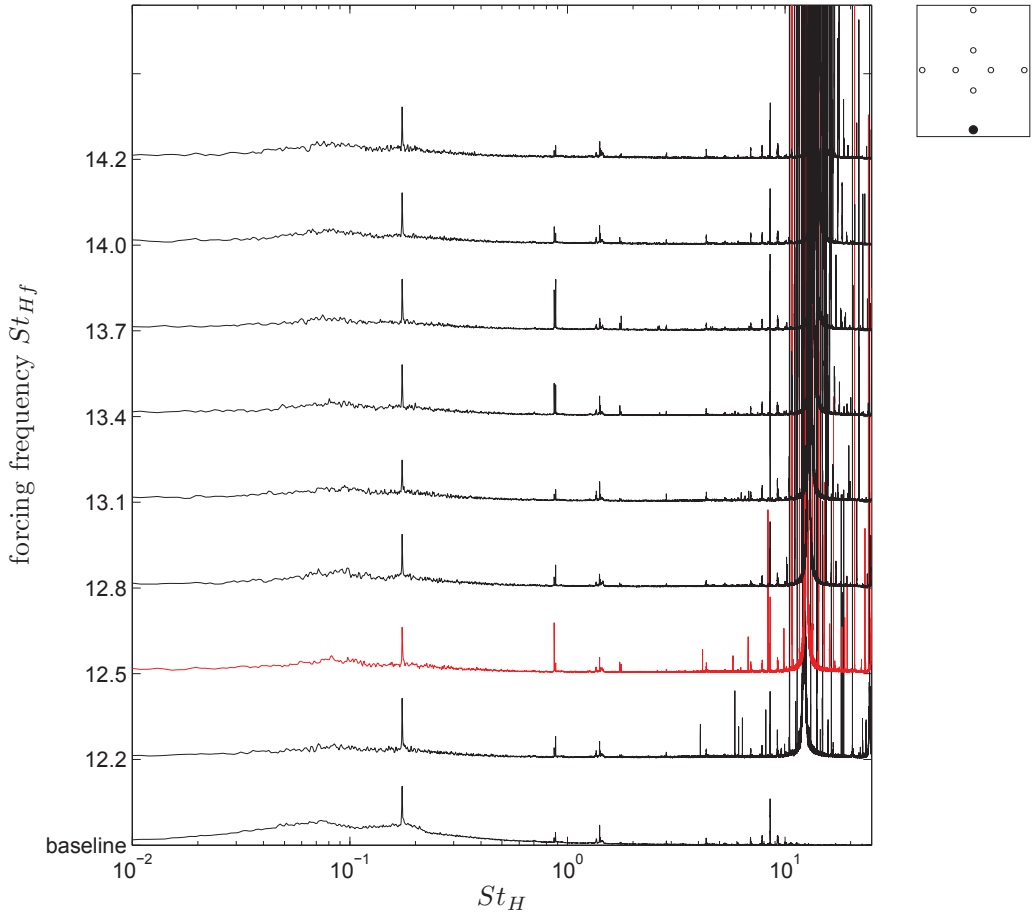

Figure 5.38: Pre-multiplied spectra from dynamic transducer E4 as a function of $St_H = fH/U_\infty$ and forcing frequency St_{Hf}. The case of maximum base pressure recovery ($\Delta C_p/C_{pB} = 0.188 \pm 0.005$) is plotted in red.

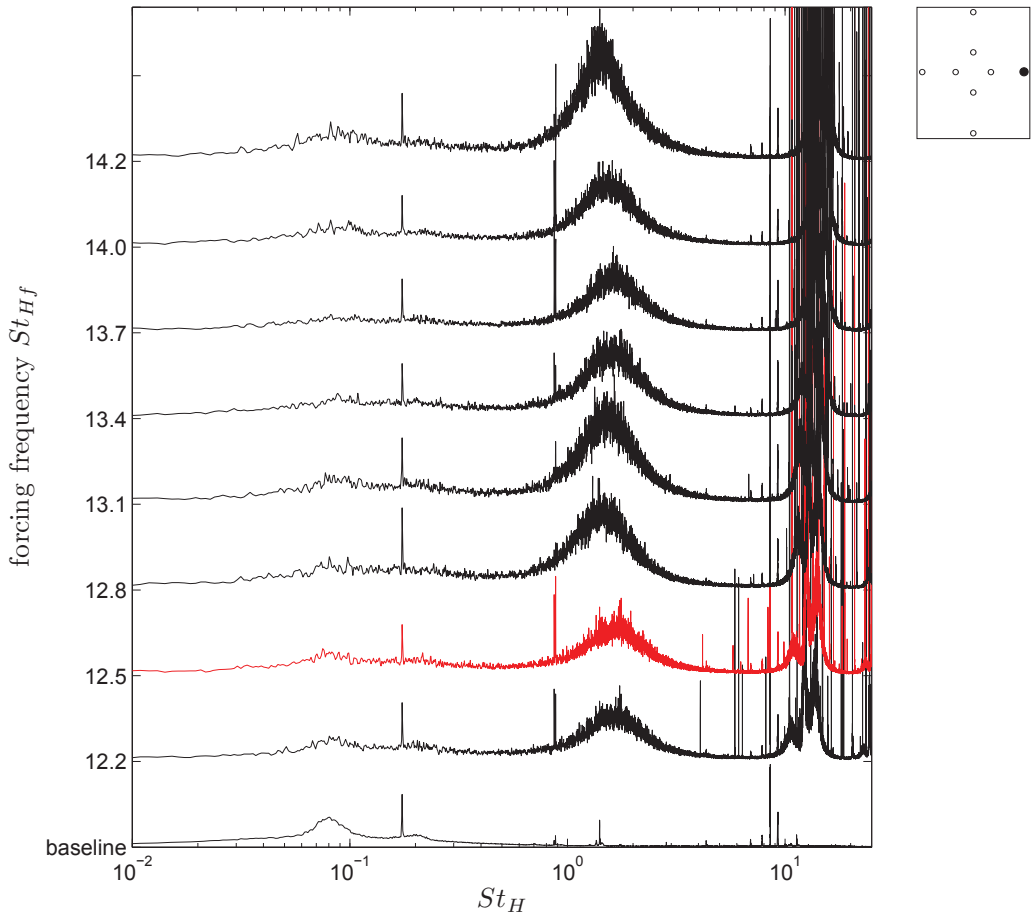

Figure 5.39: Pre-multiplied spectra from dynamic transducer E5 as a function of $St_H = fH/U_\infty$ and forcing frequency St_{Hf}. The case of maximum base pressure recovery ($\Delta C_p/C_{pB} = 0.188 \pm 0.005$) is plotted in red.

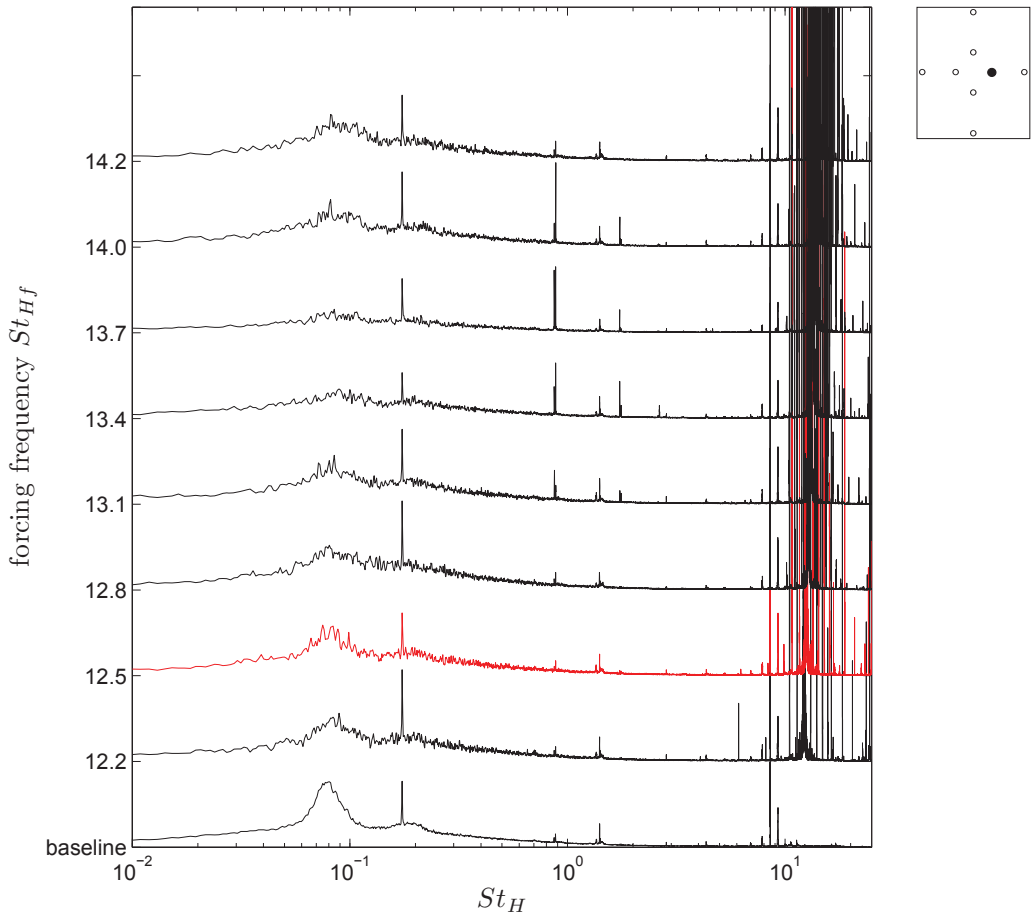

Figure 5.40: Pre-multiplied spectra from dynamic transducer E6 as a function of $St_H = fH/U_\infty$ and forcing frequency St_{Hf}. The case of maximum base pressure recovery ($\Delta C_p/C_{pB} = 0.188 \pm 0.005$) is plotted in red.

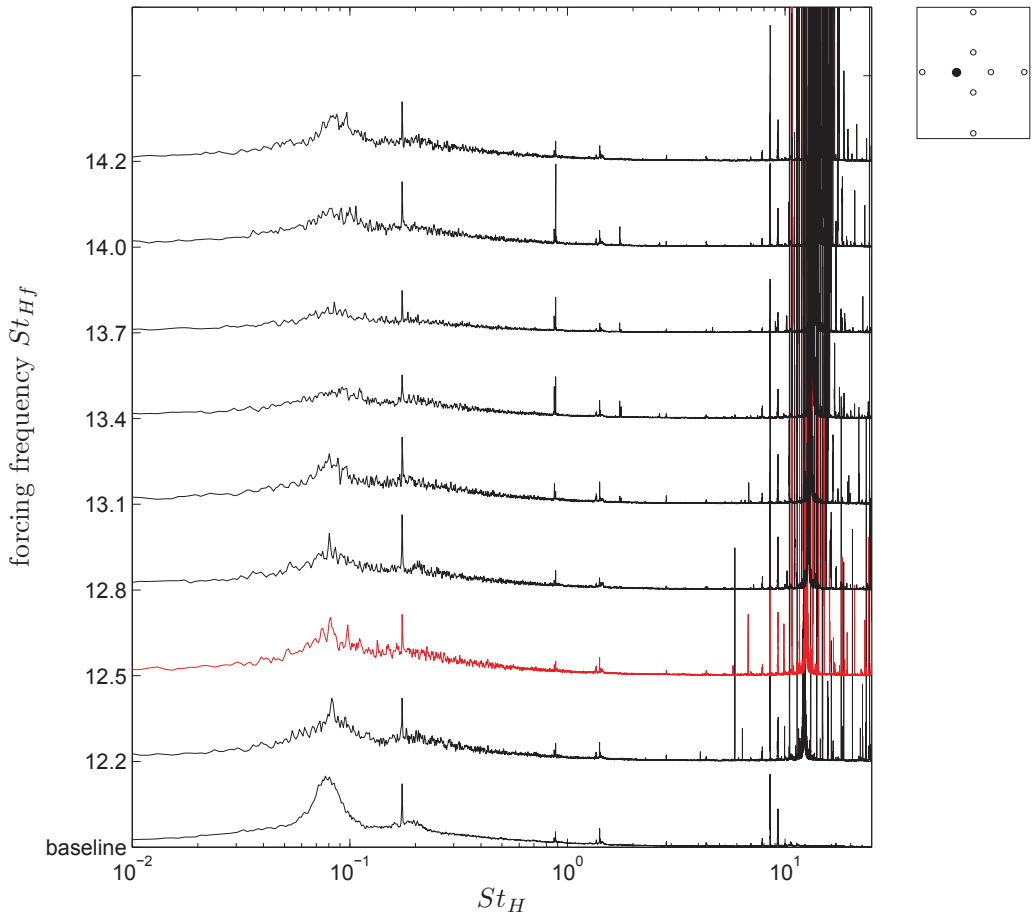

Figure 5.41: Pre-multiplied spectra from dynamic transducer E7 as a function of $St_H = fH/U_\infty$ and forcing frequency St_{Hf}. The case of maximum base pressure recovery ($\Delta C_p/C_{pB} = 0.188 \pm 0.005$) is plotted in red.

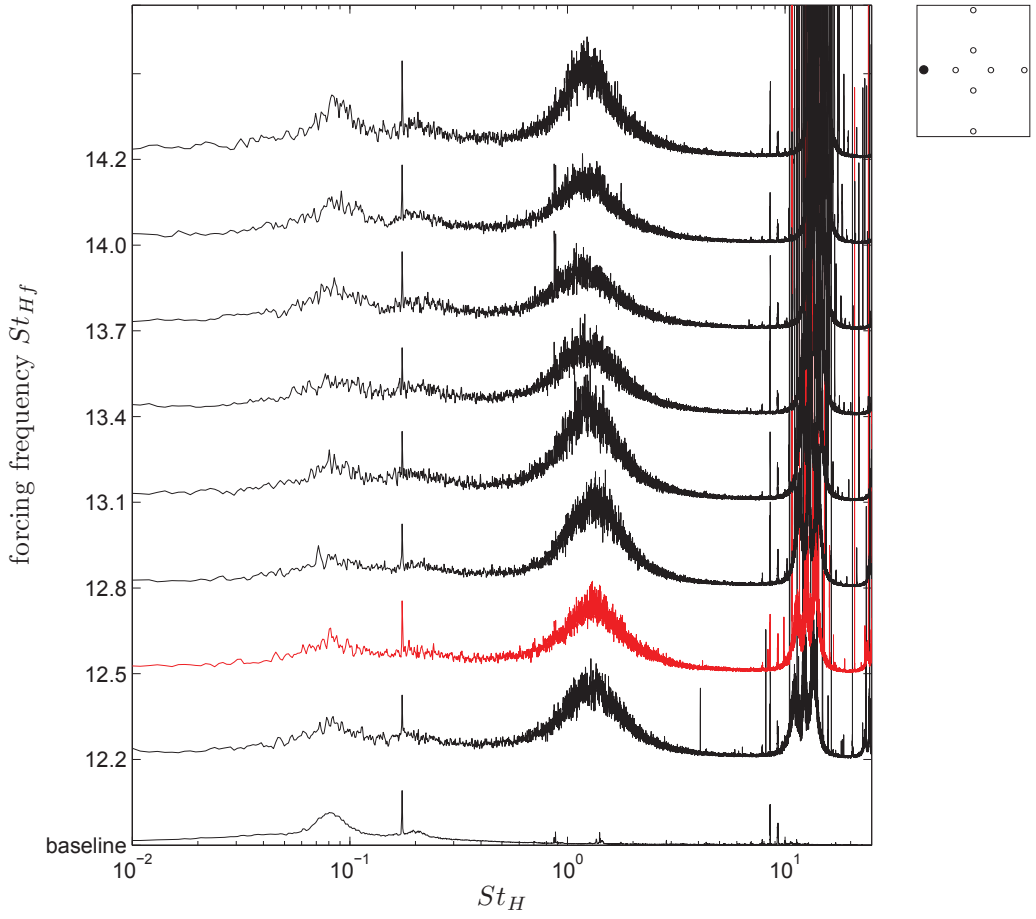

Figure 5.42: Pre-multiplied spectra from dynamic transducer E8 as a function of $St_H = fH/U_\infty$ and forcing frequency St_{Hf}. The case of maximum base pressure recovery ($\Delta C_p/C_{pB} = 0.188 \pm 0.005$) is plotted in red.

Chapter 6

Effect of Slot Width

The experiment was repeated with two more slots of different widths (3.5 mm and 5.5 mm) in order to investigate any influence of the slot width on base pressure recovery and drag reduction. The experiments were run at two frequencies, $St_{Hf} = 12.8$ and $St_{Hf} = 13.4$ (450 Hz and 470 Hz), those frequencies at which the actuator can still produce an effective jet. The samples were 100 s long. Each forced sample was repeated four times, for a total of about 5 hours and 39 minutes (6 minutes and 40 seconds per point), enough to converge the mean pressure distribution and the balance readings. The baseline samples were repeated 10 times for each slot, for a total of 32 minutes and 80 seconds. This comparison of the results allows the identification of the 4.5 mm slot as the optimal one.

6.1 Comparison of Slot Widths

6.1.1 Baseline

The comparison of baseline base pressure distribution and position of the centre of pressure for the three slot sizes tested during the experiments is shown in Figure 6.1 and Table 6.1. As can be seen from the data, no significant difference is found, as indicated by the value of the averaged base pressure, equal to -0.137 ± 0.003 for the 3.5 mm wide slot, -0.133 ± 0.002 for 4.5 mm, and -0.137 ± 0.002 for 5.5 mm. The position of the centre of pressure, as shown by the mean in Table 6.1,

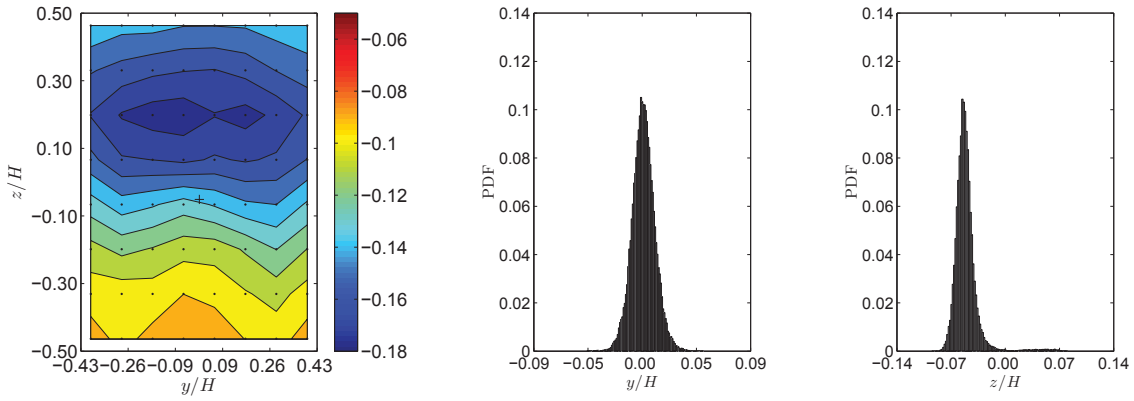

(a) 3.5 mm

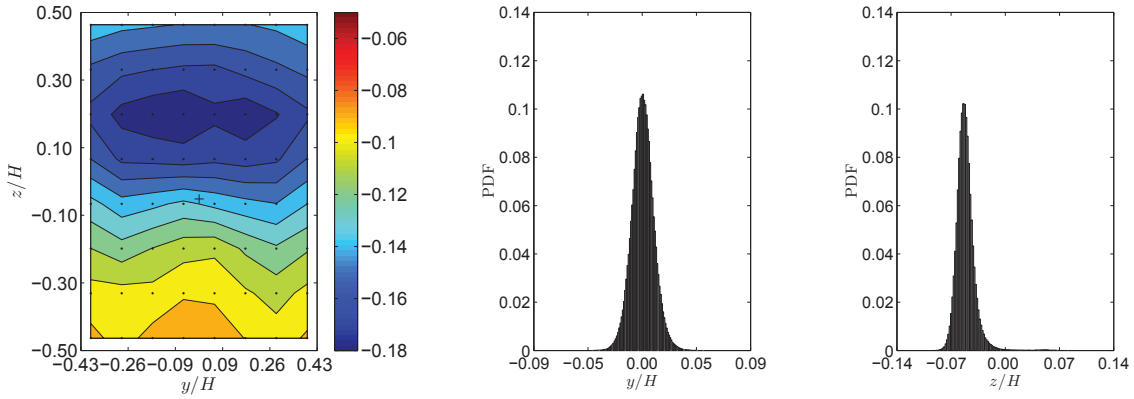

(b) 4.5 mm

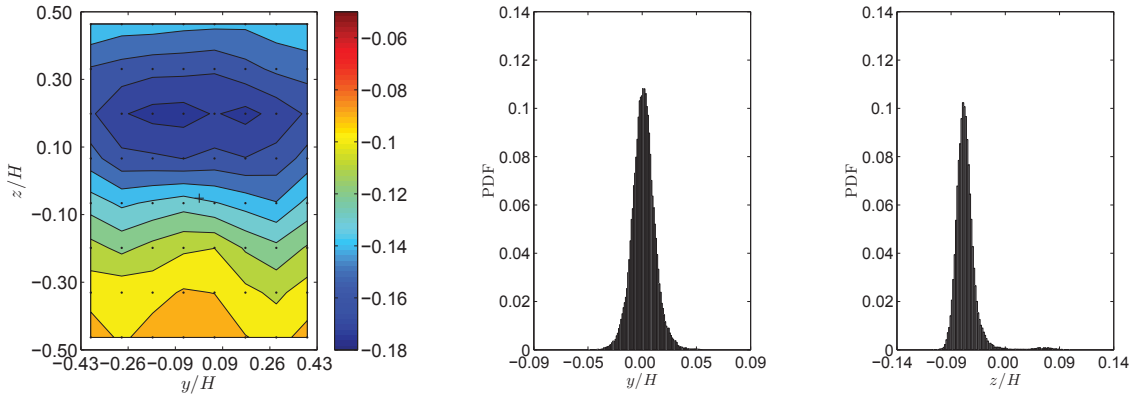

(c) 5.5 mm

Figure 6.1: C_p contours showing position of centre of pressure (+) (left), PDF of centre of pressure along the y direction (centre) as in Equation 3.4 and z direction (right) as in Equation 3.5 for (a) 3.5 mm slot, (b) 4.5 mm slot and (c) 5.5 mm slot. Baseline case.

Slot size (mm)	Pressure Coefficient C_p		Mean $\mu \times 10^{-3}$	Variance $\sigma^2 \times 10^{-3}$	Skewness γ	Kurtosis κ
3.5	-0.137 ± 0.003	y	1.2	0.10	0.08	3.8
		z	-51.1	0.26	3.59	23.2
4.5	-0.133 ± 0.002	y	0.6	0.09	0.12	3.7
		z	-51.6	0.02	2.48	19.4
5.5	-0.137 ± 0.002	y	1.2	0.10	0.17	4.2
		z	-51.1	0.02	3.54	24.0

Table 6.1: Averaged base pressure coefficient and statistical moments of the PDF distributions of the position of the centre of pressure for the baseline cases – see Figure 6.1.

	Value	Uncertainty %
Downforce coefficient (C_L)	0.032	±0.122
Drag coefficient (C_D)	0.259	±0.026
Side force coefficient (C_Y)	0.013	±0.056
Pitch coefficient (C_M)	-0.021	±0.005
Roll coefficient (C_R)	0.002	±0.007
Yaw coefficient (C_N)	-0.016	±0.022

Table 6.2: Averaged force and moment coefficients (baseline 3.5 mm slot).

	Value	Uncertainty %
Downforce coefficient (C_L)	0.031	±0.087
Drag coefficient (C_D)	0.259	±0.023
Side force coefficient (C_Y)	0.013	±0.063
Pitch coefficient (C_M)	-0.020	±0.035
Roll coefficient (C_R)	0.002	±0.009
Yaw coefficient (C_N)	-0.017	±0.021

Table 6.3: Averaged force and moment coefficients (baseline 5.5 mm slot).

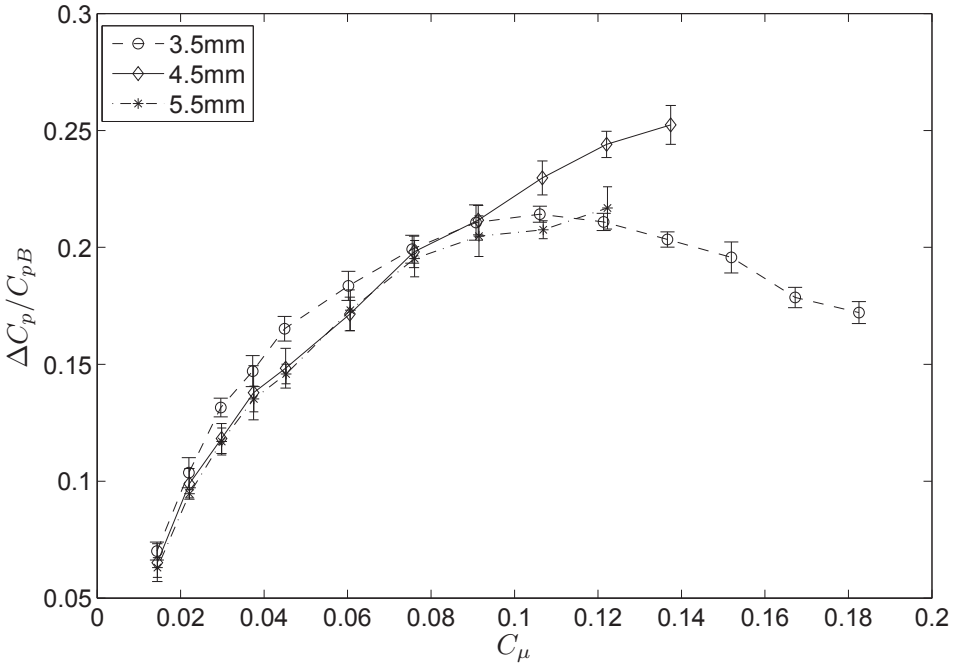

Figure 6.2: Comparison of $\Delta C_p/C_{pB}$ as function of C_μ for $St_{Hf} = 12.8$ for 3.5 mm ($\circ$), 4.5 mm ($\diamond$) and 5.5 mm ($*$) slots – see Tables C.1, C.3 and C.5.

is practically constant in the y and z directions, the small changes observed lying within the error bounds.

Tables 6.2 and 6.3 display the averaged forces and moments measured by the balance for the 3.5 mm and 5.5 mm size slots, respectively. When compared between them and with Table 4.3, it is evident that no substantial modification is introduced.

The importance of this result is twofold: (i) any passive effect induced by the changes in the actuator characteristics is not apparent, and (ii) forced flow results from different slot sizes can be compared confidently.

6.1.2 Forced Flow

Figures 6.2 – 6.5 display the base pressure rise and the drag reduction for the different slot widths at $St_{Hf} = 12.8$ and at $St_{Hf} = 13.4$. It has to be noted that the power limits of the actuator did not always allow to reach the maximum forcing amplitude. As shown, the 4.5 mm wide slot provides higher base pressure increase and drag reduction at both frequencies at high forcing amplitudes. The 3.5 mm

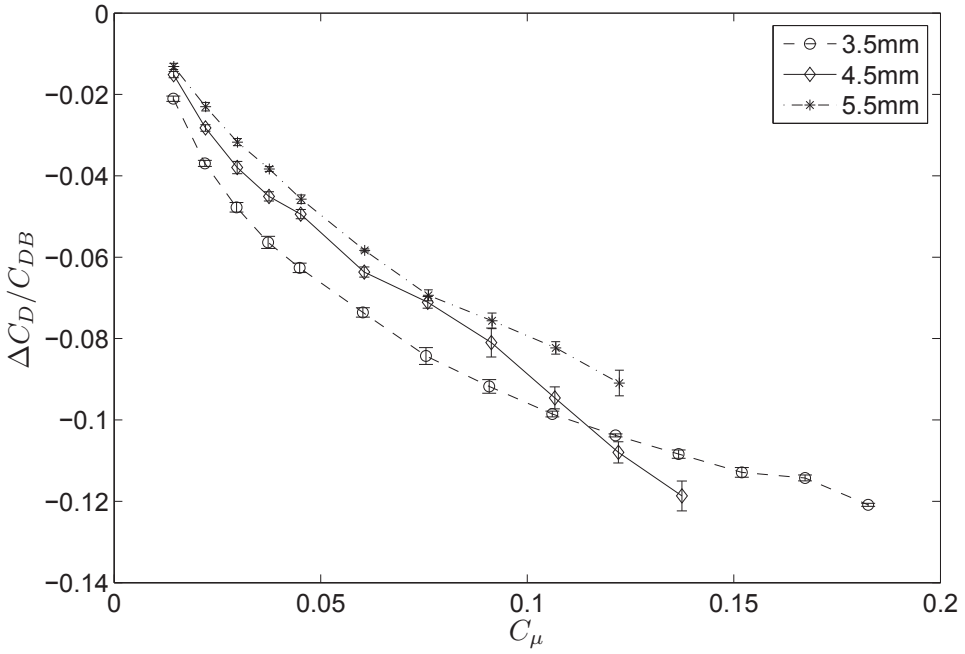

Figure 6.3: Comparison of $\Delta C_D/C_{DB}$ as function of C_μ for $St_{Hf} = 12.8$ for 3.5 mm ($\circ$), 4.5 mm ($\diamond$) and 5.5 mm ($*$) slots – see Tables C.2, C.4 and C.6.

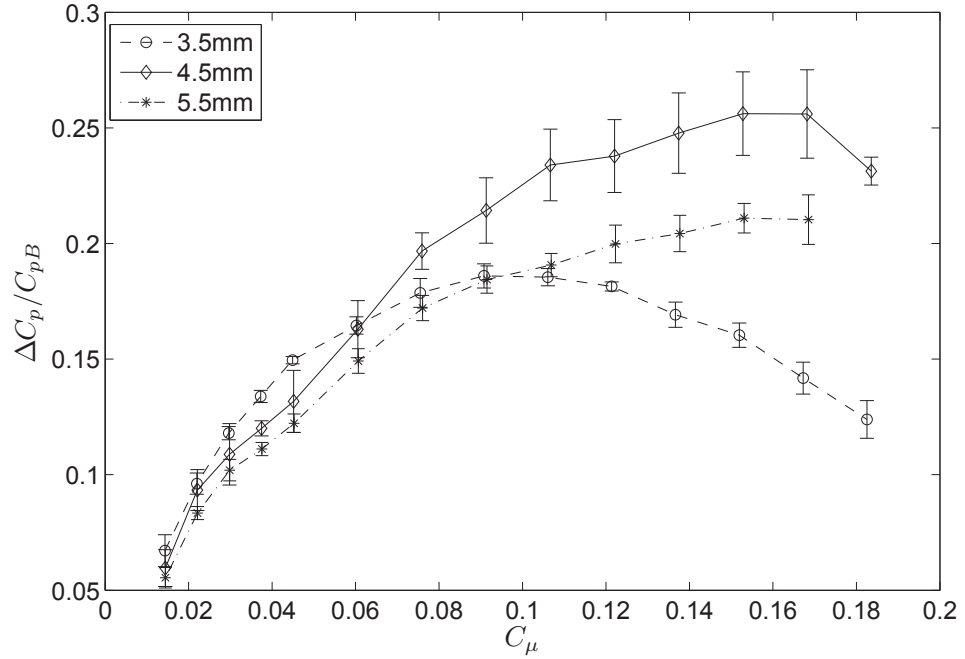

Figure 6.4: Comparison of $\Delta C_p/C_{pB}$ as function of C_μ for $St_{Hf} = 13.4$ for 3.5 mm ($\circ$), 4.5 mm ($\diamond$) and 5.5 mm ($*$) slots – see Tables C.1, C.3 and C.5.

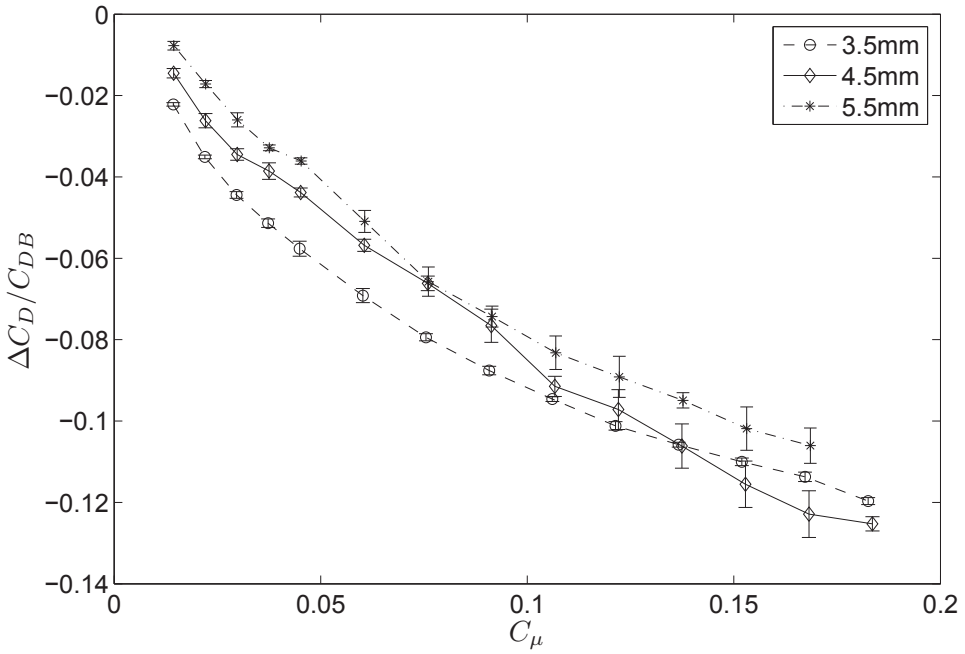

Figure 6.5: Comparison of $\Delta C_D/C_{DB}$ as function of C_μ for $St_{Hf} = 13.4$ for 3.5 mm ($\circ$), 4.5 mm ($\diamond$) and 5.5 mm ($*$) slots – see Tables C.2, C.4 and C.6.

slot performs better in terms of base pressure rise for $C_\mu < 0.09$ and in terms of drag decrease for $C_\mu < 0.11$ when forcing at $St_{Hf} = 12.8$. For $St_{Hf} = 13.4$, the 3.5 mm slot shows higher pressure gain for $C_\mu < 0.06$ and higher drag decrease for $C_\mu < 0.13$. The 5.5 mm slot provides a base pressure recovery larger than the 3.5 mm slot, but lower than the 4.5 mm, for $C_\mu > 0.12$ and $St_{Hf} = 13.4$; for different conditions its performances are lower or comparable to the ones from the other slots.

The relationship between balance and base pressure measurements for different slot sizes is shown in Figures 6.6 – 6.11, where $\Delta C_D/C_{DB}$, $\Delta C_L/C_{LB}$ and $\Delta C_M/C_{MB}$ are plotted as functions of $\Delta C_p/C_{pB}$. The same $\Delta C_D/C_{DB}$ behaviour described in Chapter 5 is registered in all the slots at both forcing frequencies (Figures 6.6 and 6.7). However, in contrast to in Figure 5.3, the curves do not collapse.

On the other hand, $\Delta C_L/C_{LB}$ and $\Delta C_M/C_{MB}$ for the 3.5 and 5.5 mm slots (Figures 6.8 – 6.11) display a different trend from what shown for the 4.5 mm slot (Figures 5.4 – 5.5). $\Delta C_L/C_{LB}$ and $\Delta C_M/C_{MB}$ vary linearly for the 3.5 mm slot, while they have an almost parabolic behaviour for the 5.5 mm slot, similar to that

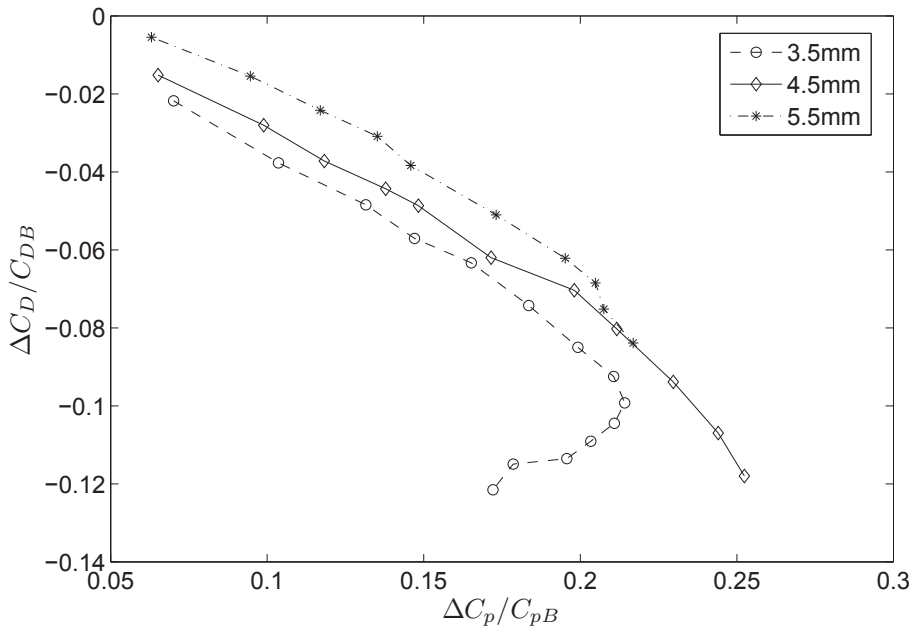

Figure 6.6: Change of the drag coefficient, $\Delta C_D/C_{DB}$, as a function of the change of the pressure coefficient, $\Delta C_p/C_{pB}$, for forcing frequency $St_{Hf} = 12.8$.

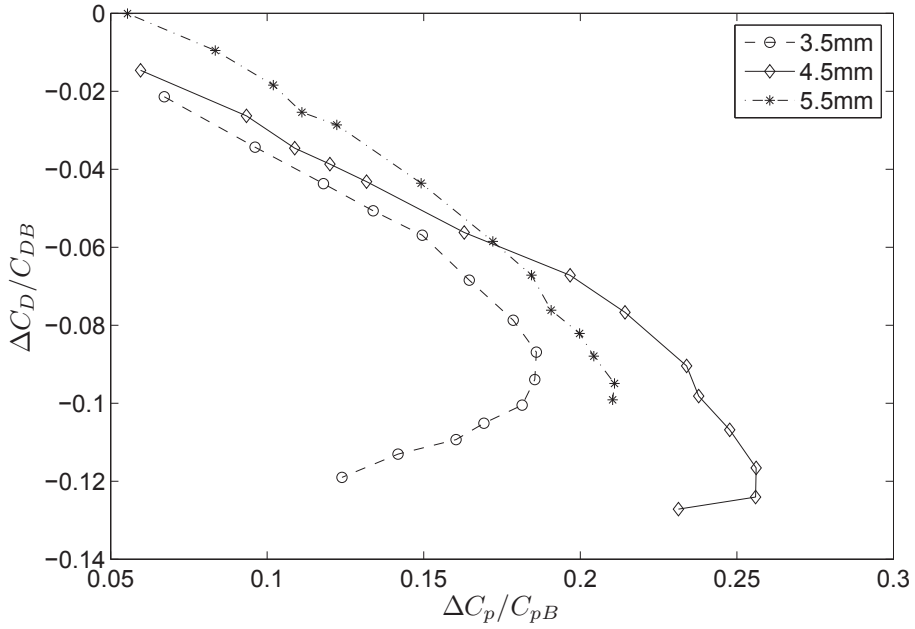

Figure 6.7: Change of the drag coefficient, $\Delta C_D/C_{DB}$, as a function of the change of the pressure coefficient, $\Delta C_p/C_{pB}$, for forcing frequency $St_{Hf} = 13.4$.

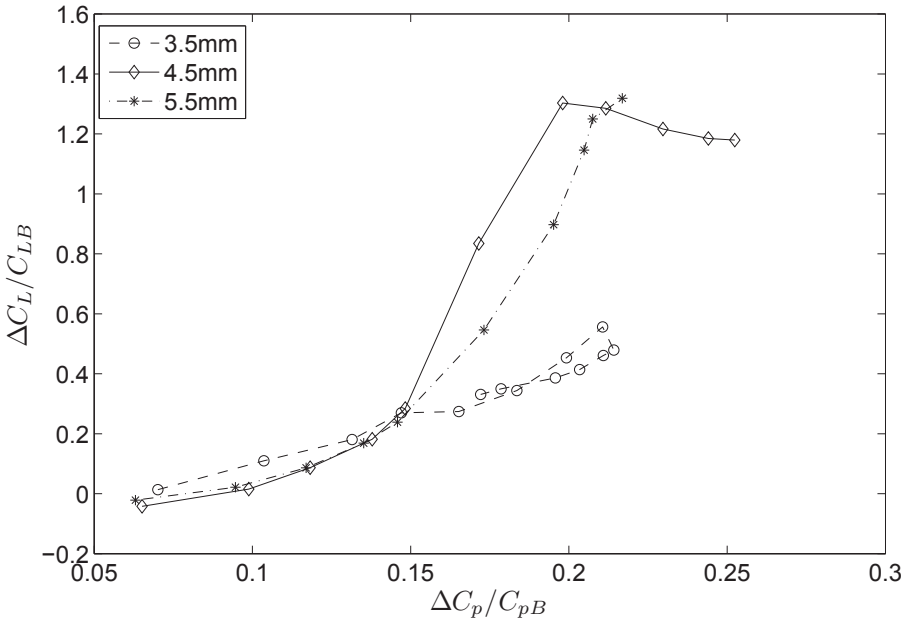

Figure 6.8: Change of the downforce coefficient, $\Delta C_L/C_{LB}$, as a function of the change of the pressure coefficient, $\Delta C_p/C_{pB}$, for forcing frequency $St_{Hf} = 12.8$.

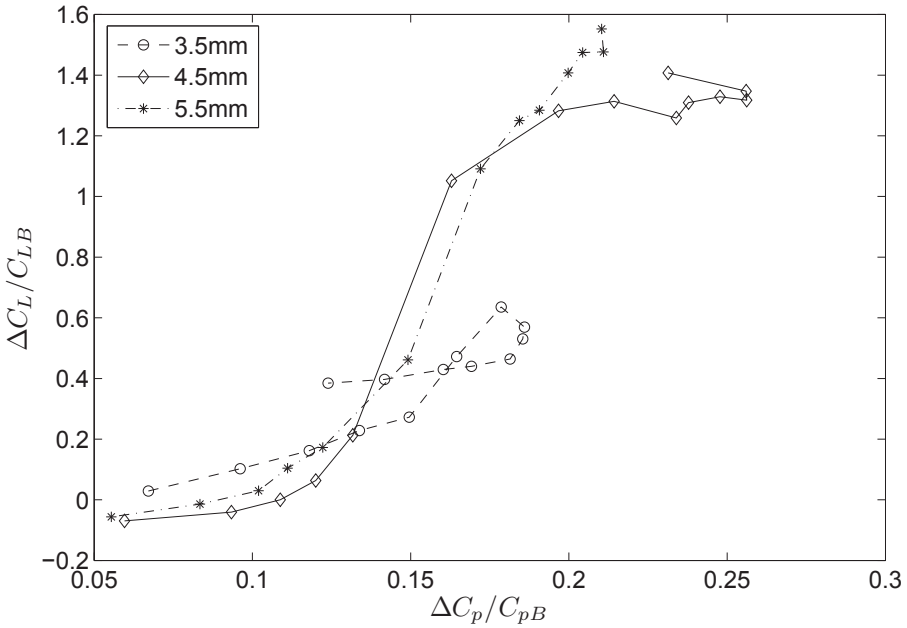

Figure 6.9: Change of the downforce coefficient, $\Delta C_L/C_{LB}$, as a function of the change of the pressure coefficient, $\Delta C_p/C_{pB}$, for forcing frequency $St_{Hf} = 13.4$.

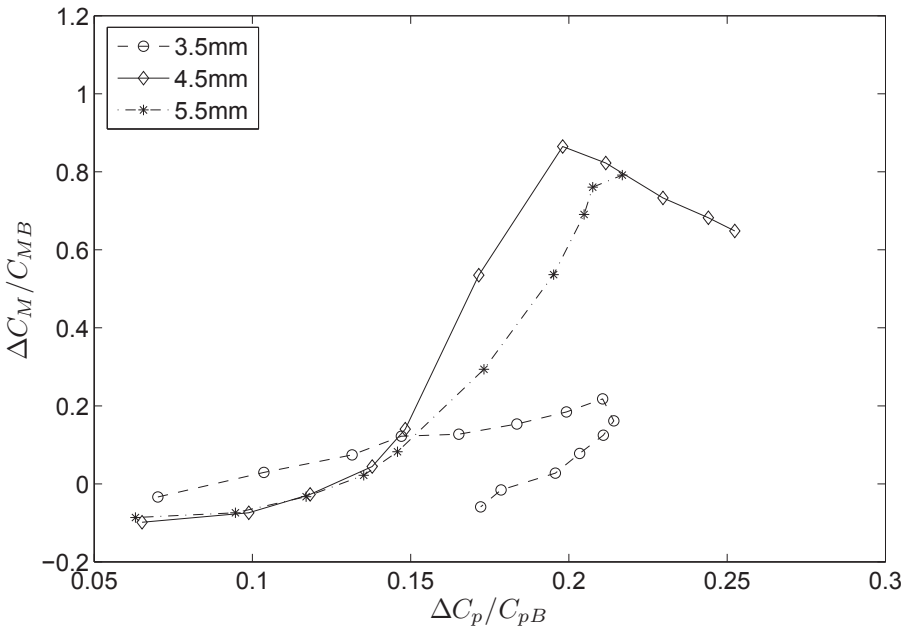

Figure 6.10: Change of the pitch moment coefficient, $\Delta C_M/C_{MB}$, as a function of the change of the pressure coefficient, $\Delta C_p/C_{pB}$, for forcing frequency $St_{Hf} = 12.8$.

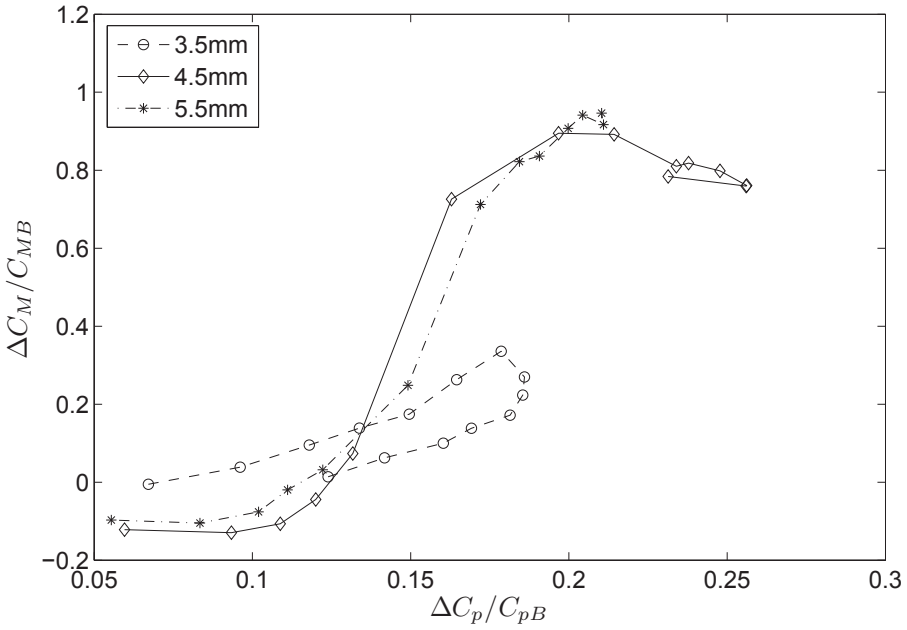

Figure 6.11: Change of the pitch moment coefficient, $\Delta C_M/C_{MB}$, as a function of the change of the pressure coefficient, $\Delta C_p/C_{pB}$, for forcing frequency $St_{Hf} = 13.4$.

Forcing Param		Press Rise		Mean	Variance	Skewness	Kurtosis
St_{Hf}	C_μ	$\Delta C_p/C_{pB}$		$\mu \times 10^{-3}$	$\sigma^2 \times 10^{-3}$	γ	κ
12.8	0.107	0.214 ± 0.003	y	13.6	2.09	-0.54	1.63
			z	-34.2	2.04	1.10	3.34
13.4	0.091	0.186 ± 0.004	y	-5.1	2.22	0.23	1.34
			z	-32.6	1.90	1.07	3.22

Table 6.4: Averaged $\Delta C_p/C_{pB}$ and statistical moments of the PDF distributions of the position of the centre of pressure for the 3.5 mm slot. Maximum base pressure recovery conditions – see Figure 6.12.

found for the 4.5 mm slot at $St_{Hf} = 12.2$. However, it has to be noted that the curves for the 4.5 and 5.5 mm slots almost collapse up to $\Delta C_p/C_{pB} \approx 0.14$ for $St_{Hf} = 12.8$.

6.2 3.5 mm Slot Details

The wake was forced with the 3.5 mm slot up to a maximum blowing coefficient $C_\mu = 0.184$ for both $St_{Hf} = 12.8$ and $St_{Hf} = 13.4$. As shown in Table 6.4, higher base pressure recovery is achieved when forcing at $St_{Hf} = 12.8$ rather than at $St_{Hf} = 13.4$. The base pressure distribution and the PDF of the centre of pressure for the conditions of maximum base pressure recovery are shown in Figure 6.12. In both cases, the bimodal PDF of the centre of pressure in y indicates bi-stable behaviour of the wake in the horizontal direction. This is not true for the z direction. It can also be observed that, unlike what happens with the other slots, the centre of pressure is located at $z < 0$ even at the conditions of maximum base pressure recovery. This is linked to the base pressure distribution typical of this slot size, characterised by higher values of pressure at the lower half.

The same drag reduction of $\Delta C_D/C_{DB} = -0.120 \pm 0.001$ is measured for both forcing frequencies at $C_\mu = 0.184$. As seen for the 4.5 mm slot, the forcing amplitude for maximum drag reduction does not correspond to the amplitude for maximum base pressure recovery.

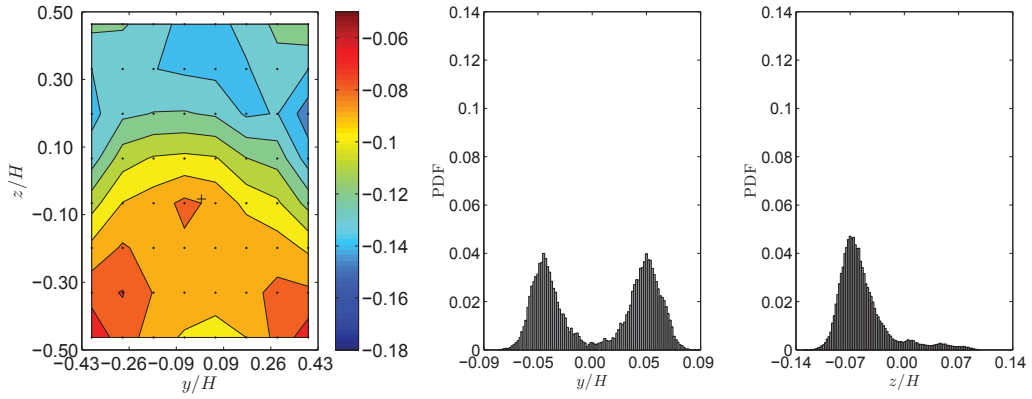

(a) $C_\mu = 0.107$, $St_{Hf} = 12.8$

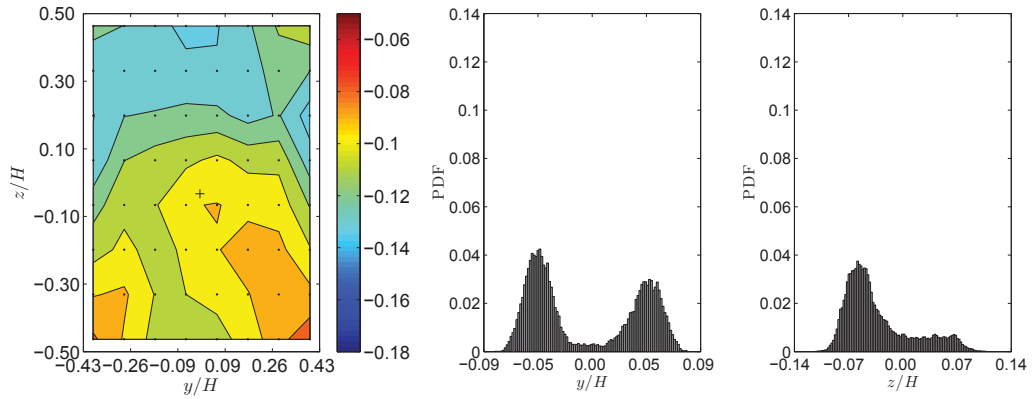

(b) $C_\mu = 0.091$, $St_{Hf} = 13.4$

Figure 6.12: C_p contours showing position of centre of pressure (+) (left), PDF of centre of pressure along the y direction (centre) as in Equation 3.4 and z direction (right) as in Equation 3.5. Conditions of maximum base pressure recovery: (a) $C_\mu = 0.091$, $St_{Hf} = 12.8$, (b) $C_\mu = 0.091$, $St_{Hf} = 13.4$ – Slot size 3.5 mm.

Forcing Param		Press Rise		Mean	Variance	Skewness	Kurtosis
St_{Hf}	C_μ	$\Delta C_p/C_{pB}$		$\mu \times 10^{-3}$	$\sigma^2 \times 10^{-3}$	γ	κ
12.8	0.122	0.217 ± 0.006	y	19.0	2.91	-0.67	1.67
			z	32.8	0.09	-0.75	3.46
13.4	0.153	0.211 ± 0.004	y	18.7	2.56	-0.80	1.90
			z	31.4	0.08	-1.15	4.60

Table 6.5: Averaged $\Delta C_p/C_{pB}$ and statistical moments of the PDF distributions of the position of the centre of pressure for the 5.5 mm slot. Maximum base pressure recovery conditions – see Figure 6.13.

Additional data for this slot can be found in Appendix C in Tables C.3 and C.4 and Figures C.3 and C.4.

6.3 5.5 mm Slot Details

Due to the resonance frequency ($St_{Hf} = 13.8$, see Table 3.2), the actuator configuration with the 5.5 mm wide slot does not allow forcing amplitudes as large as those reached for the other slots, as can be seen in Figures 6.2 and 6.4. Therefore, the plateau expected after the maximum base pressure recovery cannot be seen. The maximum values of pressure rise measured with this slot are shown in Table 6.5; both of them correspond to the largest forcing amplitudes allowed. As can be seen also from Figure 6.13, the conditions of pressure recovery, position of the centre of pressure, shape of the PDF distributions, and pressure distribution are very similar for the two forcing frequencies tested. Compared to the 3.5 mm slot, these parameters for the 5.5 mm slot are similar to those for the 4.5 mm slot.

Finally, the maximum drag reduction is reached concurrently with the highest base pressure recovery for both frequencies: $\Delta C_D/C_{DB} = -0.091 \pm 0.013$ at $C_\mu = 0.122$ for $St_{Hf} = 12.8$ and $\Delta C_D/C_{DB} = -0.106 \pm 0.014$ at $C_\mu = 0.168$ for $St_{Hf} = 13.4$.

Additional data for this slot can be found in Appendix C in Tables C.5 and C.6 and Figures C.5 and C.6.

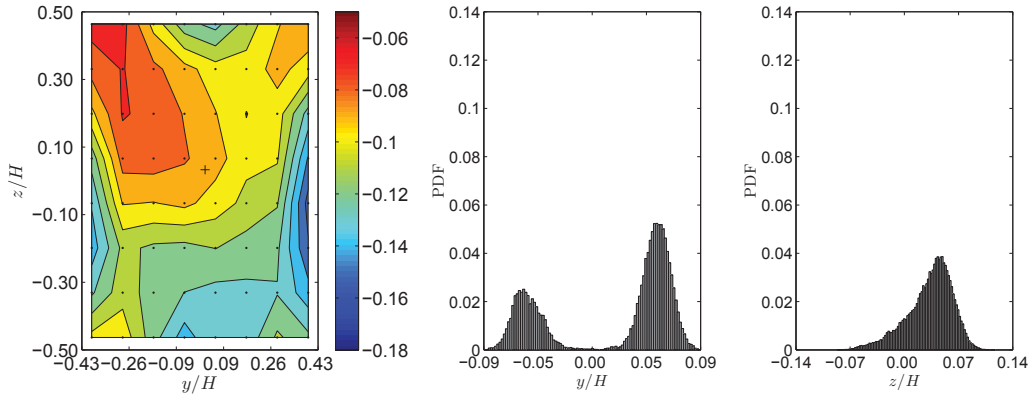

(a) $C_\mu = 0.122$, $St_{Hf} = 12.8$

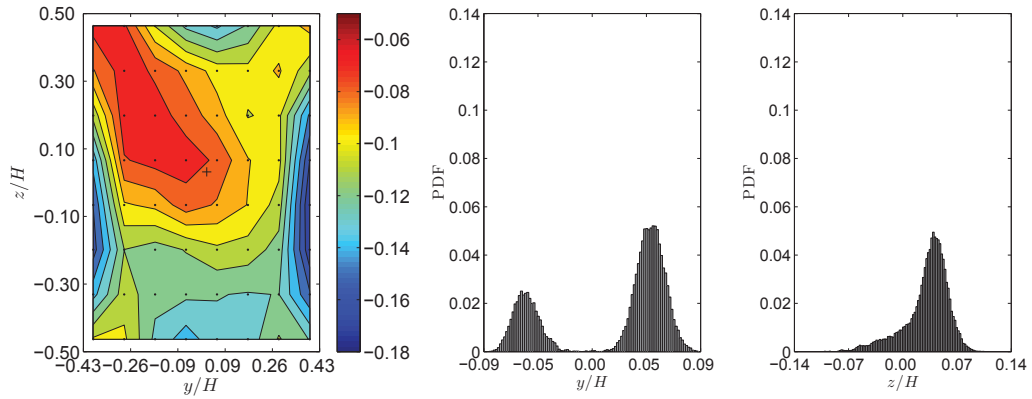

(b) $C_\mu = 0.153$, $St_{Hf} = 13.4$

Figure 6.13: C_p contours showing position of centre of pressure (+) (left), PDF of centre of pressure along the y direction (centre) as in Equation 3.4 and z direction (right) as in Equation 3.5. Conditions of maximum base pressure recovery: (a) $C_\mu = 0.122$, $St_{Hf} = 12.8$, (b) $C_\mu = 0.153$, $St_{Hf} = 13.4$ – Slot size 5.5 mm.

Chapter 7

Discussion and Conclusions

7.1 Ground Influence and Baseline Wake Structure

The asymmetry in the base pressure distribution shown in Figure 4.3 raised some questions about the influence of the wind tunnel set-up on the wake. At first, the distance between the bottom of the model and the floor ($h = 0.56H$), combined with the possible connection between the detaching boundary layers at the top and bottom of the base (Figure 4.2 and Table 4.1), lead to the exclusion of any influence of the ground on the wake. The gradient in the z direction was initially attributed to the position of the strut, which ends only 665 mm upstream of the base. However, any absence of asymmetry in the y direction, and the similarity of the pressure distribution with the ones from previous results concerning rectangular-sectioned bodies in ground effect, as those of Duell & George (1993), Grandemange *et al.* (2012*a*), Grandemange *et al.* (2013) and Krajnovic & Davidson (2001), suggested some influence from the ground. Unfortunately, the characteristics of the strut did not allow the test body to be placed at a higher position. Therefore a condition of mild ground effect had to be accepted.

A hypothesis on the near wake topology can be made by taking into consideration the similarity with previous research, the pressure distribution on the base (Figure 4.3) and the integrated mean-square pressure shown in Figure 4.10. The recircu-

lation region is inferred to have a toroidal organization, formed by two symmetric bubbles on the horizontal plane and two asymmetric ones on the vertical plane, as seen in Duell & George (1993), Grandemange *et al.* (2012*a*), Grandemange *et al.* (2013), Khalighi *et al.* (2001), Khalighi *et al.* (2012) and Krajnovic & Davidson (2001). On the vertical plane, the recirculation bubble at the top is supposed to be bigger than the bottom one and characterised by lower values of pressure, hence the minimum in the base pressure in Figure 4.3. The imprint left on the base, together with the higher value of $\tilde{p}$ measured by transducer E3 (see Figure 4.10), suggest that the upper bubble is $\sim 3/5H$ tall. This indicates that the recirculation bubble closes on a plane which is likely to be in the bottom half of the base.

Finally, some additional considerations about the strut influence on the wake have to be made. Even if it cannot be considered the main cause of the gradient in the z direction observed in the base pressure distribution, its influence on the wake cannot be excluded. It has been mentioned before the lack of the very low frequency structure in the y direction previously observed in the literature. Grandemange *et al.* (2012*a*) note the extreme sensitivity of the wake to surrounding conditions; this is confirmed by the suppression of this structure for a ground clearance $< 0.4H$, which clearly modifies the bottom shear layer. In the present investigation, the interaction of the wake of the strut with the shear layer at the top could have had the same stabilising effect.

7.2 Effects of Forcing on the Wake Structure

The analysis carried out in Section 5.3 shows the changes produced on the wake topology by forcing at different amplitudes. For $C_\mu < 0.061$, the base pressure distribution shows subtle changes in the structure of the wake. The recirculation region is expected to have a similar shape to the one supposed for the baseline case, even if the symmetry between the bubbles observed on the vertical plane increases with C_μ. The values of pressure measured on the base, higher than the ones observed for the baseline, also implies a smaller recirculation region. On the other hand, the pressure distribution found for $C_\mu = 0.061$ does not suggest a recirculation region

similar to those seen in previous studies. The uniformity of the pressure distribution on the base could be an indication of perfect symmetry of the toroidal structure on both vertical and horizontal planes, or a symptom of detachment of the recirculation bubble from the base, as seen for bodies equipped with rear cavities, as in Duell & George (1993), Duell & George (1999), Khalighi *et al.* (2001) and Khalighi *et al.* (2012). For $C_\mu > 0.061$ a toroidal recirculation region seems to be evident again, even if the imprint on the base suggests an asymmetry on both the horizontal and the vertical plane. The asymmetries of the wake topology are reflected in the changes measured by the balance, as can be seen in Figures 5.14 and 5.15.

Oxlade (2013) linked a loss in pressure recovery to the amplification of the shear layer for $C_\mu > 0.57$. However, the spectral analysis carried out in Section 5.3 shows that this is not necessarily true for this model. Figures 5.20–5.27 reveal a very strong shear layer amplification, which does not seem to influence the pressure recovery on the base.

Section 5.4 demonstrates how the forcing frequency has much less influence on the wake structure than the forcing amplitude. The base pressure distributions displayed in Figure 5.31 show very little changes with frequency, as also confirmed by the statistics in Figure 5.32 and Table 5.5. In an obvious consistent way, also the slot thickness does not seem to influence the wake topology in a sensible way, as shown in Figures 6.12 and 6.13.

Finally, the analysis of the base pressure distribution is linked to the balance results through the statistics of the position of the COP on the base, as can be seen by comparing Figures 5.14 and 5.15 with 5.17, and Figures 5.29 and 5.30 with 5.32.

7.3 Pressure Recovery Mechanism

The high resolution PIV measurements carried out by Oxlade (2013) in the near wake showed some of the changes induced by high frequency forcing, and helped to understand the pressure recovery mechanism. The main changes observed in the mean flow involved (i) the size of the recirculation bubble, made shorter and narrower, as also shown by Qubain (2009), (ii) the increase of the shear layer velocity,

and (iii) the inversion of the sign of streamline curvature immediately downstream of the trailing edge. The momentum balance showed a large local increase in the normal stress gradient. Through a comparison of the forced and unforced flow, the relative importance of streamwise and vertical momentum balance was shown to remain the same. However, the action of the jet increased the normal stress gradient by an order of magnitude. From the point of view of the mean pressure field, the jet created a region of very low pressure separating the recirculation bubble from the outer flow. The pressure recovery was observed near the base of the model and on the high speed side of the shear layer. The recovery mechanism was then explained with the formation in the near wake of a region of high enstrophy, associated with local low pressure and low dissipation, encircled by a very strong shear layer. The region of high enstrophy, and the surrounding shear layers, coincided with the vortex cores and the regions of large nearly irrotational shear around them.

The changes described above can be considered as an explanation of the reduced entrainment produced by jet forcing. As described by Papailiou & Lykoudis (1974), the entrainment brings fluid into the wake, widening the turbulent vortices and causing a constant growth of the wake itself. This process is particularly strong in the near wake, where the forcing action of the jet is also more powerful. The jet acts as a shield for the wake, limiting its growth and reducing the amount of flow involved by the dissipation.

Moreover, it can be assumed that the changes produced by the jet contribute to the stability the shear layer. The stability theory developed by Lin (1944) for laminar flows, and extended to turbulence by Papailiou & Lykoudis (1974), explains how the presence of two thick viscous 'superlayers', as the ones identified by Oxlade (2013) with his analysis of rotating and straining motion in the near wake, produces an important dissipation with stabilising effect.

7.4 Effects of Jet Thrust

The results from Mueller *et al.* (2001) show that synthetic jets have a non-negligible thrust. The measurements were performed on a round jet orifice of di-

ameter D and stroke length L by means of an analytic balance with resolution 0.5 mN. For $L/D <\sim 3$ the thrust resulted to be proportional to $(L/D)^4$, while for $L/D >\sim 3$ the thrust was proportional to $(L/D)^2$. However, the increase in thrust with frequency showed a roll-off for frequencies greater than 150–180 Hz.

The geometry of the system and the frequencies adopted during the current investigation are very different from the ones tested by Mueller *et al.* (2001), therefore it is not possible to calculate the magnitude of the thrust by using their model. Direct measurements of thrust at high forcing amplitude were very difficult to perform due to overheating of the system, therefore no data is available for the current system. However, it is likely the jet thrust to be responsible of the discrepancy between $\Delta C_p/C_{pB}$ and $\Delta C_D/C_{DB}$ seen in Figure 5.3.

A way to quantify the thrust produced by the jet would be an investigation of the flow velocity inside the cavity. This would help to work out the existence of any momentum flux generated inside the cavity and caused by the velocity on the outflux being greater than that of the influx. To first order, the jet efflux is sinusoidal, and net mass flux is zero. The positive average velocity shown by hot-wire traces is caused by the jet coupling with wake outside the cavity, which produces the pressure rise on the rear face of the body. A second order effect would be the coupling of the flow inside the cavity with the forced wake, which would cause a small but finite measurable thrust. This coupling is more likely to happen at high forcing amplitudes, where the hot-wire traces revealed some occasional alterations of the sinusoidal shape of the jet velocity, and where the discrepancies between base pressure and body forces are more evident.

7.5 Actuator Efficiency

During the experiments, the actuator power was measured in order to preserve the speakers from damage due to overheating. Unfortunately, the measuring system did not allow a reliable measure of the electrical power used by the actuator, but an estimate obtained from the AC power allows to assume an efficiency $\eta << 1$. This is mainly due to the design requirements of the actuator, which was expected to

operate over a very wide range of frequencies. A resonant design, optimised for the optimum forcing frequency, would be one of the improvements required to improve the system efficiency. Other aspects to tackle to would be the mechanical, resistive, and viscous losses. More on this topic can be found in Oxlade (2013).

7.6 Conclusions

The literature review summarises the dynamics of the wake of simplified ground vehicle models. All the studies identified the bubble-pumping mode and vortex shedding. Some investigations (Grandemange *et al.*, 2012*a*, 2013) identified also a very low frequency bi-stable behaviour of the wake. The influence of the ground on the vortex shedding in the vertical plane was also widely confirmed.

In the present study, the unforced wake was analysed from the point of view of the averaged base pressure distribution and through the spectral analysis of the high frequency response transducers located on the base. Additional information was provided by the PDF of the centre of pressure, and by the study of the averaged forces and moments and their behaviour in the frequency domain. The same type of analysis was conducted for the forced wake. A parametric study identifies the forcing parameters (frequency and amplitude) and slot size at which base pressure recovery and drag reduction are maximum. The primary conclusions of this investigation are as follows:

1. Observation of the unforced flow:

    - No difference was found in the boundary layer profile at the top and bottom of the model. However, the influence of the ground on the growth of the wake creates a strong vertical asymmetry in the pressure distribution on the base.
    - The wake is dominated by two characteristic frequencies, one linked to the bubble-pumping mode, $St_H \approx 0.08$, and the other, related to the vortex-shedding frequency, equal to $St_H \approx 0.17$ on the vertical plane and to $St_H \approx 0.20$ ($St_W \approx 0.17$) on the horizontal plane.

- The bi-stable behaviour was not detected in this case, apart from a random movement of the centre of pressure in the vertical direction.
- No passive effect of pressure recovery was found from the data collected.
- The analysis of the forces measured by the balance shows that the flow structures are able to excite the resonance frequencies of the body.

2. Study of the pressure recovery with a 4.5 mm slot, which gives maximum base pressure recovery and drag reduction:

   - At all forcing frequencies a base pressure increase and a drag reduction are demonstrated at every amplitude.
   - The maximum increase in base pressure of 27.7% occurs at a forcing frequency of $St_{Hf} = 13.9$ and amplitude of $C_\mu \approx 0.168$.
   - If the forcing amplitude had not been limited by the actuator characteristics, higher values of base pressure might have been reached at a frequency of $St_{Hf} = 12.5$ or $St_{Hf} = 12.8$, that is roughly 5 times the frequency of the shear layer mode, as reported by Oxlade (2013).
   - The wake exhibits higher sensitivity to changes in forcing amplitude rather than frequency. This supports the existence of a plateau of frequencies for the maximum base pressure recovery, as proposed by Oxlade (2013).
   - $C_\mu \approx 0.05$ appears to be a critical value for the effects produced on the wake by forcing, as shown both by the spectral analysis of the wake and by the changes in $\Delta C_L/C_{LB}$ and $\Delta C_M/C_{MB}$ as functions of $\Delta C_p/C_{pB}$.
   - Forcing at $C_\mu \gtrsim 0.06$ establishes a bi-stable behaviour of the wake in y, which is also found in z at $C_\mu \approx 0.06$. However, no specific frequency associated to this structure has been identified.

3. Results of the parametric study on the influence on the forced wake of the slot width:

- The results for the 5.5 mm slot resemble those found for the 4.5 mm slot in terms of base pressure distribution, forces and moments on the model. The 3.5 mm slot displays a different behaviour. A plausible explanation for this could be that the jet interacts differently with the surrounding flow when the slot width is roughly equal to the momentum thickness θ of the detaching boundary layer. As a consequence, the ratio between slot size and momentum thickness is an important dimensional parameter; further investigations are needed to confirm this assumption.
- The change in base pressure $\Delta C_p/C_{pB}$ and in drag $\Delta C_D/C_{DB}$ scales with the blowing coefficient C_μ depending on the frequency and on the slot width considered. Slot size and $\Delta C_p/C_{pB}$ act as dimensional parameters for $\Delta C_D/C_{DB}$; more measurements and extra data are needed to confirm this.

4. Considerations on the applicability to real vehicles:

   - The scaling of the system can be attempted by comparing Oxlade (2013) findings with the results from the present study. As shown in Table 7.1, while the slot width scales with the momentum thickness of the detaching boundary layer, hence with the length of the body, the forcing amplitude scales with its height. To allow the comparison, the dimensions of the current model are reported as a hydraulic diameter ($D_H = 4Area/Perimeter$).
   - From the point of view of the viscous losses in the actuator, the scaling for a full size truck might be advantageous since the viscous losses decrease when dimensions increase.

7.7 Future Work

Many questions still remain about the pressure recovery mechanism and the potential of the system for future applications. Significant steps have been made by previous research on the bullet-shaped body (Qubain, 2009; Oxlade, 2013), but a

	Oxlade (2013)	Current Study
Diameter D (mm)	196.5	394.7
θ/D	0.011	0.009 – 0.012 *
Optimal C_μ	0.04	0.168
Optimal St_{Hf}	9.84	13.9
Max Base Pressure Rise	33%	28%

* sides – top/bottom

Table 7.1: Comparison of current results with previous work by Oxlade (2013).

detailed analysis of the flow structures in the near wake of a rectangular-sectioned body still has to be conducted. This should be carried out for the baseline and the forced cases with simultaneous base pressure and PIV measurements (ideally stereo-PIV 2D-3C techniques), with special attention given to the flow around the corners. The actuator calibration should be further improved by installing a distributed set of *in situ* transducers, located in the neck of the actuator, in order to calibrate the jet with full wind tunnel operating conditions. Also, the thrust produced by the jet should be measured, to correct the drag force readings from the balance. The flow field should also be characterised in terms of the sum of rotating and straining motion; by identifying these quantities, the Poisson equation can be verified, as shown by Oxlade (2013). Also, even though no passive effect was identified, this should be further investigated because passive effects have been identified on the axisymmetric body. All these analyses, complemented by a complete parametric study of the key variables for the actuator alone and for the full model, should be carried out firstly in the absence of ground effect and then repeated at different distances from the floor. Oxlade (2013) stated that the base pressure increase is due to the jet's sheltering of the wake from the shear layer entrainment. Corners lead to complicated shear-layer interactions, and Qubain (2009), even though using an axisymmetric model, showed that 3-D effects render forcing ineffective. Hence, it would be interesting to investigate if higher gains can be obtained by applying different forcing conditions at the corners, such as zero or higher forcing amplitudes.

The measurement of the aerodynamic power consumed to produce the jet vortices is a lower limit for the actuator power consumption and should be further investigated. Answering these questions will bring the system a step closer to being implemented on a test vehicle, while parallel efforts should be invested in improving the efficiency of the actuator. Developing the scheme further into a closed loop system should be explored as this might have an added net energy gain.

Bibliography

Advanced Transit Dynamics, Inc. 2013 Trailertail. [Online], available from: http://www.atdynamics.com/company.htm [Accessed December 2013].

Aerodyne 2009 Truck aerodynamics and composite manufacturing. Enhancing vehicle performance and image. [Online], available from: http://www.aerodyneuk.com/index.html [Accessed December 2013].

Ahmed, S. R., Ramm, G. & Faitin, G. 1984 Some salient features of the time-averaged ground vehicle wake. *Tech. Rep.*. Society of Automotive Engineers, Inc., Warrendale, PA.

Aider, J.-L., Beaudoin, J.-F. & Wesfreid, J. E. 2010 Drag and lift reduction of a 3d bluff-body using active vortex generators. *Exp. Fluids* **48** (5), 771–789.

Airtabs 2010 Airtab fuel saver. [Online], available from: http://www.airtab.com/how.html [Accessed December 2013].

Apelt, C. J., West, G. S. & Szewczyk, A. A. 1973 The effects of wake splitter plates on the flow past a circular cylinder in the range $10^4 < \mathrm{R} < 5\times 10^4$. *J. Fluid Mech.* **61** (01), 187–198.

Argonne National Laboratory, A.N.L. 2008 Vehicle technologies heavy vehicle program: Fy 2008 benefits analysis, methodology and results – final report. [Online], available from: http://www.transportation.anl.gov/pdfs/TA/465.pdf [Acessed December 2013].

Asai, M. & Kaneko, M. 2000 Experimental investigation of receptivity of a shear layer separating at a convex corner. *Fluid Dynamics Research* **27** (2), 117–128.

Balsa, T. F. 1988 On the receptivity of free shear layers to two-dimensional external excitation. *J. Fluid Mech.* **187**, 155–177.

Bayraktar, Llhan, Landman, Drew & Baysal, Oktay 2001 Experimental and computational investigation of ahmed body for ground vehicle aerodynamics. *SAE transactions* **110** (2), 321–331.

Bearman, P. W. 1965 Investigation of the flow behind a two-dimensional model with a blunt trailing edge and fitted with splitter plates. *J. Fluid Mech.* **21** (part 2), 241–256.

Bearman, P. W. 1997 Near wake flows behind two-and three-dimensional bluff bodies. *J. Wind Eng. Ind. Aerodyn.* **69**, 33–54.

Beaudoin, J.-F. & Aider, J.-L. 2008 Drag and lift reduction of a 3d bluff body using flaps. *Exp. Fluids* **44** (4), 491–501.

Berger, E., Scholz, D. & Schumm, M. 1990 Coherent vortex structures in the wake of a sphere and a circular disk at rest and under forced vibrations. *J. Fluids Struct.* **4** (3), 231–257.

Beyma n.d. *6P200Nd Low Frequency Transducer*. [Online], availble from: http://profesional.beyma.com/pdf/6P200NdE.pdf [Accessed June 2010].

BMI Corporation 2009 Smarttruck changing the shape of trucking. [Online], available from: http://www.smarttrucksystems.com/ [Accessed December 2013].

Bruun, H. H. 1995 *Hot-Wire Anemometry. Principles and Signal Analysis*. Oxford Univ. Press.

Castrup, H. 2004 Estimating and combining uncertainties. In *8th Annual ITEA Instrumentation Workshop, Lancaster, CA, USA*.

Chaudhari, M., Verma, G., Puranik, B. & Agrawal, A. 2009 Frequency response of a synthetic jet cavity. *Experimental Thermal and Fluid Science* **33** (3), 439–448.

Choi, H. 2003 Active controls of flows over bluff bodies for drag reduction. In *Proceedings of 4th Symposium on Smart Control of Turbulence*, pp. 1–12.

Choi, H., Jeon, W.-P. & Kim, J. 2008 Control of flow over a bluff body. *Annu. Rev. Fluid Mech.* **40**, 113–139.

Chomaz, J. M., Huerre, P. & Redekopp, L. G. 1988 Bifurcations to local and global modes in spatially developing flows. *Phys. Rev. Lett.* **60** (1), 25–28.

Cooper, K. R. 1985 The effect of front-edge rounding and rear-edge shaping on the aerodynamic drag of bluff vehicles in ground proximity. *Tech. Rep.* 850288. Society of Automotive Engineers, Inc., Warrendale, PA.

Cooper, K. R. 2003 Truck aerodynamics reborn: lessons from the past. *SAE transactions* **112** (2), 132–142.

Cooper, K. R. & Leuschen, J. 2005 Model and full-scale wind tunnel tests of second-generation aerodynamic fuel saving devices for tractor-trailers. *Aerodynamics Laboratory, NRC, SAE Technical Paper Series* (01–3512).

Crighton, D. G. 1981 Acoustics as a branch of fluid mechanics. *J. Fluid Mech.* **106** (1), 261–298.

Crighton, D. G. 1985 The Kutta condition in unsteady flow. *Annu. Rev. Fluid Mech.* **17** (1), 411–445.

Darrigol, O. 2002 Stability and instability in nineteenth-century fluid mechanics. *Revue dhistoire des mathématiques* **8**, 5–65.

Doebelin, E. O. 1990 *Measurement Systems. Application and Design. Fourth Edition*. McGraw-Hill.

Don-Bur 2010 The don-bur aerodynamic teardrop. [Online], available from: http://www.donbur.co.uk/eng/products/aerodynamic_teardrop_trailers_rigids.php [Accessed December 2013].

Duell, E. & George, A. 1999 Experimental study of a ground vehicle body unsteady near wake. *SAE Technical Paper* (1999-01-0812).

Duell, E. G. & George, A. 1993 Measurements in the unsteady near wakes of ground vehicle bodies. *SAE Technical Paper* **930298**, 1–8.

El-Alti, M. 2012 *Active Flow Control for Drag Reduction of Heavy Vehicles*. Chalmers University of Technology.

El-Alti, M., Chernoray, V., Kjellgren, P., Hjelm, L. & Davidson, L. 2010 Computations and full-scale tests of active flow control applied on a VOLVO truck-trailer. *Aerodynamics of Heavy Vehicles III: Trucks, Buses and Trains* .

Englar, R. J. 2000 Development of pneumatic aerodynamic devices to improve the performance, economics, and safety of heavy vehicles. *Tech. Rep.*. Georgia Tech Research Institute, Atlanta, GA (US).

Englar, R. J. 2001 Advanced aerodynamic devices to improve the performance, economics, handling, and safety of heavy vehicles. *Tech. Rep.*. Georgia Tech Research Institute Aerospace (US).

Englar, R. J. 2005 Improved pneumatic aerodynamics for drag reduction, fuel economy, safety, and stability increase for heavy vehicles. *SAE paper* pp. 01–3627.

Ewald, B. F. R. 2000 Multi-component force balances for conventional and cryogenic wind tunnels. *Meas. Sci. and Technol.* **11** (6), R81.

Fiedler, H. E. & Fernholz, H.-H. 1990 On management and control of turbulent shear flows. *Progress in Aerospace Sciences* **27** (4), 305–387.

Gad-el-Hak, M. 1996 Modern developments in flow control. *Appl. Mech. Rev.* **49**, 365–380.

Geropp, D. & Odenthal, H.-J. 2000 Drag reduction of motor vehicles by active flow control using the coanda effect. *Exp. Fluids* **28** (1), 74–85.

Grandemange, M., Cadot, O. & Gohlke, M. 2012*a* Reflectional symmetry breaking of the separated flow over three-dimensional bluff bodies. *Phys. Rev. E* **86** (3), 035302.

Grandemange, M., Gohlke, M. & Cadot, O. 2013 Turbulent wake past a three-dimensional blunt body. part 1. global modes and bi-stability. *J. Fluid Mech.* **722**, 51–84.

Grandemange, M., Gohlke, M., Parezanović, V. & Cadot, O. 2012*b* On experimental sensitivity analysis of the turbulent wake from an axisymmetric blunt trailing edge. *Phys. Fluids* **24**, 035106.

Hannemann, K. & Oertel, H. 1989 Numerical simulation of the absolutely and convectively unstable wake. *J. Fluid Mech.* **199** (1), 55–88.

Ho, C.-M. & Huerre, P. 1984 Perturbed free shear layers. *Annu. Rev. Fluid Mech.* **16** (1), 365–422.

Holman, R., Utturkar, Y., Mittal, R., Smith, B. L. & Cattafesta, L. 2005 Formation criterion for synthetic jets. *AIAA J.* **43** (10), 2110–2116.

Hucho, W.-H., ed. 1998 *Aerodynamics of Road Vehicles*, 4th edn. Society of Automotive Engineers, SAE.

Huerre, P. 2002 *Perspectives in fluid dynamics: a collective introduction to current research*, chap. Open Shear Flow Instabilities, pp. 159–229. Cambridge University Press.

Huerre, P. & Monkewitz, P. A. 1990 Local and global instabilities in spatially developing flows. *Annu. Rev. Fluid Mech.* **22** (1), 473–537.

Hussain, A. K. M. F. 1983 Coherent structuresreality and myth. *Phys. Fluids* **26**, 2816.

Hyams, D. G., Sreenivas, K., Pankajakshan, R., Stephen Nichols, D., Roger Briley, W. & Whitfield, D. L. 2011 Computational simulation of

model and full scale class 8 trucks with drag reduction devices. *Computers & Fluids* **41** (1), 27–40.

International Energy Agency 2013 Co_2 emissions from fuel combustion highlights. [Online], available from: http://www.iea.org/publications/freepublications/publication/CO2Emissions-FromFuelCombustionHighlights2013.pdf [Accessed December 2013].

Iveco 2013 Ecostralis aerodynamic kit. [Online], available from: http://web.iveco.com/malta/products/pages/ecostralis_features_and_benefits-_aerodynamic_kit.aspx [Accessed December 2013].

Johnson, R. W. 1998 *The Handbook of Fluid Dynamics.*. Springer.

Joseph, D. D. 1976 Stability of fluid motions. i, ii. *NASA STI/Recon. Tech. Report A* **77**, 12423.

Joseph, P., Amandolese, X., Edouard, C. & Aider, J.-L. 2013 Flow control using MEMS pulsed micro-jets on the Ahmed body. *Exp. Fluids* **54** (1), 1–12.

Jost 2013 Sdr roof diffusor – fuel savings and co_2 reduction. [Online], available from: http://www.jost-world.com/en/products/jost-truck-and-trailer-components/jost-sdr.html [Accessed December 2013].

Kendall, A. & Koochesfahani, M. 2008 A method for estimating wall friction in turbulent wall-bounded flows. *Exp. Fluids* **44** (5), 773–780.

Khalighi, B., Chen, K.-H. & Iaccarino, G. 2012 Unsteady aerodynamic flow investigation around a simplified square-back road vehicle with drag reduction devices. *J. Fluids Engng* **134** (6).

Khalighi, B., Zhang, S., Koromilas, C., Balkanyi, S. R., Bernal, L. P., Iaccarino, G. & Moin, P. 2001 Experimental and computational study of unsteady wake flow behind a bluff body with a drag reduction device. *SAE paper* pp. 1–15.

Kim, J., Hahn, S., Kim, J., Lee, D.-K., Choi, J., Jeon, W.-P. & Choi, H. 2004 Active control of turbulent flow over a model vehicle for drag reduction. *J. Turbul.* **5** (019), 1–12.

Krajnovic, S. & Davidson, L. 2001 Large-eddy simulation of the flow around a ground vehicle body. *SAE Paper* .

Krajnovic, S. & Davidson, L. 2004 Large-eddy simulation of the flow around simplified car model. *SAE paper* pp. 01–0227.

Krajnovic, S. & Davidson, L. 2005 Flow around a simplified car, part 2: understanding the flow. *J. Fluids Engng* **127** (5), 919–928.

Leuschen, J. & Cooper, K. R. 2006 Full-scale wind tunnel tests of production and prototype, second-generation aerodynamic drag-reducing devices for tractor-trailers. *SAE Paper* .

Lin, C. C. 1944 On the stability of two-dimensional parallel flows. *Proceedings of the National Academy of Sciences of the United States of America* **30** (10), 316.

Ljung, L. 1999 *System Identification. Theory for the User. Second Edition*. Prentice Hall PTR.

McCallen, R. C., Salari, K., Ortega, J., DeChant, L. J., Hassan, B., Roy, C. J., Pointer, W. D., Browand, F., Hammache, M. & Hsu, T. Y. 2004 DOEs effort to reduce truck aerodynamic drag-joint experiments and computations lead to smart design. *AIAA Paper* **2249**.

Moffat, R. J. 1988 Describing the uncertainties in experimental results. *Experimental thermal and fluid science* **1** (1), 3–17.

Moin, P. & Bewley, T. 1994 Feedback control of turbulence. *Appl. Mech. Rev* **47** (6), S3–S13.

Monkewitz, P. A. 1988 A note on vortex shedding from axisymmetric bluff bodies. *J. Fluid Mech.* **192** (561-575), 1158.

Montracon 2013 Fuel saver options. [Online], available from: http://www.montracon.com/FST.html [Accessed December 2013].

Morris, S. C & Foss, J. F. 2003 Turbulent boundary layer to single-stream shear layer: the transition region. *Journal of Fluid Mechanics* **494** (1), 187–221.

Mudguard Technologies 2009–2010 V-flap smart aerodynamic mud flap with spray suppression and true anti-sail design. [Online], available from: http://www.vflap.com/index.php [Accessed December 2013].

Mueller, Michael, Bernal, Luis, Miska, Paul, Washabaugh, Peter, Chou, Tsung-Kuan, Parviz, Babak, Zhang, Chungo & Najafi, Khalil 2001 Flow structure and performance of axisymmetric synthetic jets. In *39th Aerospace Sciences Meeting and Exhibit*. A01-16802.

Nakamura, Y. 1993 Bluff-body aerodynamics and turbulence. *J. Wind Eng. Ind. Aerodyn.* **49** (1), 65–78.

OECD, International Transport Forum 2011 Permissible maximum length of coaches in europe. [Online], available from: http://www.internationaltransportforum.org/IntOrg/road/pdf/Coach.pdf [Accessed January 2013].

OECD, International Transport Forum 2012 Permissible maximum dimensions of trucks in europe. [Online], available from: http://www.internationaltransportforum.org/IntOrg/road/pdf/dimensions.pdf [Accessed January 2013].

Ortega, J., Dunn, T., McCallen, R. & Salari, K. 2004 Computational simulation of heavy vehicle trailer wake. *The Aerodynamics of Heavy Vehicles: Trucks, Buses and Trains* pp. 219–233.

Oxlade, R. A. 2013 High-frequency pulsed jet forcing of an axi-symmetric bluff body wake. PhD thesis, Imperial College.

Papailiou, Demosthenes D & Lykoudis, Paul S 1974 Turbulent vortex streets and the entrainment mechanism of the turbulent wake. *Journal of Fluid Mechanics* **62** (01), 11–31.

Pastoor, M., Henning, L., Noack, B. R., King, R. & Tadmor, G. 2008 Feedback shear layer control for bluff body drag reduction. *J. Fluid Mech.* **608** (1), 161–196.

Qubain, A. 2009 Active control of a turbulent bluff body wake. PhD thesis, Imperial College.

Roshko, A. 1961 Experiments on the flow past a circular cylinder at very high reynolds number. *J. Fluid Mech.* **10** (3), 345–356.

Roshko, A. 1993 Perspectives on bluff body aerodynamics. *J. Wind Eng. Ind. Aerodyn.* **49** (1), 79–100.

Roumeas, M., Gillieron, P. & Kourta, A. 2008 Separated flows around the rear window of a simplified car geometry. *J. Fluids Engng* **130** (2).

Rouméas, M., Gilliéron, P. & Kourta, A. 2009 Analysis and control of the near-wake flow over a square-back geometry. *Computers & Fluids* **38** (1), 60–70.

Scania 2013 Streamline. [Online], available from: http://www4.scania.com/en/streamline/Start/ [Accessed December 2013].

Schlichting, H., Kestin, J., Schlichting, H. & Schlichting, H. 1968 *Boundary-Layer Theory*, 7th edn. McGraw-Hill New York.

Schmid, P. J. & Henningson, D. S. 2001 *Stability and transition in shear flows*, , vol. 142. Springer.

Seifert, A., Dayan, I., Horrell, C., Grossmann, J. & Smith, A. 2010 Heavy trucks fuel savings using SaOB actuator. *The Aerodynamics of Heavy Vehicles III: Trucks, Buses, and Trains Lecture Notes in Applied and Computational Mechanics* .

Seifert, A., Stalnov, O., Sperber, D., Arwatz, G., Palei, V., David, S., Dayan, I. & Fono, I. 2009 Large trucks drag reduction using active flow control. In *The Aerodynamics of Heavy Vehicles II: Trucks, Buses, and Trains*, pp. 115–133. Springer.

Sevilla, A. & Martínez-Bazán, C. 2004 Vortex shedding in high Reynolds number axisymmetric bluff-body wakes: Local linear instability and global bleed control. *Phys. Fluids* **16**, 3460.

Spohn, A. & Gilliéron, P. 2002 Flow separations generated by a simplified geometry of an automotive vehicle. In *IUTAM Symposium: unsteady separated flows*.

Stern, N. 2006 What is the economics of climate change? [Online], available from: http://webarchive.nationalarchives.gov.uk/+/http:/www.hm-treasury.gov.uk/sternreview_index.htm [Accessed March 2014].

Taylor, J. R. 1997 *An Introduction to Error Analysis: the Study of Uncertainties in Physical Measurements*. University Science Books.

Department for Transport, D.f.T. 2009 Uk transport greenhouse gas emissions. [Online], available from: http://assets.dft.gov.uk/statistics/series/energy-and-environment/climatechangefactsheets.pdf [Accessed March 2014].

Department for Transport, D.f.T. 2013 Carbon dioxide emissions by transport mode: United kingdom, 1999-2011. [Online], available from: https://www.gov.uk/government/statistical-data-sets/tsgb03#table-tsgb0307-env0202 [Accessed March 2014].

Vukasinovic, B., Rusak, Z. & Glezer, A. 2010 Dissipative small-scale actuation of a turbulent shear layer. *J. of Fluid Mech.* **656** (1), 51–81.

Wang, X. W., Zhou, Y., Pin, Y. F. & Chan, T. L. 2013 Turbulent near wake of an Ahmed vehicle model. *Exp. Fluids* **54** (4), 1–19.

Wassen, E., Eichinger, S. & Thiele, F. 2010 Simulation of active drag reduction for a square-back vehicle. In *Active Flow Control II*, pp. 241–255. Springer.

Williamson, C. H. K. 1996 Vortex dynamics in the cylinder wake. *Annu. Rev. Fluid Mech.* **28** (1), 477–539.

Wood, Richard M 2004 Impact of advanced aerodynamic technology on transportation energy consumption. *Tech. Rep.*. Society of Automotive Engineers, Inc., Warrendale, PA.

Wood, R. M. & Bauer, S. X. S. 2003 Simple and low-cost aerodynamic drag reduction devices for tractor-trailer trucks. *SAE transactions* **112** (2), 143–160.

Wu, J.-Z., Ma, H.-Y. & Zhou, J. Z. 2006 *Vorticity and vortex dynamics*. Springer.

Appendix A

Actuator Characterisation for Different Slot Sizes

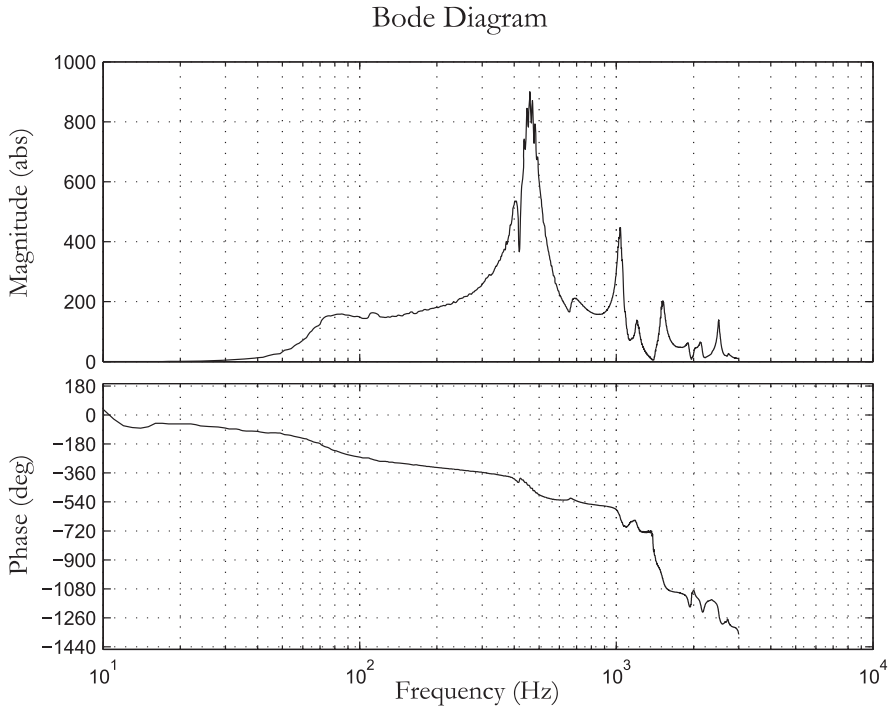

Figure A.1: Bode Diagram of the System for 3.5 mm slot

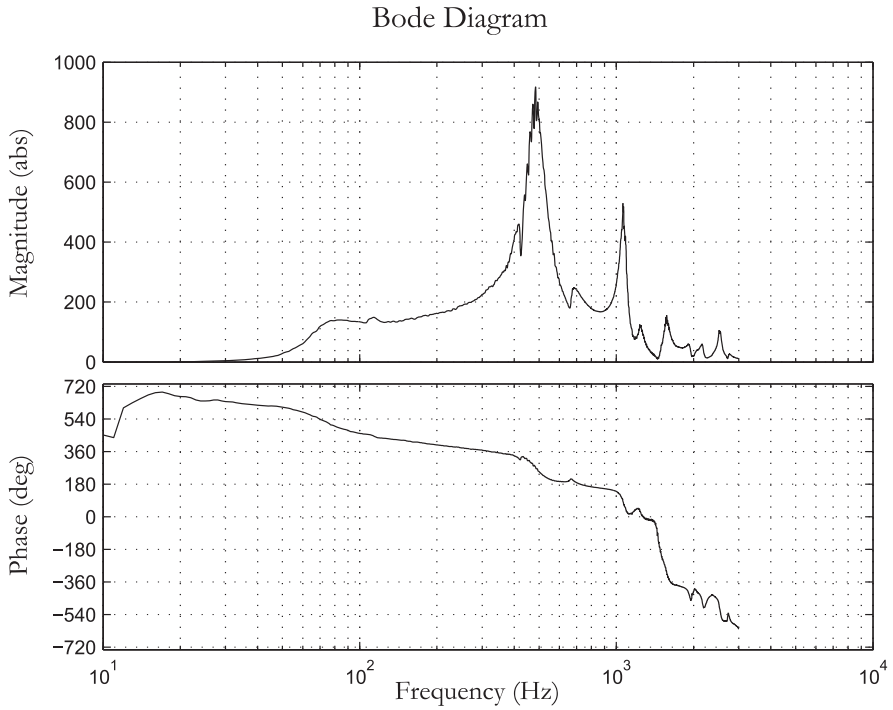

Figure A.2: Bode Diagram of the System for 5.5 mm slot

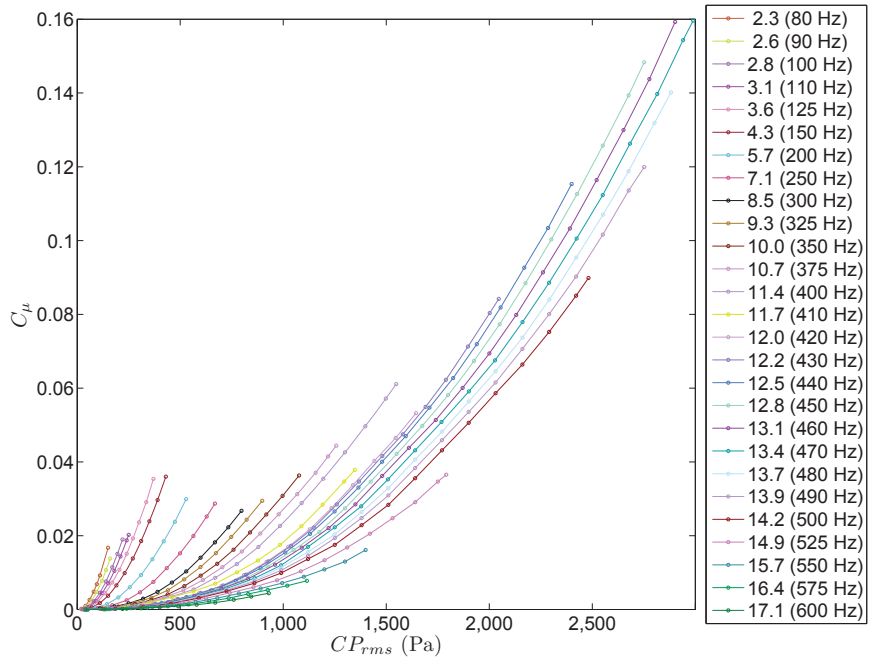

Figure A.3: Actuator Calibration for 3.5 mm slot

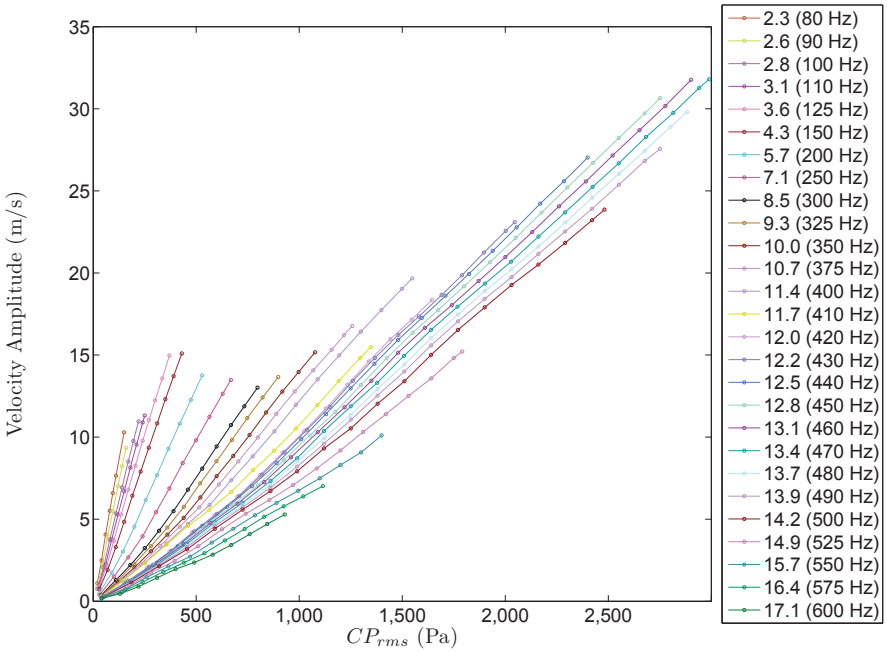

Figure A.4: Jet Velocity Amplitude for 3.5 mm slot

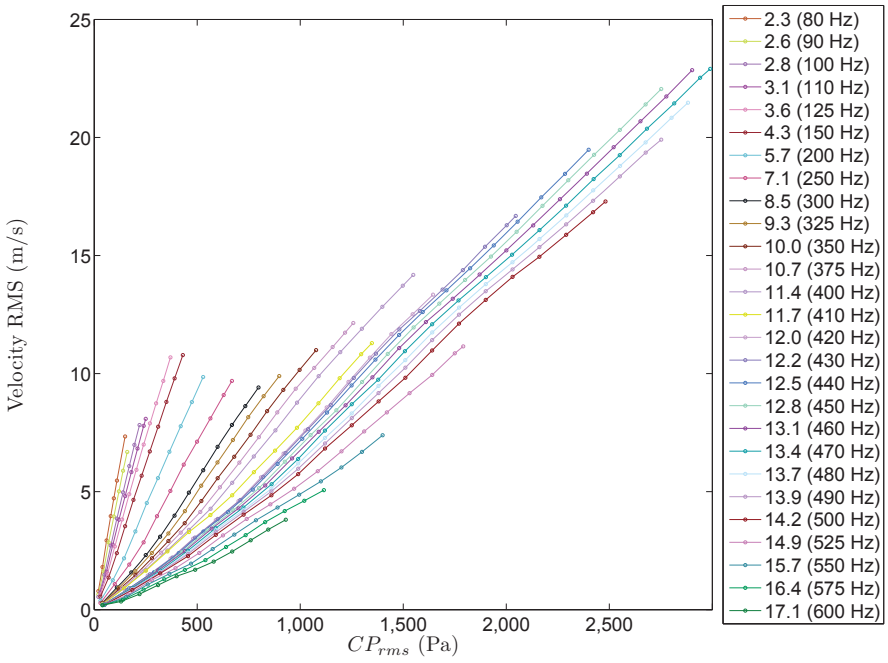

Figure A.5: Jet Velocity RMS for 3.5 mm slot

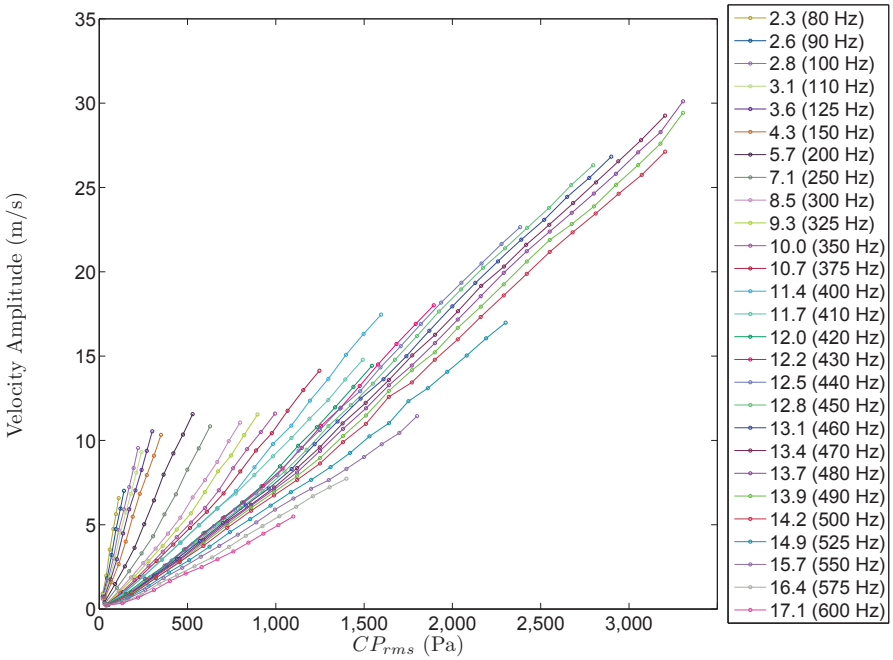

Figure A.6: Jet Velocity Amplitude for 4.5 mm slot

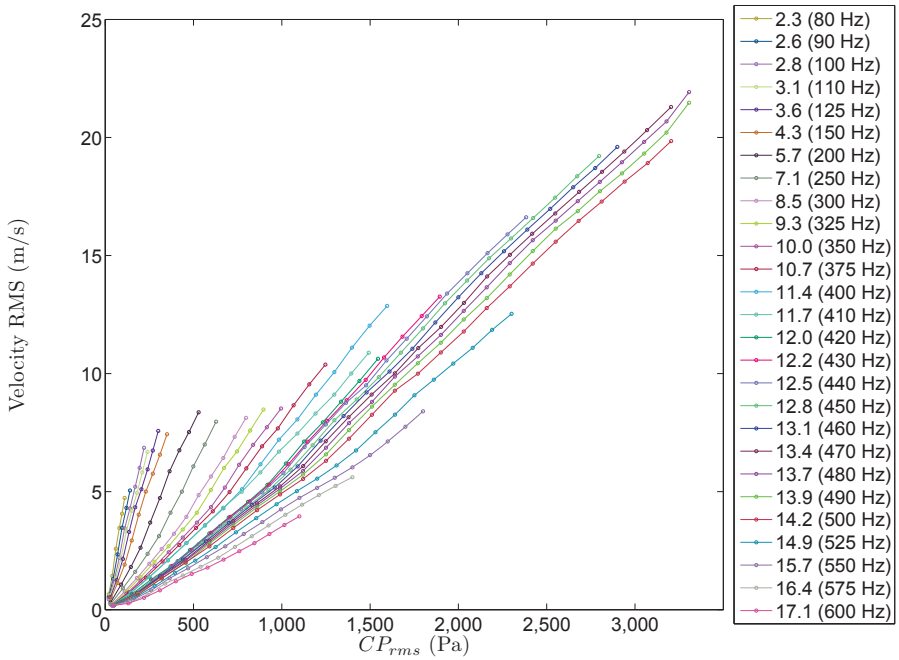

Figure A.7: Jet Velocity RMS for 4.5 mm slot

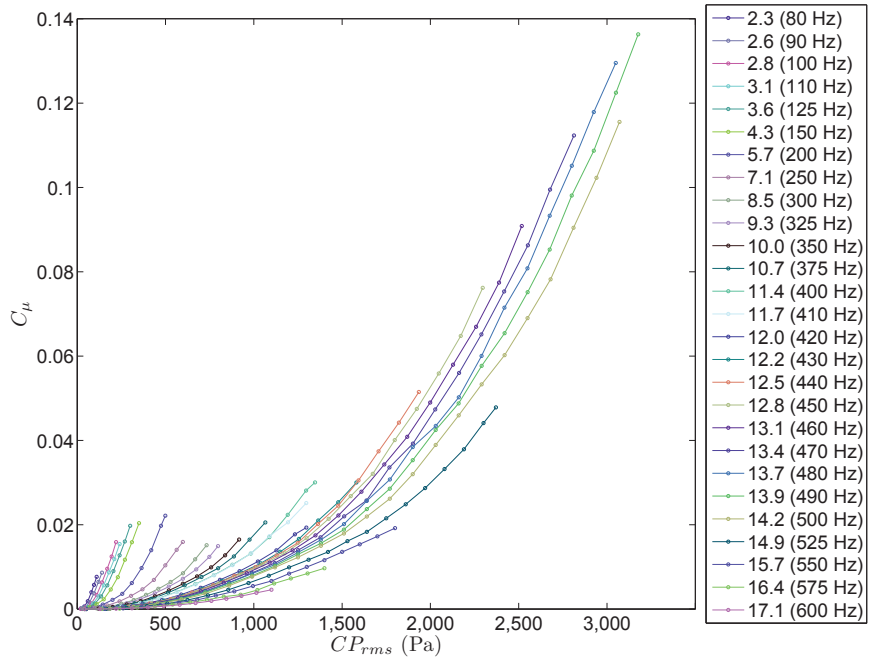

Figure A.8: Actuator Calibration for 5.5 mm slot

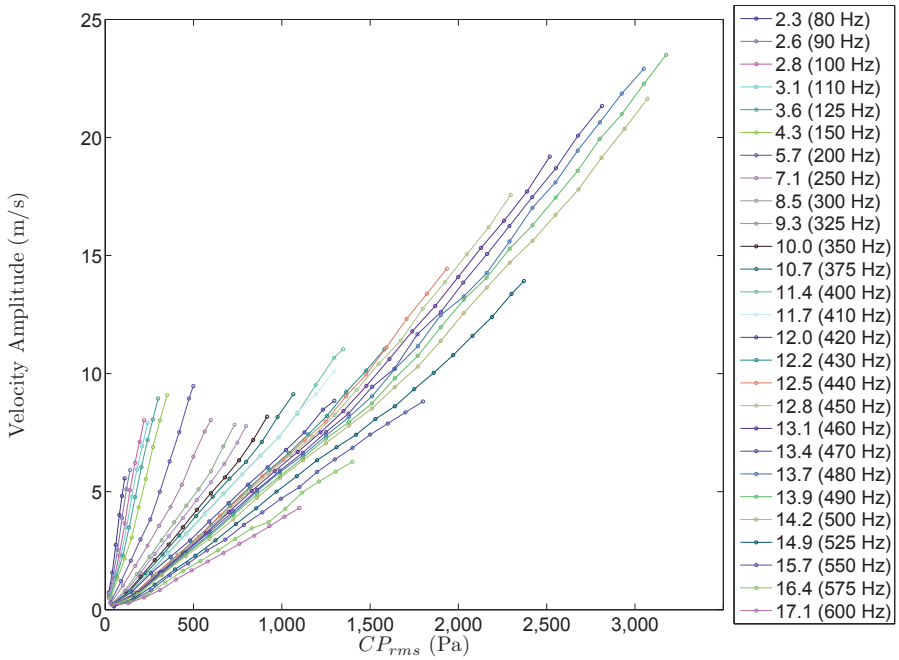

Figure A.9: Jet Velocity Amplitude for 5.5 mm slot

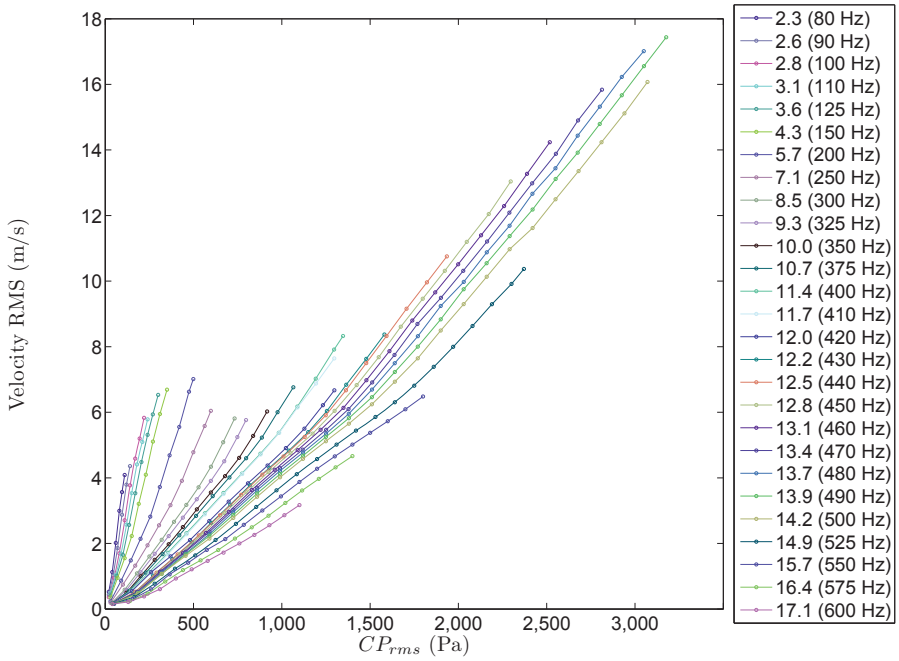

Figure A.10: Jet Velocity RMS for 5.5 mm slot

Appendix B

Calibrations Details

B.1 Endevco 8507C-2 AMG63 Transducer Calibration

Below, the data and the analysis performed for the *Endevco* transducer used to measure the cavity pressure are presented. The data collected during the calibration are listed in Table B.1, while Figures B.1 and B.2 show respectively the fit on the data with a 95% error bound and the fit plus the residuals on the samples points. Finally, in Table B.2, the fitting function and its confidence bounds are evaluated at 11 points equally spaced at 223.562 Pa; these same values are plotted in Figure B.2.

Sampling time (s)	180
Acquisition frequency (Hz)	40000
No. of FCO samples	450
Amplifier gain	100

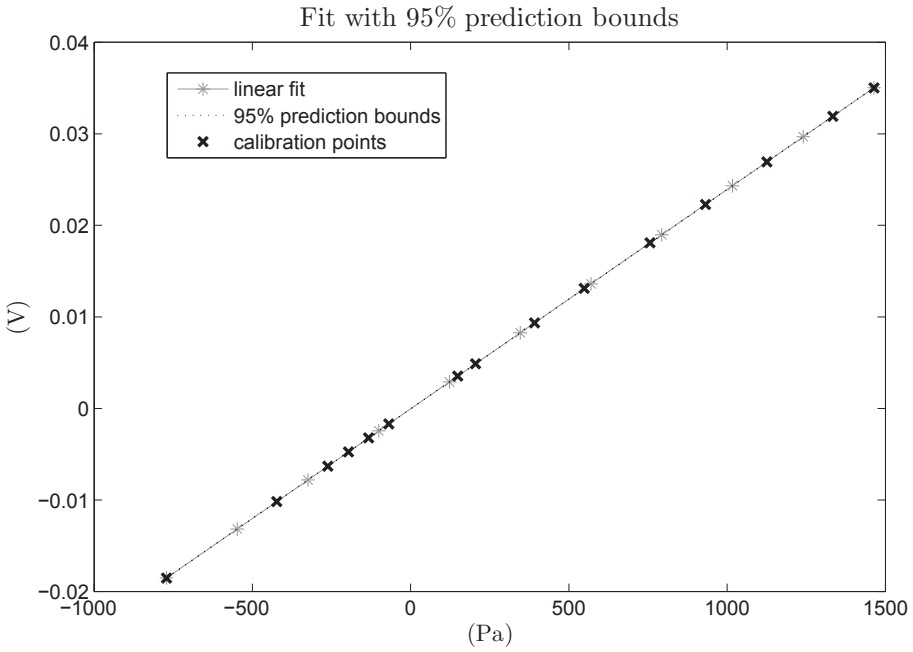

Figure B.1: Transducer characteristic and prediction bounds

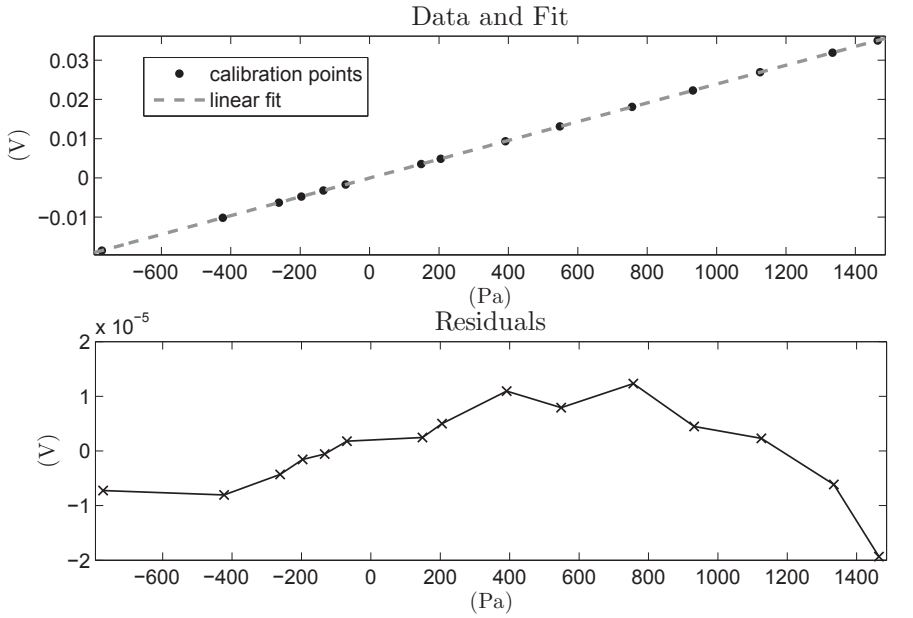

Figure B.2: Calibration points and correspondent residuals.

FCO		8507C-2	
mean(Pa)	stdv (Pa)	mean (V)	stdv (V)
1464.13089	0.319	0.03502	0.001
1334.01979	0.501	0.03191	0.001
1125.51244	0.464	0.02693	0.001
931.49422	0.608	0.02228	0.002
756.51978	0.591	0.01810	0.001
548.57289	0.687	0.01311	0.002
391.34511	0.960	0.00935	0.002
204.92044	1.051	0.00487	0.003
148.81080	0.926	0.00353	0.002
-69.01544	1.170	-0.00169	0.003
-132.91178	1.004	-0.00323	0.002
-196.58560	2.165	-0.00475	0.005
-261.45533	0.812	-0.00631	0.002
-422.86600	3.152	-0.01018	0.008
-771.48956	5.207	-0.01853	0.013

Table B.1: Values acquired during the 8507C-2 AMG Endevco transducer calibration process

Linear model:

$f(x) = p1\ x + p2$

Coefficients (with 95% confidence bounds):

$p1 = 2.396\ 10^{-5}$ $\quad (2.395\ 10^{-5}\ ,\ 2.397\ 10^{-5}\ )$

$p2 = -4.111\ 10^{-5}$ $\quad (-4.646\ 10^{-5}\ ,\ -3.575\ 10^{-5}\ )$

Goodness of fit:

SSE^2: $\quad 9.451\ 10^{-10}$

R^2 $\quad 1$

$RMSE^3$: $\quad 8.526\ 10^{-6}$

X_i	lower $f(X_i)$	$f(X_i)$	upper $f(X_i)$
-771.490	-0.019	-0.019	-0.019
-547.928	-0.013	-0.013	-0.013
-324.366	-0.008	-0.008	-0.008
-100.804	-0.002	-0.002	-0.002
122.758	0.003	0.003	0.003
346.329	0.008	0.008	0.008
569.882	0.014	0.014	0.014
793.444	0.019	0.019	0.019
1017.010	0.024	0.024	0.024
1240.570	0.030	0.030	0.030
1464.130	0.035	0.035	0.035

Table B.2: Fit evaluation at X_i. The X_i are plotted in FigureB.1

2 3

[2]Sum of Squares due to Error, also called Residual Sum of Squares (RSS)

$$RSS = \sum_{i=1}^{n} (y_i - f(x_i)) \tag{B.1}$$

[3]Root Mean Square Error (Standard Error)

$$RMSE = \sqrt{\frac{\sum_{t=1}^{n} (y_t - \hat{y}_t)}{n}} \tag{B.2}$$

B.2 Balance Calibration

This section presents detailed results about the balance calibration. First of all, the graphs relative to the data sampled during the calibration are presented (Figures from B.3 to B.8). Table B.3 reports the gradients calculated for each load cell which is expected to be linear with the load applied. The 95% confidence bounds, the coefficient of determination R^2 and the root mean square error (RMSE) are also shown. Finally, Table B.4 illustrates the matrix used to decipher the balance readings.

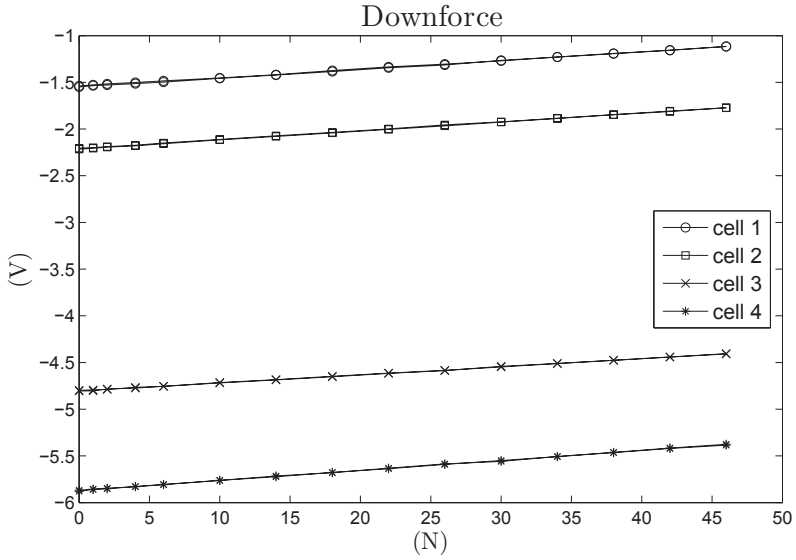

Figure B.3: Balance calibration for downforce. The result is given by the fitting of the load cells correspondent to channels No. 1, 2, 3 and 4.

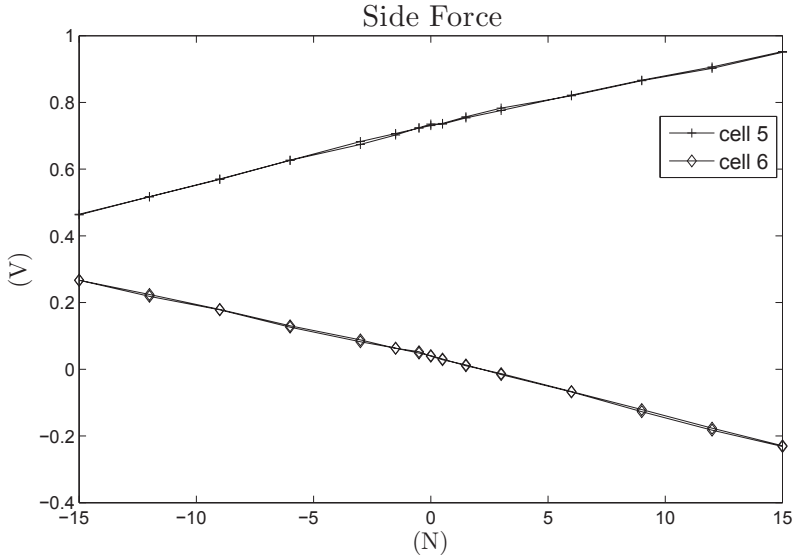

Figure B.5: Balance calibration for side force. The result is given by the fitting of the load cell correspondent to channels No. 5 and 6.

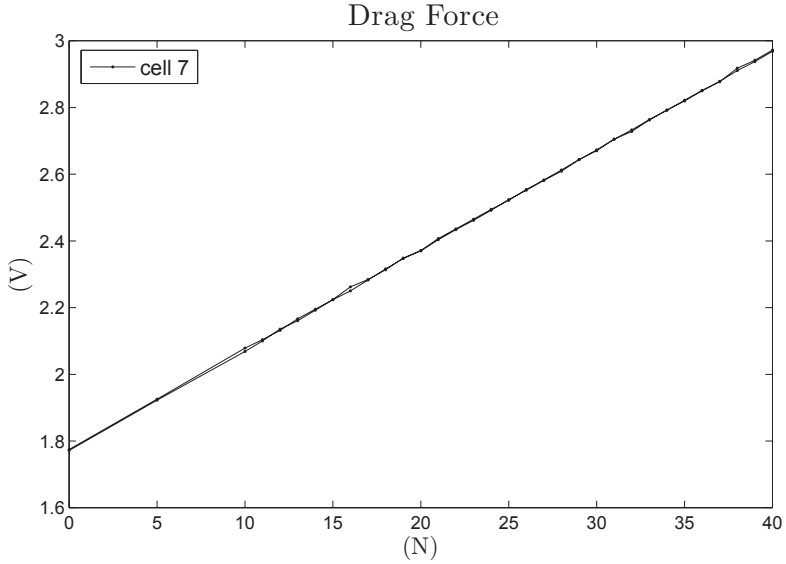

Figure B.4: Balance calibration for drag force. The result is given by the fitting of the load cell correspondent to channel No. 7.

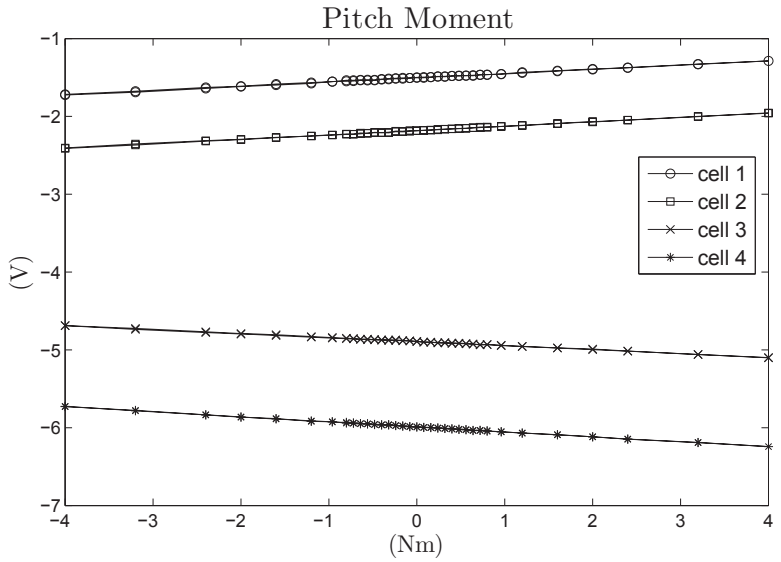

Figure B.6: Balance calibration for pitch moment. The result is given by the fitting of the load cell correspondent to channels No. 1, 2, 3 and 4.

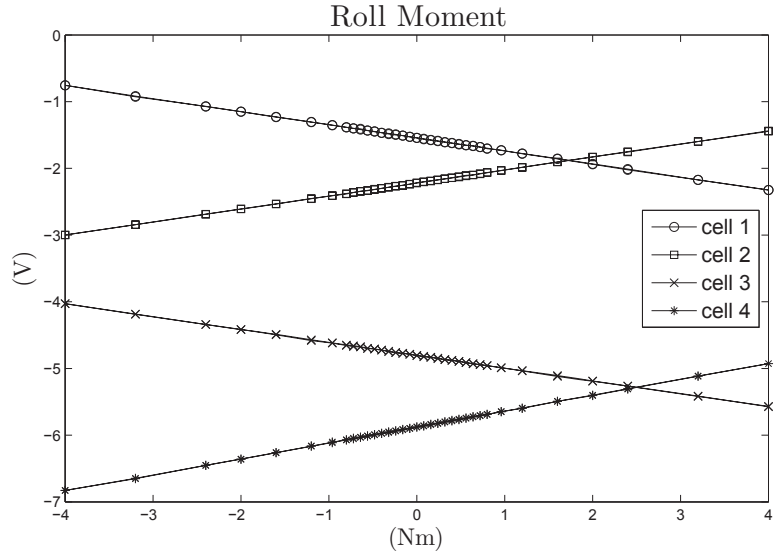

Figure B.7: Balance calibration for roll moment. The result is given by the fitting of the load cell correspondent to channels No. 1, 2, 3 and 4.

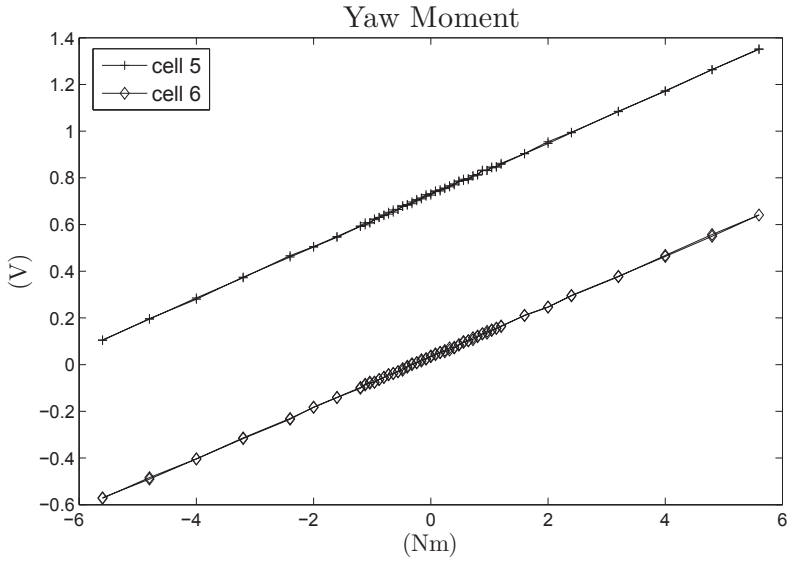

Figure B.8: Balance calibration for roll moment. The result is given by the fitting of the load cell correspondent to channels No. 5 and 6.

Load	cell	gradient	95% confidence bounds	R^2	RMSE
downforce	1	0.00926	(0.00913, 0.00939)	0.9987	0.0052
	2	0.00957	(0.00948, 0.00966)	0.9994	0.0037
	3	0.00863	(0.00855, 0.00871)	0.9994	0.0033
	4	0.01071	(0.01061, 0.01080)	0.9995	0.0037
drag	7	0.02990	(0.02984, 0.02997)	0.9999	0.0027
side	5	0.01625	(0.01582, 0.01669)	0.9953	0.00946
	6	-0.01664	(-0.01703, -0.01625)	0.9964	0.00849
pitch	1	0.05432	(0.05364, 0.05500)	0.9973	0.00451
	2	0.05637	(0.05582, 0.05692)	0.9984	0.00364
	3	-0.05116	(-0.05170, -0.05062)	0.9981	0.00357
	4	-0.06448	(-0.06493, -0.06403)	0.9992	0.00296
roll	1	-0.19620	(-0.19670, -0.19560)	0.9999	0.00340
	2	0.19500	(0.19450, 0.19550)	0.9999	0.00312
	3	-0.19260	(-0.19320, -0.19200)	0.9999	0.00368
	4	0.23870	(0.23820, 0.23920)	0.9999	0.00318
yaw	5	0.11120	(0.11080, 0.11150)	0.9998	0.00345
	6	0.10850	(0.10820, 0.10880)	0.9998	0.00308

Table B.3: Fitting results and evaluation for balance calibration.

29.7718647	0.0063590	0.3733964	3.9420930	-2.5869694	0.0536906
23.8790011	-0.0872603	0.0985702	5.0006650	2.5163594	0.0666419
25.6477289	0.0404998	0.2774027	-4.3631033	0.0092571	-0.1044699
-0.2161303	0.8044802	29.9971958	0.0130550	1.0975410	4.5977543
-0.5443211	-0.7059831	-30.7419529	0.0337124	-0.8969479	4.5062635
3.7301858	33.4715198	0.7015452	-1.6764372	0.0448091	-0.2655913

Table B.4: Calibration matrix.

Appendix C

Forced Flow Results

The following Tables C.1 and C.2 summarise the results for the forced flow with a 4.5 mm wide slot. The same results are then shown in Figures C.1 and C.2, which correspond to the projection of the Figures 5.1 and 5.2 on the planes $\Delta C_p/C_{pB}$ C_μ and $\Delta C_D/C_{DB}$ C_μ respectively.

	Forcing Frequency (St_{Hf})							
C_μ	12.2	12.5	12.8	13.1	13.4	13.7	13.9	14.2
0.014	0.074 ± 0.005	0.074 ± 0.005	0.065 ± 0.005	0.064 ± 0.003	0.061 ± 0.005	0.059 ± 0.005	0.062 ± 0.005	0.057 ± 0.004
0.022	0.110 ± 0.006	0.106 ± 0.004	0.099 ± 0.005	0.090 ± 0.002	0.093 ± 0.006	0.088 ± 0.004	0.084 ± 0.004	0.083 ± 0.004
0.030	0.129 ± 0.006	0.128 ± 0.002	0.118 ± 0.005	0.113 ± 0.004	0.109 ± 0.008	0.104 ± 0.005	0.109 ± 0.004	0.103 ± 0.003
0.037	0.148 ± 0.003	0.145 ± 0.006	0.138 ± 0.007	0.125 ± 0.004	0.120 ± 0.003	0.124 ± 0.008	0.118 ± 0.003	0.116 ± 0.006
0.045	0.166 ± 0.003	0.162 ± 0.008	0.148 ± 0.006	0.138 ± 0.006	0.132 ± 0.008	0.130 ± 0.007	0.129 ± 0.003	0.121 ± 0.004
0.061	0.184 ± 0.005	0.188 ± 0.006	0.172 ± 0.005	0.164 ± 0.004	0.163 ± 0.007	0.156 ± 0.008	0.149 ± 0.004	0.131 ± 0.003
0.076		0.208 ± 0.006	0.198 ± 0.005	0.189 ± 0.005	0.197 ± 0.005	0.182 ± 0.009	0.174 ± 0.006	0.160 ± 0.004
0.091		0.231 ± 0.008	0.212 ± 0.004	0.205 ± 0.005	0.214 ± 0.008	0.209 ± 0.007	0.194 ± 0.005	0.181 ± 0.005
0.107			0.230 ± 0.005	0.221 ± 0.004	0.234 ± 0.009	0.219 ± 0.007	0.221 ± 0.004	0.204 ± 0.006
0.122			0.244 ± 0.004	0.233 ± 0.004	0.238 ± 0.009	0.239 ± 0.009	0.236 ± 0.005	0.225 ± 0.005
0.137			0.252 ± 0.005	0.239 ± 0.009	0.248 ± 0.010	0.247 ± 0.007	0.254 ± 0.006	0.242 ± 0.007
0.153					0.256 ± 0.010	0.261 ± 0.013	0.269 ± 0.008	0.260 ± 0.003
0.168					0.256 ± 0.011	0.266 ± 0.011	0.277 ± 0.007	
0.184					0.231 ± 0.004	0.237 ± 0.004	0.273 ± 0.007	

Table C.1: $\Delta C_p/C_{pB}$ results when forcing at different C_μ for 4.5 mm wide slot – see Figure C.1.

	Forcing Frequency (St_{Hf})							
C_μ	12.2	12.5	12.8	13.1	13.4	13.7	13.9	14.2
0.014	-0.019 ± 0.003	-0.019 ± 0.002	-0.015 ± 0.001	-0.015 ± 0.001	-0.015 ± 0.001	-0.013 ± 0.001	-0.015 ± 0.001	-0.015 ± 0.001
0.022	-0.031 ± 0.003	-0.030 ± 0.001	-0.028 ± 0.001	-0.026 ± 0.001	-0.026 ± 0.001	-0.025 ± 0.001	-0.027 ± 0.001	-0.027 ± 0.001
0.030	-0.038 ± 0.002	-0.039 ± 0.001	-0.038 ± 0.001	-0.035 ± 0.001	-0.034 ± 0.001	-0.032 ± 0.001	-0.034 ± 0.002	-0.033 ± 0.001
0.037	-0.048 ± 0.003	-0.047 ± 0.001	-0.045 ± 0.001	-0.042 ± 0.001	-0.039 ± 0.001	-0.036 ± 0.002	-0.038 ± 0.001	-0.037 ± 0.001
0.045	-0.054 ± 0.003	-0.053 ± 0.001	-0.049 ± 0.001	-0.048 ± 0.001	-0.044 ± 0.001	-0.040 ± 0.002	-0.041 ± 0.001	-0.039 ± 0.001
0.061	-0.064 ± 0.003	-0.065 ± 0.002	-0.064 ± 0.001	-0.061 ± 0.002	-0.057 ± 0.001	-0.049 ± 0.002	-0.046 ± 0.001	-0.040 ± 0.002
0.076		-0.073 ± 0.001	-0.071 ± 0.001	-0.069 ± 0.002	-0.066 ± 0.001	-0.058 ± 0.003	-0.055 ± 0.002	-0.049 ± 0.001
0.091		-0.087 ± 0.002	-0.081 ± 0.002	-0.079 ± 0.002	-0.077 ± 0.002	-0.072 ± 0.002	-0.065 ± 0.001	-0.056 ± 0.003
0.107			-0.095 ± 0.002	-0.095 ± 0.002	-0.091 ± 0.002	-0.083 ± 0.002	-0.079 ± 0.002	-0.071 ± 0.003
0.122			-0.108 ± 0.002	-0.103 ± 0.003	-0.097 ± 0.003	-0.092 ± 0.002	-0.090 ± 0.002	-0.083 ± 0.003
0.137			-0.119 ± 0.002	-0.115 ± 0.003	-0.106 ± 0.003	-0.102 ± 0.002	-0.101 ± 0.002	-0.095 ± 0.003
0.153					-0.116 ± 0.003	-0.112 ± 0.002	-0.111 ± 0.002	-0.106 ± 0.003
0.168					-0.123 ± 0.003	-0.121 ± 0.002	-0.121 ± 0.002	
0.184					-0.125 ± 0.001	-0.124 ± 0.001	-0.131 ± 0.002	

Table C.2: $\Delta C_D/C_{DB}$ results when forcing at different C_μ for 4.5 mm wide slot – see Figure C.2.

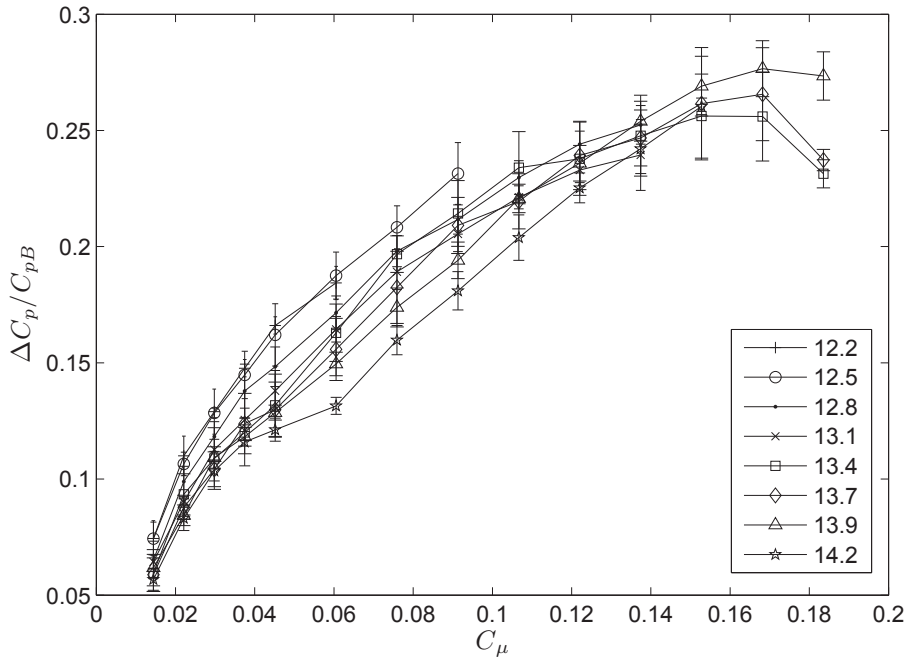

Figure C.1: $\Delta C_p/C_{pB}$ results when forcing at different C_μ for 4.5 mm wide slot – see Table C.1.

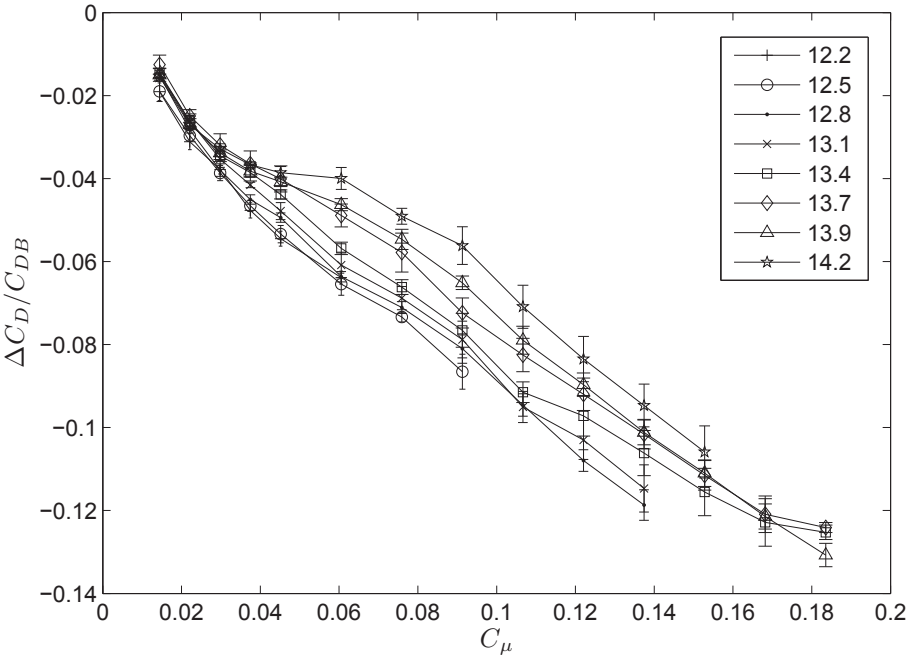

Figure C.2: $\Delta C_D/C_{DB}$ results when forcing at different C_μ for 4.5 mm wide slot – see Table C.2.

	Forcing Frequency (St_{Hf})	
C_μ	12.8	13.4
0.014	0.070 ± 0.003	0.067 ± 0.005
0.022	0.104 ± 0.005	0.096 ± 0.004
0.030	0.131 ± 0.003	0.118 ± 0.003
0.037	0.147 ± 0.005	0.134 ± 0.003
0.045	0.165 ± 0.004	0.150 ± 0.002
0.061	0.184 ± 0.004	0.165 ± 0.003
0.076	0.199 ± 0.004	0.179 ± 0.004
0.091	0.211 ± 0.005	0.186 ± 0.004
0.107	0.214 ± 0.003	0.185 ± 0.003
0.122	0.211 ± 0.003	0.181 ± 0.002
0.137	0.203 ± 0.003	0.169 ± 0.004
0.153	0.196 ± 0.005	0.160 ± 0.004
0.168	0.179 ± 0.004	0.142 ± 0.005
0.184	0.172 ± 0.004	0.124 ± 0.005

Table C.3: $\Delta C_p/C_{pB}$ results when forcing at different C_μ for 3.5 mm wide slot – see Figure C.3.

	Forcing Frequency (St_{Hf})	
C_μ	12.8	13.4
0.014	-0.021 ± 0.001	-0.022 ± 0.001
0.022	-0.037 ± 0.001	-0.035 ± 0.001
0.030	-0.048 ± 0.001	-0.044 ± 0.001
0.037	-0.056 ± 0.001	-0.051 ± 0.001
0.045	-0.063 ± 0.001	-0.058 ± 0.002
0.061	-0.074 ± 0.001	-0.069 ± 0.001
0.076	-0.084 ± 0.002	-0.079 ± 0.001
0.091	-0.092 ± 0.001	-0.088 ± 0.001
0.107	-0.099 ± 0.001	-0.095 ± 0.001
0.122	-0.104 ± 0.001	-0.101 ± 0.001
0.137	-0.108 ± 0.001	-0.106 ± 0.001
0.153	-0.113 ± 0.001	-0.110 ± 0.001
0.168	-0.114 ± 0.001	-0.114 ± 0.001
0.184	-0.121 ± 0.001	-0.120 ± 0.001

Table C.4: $\Delta C_D/C_{DB}$ results when forcing at different C_μ for 3.5 mm wide slot – see Figure C.4.

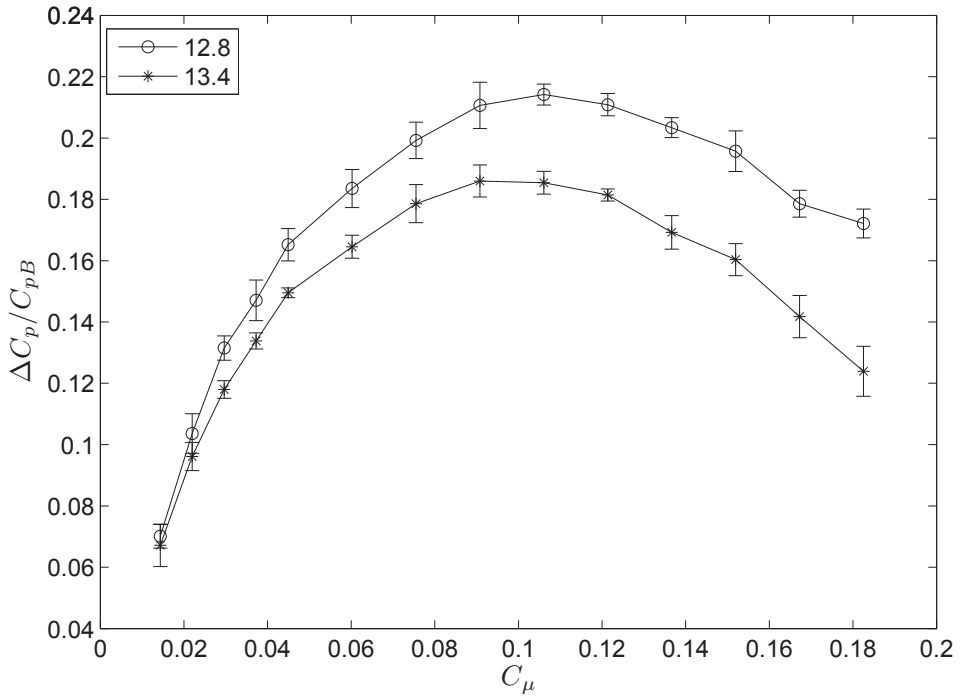

Figure C.3: $\Delta C_p/C_{pB}$ results when forcing at different C_μ and St_{Hf} for 3.5 mm wide slot – see Table C.3.

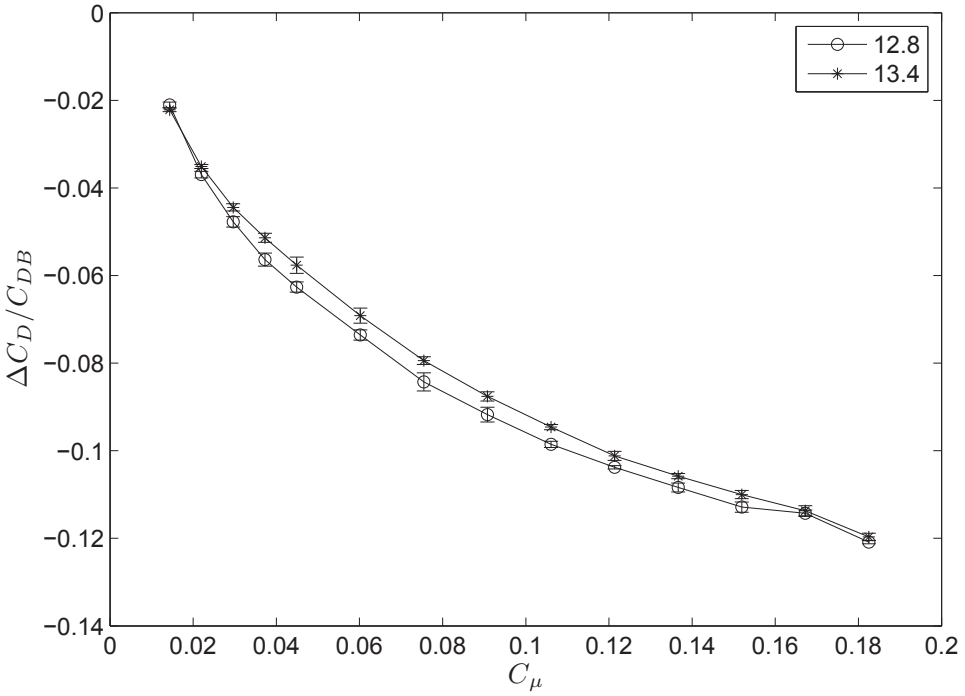

Figure C.4: $\Delta C_D/C_{DB}$ results when forcing at different C_μ and St_{Hf} for 3.5 mm wide slot – see Table C.4.

	Forcing Frequency (St_{Hf})	
C_μ	12.8	13.4
0.014	0.063 ± 0.003	0.055 ± 0.003
0.022	0.095 ± 0.002	0.083 ± 0.003
0.030	0.117 ± 0.004	0.102 ± 0.004
0.037	0.135 ± 0.004	0.111 ± 0.003
0.045	0.146 ± 0.003	0.122 ± 0.003
0.061	0.173 ± 0.006	0.149 ± 0.004
0.076	0.195 ± 0.005	0.172 ± 0.004
0.091	0.205 ± 0.006	0.184 ± 0.004
0.107	0.208 ± 0.003	0.191 ± 0.004
0.122	0.217 ± 0.006	0.200 ± 0.005
0.137		0.204 ± 0.005
0.153		0.211 ± 0.004
0.168		0.210 ± 0.007

Table C.5: $\Delta C_p/C_{pB}$ results when forcing at different C_μ for 5.5 mm wide slot – see Figure C.5.

	Forcing Frequency (St_{Hf})	
C_μ	12.8	13.4
0.014	-0.013 ± 0.012	-0.008 ± 0.012
0.022	-0.023 ± 0.012	-0.017 ± 0.012
0.030	-0.032 ± 0.012	-0.026 ± 0.013
0.037	-0.038 ± 0.012	-0.033 ± 0.012
0.045	-0.046 ± 0.012	-0.036 ± 0.012
0.061	-0.058 ± 0.012	-0.051 ± 0.013
0.076	-0.069 ± 0.013	-0.066 ± 0.014
0.091	-0.076 ± 0.013	-0.074 ± 0.013
0.107	-0.082 ± 0.013	-0.083 ± 0.014
0.122	-0.091 ± 0.013	-0.089 ± 0.014
0.137		-0.095 ± 0.013
0.153		-0.102 ± 0.015
0.168		-0.106 ± 0.014

Table C.6: $\Delta C_D/C_{DB}$ results when forcing at different C_μ for 5.5 mm wide slot – see Figure C.6.

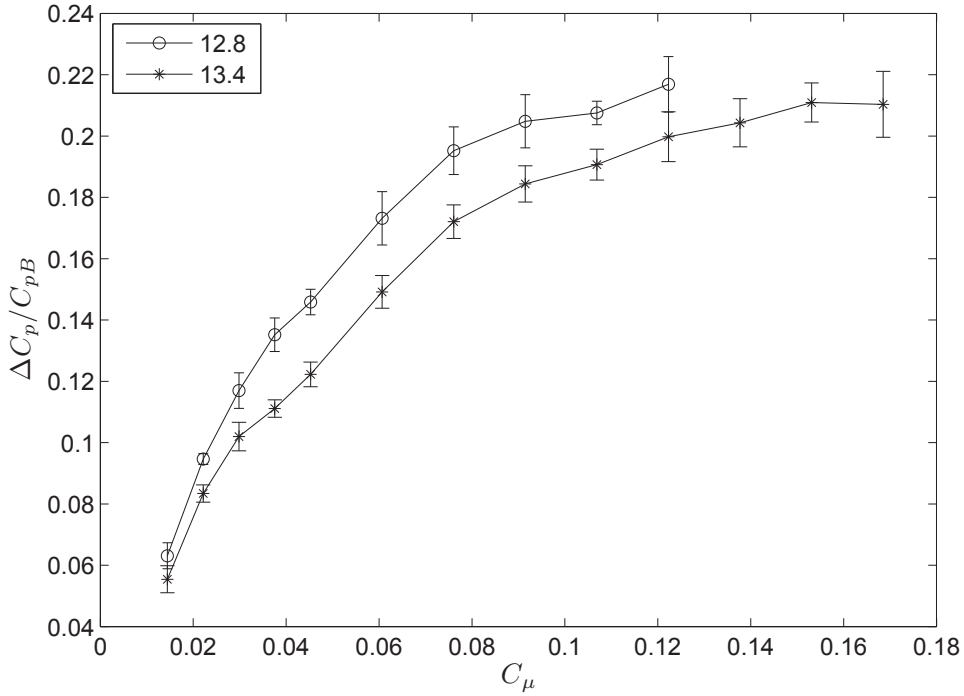

Figure C.5: $\Delta C_p/C_{pB}$ results when forcing at different C_μ and $StHf$ for 5.5 mm wide slot – see Table C.5.

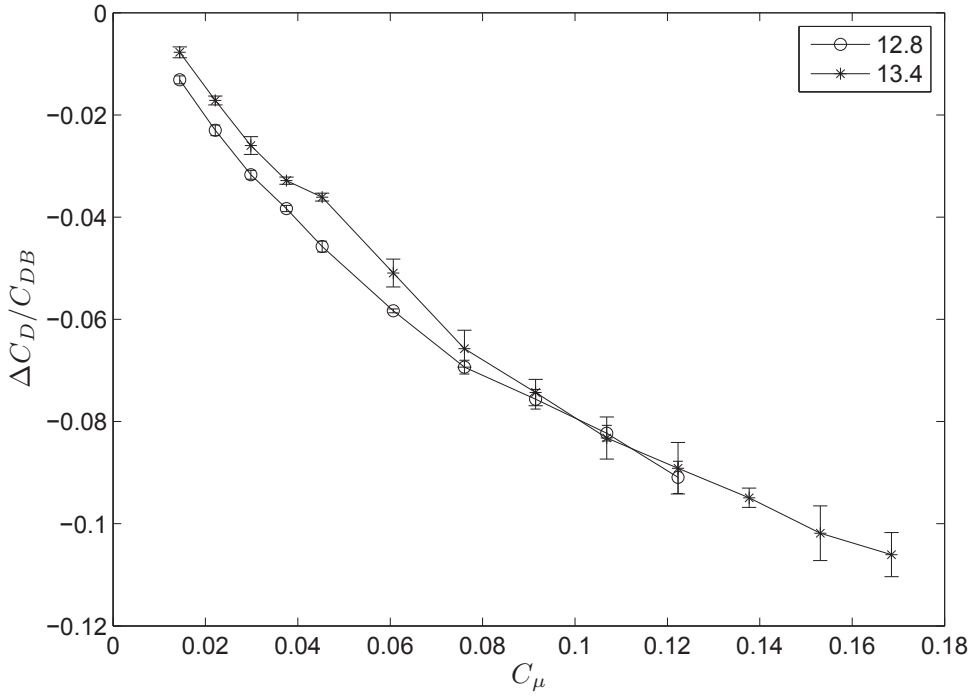

Figure C.6: $\Delta C_D/C_{DB}$ results when forcing at different C_μ and St_{Hf} for 5.5 mm wide slot – see Table C.6.

Appendix D

Measuring System Set-up and Electrical Connections Schemes

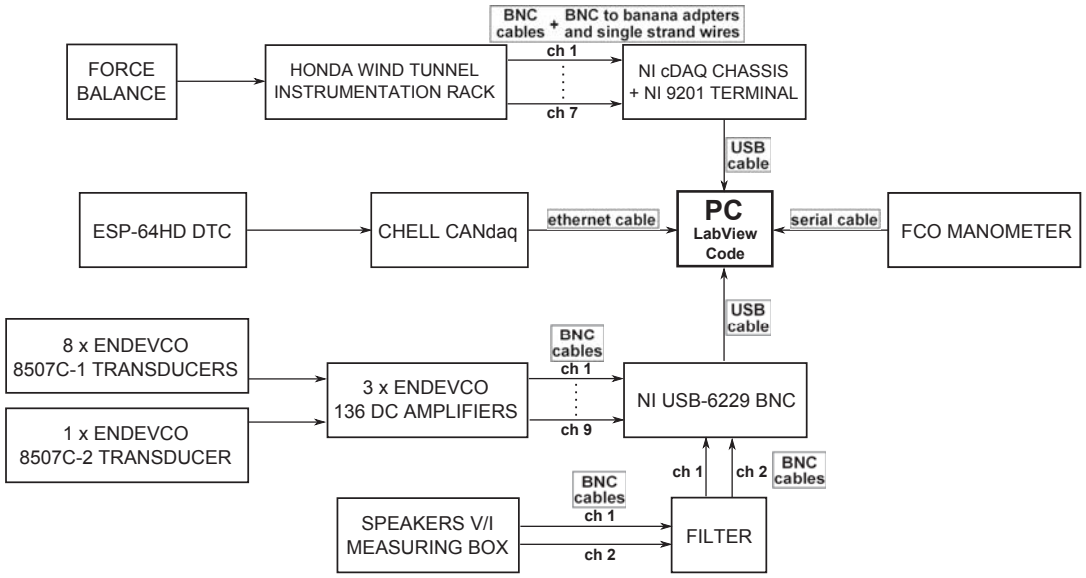

Figure D.1: Scheme of the measuring system set-up.

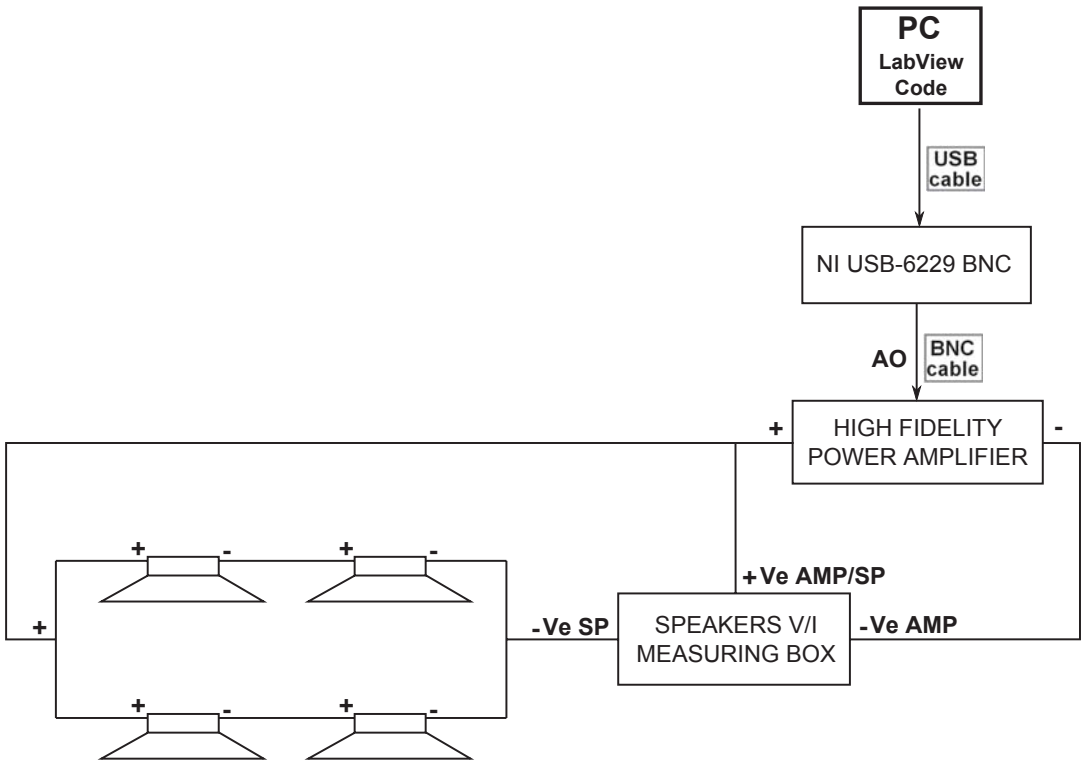

Figure D.2: Scheme of the speakers driving system set-up.

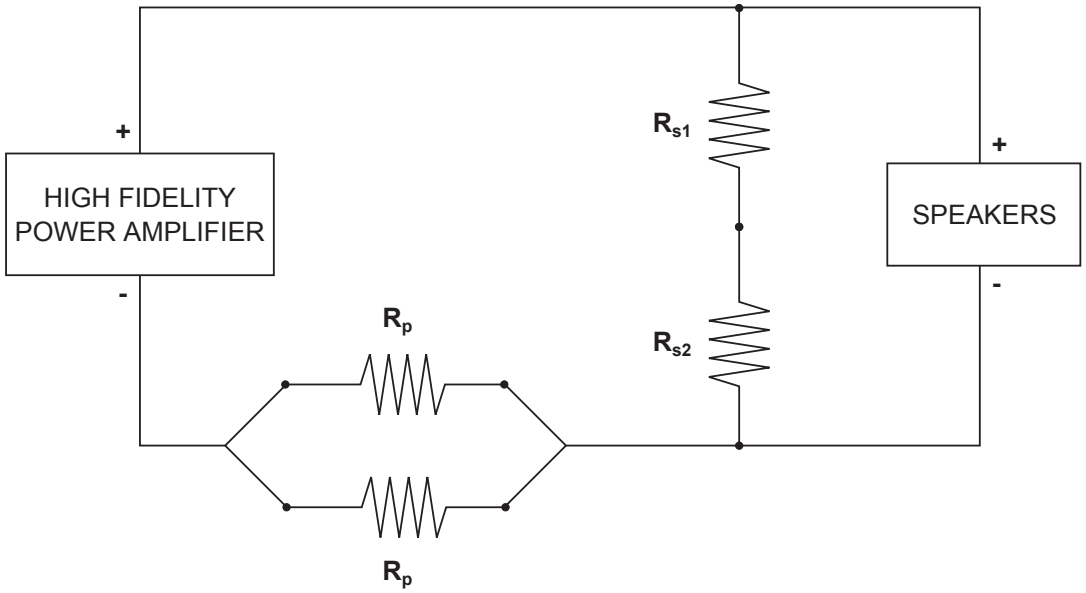

Figure D.3: Scheme of the speakers driving voltage and current measuring system. $R_p = 0.150\,\Omega$, $R_{s1} = 1500\,\Omega$, $R_{s2} = 150\,\Omega$. The voltage across the speakers is calculated as $V = V_p/R_{s2}/(R_{s1} + R_{s2})$. The current across the speakers is calculated as $I = V_s/R_s$. V_s and V_p correspond respectively to the voltages measured across the series and the parallel of resistances.

Appendix E

Technical Drawings

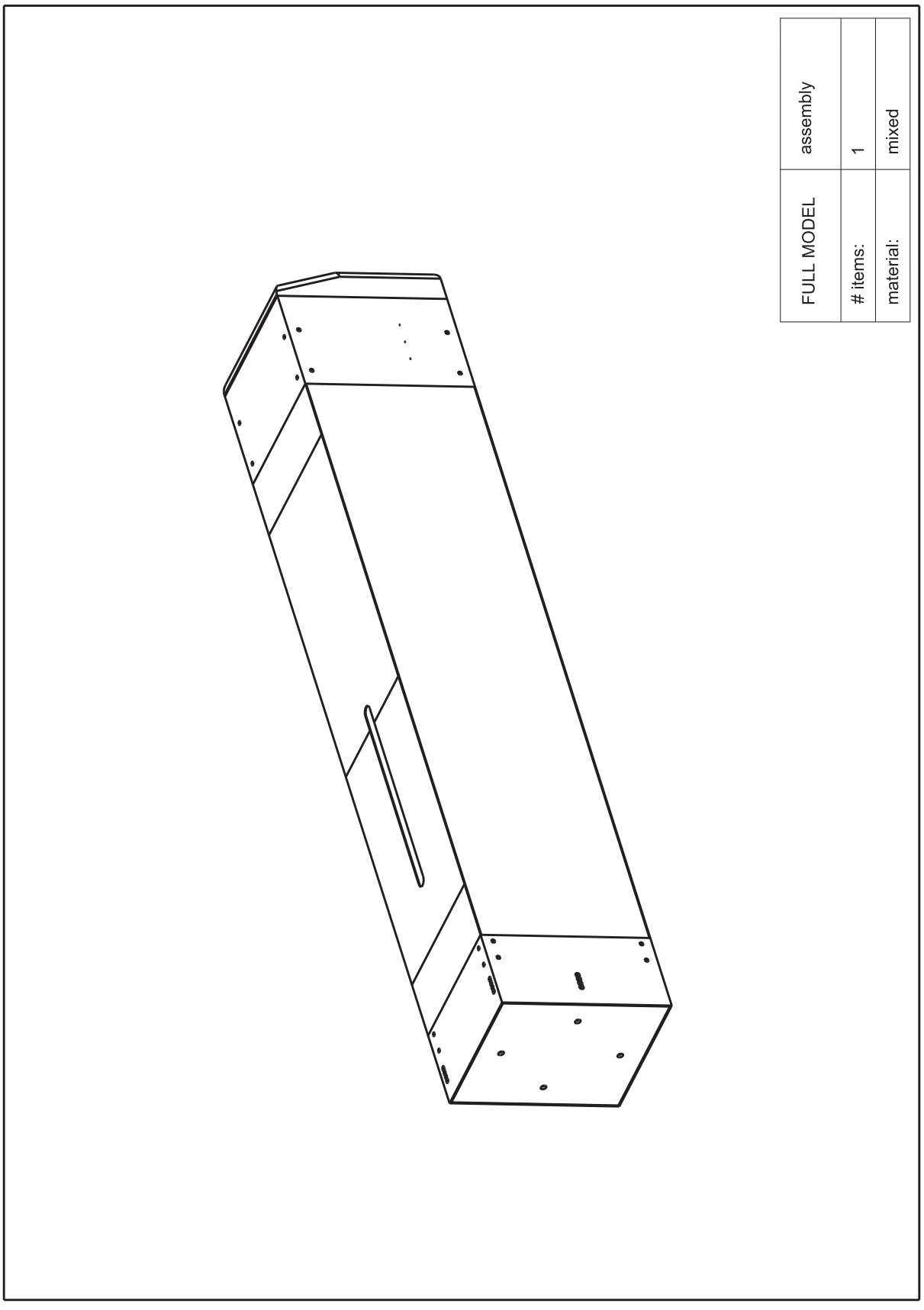
FULL MODEL
assembly
items:
1
material:
mixed

FULL MODEL
exploded view
items:
1
material:
mixed

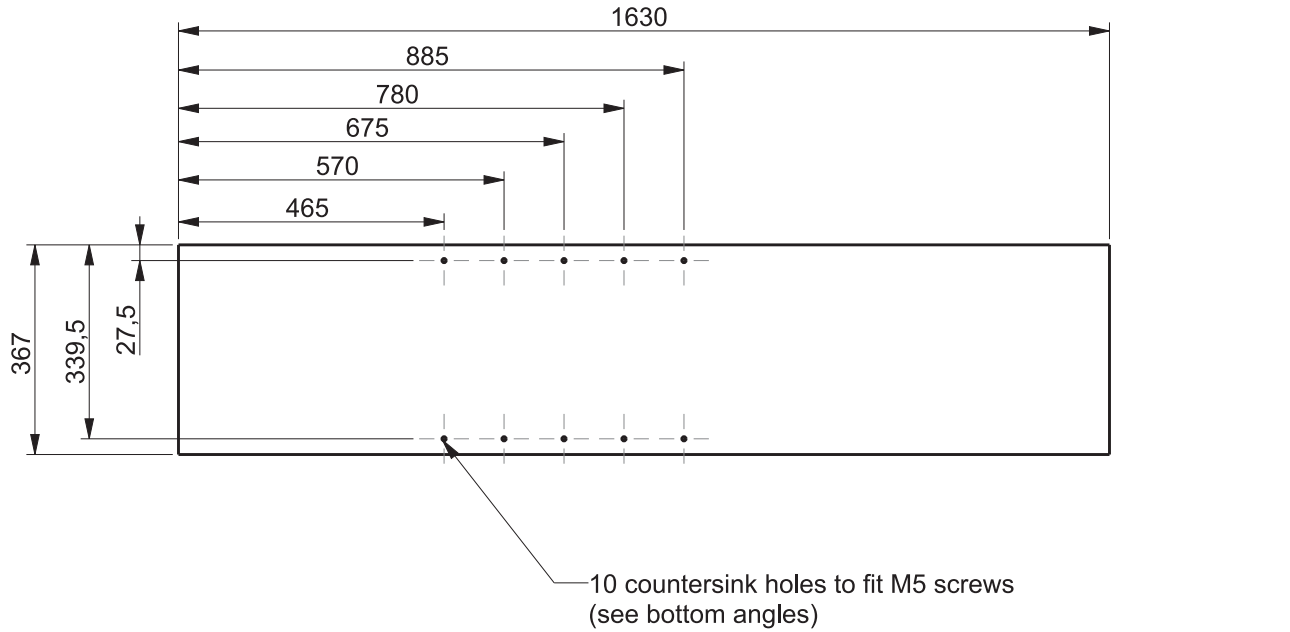

BODY BOTTOM	
# items:	1
material:	carbon fibre

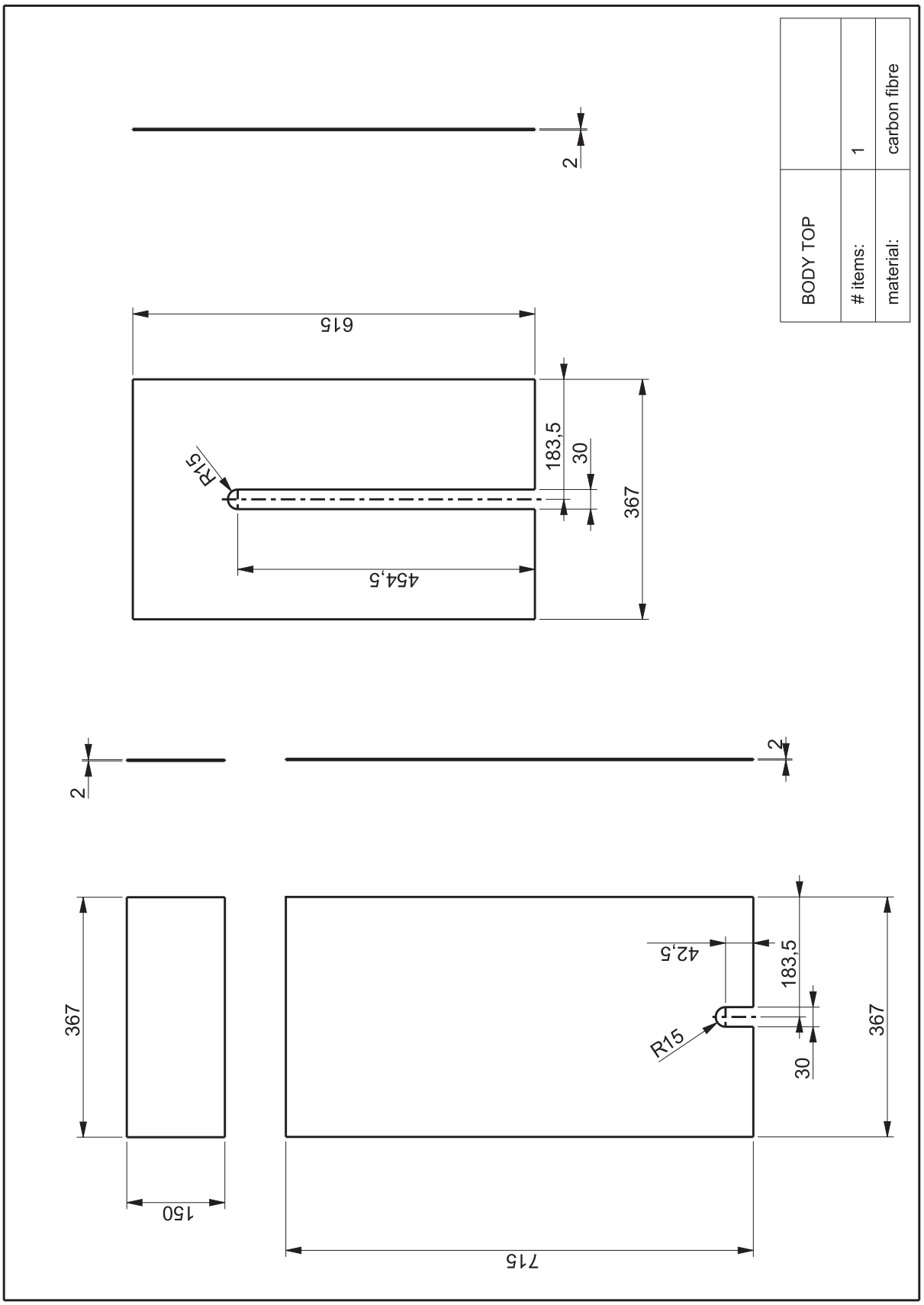
BODY TOP
items: 1
material: carbon fibre
2
615
183,5
30
367
R15
454,5
2
2
367
150
715
42,5
183,5
R15
30
367

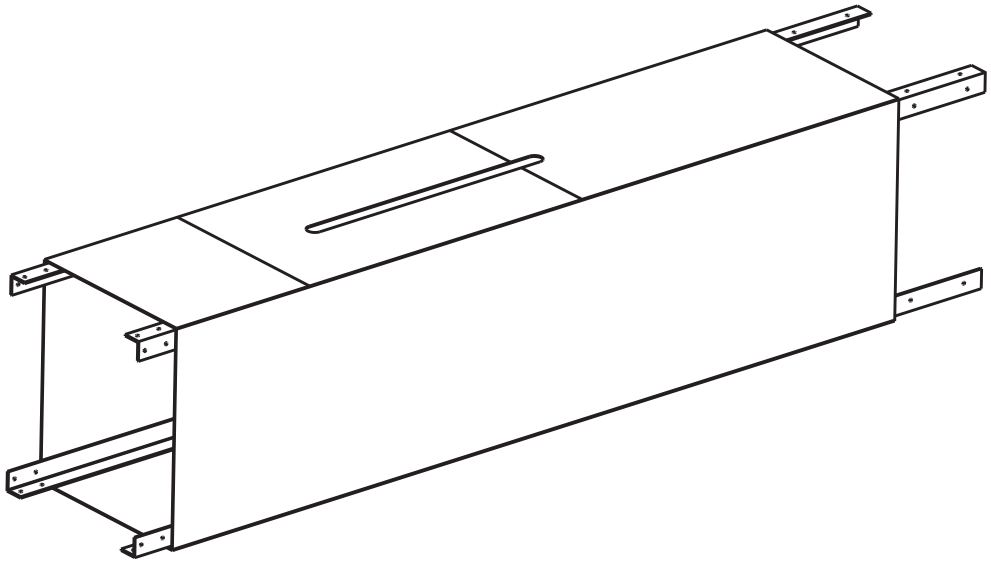

SCALE 0,100

COMPLETE BOBY	assembly
# items:	1
material:	mixed

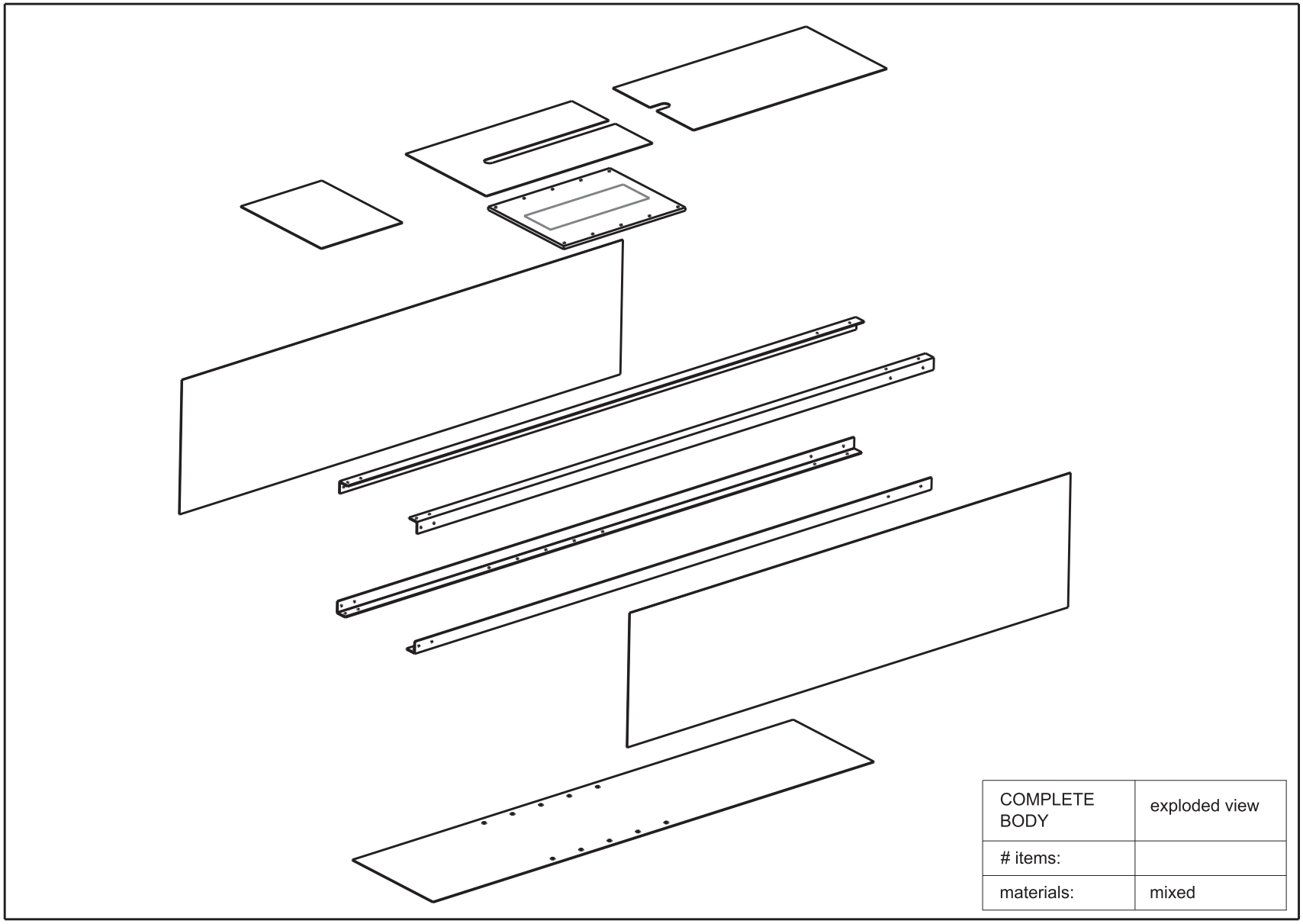

COMPLETE BODY	exploded view
# items:	
materials:	mixed

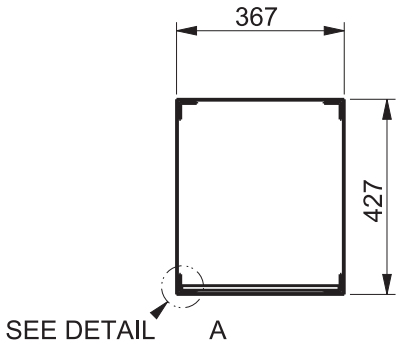

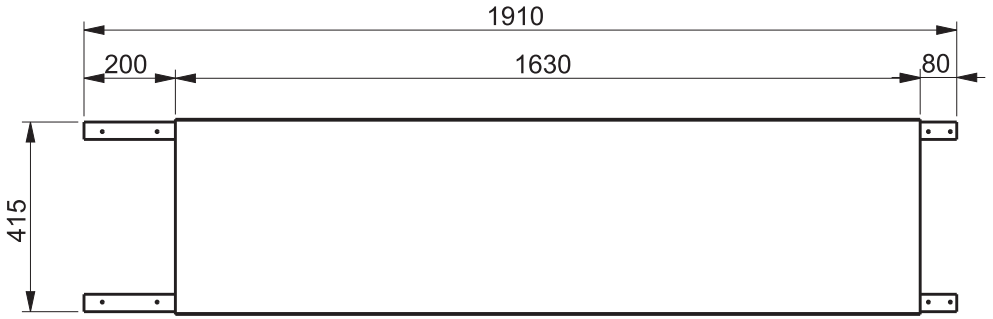

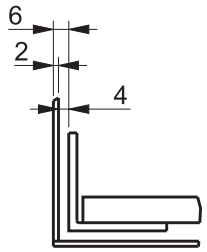

DETAIL A
SCALE 0,450

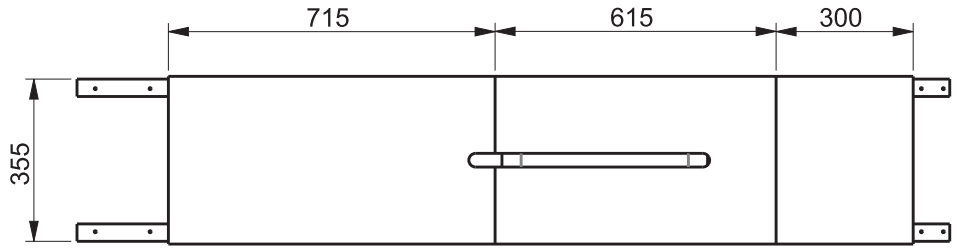

Spacers have to be put in between the panels and the angles to reach the total thickness of 6mm.

COMPLETE BODY	assembly
# items:	
material:	mixed

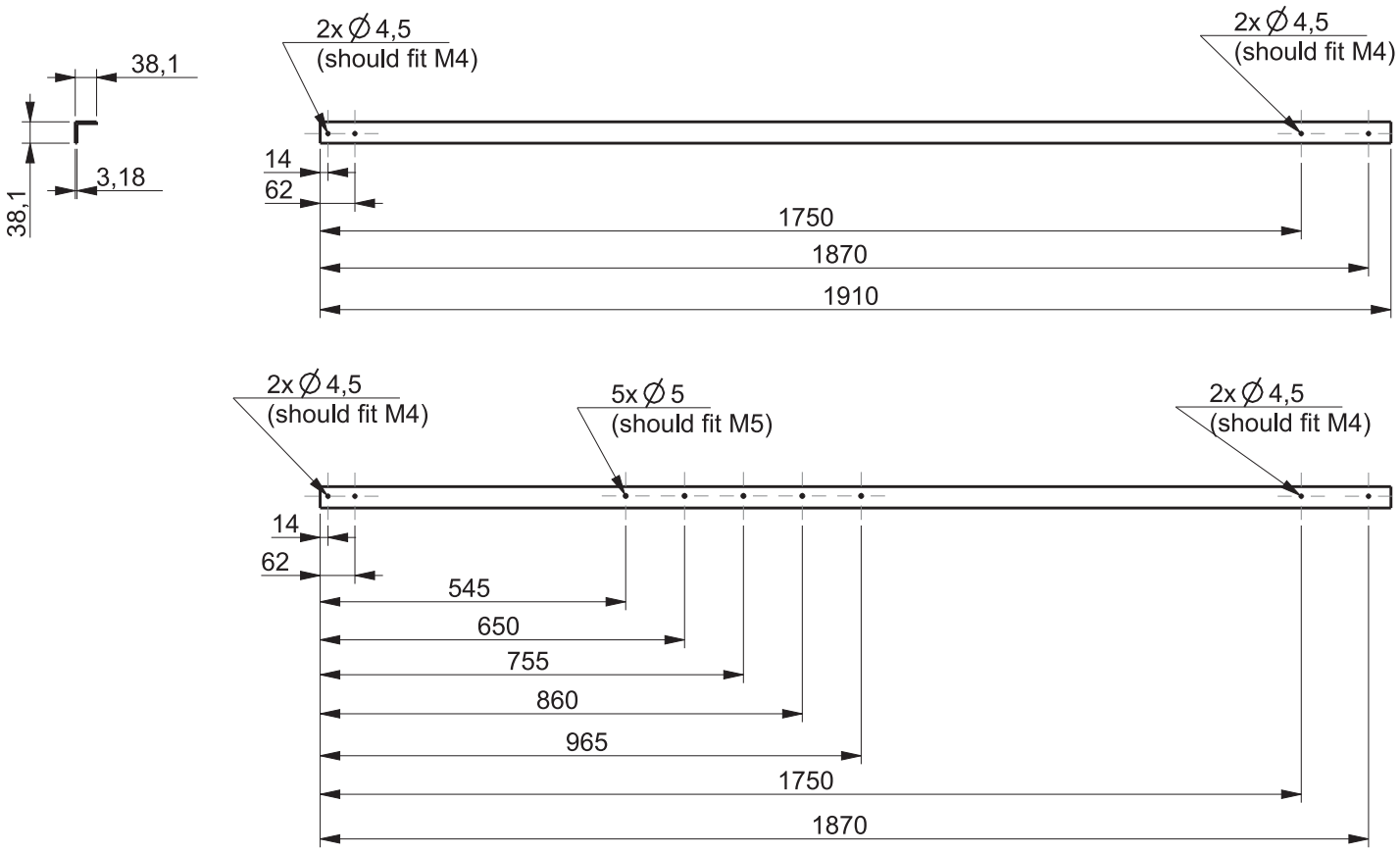

BOTTOM RAIL	right side
# items:	1
material:	aluminium

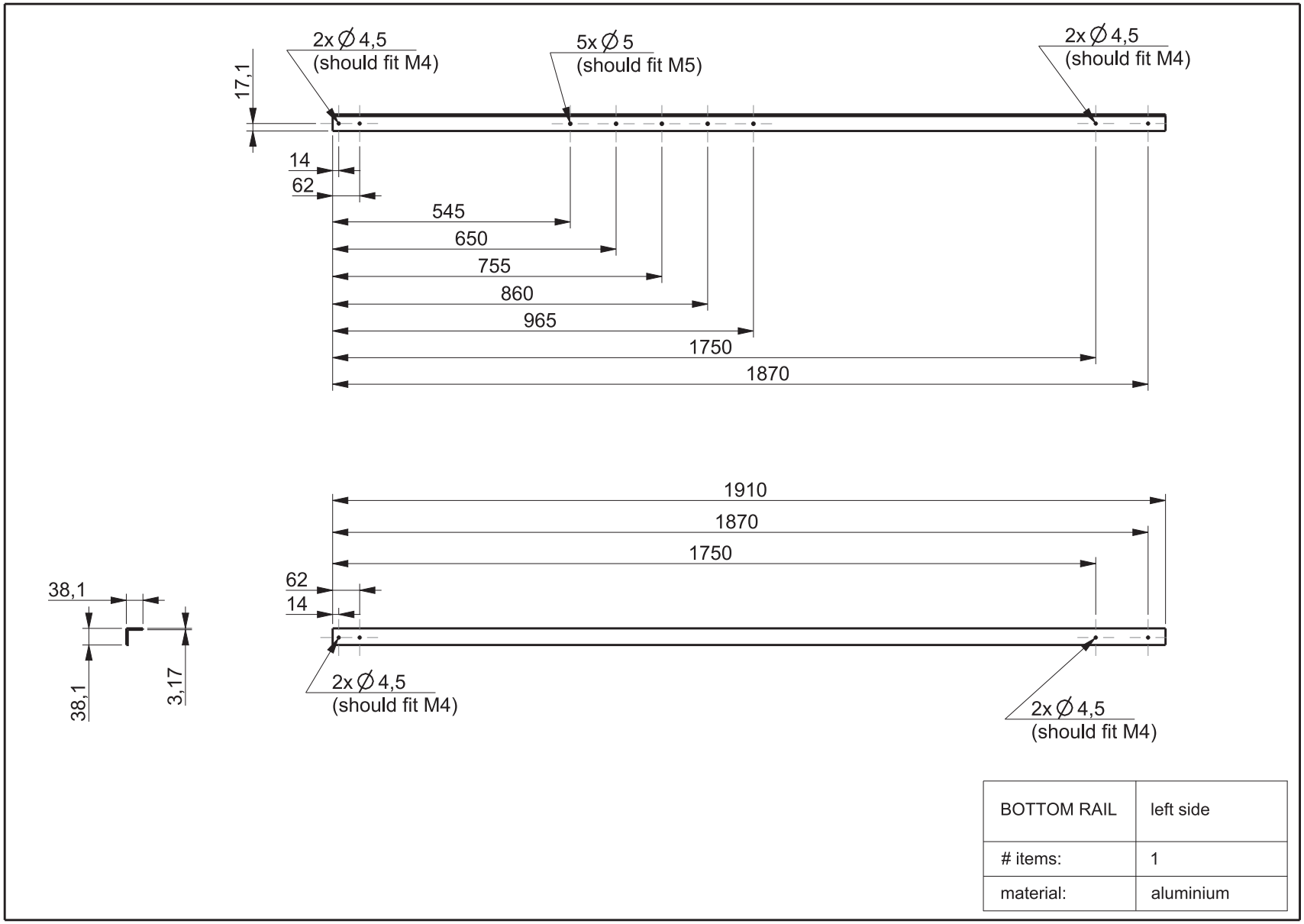

BOTTOM RAIL	left side
# items:	1
material:	aluminium

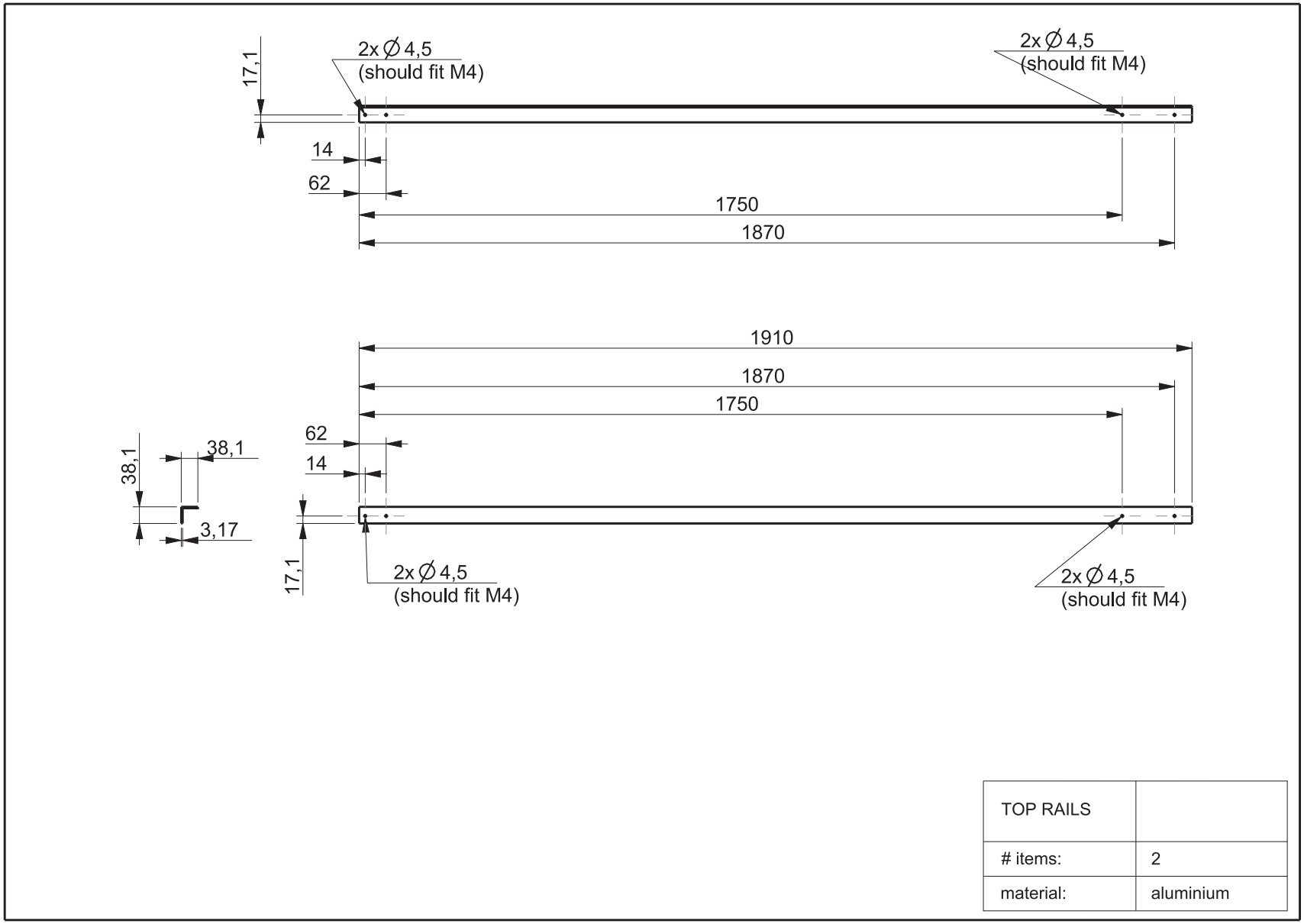

TOP RAILS	
# items:	2
material:	aluminium

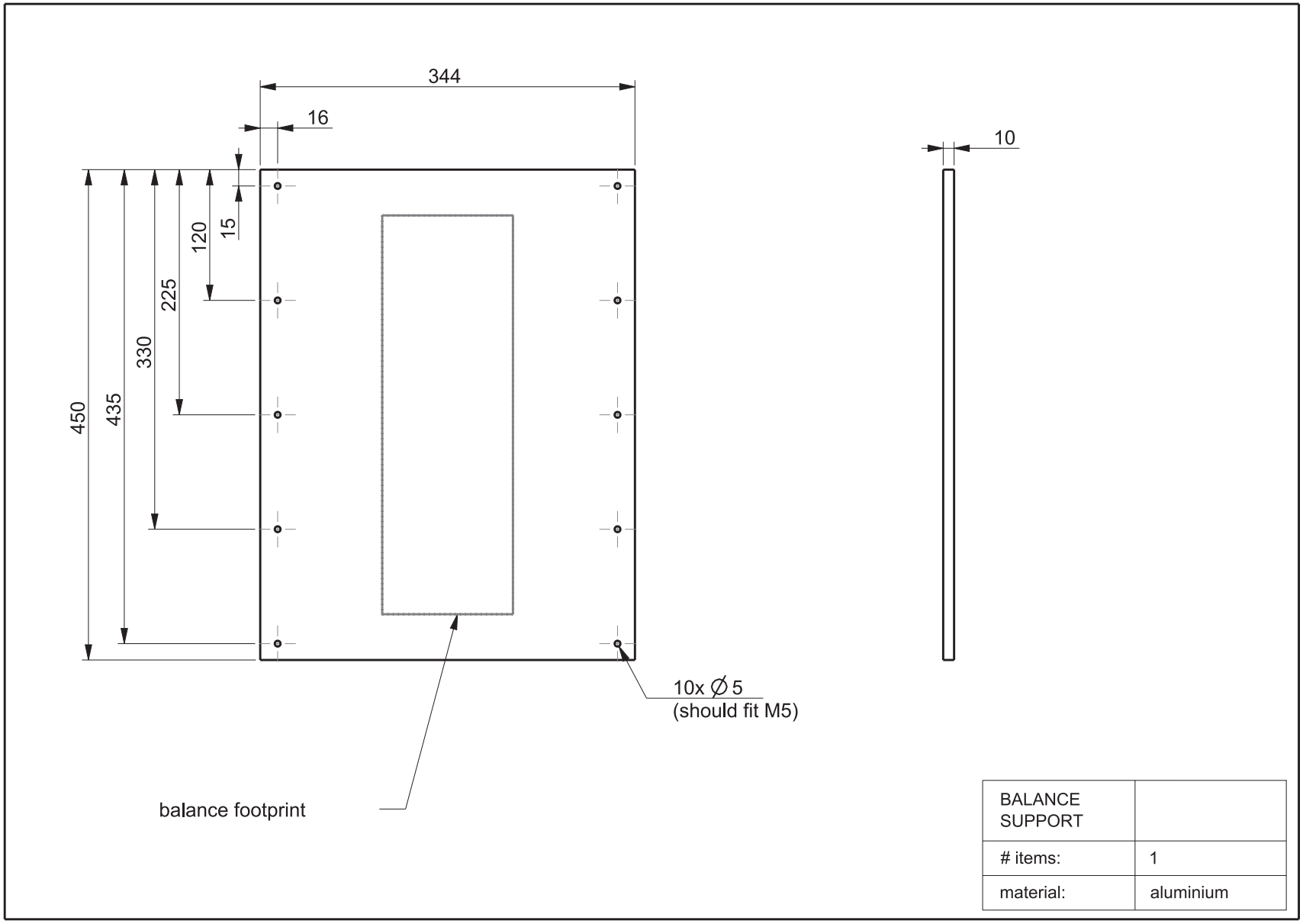

BALANCE SUPPORT	
# items:	1
material:	aluminium

BASE	exploded view
# items:	1
material:	mixed

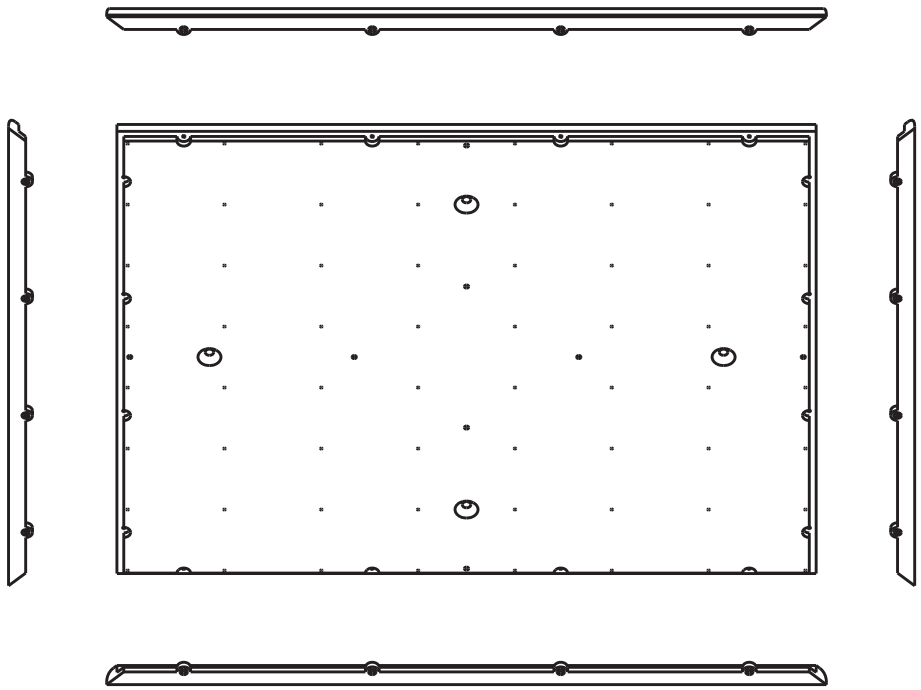

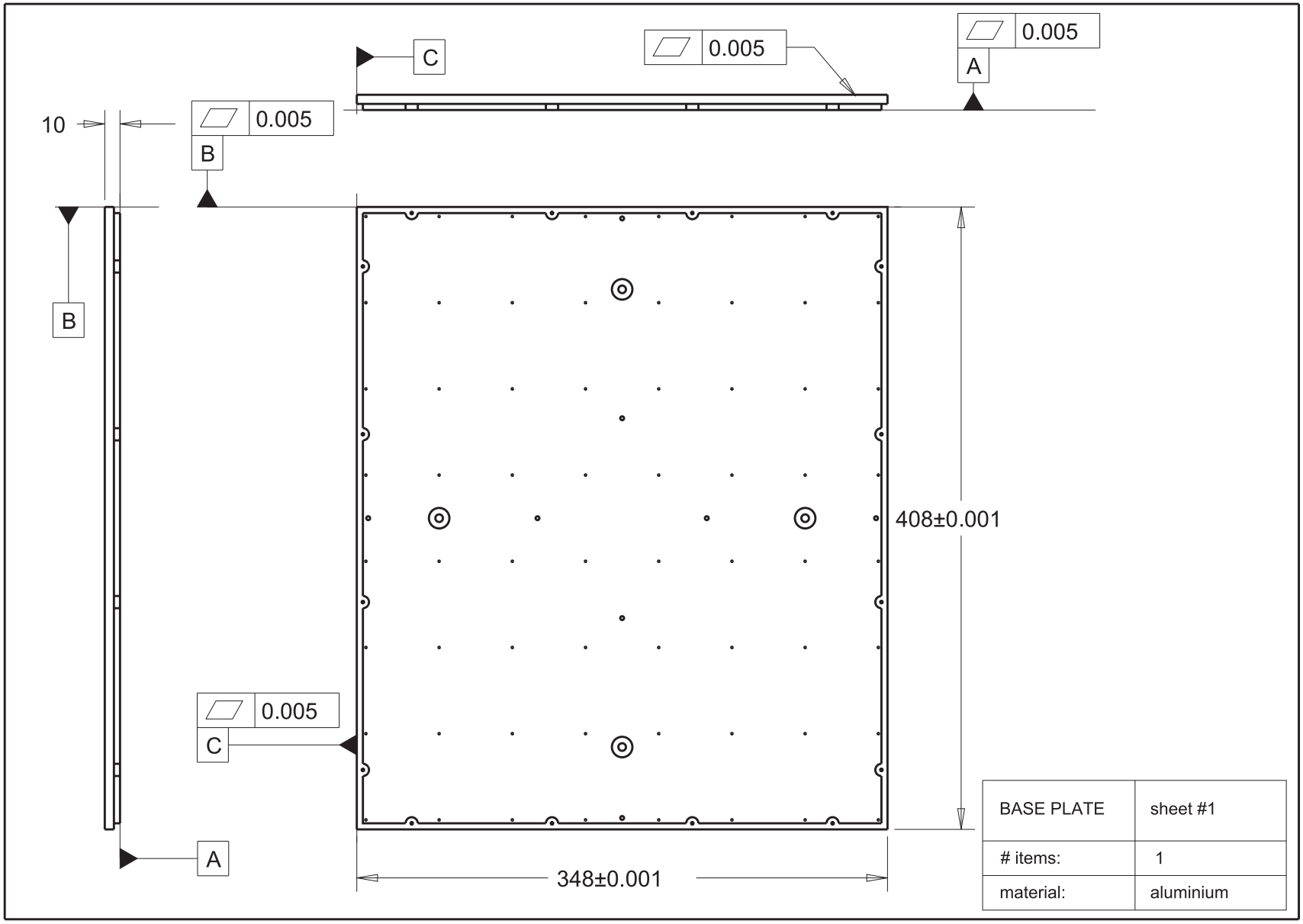
0.005
A
C
0.005
10
0.005
B
B
408±0.001
0.005
C
A
348±0.001
BASE PLATE
sheet #1
items:
1
material:
aluminium

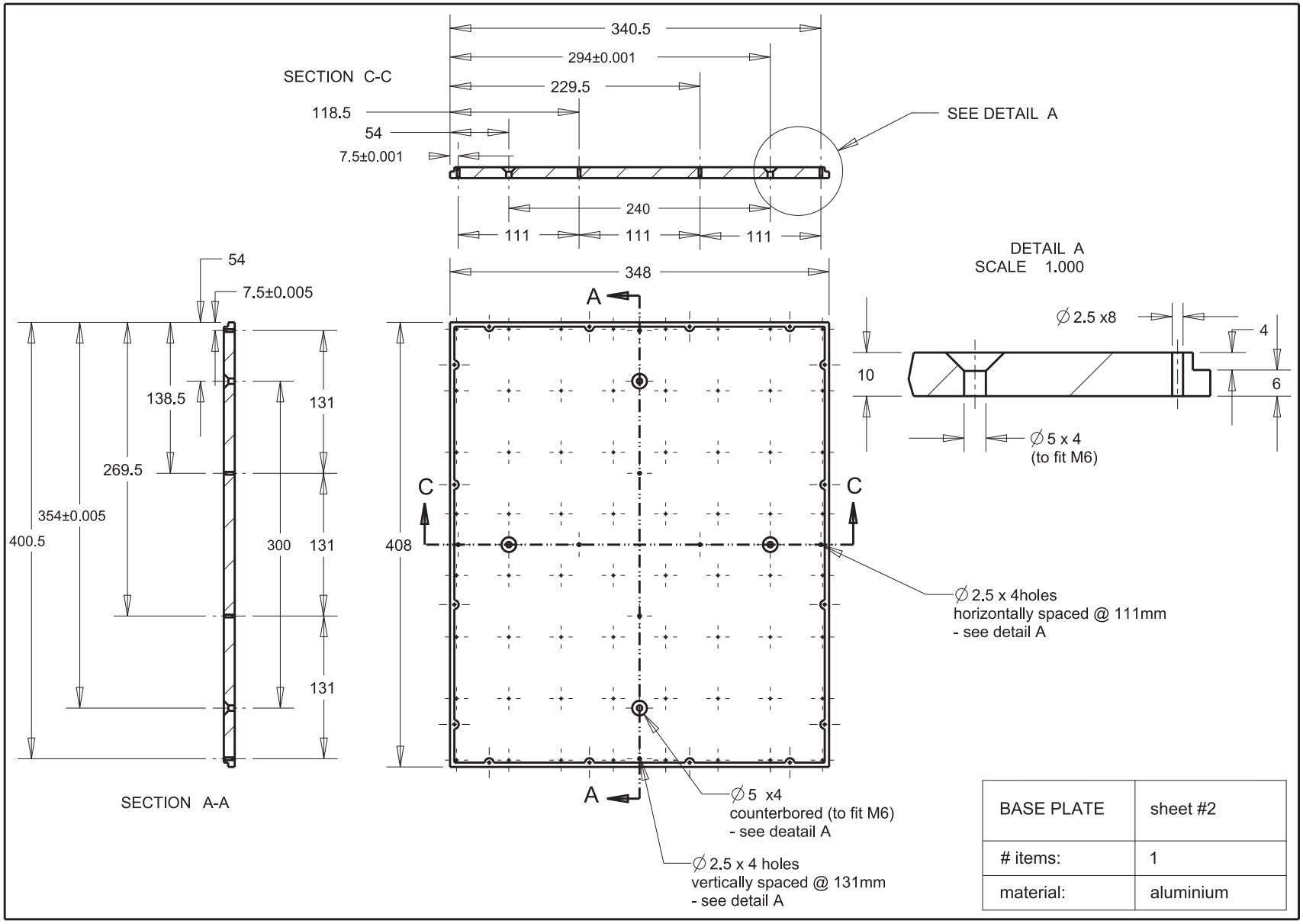

BASE PLATE	sheet #2
# items:	1
material:	aluminium

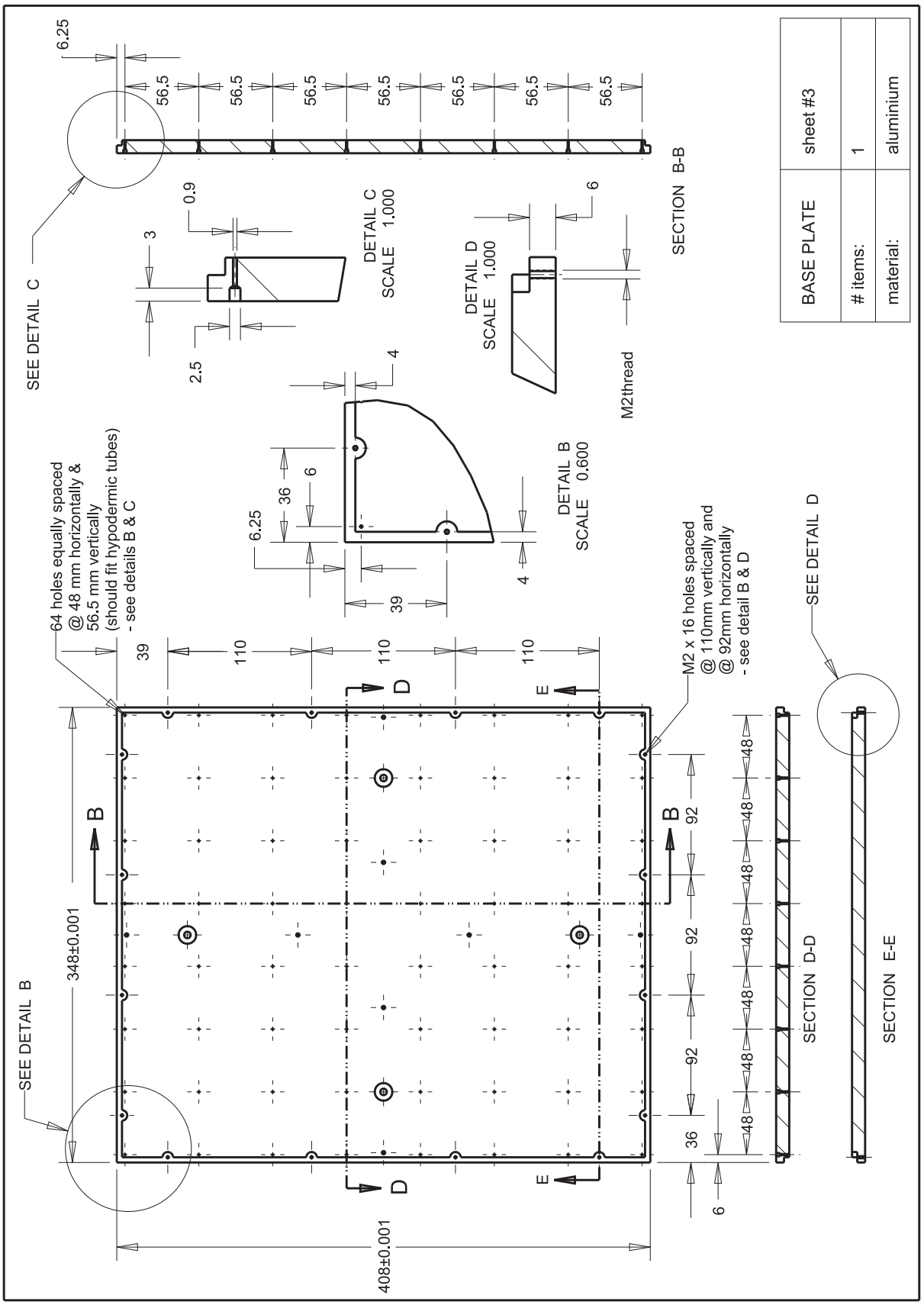
BASE PLATE
sheet #3
items:
1
material:
aluminium
SEE DETAIL C
SECTION B-B
DETAIL C
SCALE 1.000
DETAIL D
SCALE 1.000
M2thread
DETAIL B
SCALE 0.600
64 holes equally spaced
@ 48 mm horizontally &
56.5 mm vertically
(should fit hypodermic tubes)
- see details B & C
M2 x 16 holes spaced
@ 110mm vertically and
@ 92mm horizontally
- see detail B & D
SEE DETAIL B
SEE DETAIL D
SECTION D-D
SECTION E-E
348±0.001
408±0.001

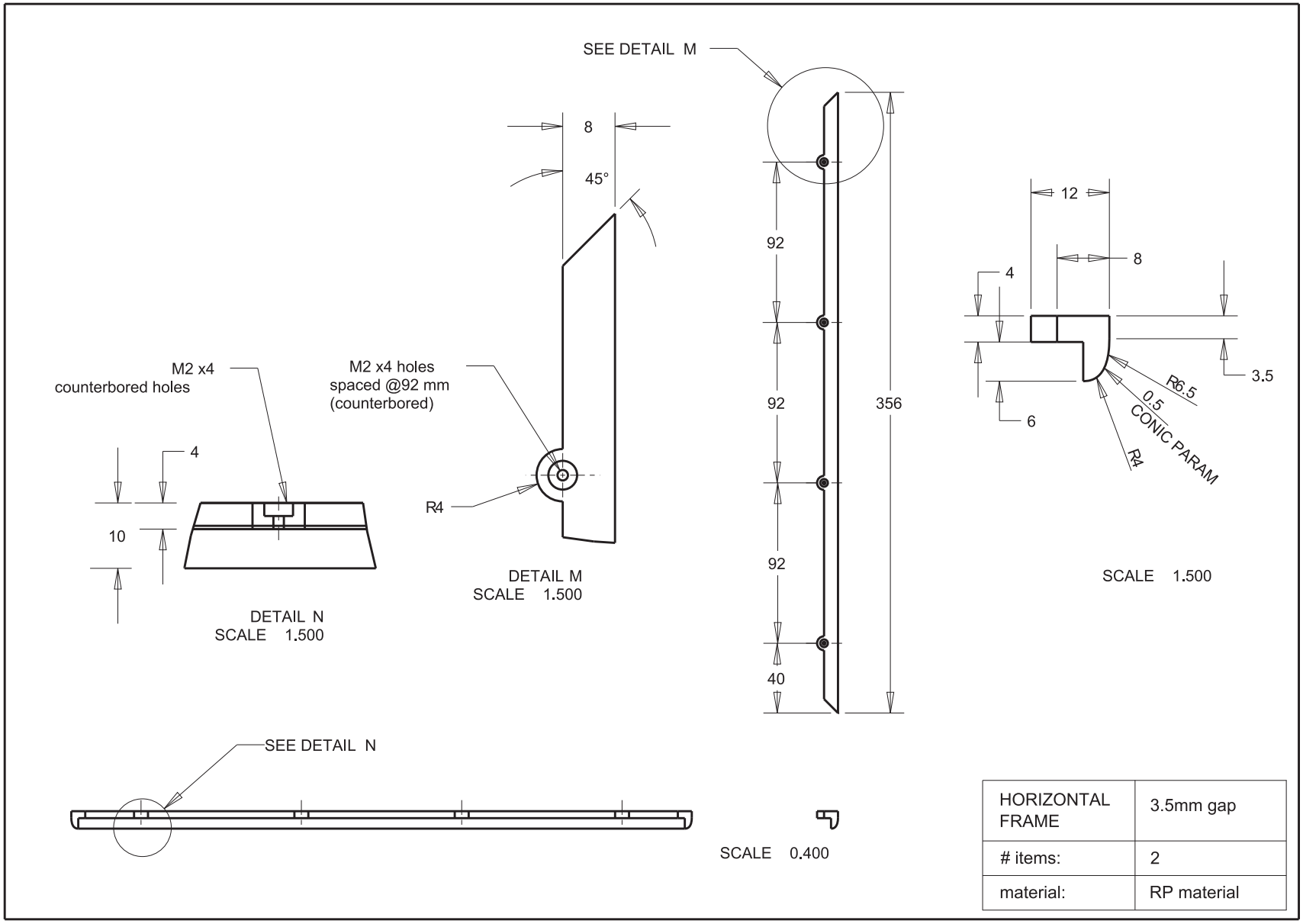

HORIZONTAL FRAME	3.5mm gap
# items:	2
material:	RP material

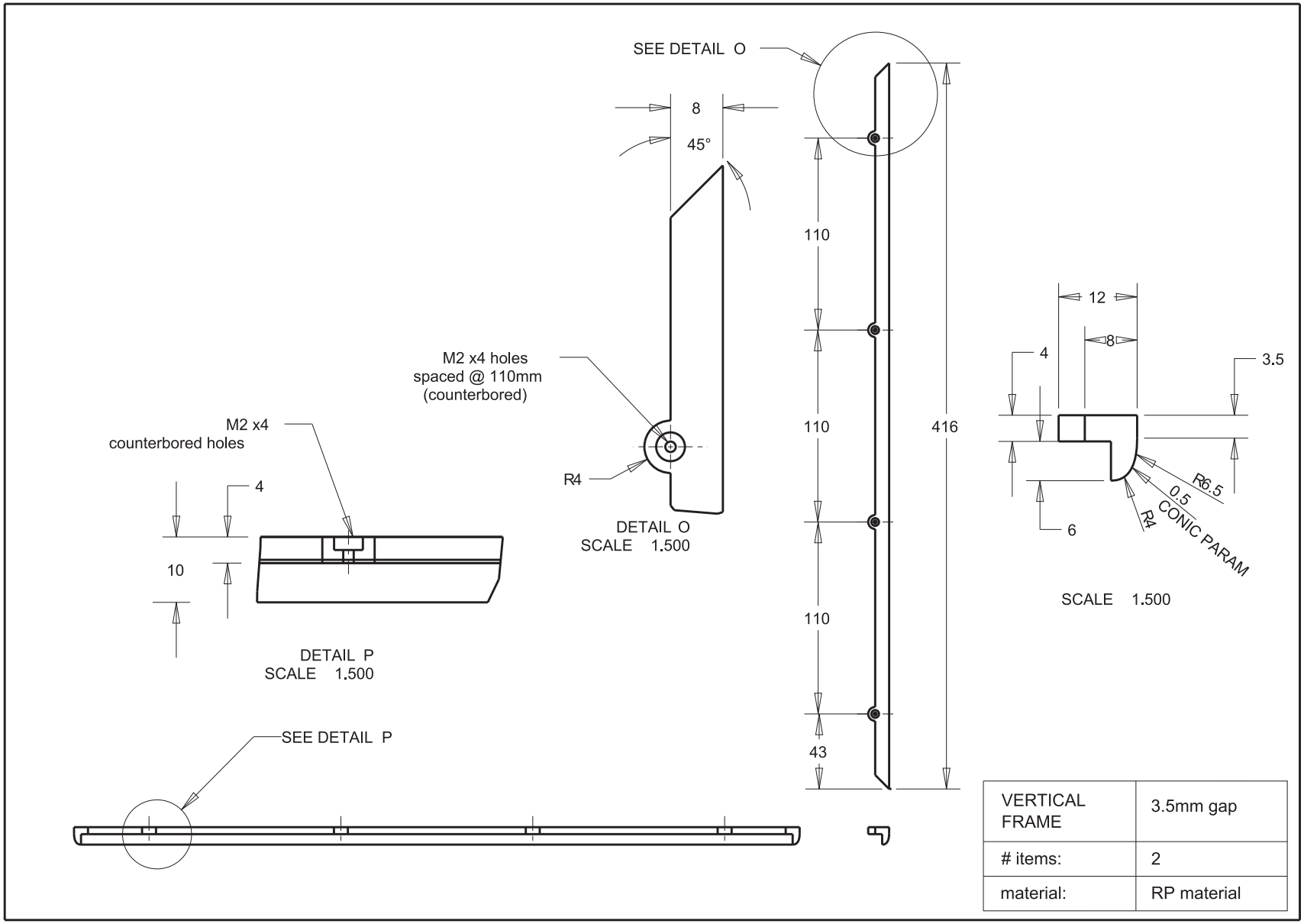

VERTICAL FRAME	3.5mm gap
# items:	2
material:	RP material

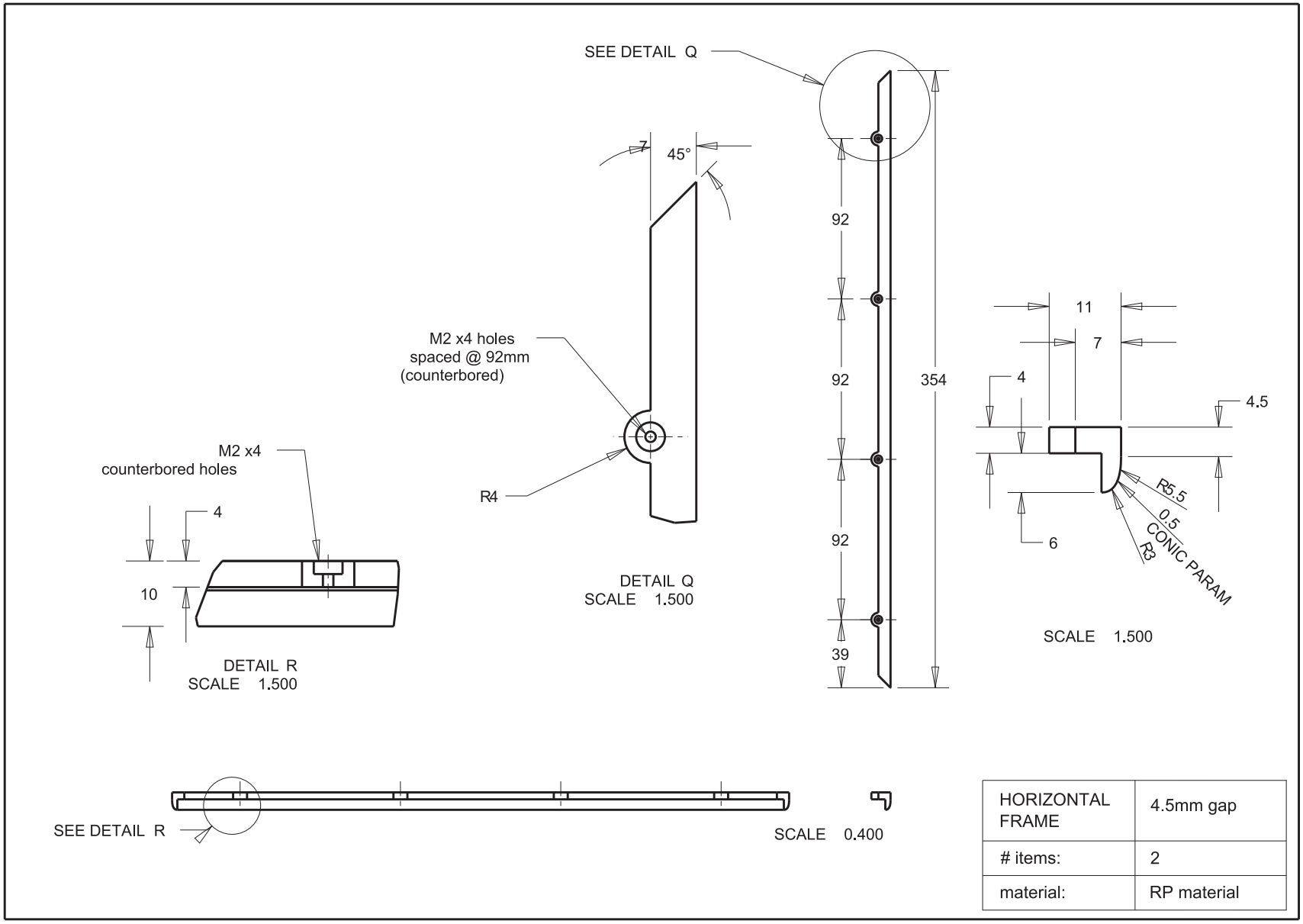

HORIZONTAL FRAME	4.5mm gap
# items:	2
material:	RP material

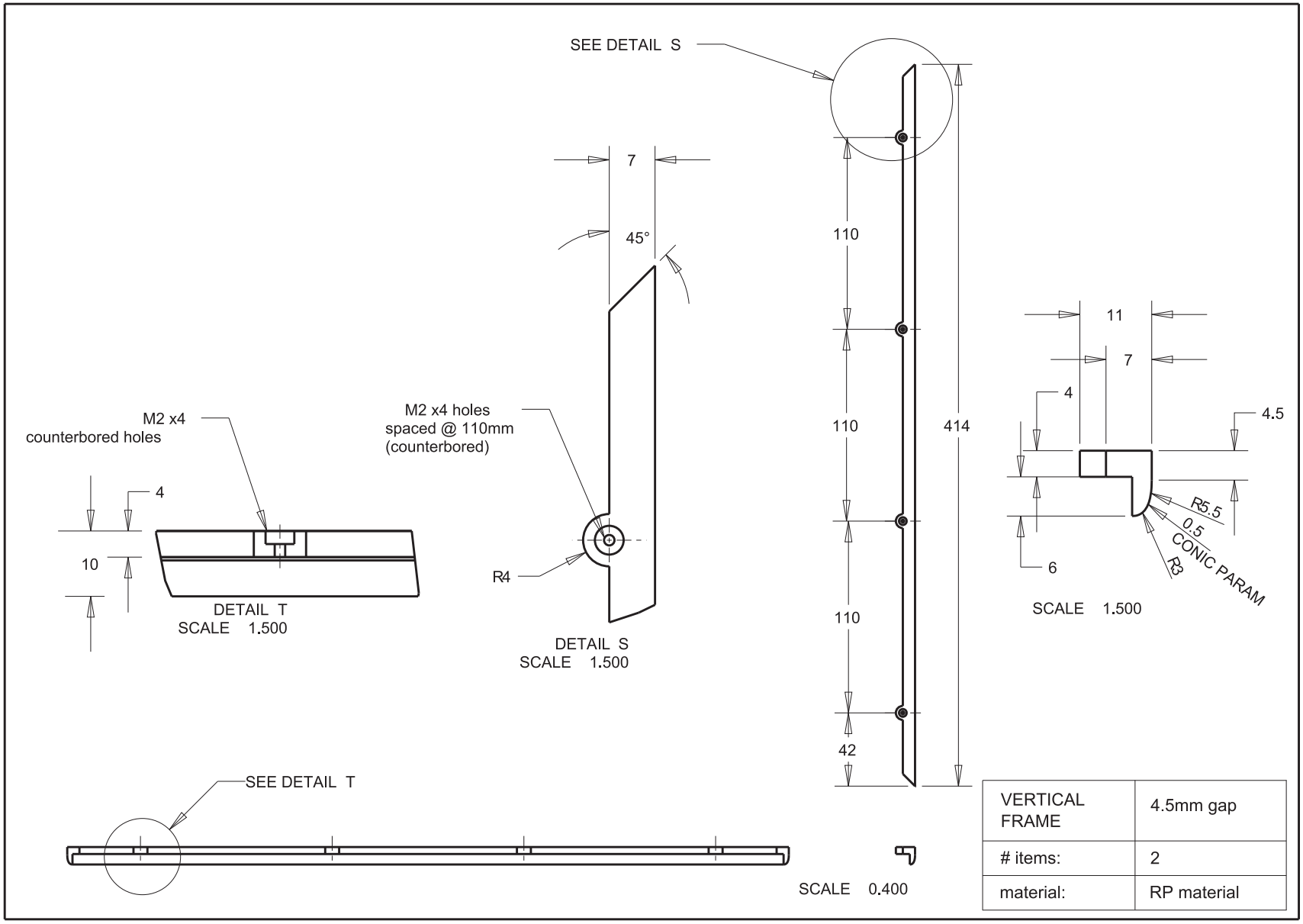

VERTICAL FRAME	4.5mm gap
# items:	2
material:	RP material

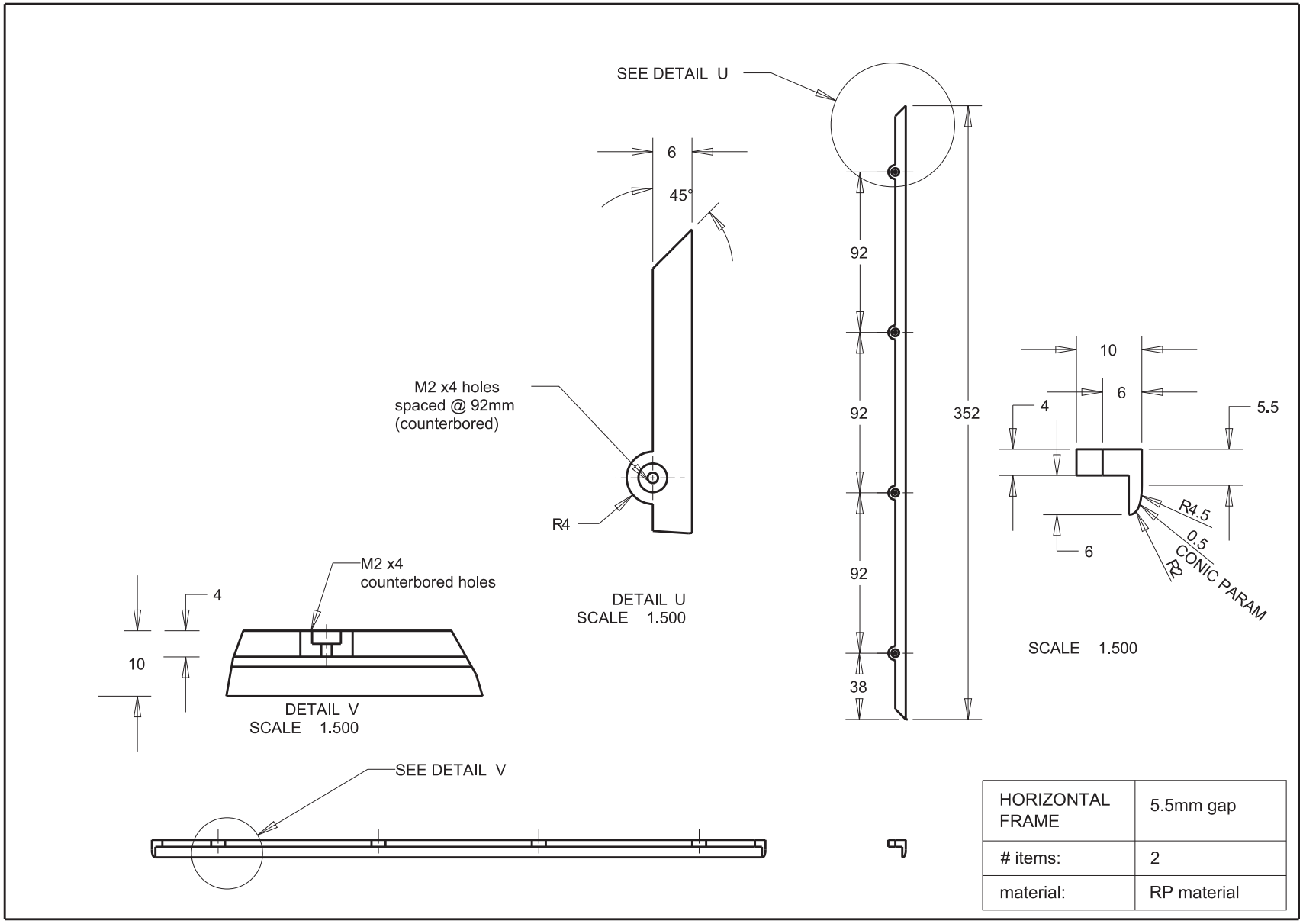

HORIZONTAL FRAME	5.5mm gap
# items:	2
material:	RP material

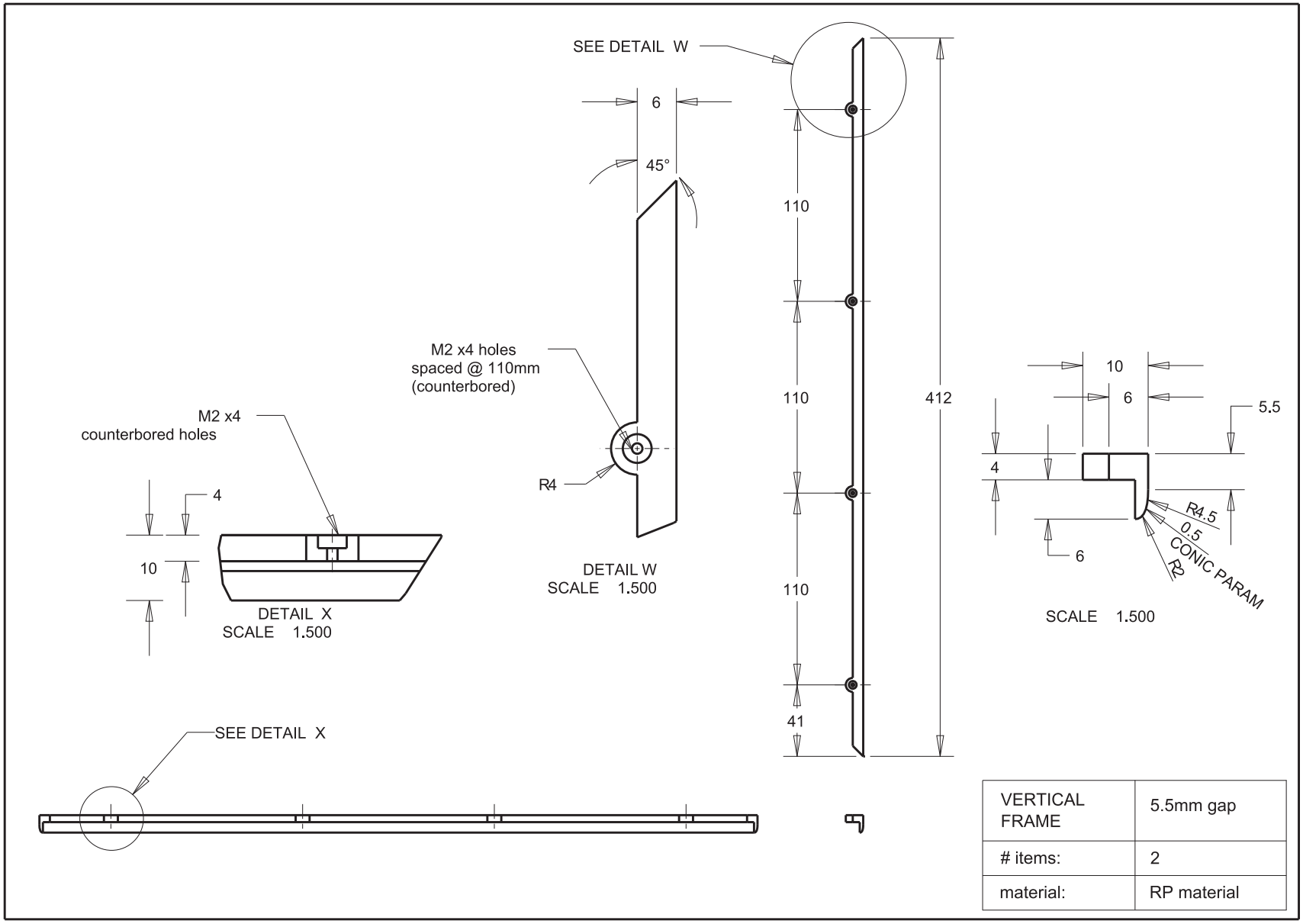

VERTICAL FRAME	5.5mm gap
# items:	2
material:	RP material

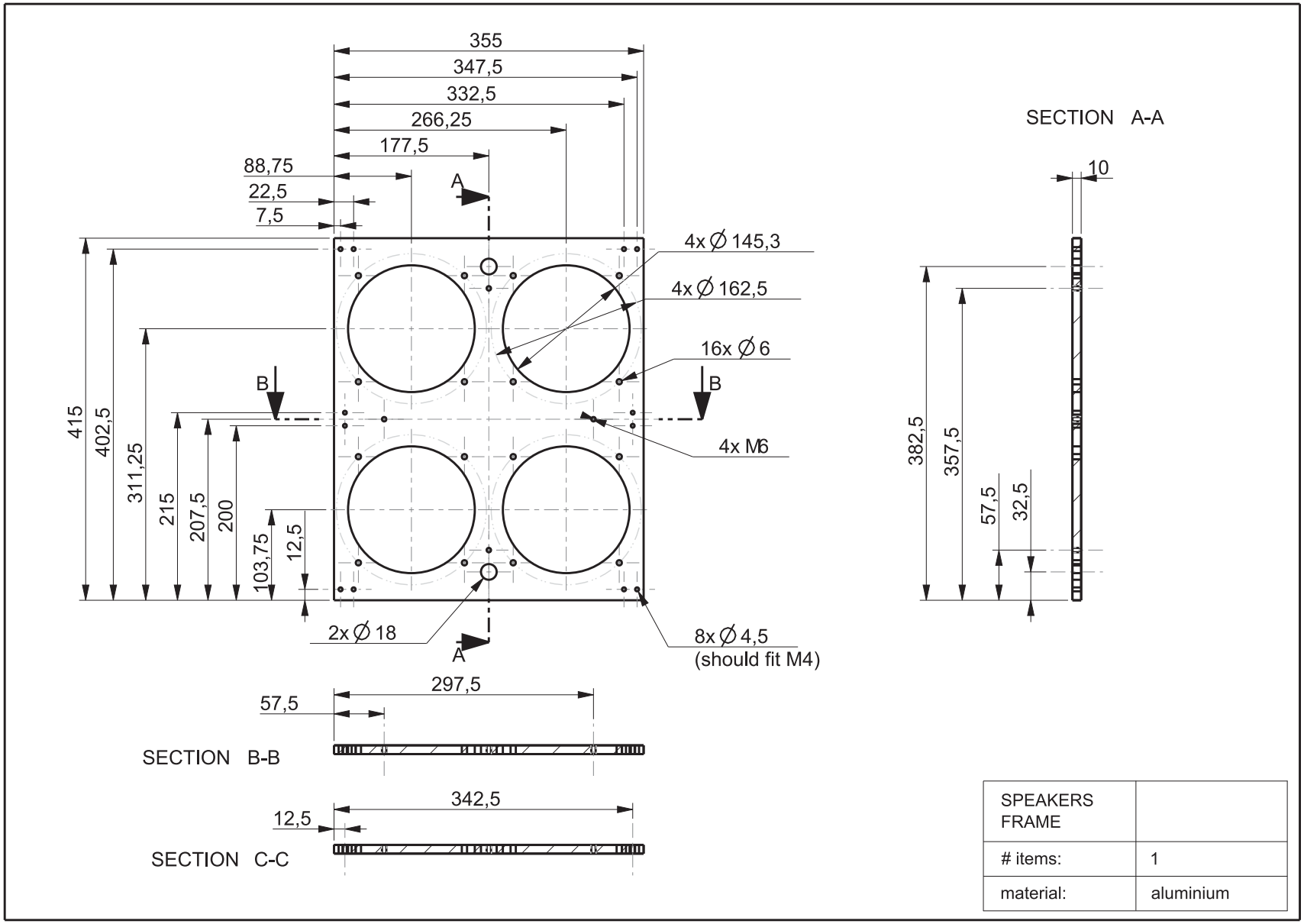
355
347,5
332,5
266,25
177,5
88,75
22,5
7,5
A
4x ∅ 145,3
4x ∅ 162,5
16x ∅ 6
B
B
4x M6
415
402,5
311,25
215
207,5
200
103,75
12,5
2x ∅ 18
A
8x ∅ 4,5
(should fit M4)
SECTION A-A
10
382,5
357,5
57,5
32,5
297,5
57,5
SECTION B-B
342,5
12,5
SECTION C-C
SPEAKERS FRAME
items: 1
material: aluminium

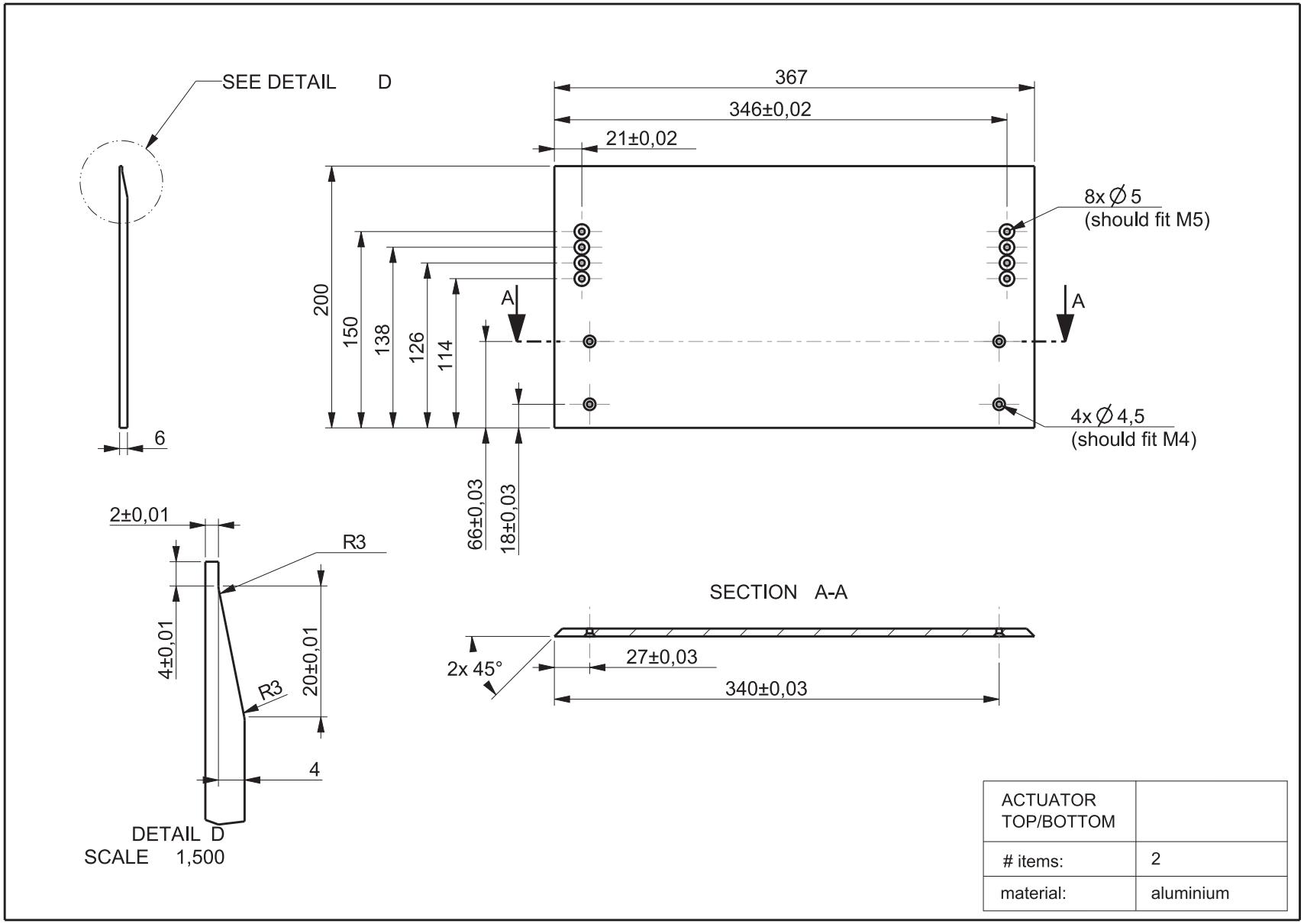

ACTUATOR TOP/BOTTOM	
# items:	2
material:	aluminium

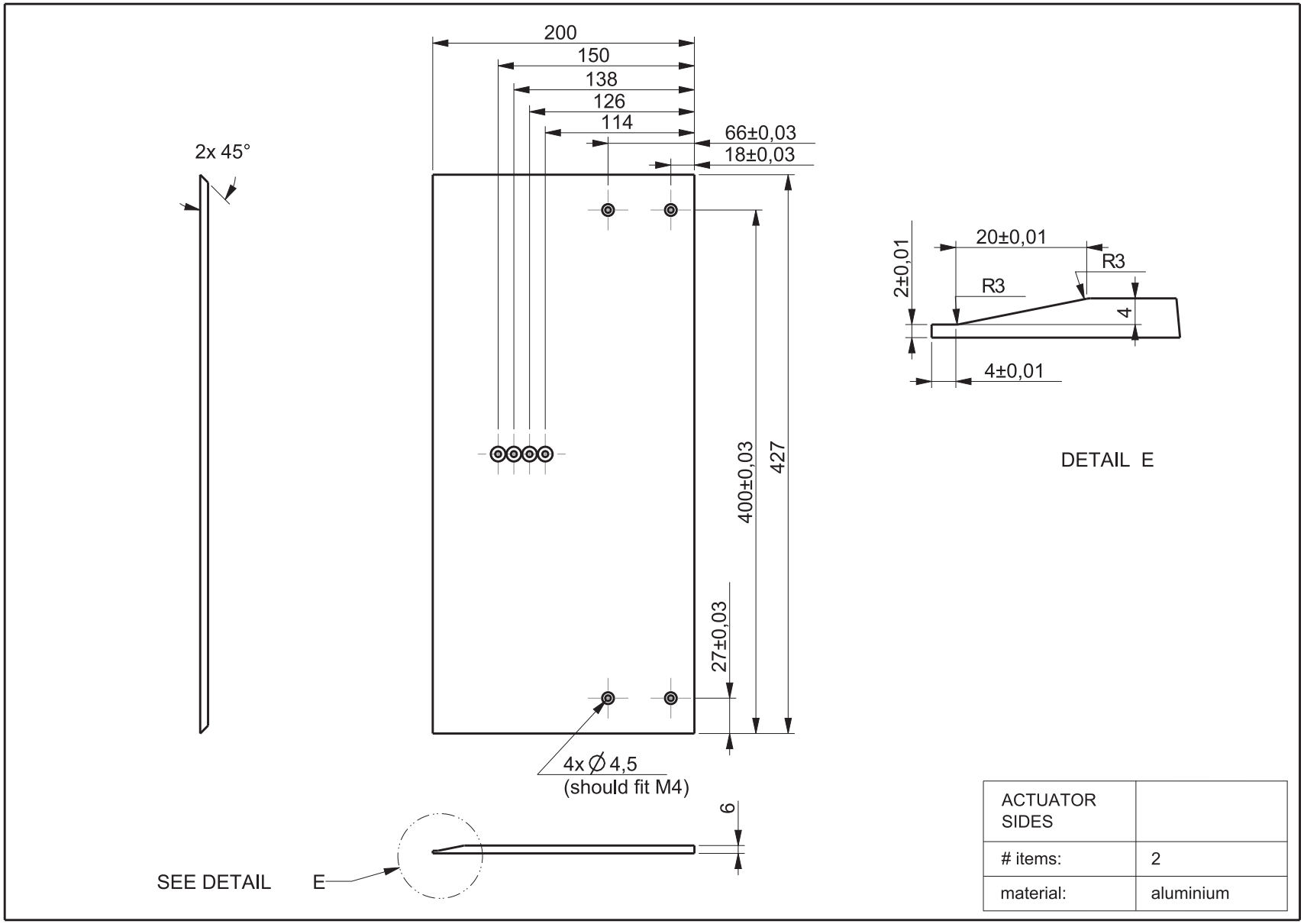

ACTUATOR SIDES	
# items:	2
material:	aluminium

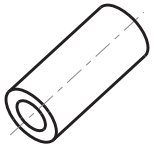

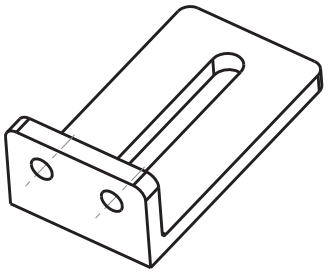

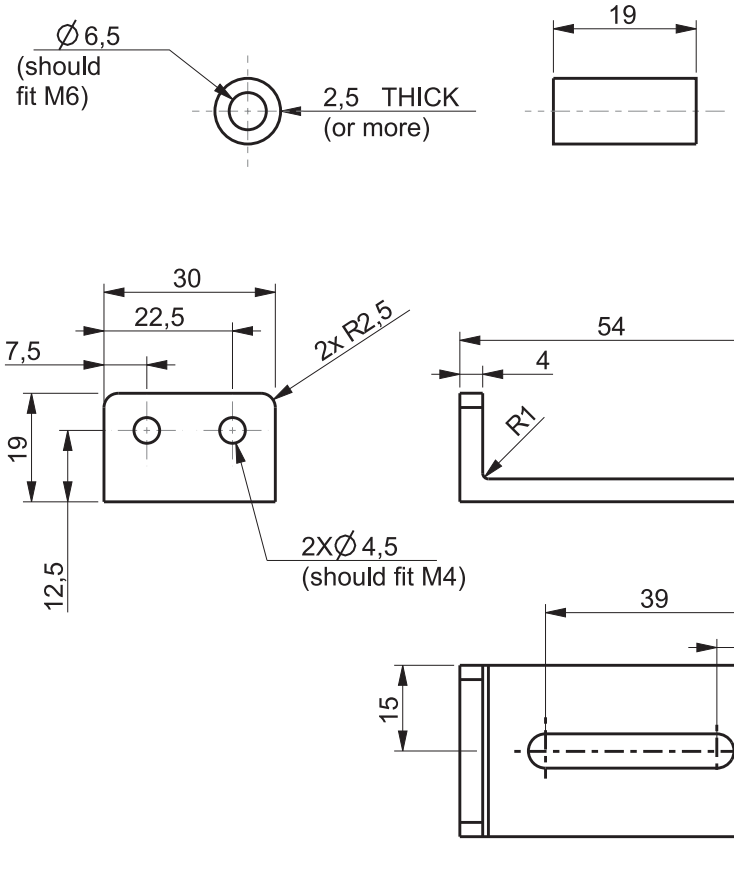

SPEAKER FRAME SUPPORTS + BASE SPACERS	
# items:	6 + 4
materials:	aluminium + steel

FRONT CAB
assembly +
exploded view
items:
material:
jelutong

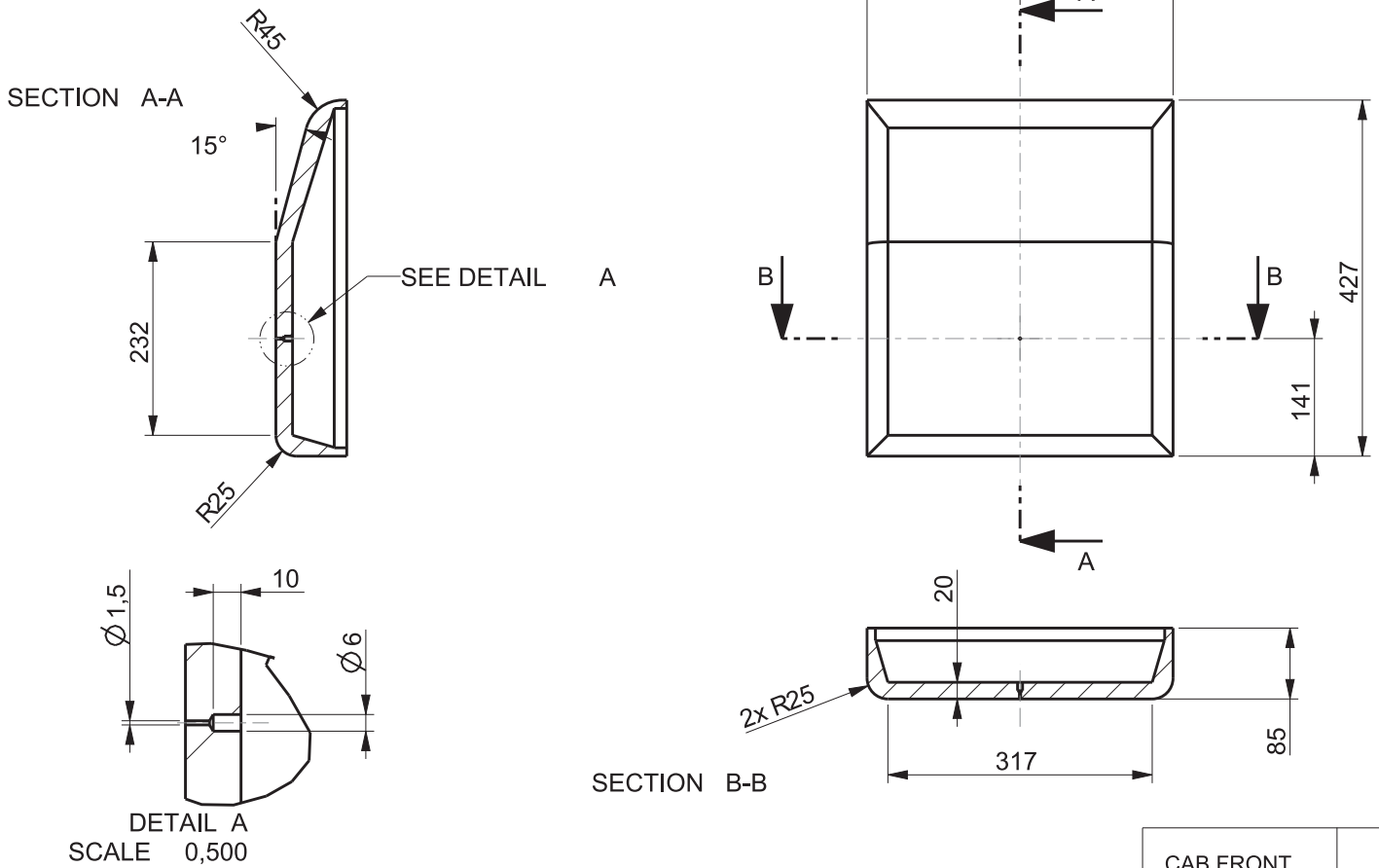

CAB FRONT	
# items:	1
material:	jelutong

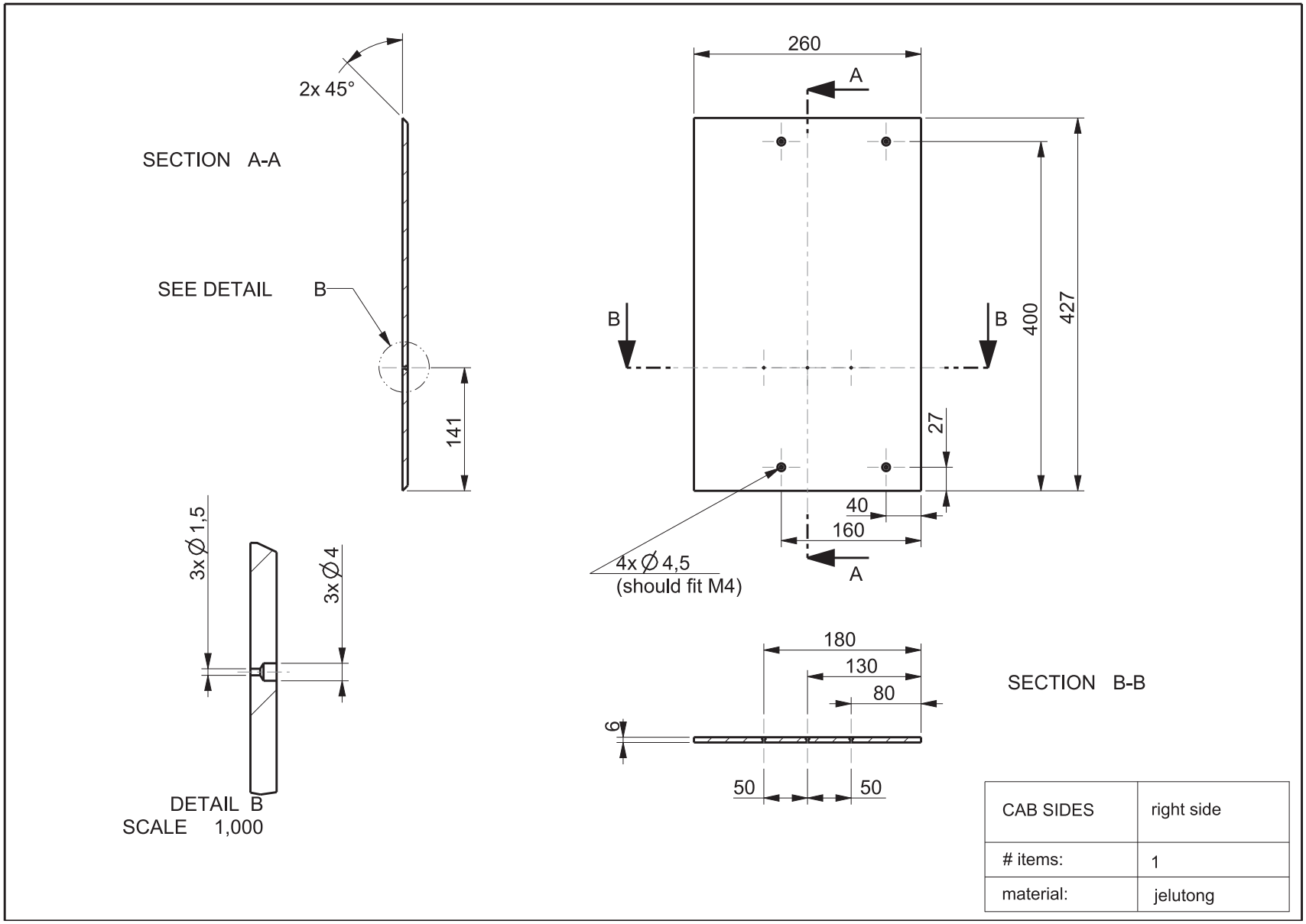
2x 45°
SECTION A-A
SEE DETAIL B
141
3x ∅1,5
3x ∅4
DETAIL B
SCALE 1,000
260
A
B
B
400
427
27
40
160
A
4x ∅4,5
(should fit M4)
180
130
80
6
50
50
SECTION B-B
CAB SIDES
right side
items:
1
material:
jelutong

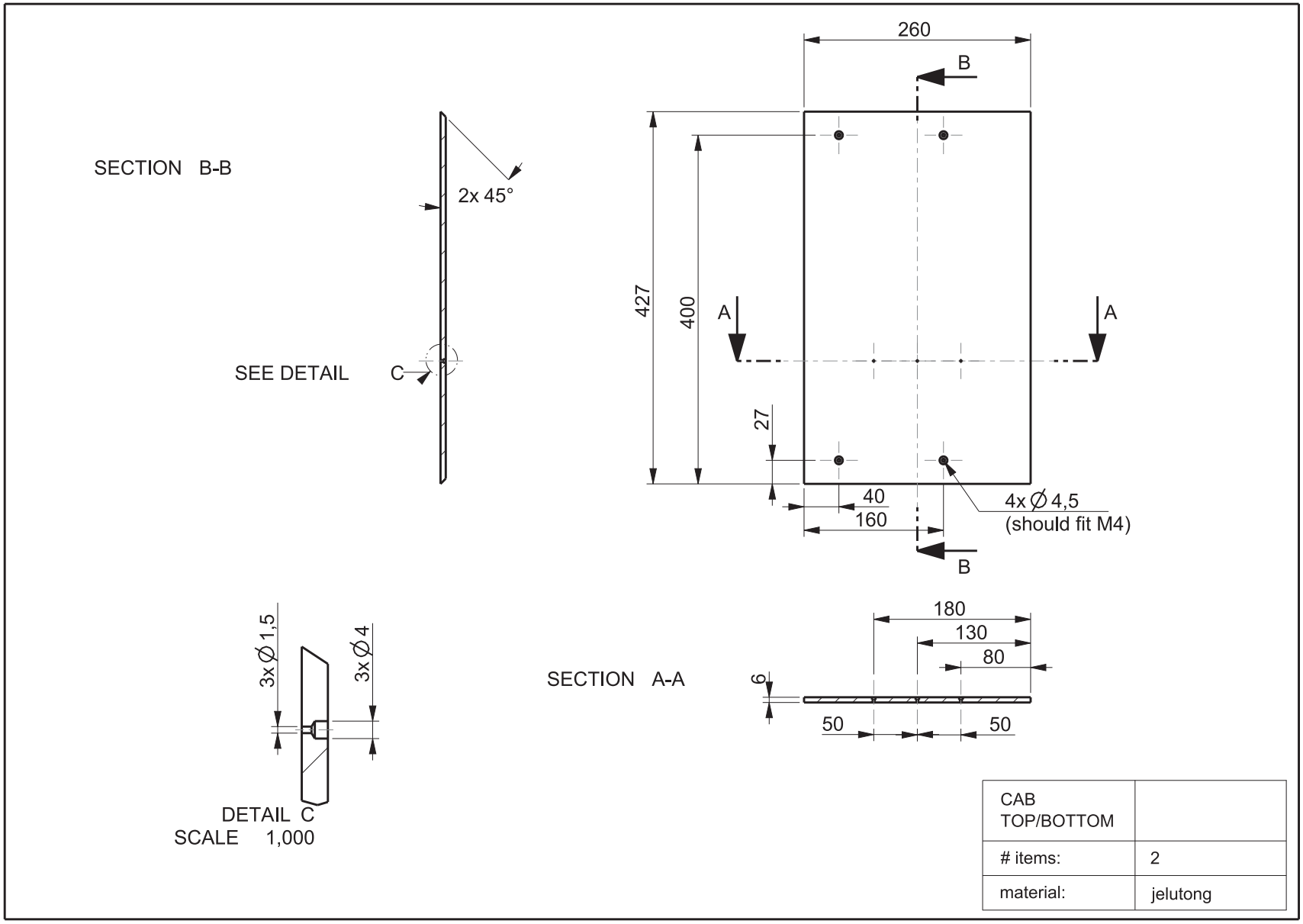
SECTION B-B
2x 45°
SEE DETAIL
C
260
B
427
400
A
A
27
40
160
4x ∅ 4,5
(should fit M4)
B
3x ∅ 1,5
3x ∅ 4
DETAIL C
SCALE 1,000
SECTION A-A
180
130
80
6
50
50
CAB
TOP/BOTTOM
items:
2
material:
jelutong

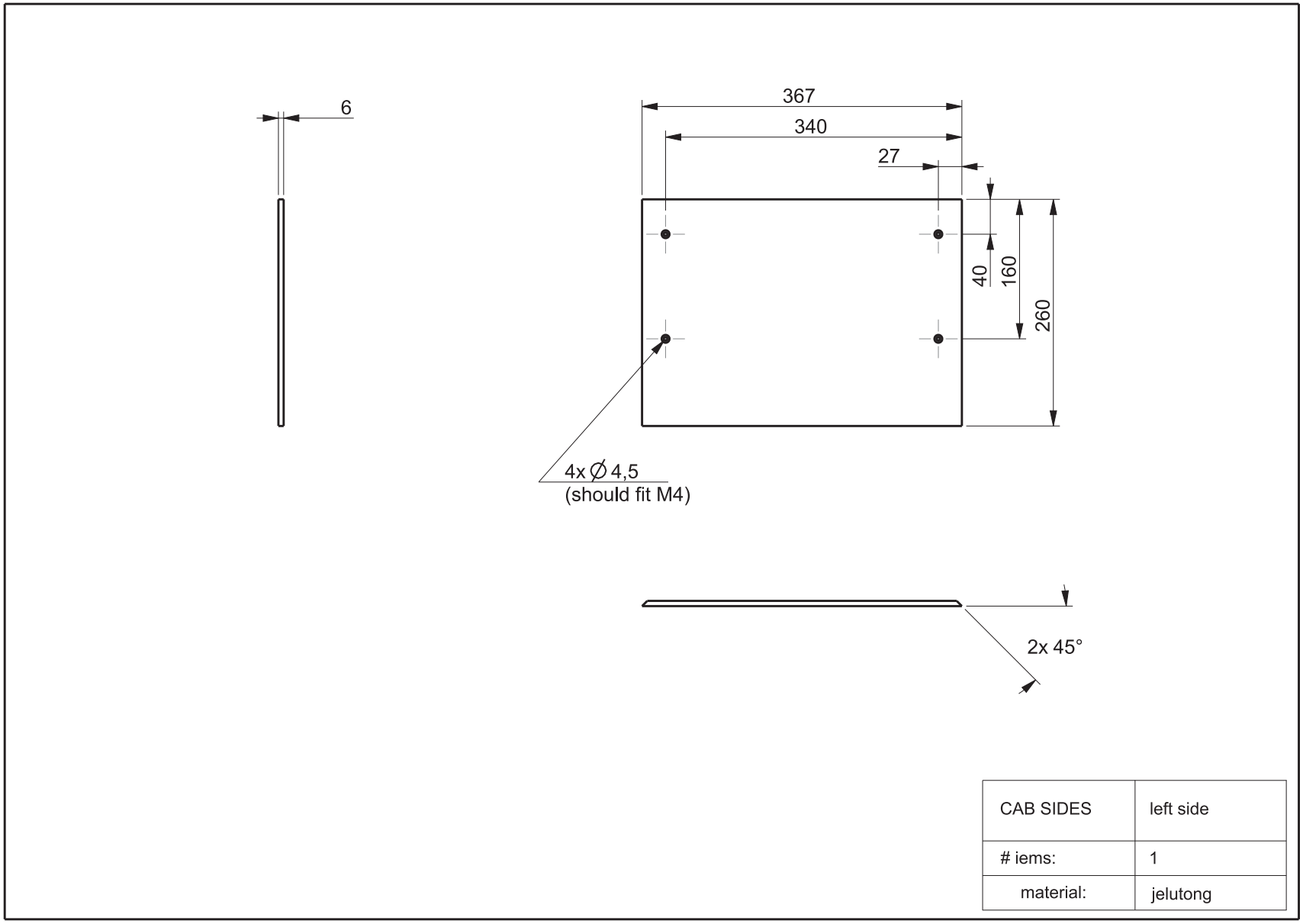

CAB SIDES	left side
# iems:	1
material:	jelutong

CAB + FOAM
assembly
items:
1
material:
mixed

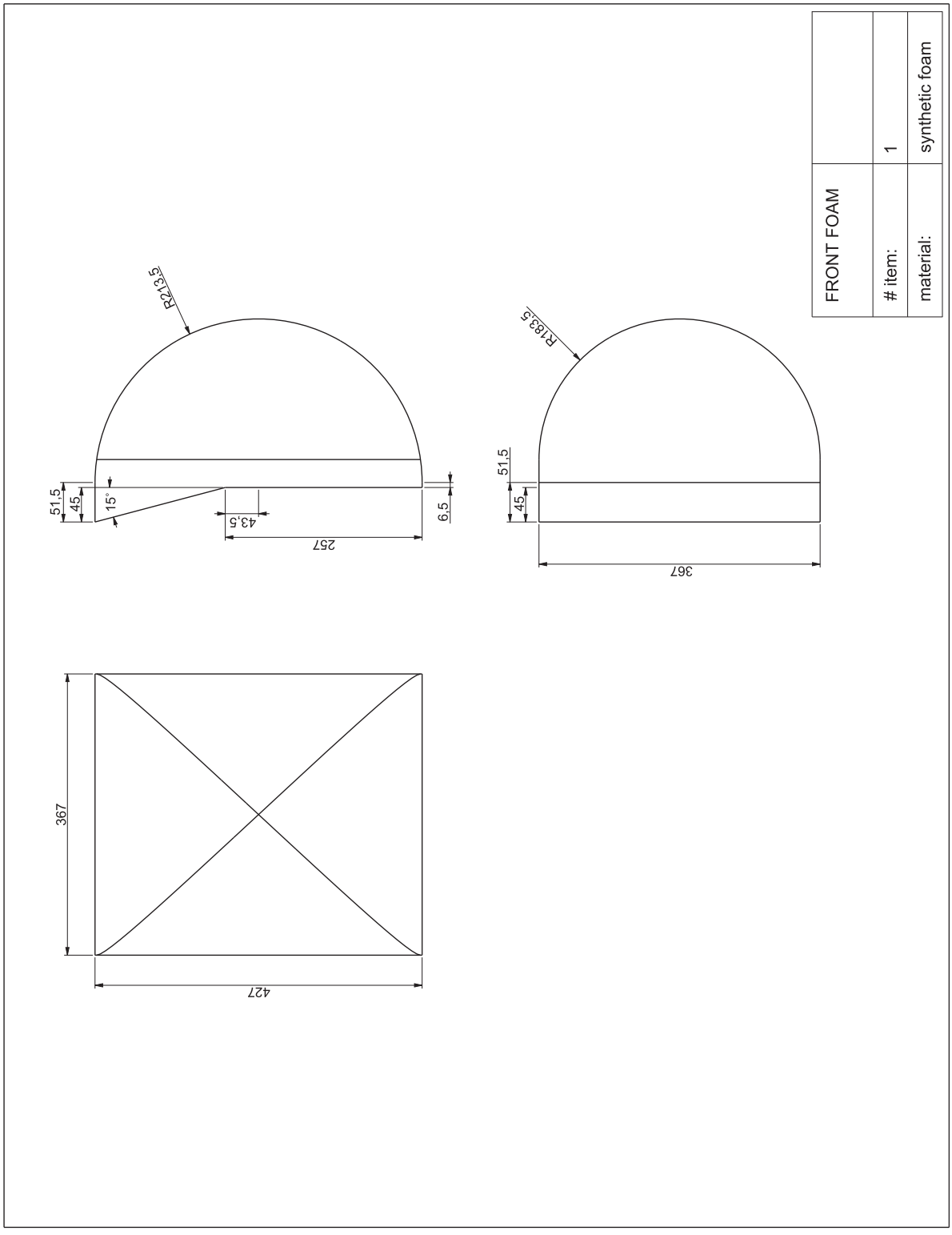
FRONT FOAM
item: 1
material: synthetic foam
R213,5
51,5
45
15°
43,5
257
6,5
R183,5
51,5
45
367
367
427

Appendix F

Photos

Figure F.1: Model in wind tunnel installation - front view.

Figure F.2: Model in wind tunnel installation - rear view.

Figure F.3: Synthetic jet actuator set-up.

(a)

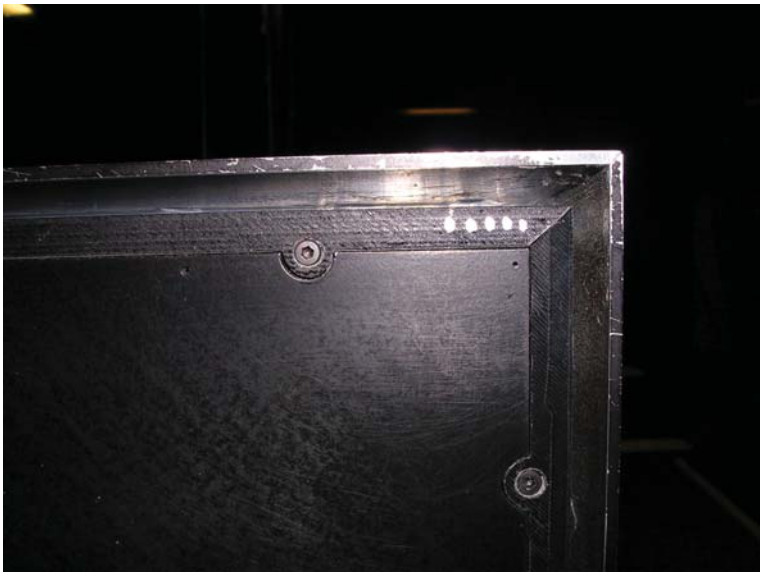

(b)

Figure F.4: Close-up of the 5.5 mm slot – side (a) top-left corner (b).

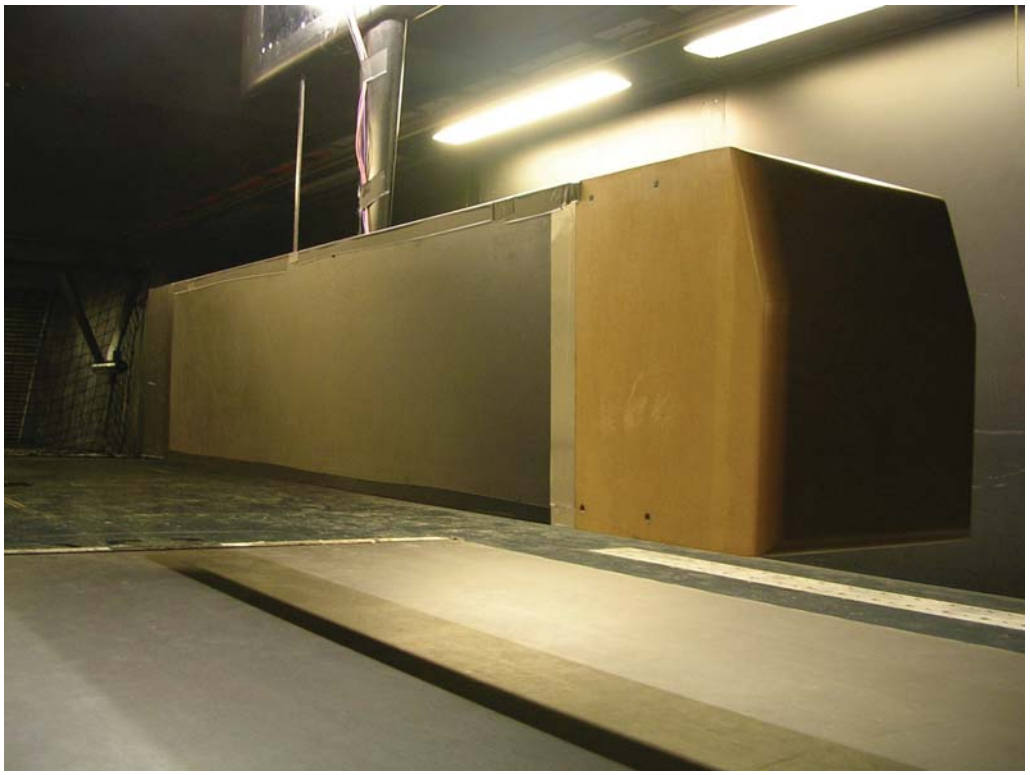

Figure F.5: Wind tunnel installation with model with square cab.

Figure F.6: Wind tunnel installation during Universities and Science Minister David Willetts' visit.